
# Nanostructured Polymer-Glass Hybrid Coatings

**Nora Iturraran Santiso**

**A thesis submitted in partial fulfilment of the requirements of London South Bank University for the degree of Doctor of Philosophy**

**June 2019**

# Abstract

The increased attention received by polymer nanocomposites in recent years, has opened the way to research on nanostructured glass polymer hybrids for coating applications. Using polyamide 11 and adding fillers (in this case glass) at the nanometre length scale can lead to innovative modifications to the polymer matrix, giving rise to new structures and properties. This could develop new materials with enhanced properties and may enlarge the coating market to other application areas. Some of the main obstacles to overcome are the control of glass particle size to obtain suitable dispersions on the nanoscale with interaction between components. Nanoscale structures require the development of optimal hybrid precursors. Finding a way to develop the hybrids using melt compounding methods like extrusion, particle size processes and coating techniques have been investigated in this research. The nanostructured hybrids are made using macroscopic fillers, which avoids problems with current regulations on ultra-fine particles.

Fourier-transform infrared spectroscopy (FTIR) and Raman spectroscopy indicate the glass structure during synthesis of tin fluoride phosphate glass was pyrophosphate, mainly built up from phosphate tetrahedral units with one bridging oxygens present within a particular phosphate tetrahedron $Q^1$ end groups with a low concentration of phosphate tetrahedral units with two bridging oxygens $Q^2$ polymeric chains. However, sub-optimal melting produced significantly higher concentrations of phosphate tetrahedral units with no bridging oxygens present within a particular phosphate tetrahedron $Q^0$ orthophosphate structural units. The variations in NH and $P-OH$ vibrations in the spectra revealed that a critical time and temperature of melting were necessary for the conversion of $NH_4H_2PO_4$ to produce sufficient $P_2O_5$ for glass forming. During melting, $P_2O_5$ and $SnF_2$ formed a low-temperature melt, which facilitated melting of the SnO and promoted the formation of a more stable glass structure. The fluorine breaks the $P-O-P$ bonds and induces depolymerisation. The density of the glass reached a maximum at 450 °C for 25 min driven by the need for conversion of $NH_4H_2PO_4$ to $P_2O_5$ and miscibility of SnO in the melt. Inadequate melting times and temperatures gave low glass transition temperature (Tg) values

because of weak $F-Sn$ and $F-P$ linkages. Glass stability improved with melting due to increased $P_2O_5$ and $SnO$ miscibility enabling stronger $Sn-O-P$ linkages. The results show that melting conditions during synthesis strongly influence critical glass properties and also provide an understanding of optimum processing necessary for future industrial scale-up.

Novel hybrids of tin fluoride phosphate (TFP) glass (composition of $50\%\ SnF_2 + 20\%\ SnO + 30\%\ P_2O_5$) were synthesized with polyamide 11 and their morphology and mechanical properties investigated. Hybridization was achieved by melt blending up to 25 vol% of glass using different compounding conditions (temperature, screw speed and residence time). Scanning electron microscopy (SEM) showed that the morphology was greatly influenced by the extrusion processing temperature and the glass content. Transmission electron microscopy (TEM) studies revealed nanoparticles of 40 nm in size and suggested good compatibility. In order to determine the existence of miscibility between hybrid components, measurement of the loss tangent using a Dynamic Mechanical Analysis (DMA), was carried out. The presence of two transition peaks in the hybrid containing 34 vol% tin fluoride phosphate glass implied an immiscible system showing heterogeneously distributed regions of very different molecular mobilities. Contrary to the plasticizer effect reported in the literature for some polyamide 6 - TFP glass hybrids, the measurements of mechanical properties by DMA showed a reinforcement effect of glass in the polymer. This was reflected by the increase of storage modulus $(E')$ at low and high temperatures in hybrids containing 13, 18 and 25 vol% tin fluoride phosphate glasses, achieving the highest modulus at 25 vol%. Tensile testing revealed a pronounced reduction in ductility for high glass contents.

Finally, the first TFP- PA11 hybrid coating was developed with enhanced fire resistance and adhesion to the metal. Hardness and abrasion tests using different glass Tgs showed an influence of the glass Tg on the final coating application.

# Acknowledgements

I would like to express my deepest appreciation to Cerdato Arkema (Normandy, France) research centre workers, without their guidance and persistent help this dissertation would not have been possible. Especially to Karine Huraux my company supervisor, who has the attitude and the substance of a genius and to Mark Audenaert, who have supported me along the way. Both convincingly and continually conveyed a spirit of adventure in regard to research and an excitement in regard to developing.

I would like to thank my thesis directors, Professor Yuqing Bao and Professor David Gawne, for the academic guidance provided along this research project. Additionally, a mention of Dr. Jiming Gao for his introduction to the university lab.

It gives me great pleasure in acknowledging the support and help of Dr. Guilment, Dr. Reyna- Valencia, David Meslet, Aude Chiqiot, Lionel Jeancolas, Dr. Ireson, Agnes Gosnet, Sylvie Lebreton in their expertise fields.

I cannot find word to express my gratitude to Rilsan fine powder team who not only provided a friendly working environment but also supported and encouraged me during my thesis. Especially thank to you Nadine Rivas for your unconditional help and love.

Luciana and Pedro, I would like to thank my colleagues and friends Pedro and Nora. These years of research would have not been the same without their friendship and support.

Finally, an especial thank you to my parents Kepa and Kontxita, my brother Kepa and especially to my sister Nahia for the constant support and belief.

The research leading to these results received funding from the European Union Seventh Framework Programme (FP7-MC-ITN) under Grant Agreement Number 264710. The authors would like to thank the Directorate-General for Science, Research and Development of the European Commission for financial support of the research.

# List of publications

## Publication

N. Iturraran, K. Huraux, Y. Bao, D. T. Gawne, J. Guilment, Effect of melting parameters during synthesis on the structure and properties of tin fluoride phosphate glasses, Journal of Non-Crystalline Solids, 489, (2018), 64–70

## Conference poster presentation

N. Iturraran, K. Huraux, Y. Bao, D. T. Gawne, R. Ireson, Influence of melting conditions on the properties of tin fluoride phosphate glass, Glass Focus- Innovation within glass and supply chain, 16th May 2014, London

## Conference papers presentation

N. Iturraran, K. Huraux, Y. Bao, D. T. Gawne, Effect of melting conditions on the properties of tin fluoride phosphate glass, Conference on Nanotechnologies Applications, Coimbra, 3rd of September 2014

N. Iturraran, K. Huraux, Y. Bao, D. T. Gawne, Effect of compounding conditions on the morphology and mechanical properties of tin fluoride phosphate glass-polyamide 11 hybrids, Manano Seminar, Kingston University, London, September 2013

# Table of contents

# List of figures

# List of tables

# List of acronyms and abbreviations

A: the sum of each non-porous height

as: asymmetric

ASTM: American Society for Testing and Materials

ATH: aluminium hydroxide

b: width

BO: bridging oxygen

c: mass concentration of the polymer (g/dL)

c: velocity of light

$CaCO_3$: calcium carbonate

CTBN: carboxyl-terminated poly (butadiene-co-acrylonitrile) -

d: depth

D: diameter

d: increment in cm

D: screw diameter

D: the sum of each porous height

d1: indent diagonal 1

d2: indent diagonal 2

DMA: dynamic mechanical analysis

DSC: differential scanning calorimetry

E*: complex elastic dynamic modulus

E': elastic storage modulus

E": elastic loss modulus

EP: epoxy polymer/resin

EXAFS: extended X-ray absorption fine structure spectroscopy

F: force

FBE: fusion bonded epoxy

FR: fire resistance

FTIR: fourier-transform infrared spectroscopy

g: grams

GPL: gel permeation chromatography

$h_{0:}$ minimum height to cause porosity (cm)

$H_3O^+$: hydronium ion

$H_3PO_4$: phosphoric acid

HDK®: walker company trademark for hydrophobic and hydrophilic fumed silica

HFIP: hexafluoro isopropanol

Hz: hertz

ISO: international organization for standardization international

K: kelvin

KTFA: potassium trifluoroacetate

$m_1$: the initial mass of the film

$m_2$: the final mass after immersion in water.

MDM: magnesium hydroxide

MMT: montmorillonite

MWNT: multiwalled carbon nanotubes

N: newton

NBO: non-bridging oxygen

$\eta_{d:}$ viscosity of dispersed phase

$NH_3$: ammonia

$NH_4H_2PO_4$: ammonium phosphate monobasic

$\eta_{m:}$ viscosity of the matrix.

nm: nanometre

NMR: nuclear magnetic resonance

OSP: silica particles

P glass: phosphate glass

P: pressure

$P_2O_5$: phosphate

PA: polyamide

PA: polyamide

PbO: lead (II) oxide

PE: polyethylene

PEEK: poly (ether ether ketone)

PU: polyurethane

PVF: polyvinyl fluoride

r: radius of the screw

R': reactive organic group

REACH: registration, evaluation, authorization and restriction of chemicals

Rpm: revolution per minutes

s: second

s: symmetric

SAXS: small-angle X-ray scattering

SD: particle size distribution

SnF2: tin fluoride

SnO: tin oxide

T: temperature

t: time

tan δ: loss tangent

TEM: transmission electron microscopy

TFP: tin fluoride phosphate

Tg: glass transition temperature

TGA: thermogravimetric analysis

$TiO_2$: titanium dioxide

Tm: melting point

Tp: crystallization peak

Ts: softening point

v: frequency

V: volume

VOC: volatile organic compounds

W: mass weight (g)

$w_1$: initial weight of the coated steel plate

$w_2$: final weight of the coated steel plate

$w_a$: sample mass (g) in air

WAXS: wide-angle X-ray scattering

$w_w$: sample mass (g) in water

ZMP: zinc molybdenum orthophosphate

ZnO: zinc oxide

Å: angstrom

µm: micrometer

γ: surface or interfacial tension

$\gamma^a$: interfacial tension of the polar component

$\gamma^d$: interfacial tension of the dispersive component

Δmass: mass variation

Δweight: weight variation

ΔGm: Gibbs free energy of mixing

ΔHm: enthalpy of mixing

ΔSm: entropy of mixing

η: viscosity

$\eta_{rel:}$ relative viscosity

ρ: density

$\rho_a$: sample density in air

$\rho_w$: sample density in water

$G$": shear loss modulus

$G'$: shear storage modulus

$G*$: dynamic shear complex modulus

$Gc*$: complex modulus of the continuous phase

$Gd*$: complex modulus of the dispersed phase

$Tc$: crystallization temperature

$\Delta\mathbf{H_0^f}$: heat of fusion of the crystalline component

$\dot{\gamma}$: shear rate

$\lambda$: wavelength

$\sigma$: stress

$\sigma E$: elongational stress

$\tau$: shear stress

$\omega$: angular frequency

$\phi$: molar fraction of a component

# List of Standards and guidelines

ASTM G14-04, “Standard Test Method for Impact Resistance of Pipeline Coatings (Falling Weight Test)”, ASTM International, West Conshohocken, PA, 2004, www.astm.org

ASTM D1243-15, “Standard Test Method for Dilute Solution Viscosity of Vinyl Chloride Polymers”, ASTM International, West Conshohocken, PA, 2015, www.astm.org

ASTM D2857-16, “Standard Practice for Dilute Solution Viscosity of Polymers”, ASTM International, West Conshohocken, PA, 2016, www.astm.org

ASTM D4603-18, “Standard Test Method for Determining Inherent Viscosity of Poly(Ethylene Terephthalate) (PET) by Glass Capillary Viscometer”, ASTM International, West Conshohocken, PA, 2018, www.astm.org

ISO 527-1:2012, “Plastics — Determination of tensile properties — Part 1: General principles”, International Organization for Standardization, Geneva, Switzerland, 2012, www.iso.org

ISO 8501-1:2007, “Preparation of steel substrates before application of paints and related products — Visual assessment of surface cleanliness — Part 1: Rust grades and preparation grades of uncoated steel substrates and of steel substrates after overall removal of previous coatings”, International Organization for Standardization, Geneva, Switzerland, 2007, www.iso.org

ISO 1183-1:2012, “Methods for determining the density of non-cellular plastics -- Part 1: Immersion method, liquid pyknometer method and titration method”, International Organization for Standardization, Geneva, Switzerland, 2012, www.iso.org

ASTM D792-08, “Standard Test Methods for Density and Specific Gravity (Relative Density) of Plastics by Displacement”, ASTM International, West Conshohocken, PA, 2008, www.astm.org

ISO 11357-1:2009, “Plastics — Differential scanning calorimetry (DSC) — Part 1: General principles”, International Organization for Standardization, Geneva, Switzerland, 2009, www.iso.org

ISO 11357-2:1999, “Plastics — Differential scanning calorimetry (DSC) — Part 2: Determination of glass transition temperature”, International Organization for Standardization, Geneva, Switzerland, 1999, www.iso.org

ISO 11357-3:2011, “Plastics — Differential scanning calorimetry (DSC) — Part 3: Determination of temperature and enthalpy of melting and crystallization”, International Organization for Standardization, Geneva, Switzerland, 2011, www.isqo.org

ISO 11357-4:2005, “Plastics — Differential scanning calorimetry (DSC) — Part 4: Determination of specific heat capacity”, International Organization for Standardization, Geneva, Switzerland, 2005, www.iso.org

ISO 11357-6:2018, “Plastics — Differential scanning calorimetry (DSC) — Part 6: Determination of oxidation induction time (isothermal OIT) and oxidation induction temperature (dynamic OIT)”, International Organization for Standardization, Geneva, Switzerland, 2018, www.iso.org

ISO 11357-7:2002, “Plastics — Differential scanning calorimetry (DSC) — Part 7: Determination of crystallization kinetics”, International Organization for Standardization, Geneva, Switzerland, 2002, www.iso.org

ASTM E928-08, Standard Test Method for Determination of Purity by Differential Scanning Calorimetry, ASTM International, West Conshohocken, PA, 2008, www.astm.org

ISO 11358:1997, “Plastics — Thermogravimetry (TG) of polymers — General principles”, International Organization for Standardization, Geneva, Switzerland, 1997, www.iso.org

ISO 6721-1: 2019, “ Plastics — Determination of dynamic mechanical properties “, International Organization for Standardization, Geneva, Switzerland, 2019, www.iso.org

ASTM D638-14, “Standard Test Method for Tensile Properties of Plastics”, ASTM International, West Conshohocken, PA, 2014, www.astm.org

IEC 60695-11-10:1999 “Fire hazard testing — Part 11-10: Test flames — 50 W horizontal and vertical flame test methods”, International Organization for Standardization, Geneva, Switzerland, 1999, www.iso.org

ISO 868:2003, “Plastics and ebonite — Determination of indentation hardness by means of a durometer (Shore hardness)”, International Organization for Standardization, Geneva, Switzerland, 2003, www.iso.org

ASTM D4060-90 **“**Standard Test Method for Abrasion Resistance of Organic Coatings by the Taber Abraser” ASTM International, West Conshohocken, PA, 1990, www.astm.org

ISO 62:2008 “Plastics — Determination of water absorption”, International Organization for Standardization, Geneva, Switzerland, 2008, www.iso.org

# Chapter 1 Introduction

## 1.1 Research background and objectives

It is anticipated that nanotechnology and nanostructured materials will be one of the most promising areas of technological development in the twenty-first century, with the potential to deliver substantial economic and social benefits. Due to their interesting thermal, mechanical and optical properties, different forms of organic-inorganic hybrids [1] are currently being studied to develop these materials. Possible applications include sensors, electrical and optical devices, drug delivery systems, catalysts, and protective coatings [2].

Polymer hybrids have the potential of being nanostructured materials with high-performance properties that could provide important industrial components. However, further research is needed to investigate the synthesis, processing, composition, and performance of these materials [3]. The objective of this project is to develop a new family of nanostructured materials based on glass-polymer composites with the potential to enhance coating properties.

In recent years, the increased attention given to polymer nanocomposites has indicated that research on nanostructured glass-polymer hybrids for coatings may prove to be a fruitful area of investigation. The appropriate choice of inorganic and polymeric precursors has been shown to produce unique chemical, mechanical and thermal hybrid properties which combine high compounding flexibility and easy processability [4]. There is a synergism in hybrid materials such that their properties are more than just a simple contribution of its constituents. This synergism between hybrid precursors depends on the chemical nature and the extent of the organic-inorganic interface, as well as the morphology of the material.

Using polymer matrices like thermoplastics and adding fillers such as glass at the nanometre length scale may enable interesting structural modifications to occur. This has the potential of forming novel structures and properties within new areas of application in the coating market. One of the main challenges for the research is in obtaining a uniform nanostructure of the glass second phase. Challenges within this

area will be addressed by controlling the interaction between components and by identifying the precursors and their optimal proportions.

Organic-inorganic hybrid nanocomposites can be prepared by using different chemical and physical routes such as the sol-gel process or the melt compounding process. Using these methods may result in the production of materials that interact by weak intermolecular forces or by the establishment of covalent bonds to give dense cross-linked networks. Determining a procedure to compound the hybrid using melt methods, like extrusion, will help in obtaining powders for further hybrid coating development. Further research is required to control the particle size distribution and properties of the glass-polymer system.

In this project, phosphate glass is selected as the second phase due to its low glass transition temperature (Tg) and its recently improved chemical durability and water resistance. In particular, its low glass transition temperature may make this material fluid at polymer processing temperatures. This will enable compounding by conventional processing techniques such as extrusion but only once the influence of processing parameters (T, screw speed and residence time) has been understood. This fluid state of the glass may reduce the viscosity of the glass-polymer composite during extrusion and thereby enable higher filler loadings and improved properties of the extrudate. It will also offer the possibility of controlling the morphology of the glass second phase and enable much greater interaction between the filler and matrix leading to enhanced properties.

The degree of dispersion of the filler throughout the matrix will depend on a number of factors including the viscosity and temperature of the material as well as the shear speed and residence time during processing. These parameters will be under investigation and control during extrusion compounding. The research of this thesis will focus on an analysis of several factors that influence particle size, morphology, and dispersion of the fillers in the matrix. The interaction will be analysed to identify the compatibilization of the polymer blends and any synergetic effects.

The project will aim to identify a suitable compositional range of the polymer-glass hybrid and the resulting properties. After the material has been ground into a powder, trials will be carried out using the fluidized-bed technique to deposit coatings on the steel substrate. The research will aim to determine the properties of the coatings and

relate them to the processing and compositional parameters as well as understanding their links with the nanostructure of the materials [5].

Previous work in the field has been aimed at developing glass-polymer hybrids containing phosphate glasses and polyamides 6 and 12. Interaction between these components has been reported, suggesting interesting properties for coating application [6]. The research in the literature has concentrated on the bulk materials, whereas the current research concerns coatings. The extrusion processing technique gives the opportunity to load the hybrid to 60 vol% of phosphate glass content by preventing the intractable processing problems inherent in classical composites [7].

There are three main surface protection systems: powder coatings, wet paints and chemical treatment (electromechanical), where polymer materials such as PU, epoxy, PVF and PA are widely used. A list of abbreviations is given immediately before the Introduction Section. Polyamide 11 (PA 11) was selected as the matrix in the current research due to its suitable properties, including functional and decorative characteristics of the coating, weatherability, corrosion, chemical resistance, heat, abrasion, impact resistance, smoothness and colour. Most of the functional characteristics will be tested on coatings produced by the fluidized bed technique using PA11 with optimum deposition parameters.

The aim of the project is to develop a new family of materials based on tin fluoride phosphate glass-polyamide 11 hybrids. The objectives of the research are to:

1. understand the relationships between structure, properties and processing of tin fluoride phosphate glasses and determine the optimum processing conditions.
2. characterize the glasses and the hybrids to identify the optimum hybrid precursors for coatings.
3. develop nanostructured hybrids from macroscopic glass fillers in a polyamide matrix.
4. investigate the synthesis of phosphate glass-polyamide hybrids by melt compounding using extrusion.
5. evaluate the properties of phosphate glass-polyamide hybrids and characterize the structure of hybrids in the bulk form.
6. evaluate the properties of phosphate glass-polyamide hybrid powders and coatings and characterize their structure in the coating form.

7. understand the formation processes and their optimization of the bulk, powder and coatings of hybrids.

## 1.2 Thesis structure

The content of this thesis is divided into 9 chapters as shown in Figure 1.1.

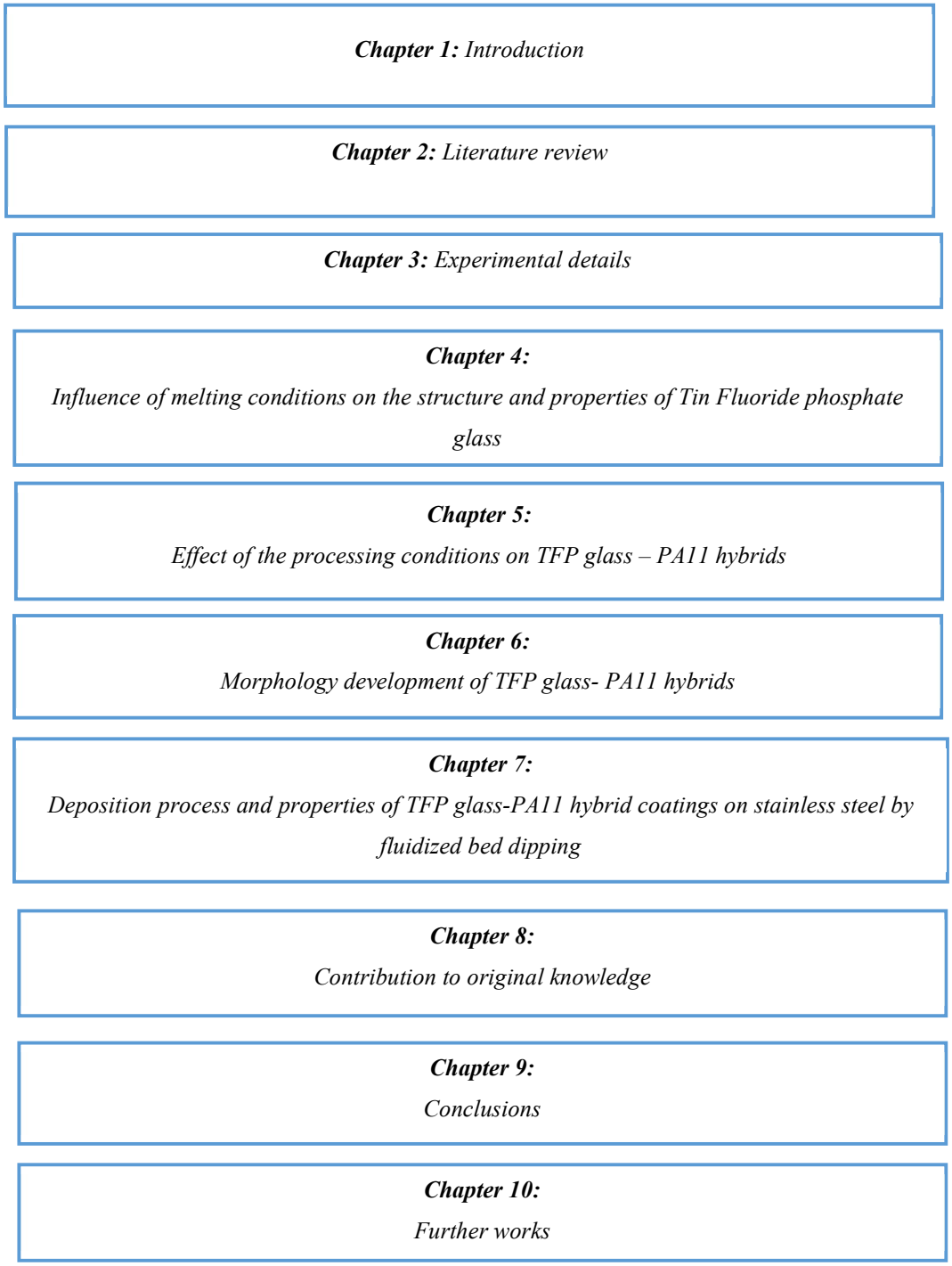


Figure 1. 1: Schematic presentation of the thesis structure.

Chapters 1-3 describe the rationale and objectives of the research, its background, the salient and critical work undertaken in the published literature. The influence of melting conditions on the structure of tin fluoride phosphate glass is investigated and reported in Chapter 4. FTIR and Raman spectroscopy showed that the structure of the glass changes depending on the melting condition of the glass. Glass samples synthesized at different melting conditions were investigated with the aim of providing new data on the sensitivity of properties to the processing parameters and improving the understanding of phosphate glass behaviour. The determination of the optimum melting conditions is important for upscaling of the glass synthesis to develop possible future industrial applications, in this case glass-polymer hybrid coatings.

Chapters 5 and 6 focus on the effect of the processing conditions and morphology development of tin fluoride phosphate glass-polyamide 11 hybrids, respectively. In Chapter 5, the influence of the hybrid processing parameters on the morphology was studied and the most influential ones were identified. Characterisation of the new material using DMA, rheology, static and dynamic mechanical properties, TGA and fire resistance was also presented in this unit. Chapter 6 consists in explaining the mechanism of the morphology development.

Chapter 7 focuses on characterizing functional properties of hybrid coatings to confirm hybrid coating feasibility for the application. Hybrid coatings with different compositions and using different Tg's were performed by dipping in the fluidized bed and adhesion, wear performance, hardness, impact resistance and water absorption were tested.

# Chapter 2: Literature review

## 2.1. General overview of Powder Coatings

Powder coating is a finishing process in which dry, free-flowing, thermoplastic or thermoset powder material is applied to a surface, melted, and hardened into a coating. This finishing process is suitable for various materials, including metals, plastics, glass, and medium density fibreboard. Coatings can provide both functional and decorative surfaces in a wide range of colours, finishes, and textures that are not readily achievable by conventional liquid coating methods.

There are two main methods of powder coating: electrostatic spray deposition and fluidized bed application. After that, the powder is heated to melt and cure. Finally, a smooth bright permanent film on substrates is formed to achieve the purpose of decoration and functional surfaces. The process flow preparation of powder coatings is separated into dry process production and wet process production.

The preparation stage of the powder coating has several steps. Before the application of any powder coating material, the surface of the substrate must be cleaned and treated to ensure that the part is free of dust, dirt, and debris. If a surface is not sufficiently prepared, any remaining residues and deposits could affect the adhesion of the powder and the quality of the final finish.

The powder coating process use two main types of coating materials, thermosets, and thermoplastics. Each type can be similarly applied, but has different curing stage, as well as distinct physical and mechanical characteristics [8].

Thermosets are capable of withstanding high temperatures and cannot be remelted, reformed, or recycled. Thermosets have higher scratch and mar resistance. Scratch and mar refer to damage from impact, rubbing or abrasion that produces visible scratches or marring and hence damages the coating. Mar is described as a physical damage that usually occurs within a few micrometres of the surface of the topcoats; these damages are usually the cause of the changes in appearance observed on the paint coatings [9]. Thermosets are susceptible to brittleness due to over-hardening. They

require a cure cycle to harden and undergo an irreversible chemical reaction. Thermosets are generally applied only via the electrostatic spray deposition method.

Thermoplastics can soften/melt at high temperatures and be remelted, reformed, or recycled. Thermoplastics have high impact resistance and are more flexible in coating thickness. They do not require a cure cycle to harden and do not change chemically. Thermoplastics are applied via electrostatic spray deposition and the fluidized bed method.

Thermoset powder coating material has short polymer molecules in the initial contact on the substrate. However, during the curing process, the powder undergoes an irreversible chemical cross-linking reaction, which bonds together long chains of polymer molecules. This reaction changes the physical properties and chemistry of the material and allows it to harden into a thin and hard finish [10].

Thermoplastic powder coatings do not require a cure cycle. Instead, the thermoplastic material only requires the time and temperature necessary to melt, flow out, and create the film-like coating. Unlike with thermoset material, which undergoes a chemical reaction during the curing stage, thermoplastic materials do not change their physical or chemical properties when heat is applied. Therefore, they can be remelted, reformed, and recycled for future coating applications.

Some considerations to keep in mind when choosing between thermoset and thermoplastic coating material are the application method and the intended application for the coating. Generally, thermoset powders are only applied via electrostatic spray deposition method. This limitation exists because dipping preheated parts into thermoset powder can cause any excess powder to cross-link due to built-up and residual heat within the fluid bed. As the cross-linking reaction causes permanent changes to the powder material, such occurrences would lead to excessive coating material waste.

The curing process enables thermosets to attain harder coatings than thermoplastics, thus allowing them to withstand higher temperatures and demonstrate greater scratch and mar resistance. However, the harder finish can also limit the impact resistance of thermoset coatings, and over-hardening can cause the coating to become brittle, particularly in thicker coatings. Thermoplastic powder can be applied via both the ESD

and the fluidized bed coating method, and generally can produce thicker, more flexible and impact resistant coatings than thermoset powder. While the ability to be remelted offers some advantage regarding material costs, it also makes thermoplastic powder coatings less suitable for high and intense heat applications as the coating material may soften or melt off [10].

The traditional polymers cannot meet all the industry needs that the coating market is requesting over the past few decades. The required performance could be achieved, following the global market towards the modification of the traditional polymers, by adding functional groups, pigments, or fillers on the matrix. The development of new composite and nanocomposite materials for coating application is leading this market to competitiveness. This evolution in materials must be followed by technological advances in the methodology, procedure, and application of the coatings. Part of the research progress made in powder coating industry is overviewed briefly.

### 2.1.1 Use of functional groups

The incorporation of functional groups to the polymeric matrix is common and requires an extended method to improve powder coating properties. The glass transition temperature of polymers containing carboxyl end groups can be increased by increasing the molecular weight and without sacrificing the reactive group concentration [11]. This approach could be used to design new carboxyl functional base polyesters. Pilch-Pitera [12] has synthesized blocked polyisocyanate cross linkers for polyurethane powder coatings to have higher wetting angle, roughness values and abrasion resistance. These crosslinkers decreased the surface free energy value of polyurethanes.

Vasil'ev et al. [13] have synthesized a series of new epoxy oligomers with per-fluorinated fragments to improve hydrophobic properties, liquid carboxyl-terminated poly (butadiene-co-acrylonitrile) (CTBN)-epoxy resin (EP) pre-polymers were prepared with different contents of CTBN. This utilises the ability of CTBN-EP pre-polymers to dramatically enhance the flexibility and impact resistance of FBE coatings without compromising other key properties such as corrosion protection as was reported by Jia et al. [14].

### 2.1.2 Use of pigments

Pigments play an important role in powder coatings. The most important properties of a pigment are homogeneous dispersion and thermal stability. Pigments can be organic or inorganic and the most commonly used in powder coating is titanium dioxide. Titanium dioxide is widely used because it efficiently scatters visible light, thereby imparting whiteness, brightness, and opacity when incorporated into a coating.

Shi et al. [15] found that by adding 2 mass % of nano- $TiO_2$ into polyester powder coatings, the pigment played a prompting role in the curing system. A delay of the melting point, and the starting and peak temperatures of curing reaction of the nano-$TiO_2$ modified system were decreased by more than 5 ˚C. Hadavand et al. [16] studied powder coating nano-ZnO to improve antibacterial properties.

The results showed that modified nano- ZnO has provided to the polymeric matrix improved thermal stability, compatible blending process and homogeneous dispersion. The antibacterial experiments confirmed better efficiency for modified coatings. Trottier et al. [17] applied zinc oxide and silica as pigments into the epoxy polyester resin system to increase the ohmic conductivity of the resin system.

Powder coating formulation with different contents of ZMP were applied over galvanized steel. The anticorrosive properties were studied by electrochemical methods [18]. At 10 % or 15 % ZMP, the anticorrosive properties were enhanced due to the barrier properties improvement and the inhibitive action of the pigment. It was found in the salt fog spray test that anticorrosive properties did not vary in samples between 10% ZMP and 15 % ZMP. In some coating applications, phosphate pigments are considered highly effective against corrosion attack.

Powder coating composites based on anticorrosive hybrids of epoxy/polyester and polyester with phosphate pigments were formulated by El-Ghaffar et al. [19]. Physico-mechanical properties and corrosion protection properties via a salt spray chamber for 1000 h were investigated on a cold rolled steel panel. Keeping the same physico-mechanical properties, high performance anti-corrosive hybrid coatings for steel protection were reported in the research results.

### 2.1.3 Use of fillers

Fillers can provide different properties to the powder coating film. Fillers are currently used to increase the thickness of the film, but they also influence other properties. Fillers can improve durability, hardness, and mechanical properties.

The tribological properties of PA-6 and PA-6 with surface layers gradient-filled with tin, lead, and bismuth nano-films in a concentration of up to 1.2 wt% were studied by Grigoriev et al. [20]. The research work proved the dependency of the hardness of the friction surface of the composites on the susceptibility of the filler metals to strain hardening and explained the different values obtained on their wear.

Vähä-Nissi [21] has investigated the porosity and average pore size of different ratios/ contents of polymer $CaCO_3$ powder by conventional paper coatings. The objective was to reach a decrease in energy consumption during the curing process and increase noticeably the adhesion and the hardness. Kalaee et al. investigated the effect of stearic acid coated $CaCO_3$ nanoparticles on the morphology, cure behaviour, adhesion and hardness properties of the polyester/epoxy blend [22]. Two thermosetting powder coatings with different weight fractions of filler were produced to evaluate the scratch and wear performance [23]. The epoxy composite coatings have a better scratch resistance response than polyester composite.

Piazza et al. [24] has investigated the properties of epoxy/MMT particle nanocomposites with intercalated structures and with epoxy/barium sulphate micro-composites. The result is coatings of epoxy/MMT particles presented better anticorrosion and physical properties. The homogeneous dispersion and interaction with the epoxy matrix of MMT produces organic coatings with higher thermal stability, higher adhesion, and improved barrier and thermal properties. The properties of the coating are influenced by the type and volume fraction of the filler.

Mirabedini et al. [25] studied novel filler for coatings. Novel HDK fumed silica nanoparticles increased the tensile strength, elastic modulus, hardness, energy to break and adhesion strength of the coating due to better dispersion and chemical interactions of nanoparticles with the polymeric matrix. Multi-functional fillers must be developed to produce high quality coatings to meet the performance requirements. Puig et al. [26] studied an organo-modified silica particle with silanes (OSP) as adhesion promoter in

polyester powder coating, obtaining an improvement of adhesion and corrosion properties.

## 2.2 Polymer – glass hybrid powder coating

Coatings with specific functionalities are of increasing importance in areas such as the display industry in which simple polymer coatings are moving into the composite and nanocomposite fields pushed by specialized demands for improved coating properties. The synergetic effect of these composites can be used to develop improved coatings to specific functionalities, like adding metallic carbon nanotubes in conductive coatings. These relatively new nanoparticle materials offer numerous opportunities for new coatings in industry. The nanoparticles provide coatings with enhanced optical, electrical and mechanical properties that are not attainable with organic material. The organic polymer material will provide easy processability during the synthesis of the hybrid by melt mixing technique due to its viscosity.

Several investigations are published showing highly improved properties of the composite coating compared to those of the single component. For example, an investigation on corrosion control techniques found that silanes can protect metal against corrosion but single silanes by themselves do not provide any significant corrosion protection [27,28]. In addition, organic-inorganic hybrid materials formed by hydrolysis and condensation of alkoxide precursors by sol-gel methods do provide protection [29,30]. It was found that they could provide improved corrosion resistance for metal substrates, because they combined the mechanical and chemical characteristics of the comprising organic and inorganic networks, producing effective coatings that were durable, scratch resistant and adherent to metal substrates. It is also reported that sol–gel-derived silica hybrid coatings could provide enhanced protection or passivation for the substrate surface particularly in high abrasion and corrosion environments [31-34].

Additionally, the incorporation of organic groups made it possible to increase ductility and thickness and to reduce the micro-cracks, thus enhancing the electrolytic anti-corrosion performance [35-36].

Organic-inorganic hybrids represent a new class of materials that could result in a nanocomposite with enhanced properties combining processability and versatility [1].

Their interesting mechanical, thermal and optical properties attract a wide range of potential applications such as drug delivery systems, electrical and optical devices, sensors, catalysts, and protective coatings. It is reported that hybrid coatings might be promising candidates for surface protection thanks to before mentioned particular properties and also because of their inert and nontoxic nature [4,37]. Nanostructured materials could also be part of the next generation of desalination systems and influence anti-bacterial efficacy [2,38]. Nanocomposites can show improved barrier properties due to more tortuous paths for the penetrant molecules [39].

The hybrid materials are composed of nanostructured organic polymer/ inorganic glass materials that could exhibit easy processability, superior mechanical performance, improved thermal stability, better corrosion resistance and excellent gas barrier properties. This makes hybrids promising candidates to achieve the goals of this research, namely, developing a new family of materials for coatings that improve mechanical, chemical, thermal properties and are adherent to the metal substrates. These properties are expected in the initial material before powdering.

The properties of composite materials are determined by the structure of the components: the shape of the filler phase, the morphology of the system, and the nature of the interface between the phases [40-42]. Thus, a great variety of properties can be obtained with composites just by alteration of one of these items (e.g. the morphological or interface properties). An important property of the interface that can greatly affect mechanical behaviour is the strength of the adhesive bond between the phases. There are many reasons for using composite materials rather than the simpler homogeneous polymers, including: increased stiffness, strength, and dimensional stability, increased toughness or impact strength, increased heat distortion temperature, increased mechanical damping, reduced permeability to gases and liquids, modified electrical properties, reduced cost [40].

In the past decades, the coating industry has suffered significant changes due to regulatory constraint such as REACH (Registration, Evaluation, Authorization and Restriction of Chemicals) which aim to eliminate hazardous products and limit volatile organic compounds (VOC) [43]. Some examples of VOCs are hydrocarbons (hexane, toluene, xylene), ketones (acetone, MEK, MIBK), alcohols (methanol, ethanol, cyclohexanol), and esters (ethyl acetate, butyl acetate, isobutyl acetate). The

application of coatings has been affected by this regulatory constrains as a wide range of conventional organic coatings use these substances [44]. As a result, powder coatings are enjoying high growth and great demand of research work to meet the challenge. The coating formulators are centred on the development of technologies that meet the dual requirements of environmental compliance and excellent performance [43-45]. This research is also affected by regulation as will be explained later on.

The objective of this research is to develop an improved polyamide 11 (PA11) with enhanced chemical, thermal, and mechanical properties for metal coating application. This project was aimed at developing new primeless coatings using polyamide 11 for the fluid transport market. Phosphate glasses could be a great adhesion promoter due to their compatibility with PA and metal surfaces. Phosphate coatings have a great metal protecting performance.

### 2.2.1 Polymer powder coating

Organic coatings are a complex mixture of polymers, fluid carriers, pigments, corrosion inhibitors, and additives and represent the oldest and most widely used method for delaying the onset of corrosion.

Organic coatings are comprised of paints, varnishes (paints without pigmentation) and high-performance coatings and are seldom used in isolation. They are typically used in a coating system that may consist of the following combination of layers: (i) a conversion coating (this layer is typically inorganic) and the associated preliminary degreasing and de-oxidation procedures, (ii) a primer coat, (iii) an intermediate coat, and (iv) a top coat. Each coating layer serves a particular function, giving rise to a total system performance that exceeds the sum of the individual coating performances.

The stand-alone performance of the individual coating layers does not necessarily represent the coating performance within the system. Broadly speaking, the corrosion protection of a metal substrate by an organic coating system is an interactive function of the environment, the organic coating system, the substrate, the physico-chemical nature of the coating substrate interface (e.g. adhesion) and the interfacial chemistry that evolves adjacent to the substrate in service. A slight change in any aspect of this

assembly of variables can alter the corrosion protection properties provided by the coating system.

The topic of organic coatings spans a broad range of technical and scientific fields, from the art of coating formulation to polymer science, rheology, colour science, surface science, mechanics, and corrosion science, among other fields [46].

The thermosetting organic powder coatings are epoxy, polyester and acrylic resin with their correspondent curing agent, pigment, filler, and additives. Epoxy resin powder coatings have excellent corrosion resistance, hardness, flexibility, and impact strength. Polyester powder coatings exhibit good flow properties, wear resistance, and overbake stability. Super-durable polyester formulations retain colour and gloss in harsh exterior applications. Polyester resin can be formulated in a wide variety of powder coatings with high-gloss, satin, metallic and sand finishes. Polyester powder coatings are especially useful in architectural, container, shopping cart, lawn and garden, agricultural and construction equipment applications. Acrylic resin powder coating is well known for its excellent weathering resistance which can provide coatings resistant to over 10 years of exposure. Acrylic powder is perfect for high performance of exterior weather-ability, durability, and abrasion resistance. Acrylic powder coating has strong metal adhesion, high quality film appearance and it is suitable for decorative coatings.

The typical organic thermoplastic coatings are polyethylene, polyamide, polyvinyl chloride, and polyvinylidene fluoride and their formula is composed of pigment, filler, plasticizer, and stabilizer. The polyethylene powder coating has excellent corrosion resistance, electrical insulation, and ultraviolet radiation resistance. Polyamide powder coating has high mechanical strength, impact resistance and hardness. Polyvinyl chloride powder coating has excellent solvent and corrosion resistance, impact resistance and salt spray resistance. PVC coating can prevent food pollution and poly (trifluoro vinyl chloride) powder coating acts as a protective barrier against chemicals [47] [11].

In Figure 2.1 polymer powder coatings are classified according to their performance and sales volume.

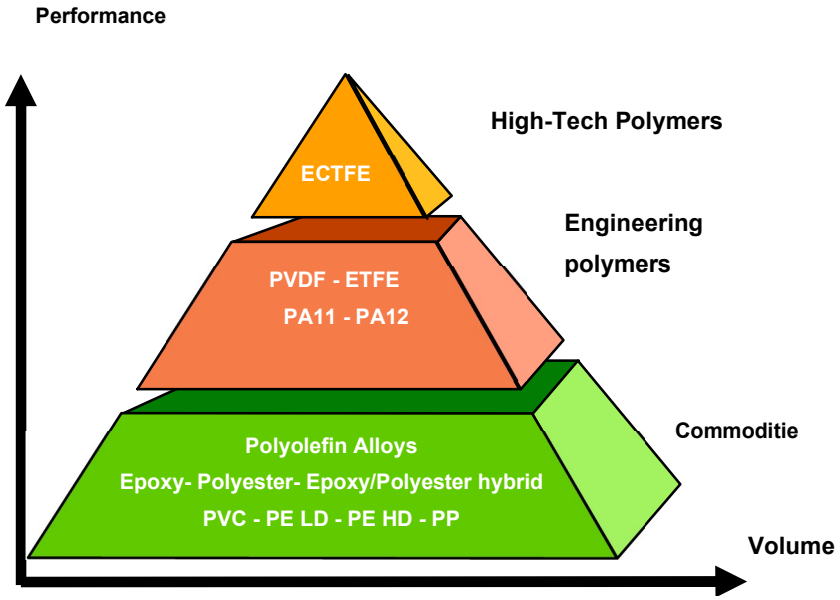


Figure 2. 1: Market powder coating.

Important Factors in coating selection are:

- Mission/operational needs
- Exterior weathering
- Water, fuel, solvent, or chemical resistance
- Abrasion, heat, or mildew resistance
- Appearance
- Drying time
- Ease of application and maintenance

The selection of coatings depends upon factors including their intrinsic properties, the environment, and the application method of deposition.

#### 2.2.1.1 Polyamide 11 coatings (Rilsan® fine powder)

The research and development of this project was carried out in the fine powder department at Arkema Chemistry Company in France. Rilsan® Fine powder is an Arkema engineering polymer for coatings. Rilsan® is a renewable thermoplastic PA11 powder that combines strong physical properties with chemical durability. Appendix A and B shows information taken from Arkema's technical brochure.

This research is only developed by Rilsan® and the principle of film deposition onto the substrate is called Rilsanisation® [48].

Before coating the part with Rilsan®, it is necessary to prepare the metal surface of the substrate which will influence (condition) the adhesion characteristics and effectiveness of the coating. This preparation has three stages before applying the polymeric coating (Figure 2.2).

(i) Degreasing

It eliminates most grease on the surface of the support, coming from cutting oils or storage greases avoiding oxidation. It is carried out in a tank saturated with trichlorethylene vapor. The plates are then wiped and stored in an oven at 50 ° C.

(ii) Pre-treatment

Promotes a mechanical adherence of the coating. The pre-treatment is carried out in a rotary grit blasting machine with abrasive particle projection.

(iii) Application of an undercoat adhesion primer

A primer, usually based on phenolic epoxy, is sprayed in a thin layer on the surface of the metal and then dried. Compatible with the coating and metal, it promotes chemical bonding to Rilsan® and protects the metal against corrosion in the event of deep damages on the coating. A primer ensures the adhesion between the polyamide and the metal surface.

Finally, Rilsan® coating with 100 µm to several mm thickness is achieved by a coating method. The thickness depends on the coating method.

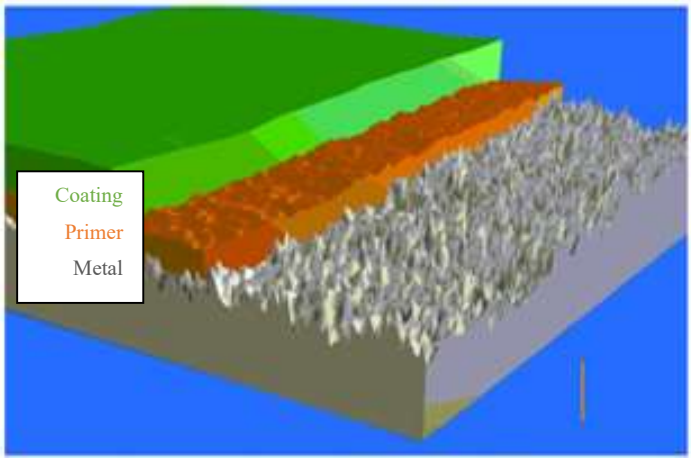


Figure 2. 2: Rilsanisation process.

Over the years, several coating methods have been developed. In the 1930s, flame spraying had opened the prelude of powder coatings which ensured polyethylene

polymer (undissolved in solvent) and successful metal coating. In 1952, Gemmer Company invented the fluidized bed coating technology. The first generation of pure epoxy powder coating was born in the end of the 1950s in the United States. Then in 1961 with the melt extrusion machine and electrostatic spraying technology coating processes, groups of powder coatings started appearing. There are different processes to apply powders for coating. The most used one is the fluidized bed process. Here, a hot metal test piece is dipped into fluidized powder. The second most used process is applying powder by electrostatic processes [47].

(i) Fluidized bed

The fluidized bed process involves bringing and maintaining the workpiece at a specified temperature for a given period depending on its shape and mass. This uniform temperature exceeds the melting point of several organic powders, including the Rilsan® powder. The oven temperatures can vary between 250 °C and 450 °C.

The workpiece is then removed from the oven and soaked in a powder bath. The bath is suspended or fluidized by a small stream of air diffused through a porous membrane at the bottom of the bath. The powder behaves in the same way in suspension as in a fluid so that the particles of powder are distributed perfectly on the surface of the pieces, including in the least accessible corners. In contact with the hot surface, they melt to form a uniform layer with a coating thickness between 250 and 500 microns. The soaking time usually ranges from two to four seconds and can be extended if it is necessary to obtain a thicker coating.

The factor with the greatest influence on the heat transfer, apart from the fluidization velocity, is the particle size. Particle size influences the change of the relative contribution of various mechanisms in the overall heat transfer. In the fluidized bed with small (< 0.1 mm) particles, convection by particles accounts for 90% of the overall heat transfer, while in the beds of large particles (> 1 mm) only 20% of the heat transfer is done by particle convection. Particle heat capacity is also important for heat transferred by particle convection.

## 2.2.2 Inorganic coatings

Surface conversion, anodizing, enamelling, and metallic coatings are part of the inorganic coating category. All of them provide barrier protection and the metallic

coatings are the ones that stand out, playing a more active role. With a less noble metal (e.g. zinc on steel), even corrosion due to surface damage in the coating can be prevented. With a more noble coating (e.g. nickel on steel) there is risk of accelerated corrosion in pores and damaged areas of the surface.

There are various methods for applying metal coatings: hot-dip galvanizing, thermal spraying, electroplating and chemical and vacuum coating. The choice of the metal for coating and method are determined based on base metal, size and shape, application area, cost, and requirements for physical properties.

The objective of this research is to develop a new nanohybrid material with enhanced properties for metal coating application. So, the hybrid precursors selection was limited to organic - inorganic coating materials. The PA 11 powder coating was selected as organic material and phosphate glass was identified as promising inorganic material to achieve the goal.

#### 2.2.2.1 Phosphate coatings

Phosphate coatings are the most often used steel surface treatment due to their notable adhesion, high corrosion resistance, improved abrasive resistance of the structure, and acceptable costs of manufacturing [49-51]. Corrosion protection for steel could be achieved by the application of modified phosphate [50-51], zinc phosphate [52-63], iron phosphate [64-66], as well as manganese phosphate coatings [67-75]. It was found that, of the above-mentioned phosphate coatings, the manganese phosphate coatings have the highest hardness in addition to their remarkable corrosion and wear resistance [75].

The application of phosphate coatings makes use of phosphoric acid and takes advantage of the low solubility of phosphates in medium or high pH solutions. Iron, zinc, or manganese phosphate salts are dissolved in a solution of phosphoric acid [76].

When steel or iron parts are placed in the phosphoric acid, a classic acid and metal reaction takes place which locally depletes the hydronium ($H_3O^+$) ions, raising the pH, and causing the dissolved salt to fall out of solution and be precipitated on the surface. The acid and metal reaction also create iron phosphate locally which may also be deposited. In the case of depositing zinc phosphate or manganese phosphate the

additional iron phosphate is frequently an undesirable addition to the coating. Phosphate conversion coatings can also be used on aluminium, zinc, cadmium, silver, and tin [77].

The process of phosphating aluminium and steel parts is typically listed as a conversion coating because the process involves metal removal as part of the reaction. However, it is not like anodizing or black oxide in that the phosphate coating is a precipitation reaction. The final surface is a layer of very fine phosphate crystals adhering to the surface of the metal.

For paint and powder coatings, a phosphate coating might accomplish two main functions. First, the organic layer is stabilized by the oxide resulting in lubrication and surface damage prevention [78]. The metal oxide film is reported to act as an anchor or primer for the organic coating to the glass surface container [79]. There are two possible explanations to organic layer stabilization. The anchoring function of the primer would originate from its ability to increase the bond strength of organic coatings to the glass. This assumption is based on an overview by Smay [78-79], the coating provides improved paint and powder coating adhesion since the phosphate crystals act as organic coating anchoring sites. Second, the phosphate layer acts as a corrosion barrier should the organic coating get scratched. In rust creep testing, the rust creep is reduced when phosphate is present under the paint layer or powder coat layer compared to no conversion layer under the organic coating.

Phosphate surface treatments are used to enhance paint adhesion and aid in corrosion protection, primarily on steel. Strong adhesion results from formation of $\mathrm{P-O-C}$ primary bonds at the polymer coating/phosphate interface and $\mathrm{P-O/Fe}$ complexes at phosphate/steel interfaces [80]. Corrosion protection is provided by the nonconductive, kinetic barrier provided by the phosphate layer (as well as the strong bonding with the protective paint coating) [80]. Zinc phosphate coatings are widely used on steel, zinc, aluminium, and sometimes cadmium, tin, and magnesium surfaces. Based on the design need, phosphate treatments can provide corrosion protection in combination with bonding enhancement or even electrical insulation [81].

Mostly, phosphate coatings are conversion coatings, requiring reaction of the bare metal surface in a solution containing soluble primary metal phosphates, phosphoric acid, and various accelerators [82]. In the conversion mechanism, activated metal

dissolution from the surface consumes protons from the conversion complex, resulting in an insoluble product that is deposited on the substrate surface.

The main components of a phosphating solution are phosphoric acid ($H_3PO_4$), ions (cations) of divalent metals ($Zn^{2+}, Fe^{2+}$ $Mn^{2+}$) accelerator – an oxidizing reagent (nitrate, nitrite, peroxide) to increase the coating process rate.

## 2.2.3 Phosphate glass

Glass is a transparent solid and can be among the most ancient materials in human history. Despite of being known such a long time, the research of its structure is paradoxically far from being complete. In the last 5 decades the science of glass has made exciting progress. Glass is no longer solely a material of primary technological value; glass is playing an important role in modern markets (optics – lasers-energy conversion) thanks to the research and development of new types of glasses.

Phosphate glass exhibits attractive properties such as low glass transition, high thermal expansion coefficients, biocompatibility, and high refractive indices. These specifications are suitable for many applications in photonics, fast ion conductors [83-86], glass-to-metal seals [87–89], low-temperature enamels [89], $NH_3$ gas adsorption [90], and biomedical engineering [91].

Phosphate glasses are composed by cross-linked and chain-like polymer structures, they are very similar to a network of polymer chains [6]. Phosphate glasses are generally considered as polymers in nature [6-7]. However, phosphate chains are much shorter than those of organic polymers and often an alkali metal cation aids are needed in the network formation.

### 2.2.3.1 Principle of glass

Glass is usually a material which is produced by cooling a liquid so quickly in order to avoid presence of crystallization [92]. The use of rapid cooling of the material implies a fairly rapid temperature drop on the liquid with a continuous increase in viscosity. The continuous increase in viscosity results in a progressive freezing of the liquid to its final solidification [93]. In Figure 2.3 the variation of the specific volume against temperature is plotted to show the two possible cases that can happen.

The principle of glass formation is illustrated in Figure 2.3 [94]. This picture represents a heated melt of fixed volume cooled to room temperature at a controlled rate. The path A-B-C corresponds to the cooling trajectory slightly below the melting point Tm. Point A represents a sufficiently high temperature for the material to be in liquid state. Point B represents the point where the liquid and solid forms have equal free enthalpies. As the temperature drops below Tm, the crystalline state is at the equilibrium state (trajectory B-D) and the thermodynamic system tends to reach its lowest enthalpy (trajectory D-E). Typically, the crystalline state displays long range periodic atomic arrangement.

The formation of glassy materials depends on achieving cooling rates high enough for kinetic factors to dominate the thermodynamic system and prevent crystallisation: if the crystallization rate and nucleation rate are slower than the cooling rates, the crystallization can be inhibited and the enthalpy of the system deviates from the equilibrium state.

The path B-C-F [94] represents the metastable state of a super-cooled liquid. This trajectory has a gradual slope defined as the range of glass transition.

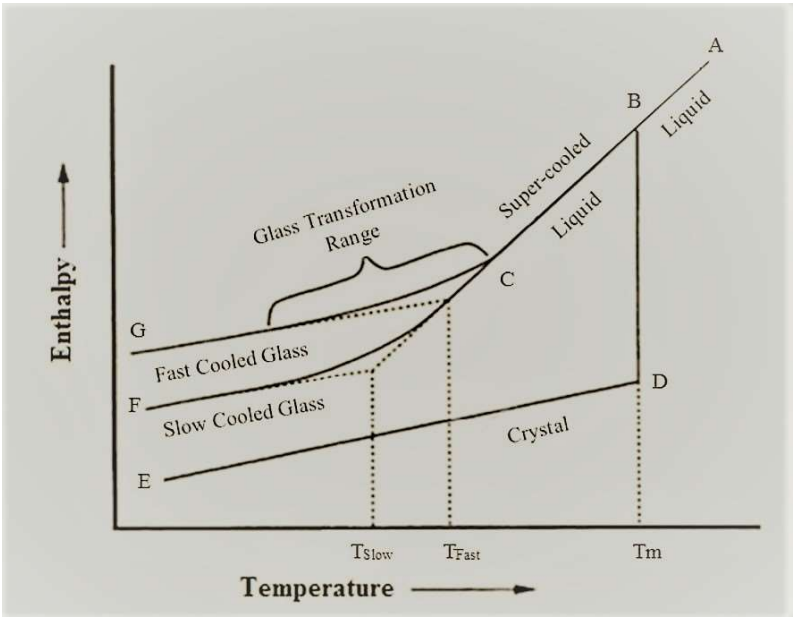


Figure 2. 3: Enthalpy-temperature diagram showing formation of crystalline and glassy materials; the effect of cooling rate on glass formation is elucidated [94].

At the glass transition zone, the increasing viscosity of the liquid associated with the progressive cooling process leads to a structure becoming fixed without any atomic rearrangement. The so-called *frozen liquid* can now be considered as a glassy material.

Additionally, since deviation from the equilibrium state is dictated by the cooling rate, this kinetic factor controls the temperature at which the sample enters the glass transition region. For example, if a material is cooled at a reduced rate, the B-D-E trajectory is observed.

#### 2.2.3.2 Phosphate glasses and their implications

Inorganic glasses are attractive materials to study from a fundamental point of view as they pose challenging and yet unsolved problems in the field of condensed matter physics [95].

In the last decade, our understanding of the static atomic structure of inorganic glasses has advanced substantially due primarily to huge improvements in experimental methods like Nuclear Magnetic Resonance (NMR), Extended X-ray Absorption Fine Structure (EXAFS) spectroscopies, elastic and inelastic neutron and X-ray scattering, Small-Angle and Wide-Angle X-ray Scattering (SAXS/WAXS) and to major developments in the techniques of in situ experimentation with solids and liquids at high temperatures and pressures. At the same time computer simulation methods have enabled direct visualization of structure and dynamics in the glassy and liquid states.

Phosphate glasses have a long history with wider application and broadly studied structural properties. Phosphate melts have comparatively low glass transition temperatures of 327 – 427 °C making them easily processable and, with high thermal expansion coefficients well-matched to those of metals, phosphate glasses are commonly used for hermetic seals. Phosphate melts have high solubility factors for heavy cations and anions. Initial development of phosphate glasses was hampered by their poor chemical durability but eventually solved by the inclusion of intermediates like Zn and Fe which has led to the development of phosphate glasses as potential hosts for nuclear waste [96]. In recent years, the biocompatible phosphate glasses have gained a particular interest thanks to their ability to react with water and emulate the function of hydroxyapatite, the mineral of bones and teeth. Indeed, the low processing temperature of phosphate glasses are enabling low-density foam matrices to be fabricated as possible candidates for bone prosthesis [97].

The structural physics of phosphate glasses is equally fascinating. Like silicate glasses, the phosphate glasses are constructed from corner-sharing tetrahedra, with the

important difference that these are three-fold rather than four-fold coordinated. The basic building block of phosphate glasses is the $PO_4$ tetrahedron where each has a short apical $P^{1}/_{4}O$ double bond and three longer $P-O$ bonds. The latter three oxygens can be shared by other $PO_4$ tetrahedra to form corner-shared $P-O-P$ linkages. Accordingly, the $PO_4$ tetrahedra can be designated as $Q^n$ units where n varies between 0 and 3 and corresponds to the number of $BO_s$ (bridging oxygens). $Q^4$ $PO_4$ species are not found – not even in the glass-former $P_2O_5$, so phosphate glasses remain three-fold coordinated [98].

#### 2.2.3.3 $P_2O_5$ glasses and bridging mechanisms

A fundamental work by Zachariasen (1932) introduced the theory of phosphate glass structure [99]. This study describes the phosphate glasses as composed of a three-dimensional structural network produced by reaction of glass forming phosphorus pentoxide ($P_2O_5$) compounds. Further influential studies by Hägg and Van Wazer questioned the Zachaniasen theory, demonstrating that even a large one-dimensional molecular group alone could constitute the phosphate glass structure [100]. Following these researches, different glass structure models were developed and represented in terms of the short-range bonds and long-range length scales throughout the material's overall structure [98, 99].

The orthophosphate P-tetrahedron ($PO_4^{3-}$) is the basic structural unit (Figure 2.4) of phosphate glasses. The electronic configuration of phosphorus is $3s^2$, $3p^3$ with five valence electrons. In oxide systems, the favoured coordination is tetrahedral, which can be considered as $sp^3$ hybridization of the phosphorous valence shell atomic orbitals, with the third p electron promoted to an empty 3d orbital, where a strong $\pi$ bonding molecular orbital is formed with 2p orbitals on the oxygen atoms [98]. In the absence of cations, the molecule's three oxygen atoms are free, and the tetrahedral phosphate anion can form covalent bonds via these bridging oxygens ($BO_s$) with any surrounding P-tetrahedrons ($P-O-P$ bonds) (Figure 2.5). Thus, the combination of orthophosphates allows the formation of various polyphosphate anions which may be branched or linear or a combination of the two.

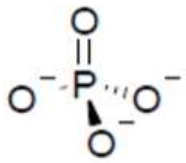

Figure 2. 4: The tetrahedral phosphate anion; charges are balanced by either polymerisation or cations [98].

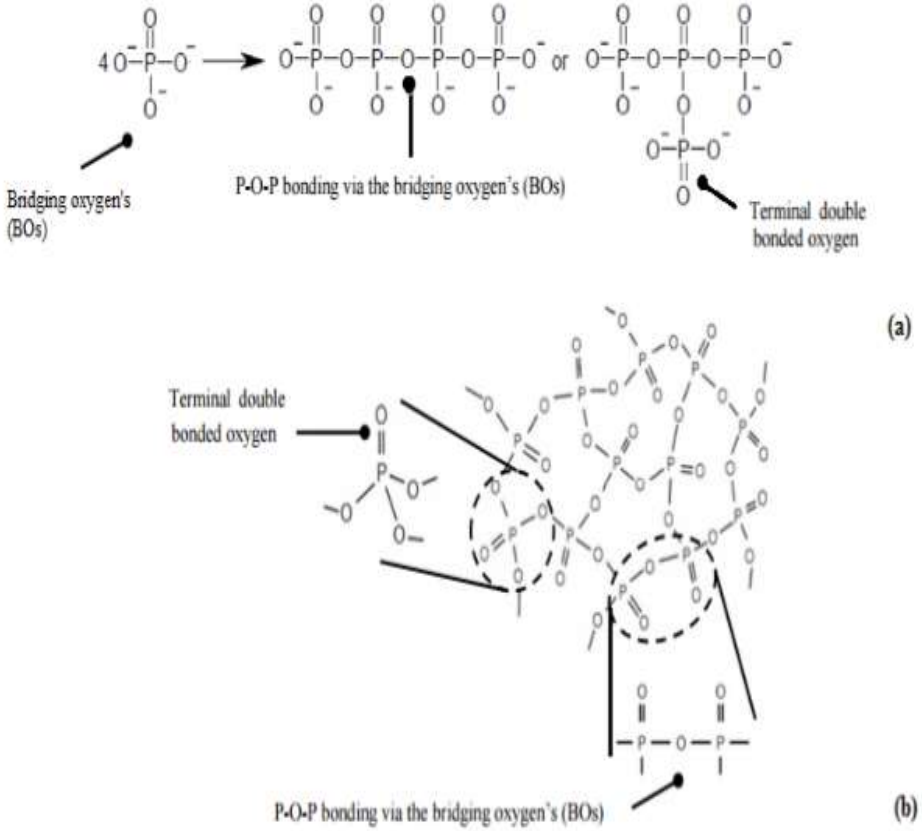


Figure 2. 5: Polymerisation of the phosphate anion gives rise to various polyphosphate anions linked via oxygen bridges which may be linear or branched (a), or a combination of the two (b) [98].

The corresponding structure of a phosphate glass network is typically classified under the $Q^i$ terminology where i represents the number of bridging oxygens $BO_s$ per tetrahedron (Figure 2.6). This terminology was originally devised for silica glasses but has been applied to phosphates [98].

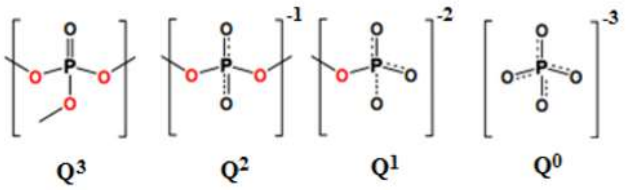


Figure 2. 6: Schematic representation of phosphate tetrahedral units: the four types of Qi represent the species found in phosphate glasses, where i is the number of bridging oxygens present within a particular phosphate tetrahedron [98].

The structure of the simplest phosphate glass $P_2O_5$ has been studied relatively recently by neutron and X-ray diffraction, Raman scattering and 31P NMR spectroscopic techniques. These studies indicate that the glass structure is indeed made up of three-dimensionally corner-linked units.

Three corners are linked via $BO_s$ with the remaining oxygens in NBO (non-bridging oxygen) or terminal configurations, i.e. phosphorus polyhedra are $Q^3$ in $P_2O_5$ glass. From spallation neutron and high-energy X-ray scattering experiments, the geometry of the Q species is now well determined, with $P-O$ distances for $BO_s$ and $NBO_s$being 1.60 and 1.49 Å (angstrom) respectively. However, the relationship between intermediate-range order and the topology of the network is still not well understood. So far, all spectroscopic results point towards a topology comprising a mixture of molecules and chains that has aspects in common to both the hexagonal and orthorhombic crystalline polymorphs of $P_2O_5$.

### 2.2.3.4 Low Tg phosphate glasses

Considerable research has already been carried out on phosphate glasses, as a result of their interesting properties such as ultra-low glass transition temperature. The use of phosphate glasses as fillers has many advantages over the more traditional inorganic materials. Phosphate glass is considered polymeric in nature, because of its similar chain network-cross-linked structures. The chains are much shorter than organic polymer chains and are composed of phosphate anion tetrahedra, Figure 2.4.

Its Tg is lower than the more traditional inorganic fillers, which makes it attractive for academic and industrial use. However, there are limitations for many applications due to the poor chemical durability of phosphate glasses [99].

In terms of hybrid compounding for coatings, it is essential to select a glass with acceptable chemical durability. There is a study [101] related to the development of chemically durable phosphate glasses that have low glass transition temperatures. This study is aimed at obtaining mouldable glass-polymer composites with special characteristics such as stiffness, strength, and dimensional stability at high temperatures for the benefit of high-end engineering uses. The molar composition of the glass in this study is $50\%\ SnF_2 + 20\%\ SnO + 30\%\ P_2O_5$ and designated tin fluoride phosphate (TFP) glass. Thus, this type of glass was selected for the current research because of its low melting temperature, improved water resistance and chemical durability. The TFP glass was discovered in 1982 and patented by Tick [102-103].

Incorporating tin oxide into the structure of the phosphate glasses is expected to improve the chemical durability and water resistance of the glass. The expected role of $SnO$ in this system is to act as network former in a tetrahedral coordination and bond with the phosphorous via oxygen forming $Sn-O-P$stronger linkages. Replacing weak bonds as $F-P-F$, $Sn-P-F$ or also $P-O-P$ by $Sn-O-P$ strong bonds the connectivity of the network will be increased and as a result, water resistance and chemical durability improved. On the other hand, adding a fluorine atom into the glass structure will break the polymer chain with the formation of a $PO_3F$ terminal group. When oxygen is replaced by a fluorine atom, the intermolecular interactions increase due to the decrease of the average length of the chain and so the packing density of the structure increases. As a result, a lower vitrification temperature should be achieved [100].

The expected glass transition temperature is approximately 125 °C and the density is approximately $3.75\ gcm^{-3}$. The repeating unit of phosphate glass (Equation 1) is shown below [100]:

$$SnO_2F - PO_3F \qquad (1)$$

The glass behaves as a Newtonian-fluid at several frequencies and temperature ranges. Its viscosity is strongly dependant on temperature. This glass is ideal for use as a filler in a polymer matrix because of its rheological behaviour combined with a low glass

transition temperature. The structure of the glass depends on the $P_2O_5$ content and $PO_4$ interconnections.

The structure of phosphate glasses can be studied using various techniques such as the infrared and Raman spectroscopy, nuclear magnetic resonance, and X-Ray photoelectron spectroscopy. From the results published so far [104], it follows that in ultra-phosphate glasses (where $[P_2O_5]$ > 50 mol. %) the metal oxides of SnO, PbO and ZnO enter the network mainly as modifiers. The further lowering of $P_2O_5$ content forms metaphosphates ($[P_2O_5]$ = 50 mol. %) and then polyphosphates with $[P_2O_5]$< 50 mol. %. This is associated with the formation of covalent $P-O-x$ (where x is Sn, Pb, Zn etc) linkages, which give rise to an increase of connectivity and cross-linking of the network. Hence, Tg increases and the stability of the glass to water corrosion [105]. In polyphosphate glasses, where $[P_2O_5]$ = 40 mol. %, however, MO has the role of network changers while the atoms can act as network former and network modifier. At $P_2O_5$ = 50 mol % metaphosphate glasses are obtained with mainly $Q^2$ tetrahedra and few chains ends $Q^1$ ($PO_3^-$).

### 2.2.3.5 Effect of adding F in $P_2O_5$ glass structure

The addition of F to the glass structure results in network depolymerisation and it breaks the $P-O-P$ bond to form fluorophosphate ($PO_3F$) $Q^1$ units or difluoro-phosphate ($PO_2F_2$) $Q^0$ units [92]. A proportional decrease of the average length of the phosphate chains, increasing the fluorine species into the phosphates is observed and a successive conversion leads to pyrophosphate dimers [106]. The process can be detected by a Raman peak at 1020 $cm^{-1}$ attributed to the $\upsilon_s$ stretching vibration $PO_3^{2-}$ of the $Q^1$ [107]. The addition of $SnF_2$ provides an electron to form another chemical species in a redox chemical reaction. Since the reducing agents is losing electrons, it must be oxidized ($Sn^{2+}F^-$).

### 2.2.3.6 Effect of adding Sn in $P_2O_5$ glass structure

The addition of SnO to $SnF_2-P_2O_5$ glasses should decrease the volatility of the melt and increase the chemical durability of the glass [106]. Divalent tin plays the role of a network former in a tetrahedral coordination and bonds with phosphorus via oxygen $Sn-O-P$. Here $Sn^{2+}$ acts as a network former to produce cations.

$P-O-P$ and $Sn-O-P$ bridges increase the linkage of the glass network, while $F-Sn-F$ bridges are of lesser importance. $F-Sn-F$ and $P-O-P$ bonds are easily attacked by water and provide weak points in the network. Since $P-O-P$ bridges are incorporated in the basic structural unit, it follows that durability would be inversely proportional to the number of $P-O-P$ bridges. The increase in chemical durability through the increase of $SnO$ content takes place because the weaker linkages of $F-Sn-F$, $Sn-P-F$ and $F-P-F$ are gradually replaced by stronger $Sn-O-Sn$, $Sn-O-P$ and $P-O-P$ linkages. The replacement of $P-O-P$ bonds by $Sn-O-P-O$ bonds increases the connectivity of the network and decreases its susceptibility to attack by water [ 93,106-107].

### 2.2.3.7 Characterization of phosphate glass structure

Phosphate glasses have been developed over recent years with much lower glass transition temperatures (Tg) than those of conventional silicate glasses [108-109]. Specifically, phosphate glasses can have Tg values as low as 100 °C as compared with 50 °C for typical silicate-based glasses. These unique thermal properties offer major potential in engineering applications including sealing [110], nuclear waste storage [97] and biomedical implants [105]. A further possible application is in polymer composites.

Phosphate glasses have the glass transition temperatures in a broadly similar range to the melting temperature of organic polymers and so co-processing by extrusion in which both components are fluid is a possibility. A molten rather than a solid (as it is the case in conventional polymer processing) glass phase should in principle allow much higher glass loadings and enhanced properties. One part of this research is directed at developing an understanding of the mechanisms of melting and defining the processing conditions of phosphate glasses for co-extrusion with polymers with the ultimate aim of producing high-performance glass-polymer hybrids.

The structure of vitreous phosphates is based on a molecular tetrahedral building block [98,102]. Phosphorus is a pentavalent ion and so the formation of a phosphorus-oxygen tetrahedron with four bridging oxygens would result in an impracticable unit with a net positive charge of +1. Nevertheless, a charge-neutral tetrahedron can be formed if one of the oxygens forms a double bond with the pentavalent phosphorus ion $(P-O)$,

while the other three oxygens form bridging oxygens $P-O-P$ with adjacent tetrahedra.

In practice, the tetrahedra link up, using the covalent bridging oxygens, to form various phosphate anions. The tetrahedra may be classified using the $Q^i$ terminology [111-112], where i represents the number of bridging oxygens per tetrahedron. Phosphate glasses can be made with a range of structures, from a cross-linked network of $Q^3$ tetrahedra as in vitreous $P_2O_5$, to polymer-like metaphosphate chains of $Q^2$ tetrahedra, to glasses based on small pyrophosphate $Q^1$and orthophosphate $Q^0$anions, depending on the oxygen-to-phosphorus ratio as set by the glass composition.

Low-temperature glasses tend to show inferior chemical durability in humid environments and these hygroscopic characteristic limits their practical application. However, glasses have now been developed with much higher stability, particularly tin phosphate oxyfluorides [111-112]. The addition of $SnO$ to binary stannous fluorophosphates glass resulted in a decrease in the volatility of the melt and dramatic improvements in the chemical durability of the glass [111-112]. The substitution of $SnO$ for $SnF_2$ drastically reduced dissolution to rates comparable to soda-lime silica glass [111,112]. The increase in chemical durability is attributed to the weaker linkages of $Sn-F-Sn$, $Sn-F-P$ and $P-F-P$ being replaced by the stronger $Sn-O-Sn$, $Sn-O-P$ and $P-O-P$ linkages. The composition of the glass will have a direct bearing on its blending with polymers as well as influencing the properties of the resulting composite [113].

A tin fluoride phosphate glass with a molar composition of 50 mol% tin fluoride ($SnF_2$), 20 mol% tin oxide ($SnO$) and 30 mol% phosphorus pentoxide ($P_2O_5$) was selected for investigation due to its unique combination of low Tg, rheological properties, water resistance and chemical durability. The low Tg has the possibility of making the phosphate glass fluid during polymer processing. In addition, the glass has been reported to have an affinity with some polymers, which may provide possibilities for hybridization [113–114].

For a fixed glass composition, however, the processing conditions are also expected to influence the formation of its final structure and the properties. No systematic

investigations were found in the literature on the quantitative effect of melting conditions on the final properties of tin fluoride phosphate glass.

This research will characterize the effect of melting on glass structure [115] and properties [116] by techniques including FTIR, Raman, DSC, TGA and density and complex viscosity in comparison with related systems in the literature. The research will have value in understanding the sensitivity of glass performance to melting conditions and relevance for upscaling of the glass synthesis in the development of possible future industrial applications.

## 2.3 Phosphate glass- polyamide 11 hybrid powder preparation for industrial application

The composition and properties of the coating material are vital not just for the mass-based coating efficient but also for the quality of the final coating. The optimisation of the coating is more a fundamental chemical rather than a process challenge. More than one attempt is always needed before finding the correct coating composition that meets all the requirements demanded by the final target of the research. A selection of additives such as surfactants, plasticisers, texturisers, emulsifiers, anti- adherent agents, and stabilisers can indeed improve the coating properties and avoid unwanted agglomeration. Such additions, however, often cause other problems like decreased adhesion on the particles and/or reduced mechanical or leaching properties.

### 2.3.1 Design of the formula

In industrial scale, it is often difficult to add new compounds. Compromises must be found between the composition of the coating, solution, economics, process conditions and legislation. Hence, there are often a limited number of new additives, which in practise may be chosen from.

The final approach of this research project was to develop a new family of nanostructured organic-inorganic hybrid coatings for industrialization in the fluid market. A common polymer coating used for this market is Rilsan fine powder PA11. Thus, Rilsan was selected as the first organic component of the hybrid to develop this new nanohybrid coating.

Prior to opening the workflow of the activities to attain the exciting and ambitious objectives of the research, it is important to define two things first:

1) Finished product expectations in term of surface protection for the fluid market
2) The environmental conditions that the nanohybrid coating will experience throughout its working life in this market.

The surface protection requirements for the fluid market are summarized in Table 2.1.

Table 2. 1: Coating characterization requirements for fluid market.

| Characterization method | Test condition | Required result | PA11 results | Hybrid expectation |
|---|---|---|---|---|
| Hot water immersion | 14 days at 50 °C | Adhesion test > or = 1 | Limit or no | Yes |
| Water absorption | 100 days at 23 °C | < 4% | 1,5 | 1.2 |
| Impact resistance | ASTM G14 | 2J | 2,1 | 2.8 |
| Abrasion resistance | CS17 | < 40 mg | 12 | 12 |
| Thermal stability | 28 days | Adhesion test > or = 1 | No | Yes |
| Chemical resistance | Salt | hydrocarbons | No | Yes |
| Effect on water quality | Potable water | Agre.AS/NZS | - | - |

It is mentioned along the research that in the last years due to health, safety, and environmental regulations, an urgent need to reduce the use of volatile organic compounds (VOCs) in the coating market is prioritizing. To have adhesion of Rilsan® on metal, it is necessary to apply a primer. This primer layer is an epoxy resin where solvents and bisphenol A are present. Thus, another alternative to replace the primer has been demanded. The over cost engendered by primer application compared to competing products such as epoxy or polyolefin coatings (Plascoat company products) applied directly to the metal, makes Rilsan coating not competitive for the market.

Therefore, this research is focused on designing coating powders to develop a functional polymer-glass hybrid coating, to fulfil the fluid market requirements, respect the European regulations and show competitiveness by self-priming in the market. The focus is on the inorganic phase of the hybrid.

The main points to work on are:

- The enhancement of mechanical and thermal properties together with chemical resistance in the powder (via nanoparticles).
- The development of a primeless coating (via a metal- glass- polymer hybrid which could react with the matrix and substrate).

Phosphate glasses and PA11 were selected as components in order to take advantage of their high coating performance and their compatibility which was expected to achieve a nanosized hybrid coating. The thermal stability and decomposition temperature can be improved with nanoparticles due to two facts:

1. The superior thermal stability of the nanofillers, which promotes the stability of polymer matrix via the formation of protecting layers or chars during decomposition. In nanocomposites of MWNTs throughout PA11, the thermal stability was improved by about 20 °C when the nanotube concentration is 1 wt% [117].

2. The excellent thermal conductivity of the nanoparticles. It was reported [117] that the enhanced thermal conductivity of a composite (PA11/conventional flame retardants additives) can facilitate heat transport and increase its thermal stability through the incorporation of high thermal conducting nanofillers like carbon nanofillers.

A synergism between conventional flame-retardant additives (phosphorus chemicals like polyphosphoric acid, phosphorus pentoxide and specialty organophosphorus compounds) and two types of nanoparticles (carbon nanofillers (CNF) and montmorillonite (MMT) nanoclays PA11 matrix) is reported [117].

The incorporation of MMT nanoclays or CNF nanoparticles into the PA11 has been shown to be an effective method for developing Fire Resistance (FR) thermoplastic polymers by twin-screw extrusion (a melt blending process). It has been demonstrated that small amounts of those nanoparticles (<7%) are required to make nanocomposites to exhibit similar enhanced flame-retardant properties when compared with the FR thermoplastic generated by conventional methods [118-125]. However, unlike the conventional FR thermoplastics, the resulting nanocomposites exhibit enhanced mechanical properties such as improved strength/modulus, moisture resistance and

higher heat deflection temperature. Therefore, nanotechnology can be used to develop novel FR thermoplastic structural components with high performance characteristics.

There are several applications where high pressures and temperatures dictate the use of fire-resistant material to mitigate the potential for dangerous and expensive fires. Flame retardants are chemical additives used in thermoplastics, thermoset, textiles, and coatings. The fire resistance of the material is its ability to withstand fire, retain structural integrity and prevent fire spread to an adjoining area for a period of time. They limit the spread of fire by containing it within designated spaces or zones and preventing structural collapse. It is reported that common phosphate plasticisers impart some flame resistance to polymers. Preliminary evidence of flame resistance improvement is reported for P/Glass PA6 hybrids [5].

On the other hand, phosphate is used as a flame retardant in polyamides. For example, different polyamides, especially glass fibre reinforced grades, can be effectively flame retarded with halogen-free products based on the phosphonates. The required dosage for a UL 94 V-0 performance (see Experimental Details Section) is lower than for other flame-retardant formulations apart from red phosphorus. The flame-retardant effect is achieved in the solid state leading to enhanced char formation which is typical of phosphorus-based flame retardants [126].

Considering the preliminary reported improvement of flame resistance, and the importance of this property for coatings, the UL 94 test was carried out in this study into the new nanostructured polymer-glass hybrid. Fire resistance will be evaluated for the first time in this material.

UL 94 is the Standard for Safety of Flammability of Plastic Materials for Parts in Devices and Appliances testing. It is a plastics flammability standard released by Underwriters Laboratories of the United States [127]. The standard determines the material's tendency to either extinguish or spread the flame once the specimen has been ignited.

Certain polymeric material coatings like PA11 have poor adhesion to metal surfaces, while inorganic coatings may lead to thickness limitations, porosity, micro cracks, and high internal stress. Research has therefore intensified in recent years on inorganic-organic hybrid materials deposited by diverse coating techniques. The excellent

anticorrosion performance of these materials has opened up interesting possibilities. The enhancement of anticorrosion is partly due to the improvement of adhesion.

The low $T_g$ is expected to make the phosphate glass fluid during polymer processing and its reported affinity may improve the possibilities for hybridization [128-130]. It is reported that good affinity and miscibility between phosphate and PA 6 takes place due to results obtained by the author [5], which may encourage the formation of nanoparticles using PA11 and TFP glass.

One way to improve the barrier properties and consequently chemical resistance is by creating a maze or "tortuous path" by nanoparticles that retards the progress of the water molecules through the matrix and improves the adherence to the metal surface by the affinity of the metal-glass; the glass being fluid during the coating application.

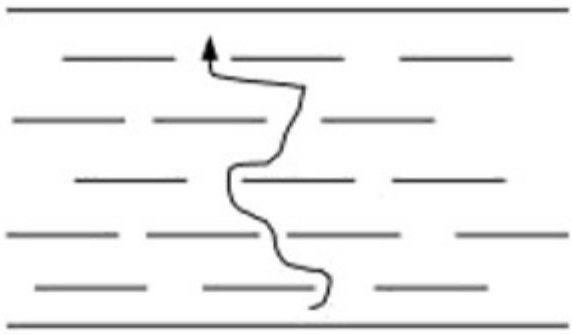

Figure 2. 7: The tortuous path of polymer/layered silicate nanocomposite.

A high aspect ratio of nanofillers in nanocomposites can reduce the gas permeability. The dependence on factors such as the relative orientation and dispersion is still not well understood. The gas will pass through the film of the nanocomposites by a tortuous path as illustrated schematically in Figure 2.7. Besides the particle length, the concentration, state of aggregation and the relative orientation of the particles in the matrix are also important parameters for barrier properties. The enhanced barrier characteristics, which benefit from the hindered diffusion pathways through the nanocomposites, will lead to improvement of flame retardant and chemical resistance through reducing solvent uptake.

Water absorption and vapor permeability tests are useful techniques for evaluating chemical resistance. In general, composites can be designed within defined limits by tailoring their properties depending on the selection of components.

The most important testing to evaluate the adhesion are hot water immersion and impact resistance. Both, together with additional testing such us hardness and abrasion, were carried out to evaluate mechanical properties. Polymeric gas barriers which have improved resistance to oxygen and/or water vapor transmission as a result of the inclusion of nanoparticles, which create a tortuous path through the polymeric material, were contemplated too.

## 2.3.2 Characterization of surface energies

Given that the action of tin fluoride phosphate (TFP) glass-PA11 hybrid takes place essentially at the level of metal / polymer or polymer / glass interfaces, it is essential to properly characterize the surface energies of the different precursors as well as the interfacial energies at the temperature of the extrusion process.

### 2.3.2.1 Surface energy and surface tension

The surface has a molecular or atomic organization different from that of the volume of the material, due to a different number of neighbours, which makes it less thermodynamically stable and more reactive. The surface energy $\gamma$ is defined from a thermodynamic point of view as the work necessary to create a unit of interface area (in $\mathrm{mJm^{-2}}$) at constant temperature, volume, and chemical potentials. Surface tension is defined mechanically as the force per unit of length required to keep the surface in balance (in $\mathrm{Nm^{-1}}$).

In the case of liquids, $\gamma$ is independent of the surface deformations and the surface is isotropic, the surface energies and surface tensions are equal. Thus, in the literature [131], the two terms are often confused. However, in the case of solids, the quantities of the two terms are distinct, and it is often the surface tension which is characterized experimentally. In the case of viscoelastic polymers in the solid state, where the surface is isotropic, the variation of the surface energy compared to the elastic deformations of the surface is often negligible if the surface has no surface roughness, therefore very smooth.

#### 2.3.2.2 Interfacial tension

The interfacial energy (or interfacial tension) $\gamma_{AB}$ is the asymmetry of the forces of attraction of the molecules between two immiscible condensed phases. The Gibbs equation in thermodynamics (Equation 2) expresses the variation of surface and interfacial energies as a function of temperature and chemical potentials [132]:

$$(d\gamma_{AB} \text{ or } d\gamma) = -sdT - c_i d\mu_i \quad (2)$$

where s is the surface entropy per unit area, $c_i$ and $\mu_i$ respectively the concentration and the chemical potential of constituent i.

Equation 2 shows that surface energy and interfacial energy decrease with temperature due to the increase in the mobility of molecules. This relationship is notably verified in the case of polymers with a variation of $-0.05\ mJm^{-2}$ by increase of + 1 °C against $-0.01\ mJm^{-2}$ for polymer interfaces [132].

##### *2.3.2.2.1 Work adhesion*

The adhesion work $W_a$ (Equation 3), which is the reduction of Gibbs free energy per unit area, can be defined from the interfacial and surface energies, according to the equation of Dupré [132]:

$$W_a = \gamma_A + \gamma_B - \gamma_{AB} \quad (3)$$

where $\gamma_A$ and $\gamma_B$ are the surface energies of phases A and B.

Consequently, the higher the interfacial energy $\gamma_{AB}$ the lower the adhesion work, which is a favourable situation for the establishment of an interface. However, poor adhesion work also results in an interface that is not very stable because it is weakly maintained by adhesion. The difference in phase polarity is the first factor affecting the amplitude of the interfacial energy. Thus, Girifalco and Good [133] introduce the interaction parameter φ (Equation 4) to account for the similarity of the interactions of the two phases:

$$\gamma_{AB} = \gamma_A + \gamma_B - 2\varphi\sqrt{\gamma_A\gamma_B} \quad (4)$$

The interaction parameter φ varies from 0 to 1, with φ tending to 1 when the two phases have close polarity.

*2.3.2.2.2 Interdiffusion area*

Two condensed phases A and B in contact have an interface in which the two components suffer interdiffusion. In the case of polymers, it is possible to go back to the thickness of the interdiffusion zone $L_i$ of the two phases A and B, via the Flory-Huggins parameter and from the interfacial tension. According to the mean field theory, the interdiffusion zone $L_i$ is inversely proportional to the interfacial tension $\gamma_{AB}$. Wu [132] establishes the empirical relation $\gamma_{AB} = 102L_i^{-1}$ with $L_i$ in angstrom. The interface for immiscible polymers is generally on the order of 1 to 10 nm.

*2.3.2.2.3 Case of a solid / liquid interface*

The deposit of a drop of liquid on a solid substrate can generate several situations with contact angle $\theta$, between the tangent to the drop and the surface, being different according to the interfacial tension role (Figure 2.8):

(a) total wetting: the liquid spreads completely on the solid surface ( $\theta = 0^\circ$ )

(b) partial wetting: the liquid is a drop in the shape of a spherical cap with a contact angle $\theta$ with the surface ($0 < \theta < 180^\circ$ )

(c) zero wetting: the liquid forms a spherical drop on the surface ( $\theta = 180^\circ$ )

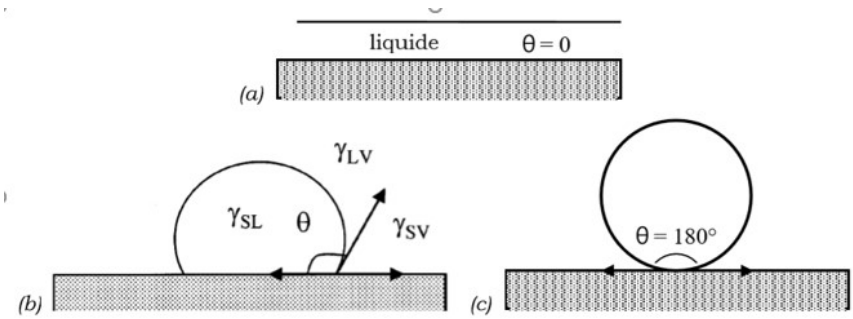


Figure 2. 8: Different wettings: a) total wetting; b) partial wetting; c) zero wetting.

The spreading coefficient $\lambda_{AB}$ of A over B defined by Equation 5 makes possible to predict the different wetting situations: if $\lambda_{AB} \geq 0$, there is total wetting and if $\lambda_{AB} < 0$, there is partial wetting.

$$\lambda_{AB} = \gamma_B - \gamma_A - \gamma_{AB} \quad (5)$$

In the case of partial wetting and zero wetting, the Young's equation, Equation 6 [135] links the different interfacial tensions between the three phases involved:

$$\gamma_{SV} = \gamma_{SL} + \gamma_{LV}\cos(\theta) \quad (6)$$

Where $\gamma_{SV}$, $\gamma_{SL}$ and $\gamma_{LV}$ are, respectively, the solid-vapor, solid-liquid and liquid-vapor interfacial tensions.

The spread pressure at equilibrium $\pi_e$ (Equation 7) is related to the surface tension of the solid $\gamma_s$ to $\gamma_{sv}$ by:

$$\pi_e = \gamma_s - \gamma_{sv} \quad (7)$$

According to Wu [135], this pressure is negligible for polymers if the contact angle is large (typically greater than 10 °).

2.3.2.2.4 Measurement methods

The surface energy measurement methods used in the case of molten polymers can be classified into two categories:

- experimental methods, which are based on the equilibrium of known forces, such as sessile drop, hanging drop or rotating drop. However, many experimental difficulties result from the high Newtonian viscosity of the polymers, implying a long duration of experiment and therefore risks of degradation.
- semi-empirical methods, which are based on theoretical considerations. The methods are those of the homologous liquid, the molten polymer, the equation of state and the harmonic mean [135].

The different methods used for the characterization of the surface energies of the polymers are presented below.

a) Pendant drop method

The principle of pendant drop method is to determine the surface energy of the liquid γ (Equation 8) forming a hanging drop, at equilibrium between the forces of gravity and capillarity:

$$\gamma = (\Delta\rho g D^2)/H \quad (8)$$

where Δρ is the density difference between the gas phase and the liquid phase, g the acceleration of gravity, D the maximum diameter of the drop and H a correction factor depending on the shape of the drop [135].

b) Method of the equation of state

The equation of state method proposed by Wu [135] makes possible to deduce the surface energy of a polymer solid surface from a whole spectrum of drops of liquids of different polarities and surface energies.

c) Harmonic mean method

The equation of the harmonic mean (Equation 9) is quite often used in the literature to calculate surface or interfacial energies [133]. It is based on the theory of fractional polarities which postulates that the surface energy can be decomposed into a polar component $\gamma_p$ and a dispersion component $\gamma_d$:

$$\gamma = \gamma_p + \gamma_d \quad (9)$$

The polar and dispersion components consider the ability of the material to induce respectively:

- Short-range Lewis acid-base interactions, for example if the material can be electron donor (base) or acceptor (acid). They include dipole forces, induction forces or hydrogen bridge interactions.
- Long-range Lifshitz-van der Waals interactions. They include the dispersion forces of Keesom, Debye and London.

Similarly, the adhesion work can be broken down into dispersion and polar part by a harmonic mean, in the case of low energy materials, such as polymers.

### 2.3.3 Industrial preparation of powder coatings

In Figure 2.9, the manufacturing process of powder coatings is explained. The first step is to design the formula and weigh the raw materials. The second one is the melting and extruding as explained below.

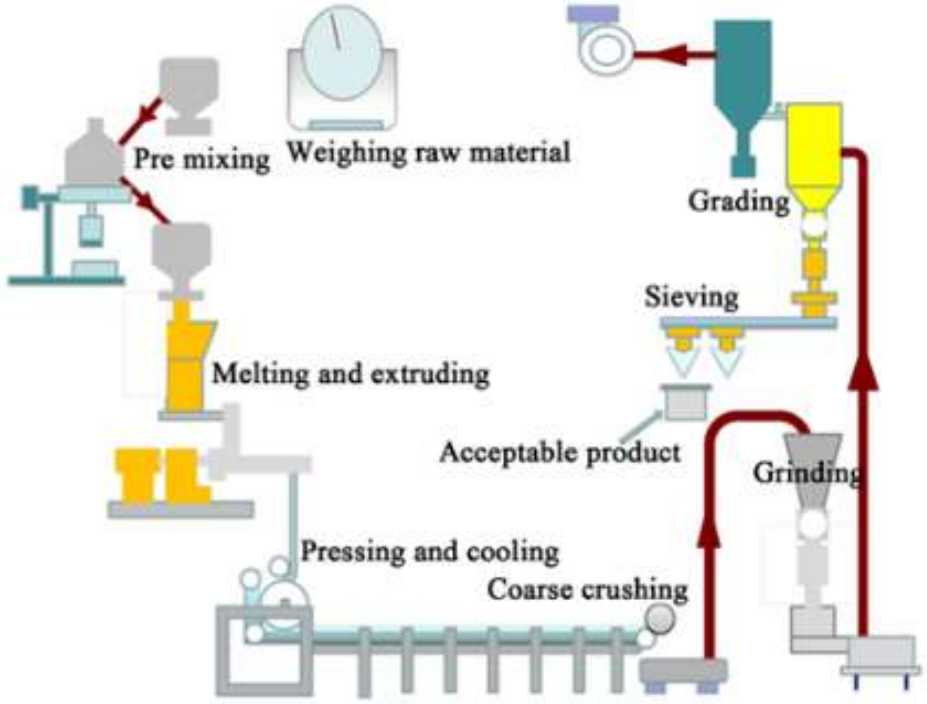


Figure 2. 9: Powder coating preparation process.

### 2.3.3.1 Melting and extruding

Initial laboratory research is necessary to start the industrialization process. This research provides guidance data for the high scaling step. The morphology of the hybrid was developed in the laboratory step.

The literature research [135] of the action of polymers in the flow shows that the understanding of these phenomena passes through polymer mixtures. It is the properties of the constituents and the physical parameters of the process that will control the dispersion of the minority phase. The literature [136] relating to the development of structures under thermomechanical action is very extensive.

The first theoretical and experimental studies on the deformation of simple shear mixtures were carried out on Newtonian fluids by Taylor [135]. He observed a spherical drop in a shear flow. The spherical particle is deformed into an ellipsoid, whose geometric characteristics depend on two dimensionless numbers: the ratio of the viscosities, $\rho$ , with $\eta_d$ and $\eta_m$ respectively, the viscosities of the drop and the matrix (Equation 10).

$$\rho = {}^{\eta_d}/_{\eta_m} \qquad (10)$$

The capillary number, Ca, which represents the ratio of the viscous stress to the stress due to the interfacial tension is given in Equation 11. The viscous forces tend to deform the inclusion, while the interfacial tension tends to oppose the deformation.

$$\mathrm{Ca} = \eta_m \dot{\gamma} / (\gamma_{AB} / R_0) \qquad (11)$$

Where $\dot{\gamma}$ is the shear rate, $R_0$ is the initial radius of the drop, $\gamma_{AB}$ the interfacial tension between the drop and the matrix. Taylor predicts a $\mathrm{Ca_{crit}}$ failure criterion that can be represented in a diagram as a function of the ratio of viscosities ρ (Figure 2.10).

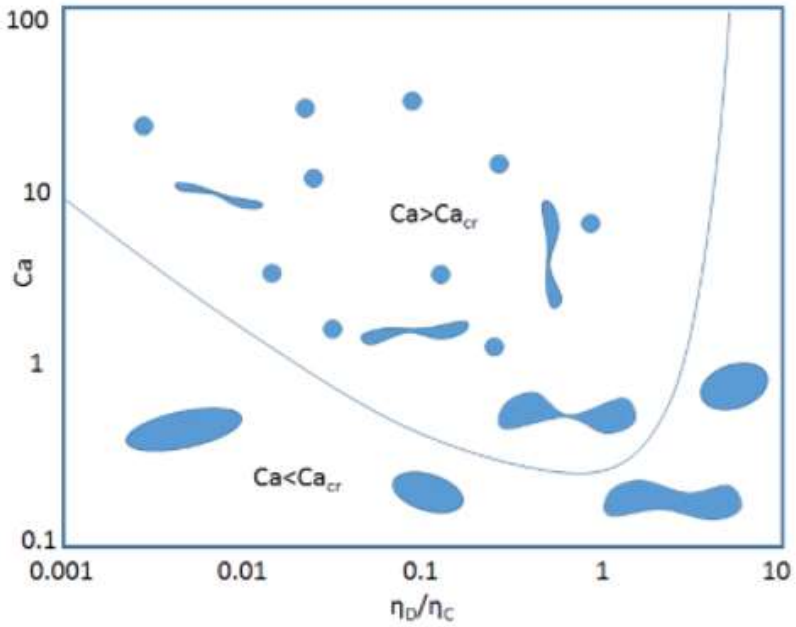


Figure 2. 10: Critical capillary number versus viscosity ratio (***ρ***) in the case of simple shear and Newtonian flow elongation [135].

Depending on the value of the capillary number, different mechanisms take place in the deformation of the inclusion (Figure 2.11). If $\mathrm{Ca} << \mathrm{Ca_{crit}}$, the drop does not deform. On the other hand, if $0.1\ \mathrm{Ca_{crit}} < \mathrm{Ca} < \mathrm{Ca_{crit}}$, the particle is deforms in an ellipsoid but without breaking. If $\mathrm{Ca} \geq \mathrm{Ca_{crit}}$, the drop will deform and break.

Figure 2. 11: Mechanism of rupture by Rayleigh instabilities [135].

The polymer mixtures obey complex phenomena controlling the dispersion and the granulometry of the constituents of the mixture. The mechanisms of coalescence and deformation / rupture of the minority phase involve the operating conditions of the processes used but also the intrinsic properties of the materials. It is, therefore, interesting to determine these conditions in order to see that such phenomena exist in the flows of PA and TFP glass.

The research was focused on characterizing the chemistry, rheology, and surface physico-chemistry of the polymers of the study, which will then allow to compare the performances of the hybrids according to their intrinsic properties.

#### 2.3.3.2 Polyamide 11- TFP glass hybrid compounding

The processing of TFP glass-polymer hybrid using conventional methods like extrusion is feasible because of the low glass transition temperature (125 °C) of the glass [6]. Both the polymer and the glass are fluid during the processing of the hybrid. This facilitates the control of the morphology by tailoring the molecular interactions and avoiding intractable processing problems.

As a result, the synthesis of glass-polymer hybrids is carried out by aiming to enhance the interactions between phosphate glasses and highly interacting resins, as with polyamide. The key advantage of the TFP glass is its Tg, which is low enough to allow melt processing with engineering thermoplastics to produce composite hybrid systems. The interaction between polyamides and phosphate glasses is widely documented [6], where it is shown that there are exceptional physicomechanical interactions between the components. The absorption of ammonia to the phosphate glass surface is one such classical interaction of these hybrid components. The hybrid components undergo a high degree interaction, which contributes towards their miscibility in the melt and the polymer-glass adhesion in the solid state. This could possibly result in the dissolution of particles to achieving nanometric-scale morphologies. This offers the possibility of materials with compatibility and interesting melt behaviour. The structure of the hybrid (Equation 12) may facilitate the interaction between two structures:

$$\underset{\text{Polyamide 11}}{-[\mathrm{HN}-(\mathrm{CH_2})_{10}-\mathrm{CO}]_n-} \qquad \underset{\text{Tin fluoride phosphate glass}}{\mathrm{SnO_2F}-\mathrm{PO_3}} \tag{12}$$

The measurement of rheological properties will be important in controlling the coating formation in the deposition process. Other possible options to improve interactions and miscibility include changing the matrix, using additives such as coupling agents and manipulating the molecular weight distribution.

## 2.3.4 Powder Characterization

In this research, the fluidized bed dipping powder coating technique was chosen as coating process. The principle of a fluid bed is to maintain particles in suspension in a close area by blowing air through the particle bed. The state of the bed depends thereby on the air velocity and on the particle properties. A fluidised bed behaves like a boiling liquid [137].

### 2.3.4.1 Mean particle size and density

The most important parameters regarding the air velocities of fluidized bed dipping coating process are fluidisation properties. The importance of particle size and density on fluidisation properties is recognized. Thus, for any particle of known mean particle size and density , the Geldart chart (Appendix C) indicates the type of fluidisation to be expected [138].

Geldart [137-138] has found four overall fluidisation modes (C, A, B and D) and determined a general particle classification chart. The particles suited for coating often come from group A as the particles have the aeration properties required for coating purposes. Group A particles have small mean particle size and/or density less than 1.4 g/cm$^3$. Commercial PA 11 Rilsan® fine powder has 100 μm of mean particle size and 1.02 g/cm$^3$ of density.

The achievement of Group A classification for this novel hybrid was expected to reach by TFP glass – PA hybrid reported interaction [6]. Homogeneous dispersion and nanosized particles morphology were identified as key point.

### 2.3.4.2 Viscosity characterisation

The rheological properties of coatings (that is, their ability to flow) are of prime importance in their preparation, storage, and application. Coatings key factor in rheology is the viscosity of the fluid [139]. In some cases, the viscous properties of the

combination of the polymer, pigments, and solvent is sufficient to provide the correct viscosity for the coating. In other cases, however, specialty additives must be employed to achieve precise control of viscosity. These materials are often known as thickeners, and, as their name suggests, they are used to increase the viscosity of, or thicken, a coating when added in small amounts.

The most important rheological parameters [139], with respect to the application process are the measurement of:
(i) the change of viscosity during the drying period.
(ii) the viscosity of the coating, ready for application, in the shear range from below 1 $s^{-1}$ to more than 10000 $s^{-1}$.
(iii) the thixotropic recovery of viscosity at a shear rate below 1 $s^{-1}$ following shearing at a shear rate or the increase of viscosity over the time.
(iv) the stress relaxation from a low shear rate where relaxation times are largest or from a realistically high shear rate.
(v) the change in the composition of the material during drying in terms of evaporation.

This characterization is found to be closely related to many of the different flow problems occurring in the application process. Rotational viscometers, normally used in coatings laboratories, are the most advanced instruments required for the characterization. This characterization, furthermore, is consistent with theoretical approaches to rheology, thereby giving access to an extension of the validity of the measurements on theoretical grounds and to use of extensive knowledge of how well-defined materials behave and interact in the design of coatings with a certain flow. The framework of the characterization is found to be crucial in relating application process and rheology, whereas the specific measurements can be made in various ways.

The progress of the reaction is monitored by an inherent viscosity measurement of the powder. Inherent viscosity provides information about the molecular weight of the polymer which has direct influence on the applicability of the powder. To be marketed, the powder must have an inherent viscosity within a specific range. Too low viscosity of the powder gives a very brittle coating and reduces its mechanical properties. On the other hand, a powder with too high viscosity is inapplicable because the powder grains no longer coalesce to form a film. To monitor the progress of the reaction in

relation of hybrid molecular weight. The specific range to avoid coating applicability problem for PA11 is 1.0 -1.1.

## 2.4 Coating characterisation

Coatings are applied to a variety of surfaces for aesthetic and/or functional purposes. In general, coatings are used for corrosion resistance, adhesion properties and wear resistance. Coatings are generally applied and then undergo a curing or solidification process. Understanding the capabilities of the coating properties enables engineers to develop performance-enhancing coatings as well as optimize processing techniques.

A broad set of coating characterization techniques are available in the market:

- Salt Spray
- Humidity Testing
- Chipping Resistance
- Hot Water Resistance
- Accelerated Weathering
- Acid Resistance
- Gasoline Resistance
- Alkali Resistance
- Oil Resistance
- Bending Resistance
- Impact Resistance
- Pencil Hardness
- Coating Thickness
- Coating Weight
- Adhesion
- SEM Analysis

Some techniques from this set were selected to characterize the novel TFP glass – PA11 hybrid coatings:

- Hardness
- Resistance to immersion in hot water
- Adhesion
- Roughness

- Hardness (Shore D)
- Abrasion (Taber)
- Impact resistance The ASTM G14, Standard Test Method for Impact Resistance of Pipeline Coatings (Falling Weight Test), impact test materializes the resistance to a falling object on the coating.

### 2.4.1 Coating aspect

To obtain a proper performance of the film it must be free of defects. The coating must have total recovery of edges and no orange peel appearance. There are other defects that it is necessary to avoid. They are listed below:

- Poor adhesion can appear due to too little or too much primer, wrong preheating temperature and/or time and degassing of the part.
- Bubbles are present when the primer coating is too thick and air inclusion appears due to an excessively long dipping time.
- Clusters result from poor fluidization of the powder, insufficient or inadequate motion during dipping and contaminated powder.
- Black spots are due to the presence of impurities around the tank, pollution in the post-fusion oven and too high a preheating temperature.
- Yellowing can appear when preheating time is too long, dipping time too short and insufficient shaking during dipping.

### 2.4.2 Influencing parameters on the coating properties

Polymer toughness is a measure of the ability of a material to withstand the application of a sudden load without "failure". Impact resistance is therefore a complex function of several factors like geometry, mode of loading, load application rate, environment (thermal and chemical), and material properties (chain length, packing, tacticity, alignment and bonding forces). The measured impact strength of a polymer must be the result of the sum of the contributions of all processes that dissipate any of the energy of the impact blow. Impact behaviour can be improved by optimizing crystalline morphology, incorporating a discrete rubbery phase (via blending or copolymerization) or adding a reinforcement to the polymer matrix [140]. In this research, the third option was chosen.

There is currently no theory to predict the impact resistance of a charged polymer according to the characteristics and the amount of charges introduced. Experience in the field of polyamides and, more particularly in that of polyamide 11 coatings, is limited. In addition, the bibliographic references about the impact resistance mainly concern impact tests on massive parts such as Charpy shock. However, in the case of thermoplastics, the impact resistance follows some general rules.

The influence of the load on the coating will depend on the shape of the particles, their dispersion, and their cohesion with the polymer matrix. Depending on the behaviour of the particles into the matrix, reinforcement or strengthening mechanism can occur and two types of composites can be distinguished [140].

a) Dispersion-strengthened composites

Stretching is applied to prevent dislocation motions and propagation. The mechanism is like that of a precipitation hardening in metals. It occurs at the atomic/molecular level and involves interactions between the particles and dislocations within the matrix. Particles are smaller, 0.01-0.1μm in size.

For the material that has been strengthened by some processing method, the amount of the force required to start irreversible plastic deformation is greater than the original material.

Load interactions

- The matrix bears the major portion of an applied load while dispersoids hinder/impede the motion of dislocations.
- Plastic deformation is restricted, and yield, tensile strengths, and hardness are improved.

b) Particulate-reinforced or large particle composites

The term “large” is used to indicate that particle–matrix interactions cannot be treated on the atomic or molecular level.

Load interaction.

- These reinforcing particles tend to restrain movement of the matrix phase in the vicinity of each particle. The matrix transfers some of the applied stress to the particles, which bear a fraction of the load.

- The degree of reinforcement or improvement of mechanical behaviours depends on strong bonding at the matrix–particle interface.

The way in which contact, and interface phenomena occur leads to changes in the behaviour of the material. Wettability depends on the specific surface and the chemical composition of the surface of the load. It is necessary to have a good wettability of the charges to have a good dispersion. The effectiveness of reinforcement essentially depends on the adhesion between matrix and fibre, so this is a key factor in determining the final properties of the composite material, particularly its mechanical properties. To have good impact properties, the surface energy of the filler and that of the polymer matrix must be comparable. However, the adhesion between the polymer and the filler must not be too strong to allow the interface detachment that is necessary for the dissipation of the impact energy [141].

Many blends are two-phase, and their morphology depends on the type of molecular interaction and the resultant interface, the rheology of the components, and the processing history. As the interfacial energy between the phase's decreases, particle size will generally decrease and the extent to which the dispersed phase droplets deform under stress increases[142].

The impact resistance decreases with increasing crystallinity and especially the size of spherulites. The fillers can initiate heterogeneous crystallization and change the thermal characteristics of the material. Nucleation modifies the crystalline structure of PA 11 by increasing the size of the lamellae inside the spherulites, which puts the coating at a disadvantage.

The thickness, bond strength, and porosity of a coating directly affect its protective properties for a metal which is directly related to adhesion [143]. Powder Coating's adhesion depends upon wetting, viscosity, fillers, material flow and molecular weight. Modifying resin characteristics to improve flow by reducing polymer melt viscosity is one way to improve wetting thus improving mechanical bonding. This is a balancing act to achieve lower viscosity while not sacrificing other properties is important. Residual carboxyl functionality can help improve polar - polar bond attractions. This functionality could also contribute to moisture sensitivity, conflicting properties again. Research to find a means to induce chemical bonds between the polymer and substrate is a hard challenge. Good adhesion requires that the coating material be brought into

intimate contact with the surface itself or a firmly bonded chemical pre-treatment layer [144].

For coatings with different functions, including novel intelligent coatings, a reliable evaluation of adhesion is one of the key factors that affect the strategies for its improvement and the coating's overall performance [145].

# Chapter 3 Experimental details

## 3.1 Materials

The chemical components to synthesize the glass were supplied by Sigma Aldrich Company. The products' identifiers are summarized in Table 3.1:

Table 3. 1: Raw materials for glass composition.

| Product name | Chemical formula | Product number | CAS-N° |
|---|---|---|---|
| Tin (II) oxide | SnO | 244643 | 21651-19-4 |
| Tin (II) fluoride | $SnF_2$ | 334626 | 7783-47-3 |
| Ammonium phosphate monobasic | $NH_4H_2PO_4$ | 216003 | 7722-76-1 |

Properties of these reagents are summarized in Table 3.2:

Table 3. 2: Raw material properties.

| Properties | $NH_4H_2PO_4$ | SnO | $SnF_2$ |
|---|---|---|---|
| Molar mass / $gmol^{-1}$ | 115.03 | 134.71 | 156.69 |
| Density / $gcm^{-3}$ | 1.8 | 6.45 | 4.57 |
| Melting point / ° C | 190 | 1080 | 255 |

The polymer selected was polyamide 11 BMNO grade. It was supplied by ARKEMA as a trade name of Rilsan®. BMNO is a commercial grade in pellets. For a better mixing with glass, BMNO pellets were ground using Micropull 20H hammer mill cryogenic grinding with a grill of 0.2 µm. The mean diameter of particles is approximately 0.1 µm and inherent viscosity in solution (concentration in mass) is 0.97-1.16. Inherent viscosity ($\eta_{inh}$) is the ratio of the natural logarithm of the relative viscosity ($ln\eta_{rel}$) to the mass concentration of the polymer following the ASTM D1243 /D2857 /D4603 methods . Inherent viscosity (Equation 13) is defined as:

$$\eta_{inh} = ln\eta_{rel}/c \qquad (13)$$

where c is the mass concentration of the polymer and $\eta_{rel}$ is the relative viscosity (Equation 14), which is defined as:

$$\eta_{rel} = \eta/\eta_s \quad (14)$$

where $\eta$ is the viscosity of the solution and $\eta_s$ is the viscosity of the solvent.

## 3.2. Preparation of the glass

Tin fluoride phosphate glass, having a molar composition of $50\%SnF_2 + 20\%SnO + 30\%P_2O_5$, was selected and prepared using similar procedure to that reported in the literature [102-103]. The glasses were prepared by manually mixing tin fluoride, tin oxide, and ammonium phosphates in porcelain crucibles at room temperature. The ingredients were melted at temperatures between 350 °C and 550 °C - from 15 to 45 minutes in an electrically heated furnace. The glass was then poured onto a stainless-steel mould and left cooling to room temperature.

Considering the following Equation 15, approximately 30 g batches were synthesized following the calculation shown in Table 3.3. 30 g has been shown in both the literature [6] and the author's experimentation to be optimal.

$$2NH_4H_2PO_4 \rightleftarrows P_2O_5 + 2NH_3 + 3H_2O \quad (15)$$

Table 3. 3: Composition of experimental materials.

| Properties | $NH_4H_2PO_4$ | $P_2O_5$ | SnO | $SnF_2$ |
|---|---|---|---|---|
| Mol / % | | 30 | 20 | 50 |
| Content in g | 15 | 9.23 | 5.79 | 16.92 |

Different glasses were synthesised to check the effect of the melting conditions of the glass on its properties using different melting conditions. The melting temperature range was from 350 to 550 °C and the melting time from 15 to 45 minutes. The reference glass was melted at 450 °C for 25 minutes.

Research on glass melting conditions provides substantial understanding regarding the structure-properties relationship of the glass and the information required to design an appropriate scaling-up of the glass. The scaling-up of the tin fluoride phosphate glass for coating development was achieved with the help of GTS Ltd as the company had the expertise and necessary equipment. A series of glass batches using various glass melting conditions were synthetized for further experimental work.

## 3.3 Preparation of the hybrids

### 3.3.1 Laboratory scale hybrids

Prior to compounding, the glass was ground using a mortar and sieved at 400 µm. TFP glass- polyamide 11 hybrids were extruded using a DSM research 15 $cm^3$ micro compounder equipped with a DSM research laboratory injection moulding machine (Figure 3.3). Additional information is in Appendix D. The extrusion compounding conditions of the hybrids were selected within the following ranges:

- Glass content: 0-60 wt%
- Screw speed: 50-200 rpm
- Residence time: 2-10 minutes
- Processing temperature: 200-300 °C

The extrusion cycle can be monitored in a chart of force (N) versus time (Figure 3.1). Most of the melt-mixed hybrid materials were collected in extruded form (extruded strands). Furthermore, some characterization tests require dumb-bell injected samples processed according to ISO 527 BA1.

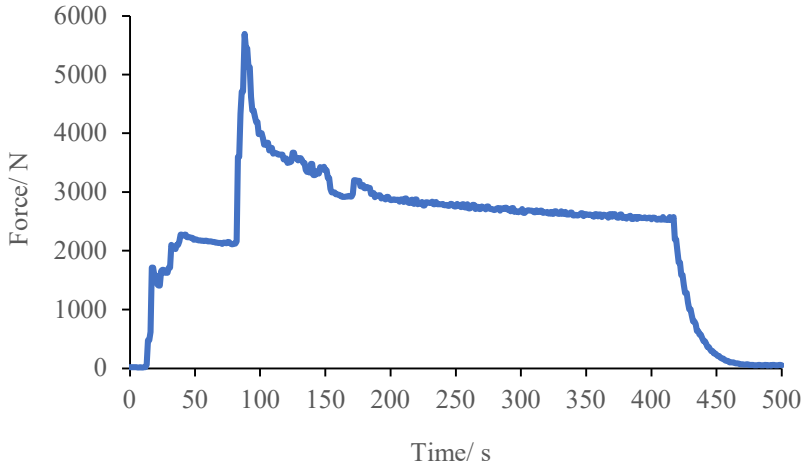


Figure 3. 1: Typical force versus time graph recorded during the mixing process for TFP glass/ Polyamide 11 hybrids.

The micro-injection processing parameters were mould temperature 40 °C, injection temperature 250 °C and maximum pressure 16 bars.

Figure 3.2 represent the different steps of an injection cycle. In this test, cooling times were variable from one sample to another and the values used for each step were:

| | Pressure/ bar | Time / min |
|---|---|---|
| Step 1 - filling | 4 | 1 |
| Step 2 (packaging) | 6 | 5 |
| Step 3 (holding) | 6 | 3 |

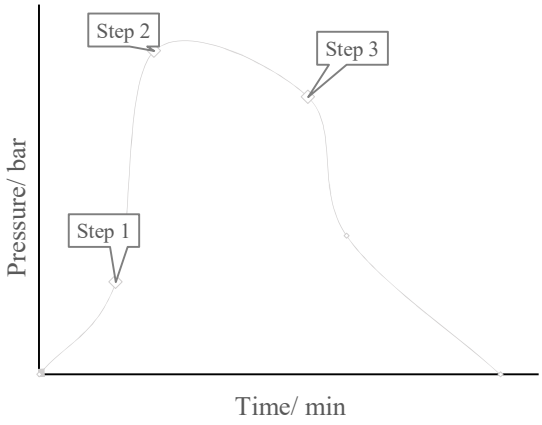


Figure 3. 2: Graphic of different steps related to pressure in an injection cycle.

a) b)

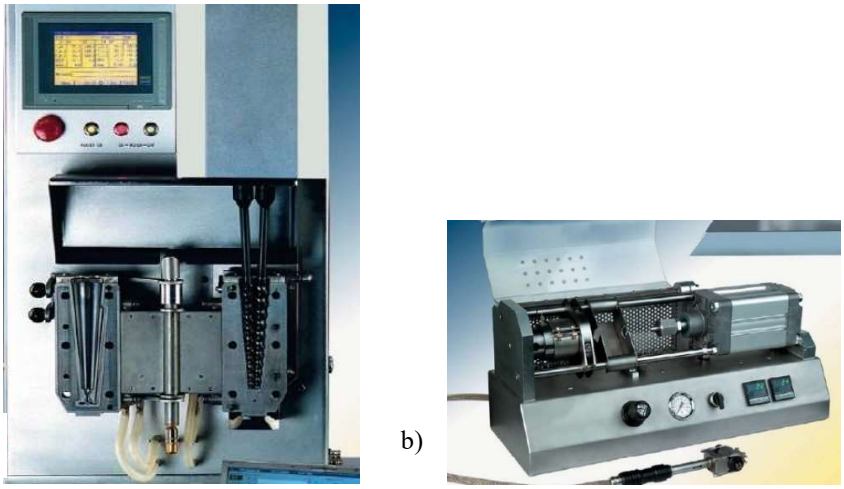

Figure 3. 3: DSM Research micro-equipment: a) twin screw extruder; b) injection machine.

The composition and compounding conditions for each research are summarized at the beginning of the chapters. The glass content is determined in wt% and vol% and ranges from 10 to 60 wt% were used. Different processing temperatures (from 200 to 300 °C) were used for the experimental work. The residence is the average time that a material stays in a vessel or stage during a continuous process. Residence times from 2 to 10 minutes were tested.

### 3.3.2 Hybrids for coating application

The dipping in fluidized bed coating technique requires the development of material in powder shape for its application. The procedure followed to develop glass-polymer hybrid powders generally is shown in Figure 3.4.

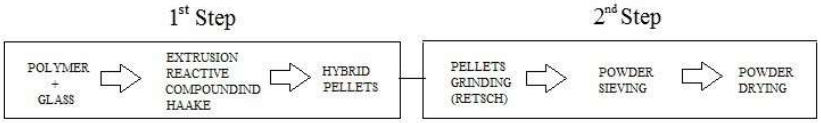


Figure 3. 4: Hybrid powder preparation procedure.

The powder preparation procedure was divided into two steps:

A) From hybrid precursors to hybrids pellets

The knowledge acquired developing the research about the influence of the melting conditions on the glass properties was used to synthesize the scaling-up batches of 500 g for coating application. The melting conditions of the glass are described in Table 3.4:

Table 3. 4: Melting conditions of the glass scaling-up batches for coating.

| Glass batch | Melting time / s | Melting temperature / °C |
|---|---|---|
| 13BR030-034 | 20 | 450 |
| 14RI16 | 25 | 450 |
| 14RI37 | 35 | 450 |
| 14RI35-36 | 45 | 450 |

The compounding of tin fluoride phosphate glass to PA 11 was done in a twin-screw extruder Thermo Haake PTW-16 using the profile described in Figure 3.5. The profile is composed of different types of elements. They are selected depending on function and its relationship to the appropriate zone. D is the diameter of the profile. The feeding zone of the profile is composed of 2D length type elements, which are typical elements for transporting material, in this case from the hopper to the fusion zone. The shear is higher when the angle of the screw is greater. Thus, the fusion zone of the profile starts with a KB30-5 element, which has an angle of 30°, 5 elements and the length (L) 1.25D, then KE0 elements with an angle of 60° and the length of 0.25D, finishing with KB 90-5, 5 elements with an angle of 90°and the length of 1.25D. The mixing zone is composed of 1D length elements for material transportation and 5 KB 0 elements to

obtain 60° for optimal shear. At each end of the mixing zone, inversion is established by the positioning of the elements to trap material under shear within the mixing zone to maximize mixing potential. The final zone is the material transport zone, which pushes out the well mixed material from the extruder.

The precursors were weighed at specified content in a PE (polyethylene) sac and mixed manually. The hybrid was obtained in the strand shape, which was cooled in the water bath at 10 °C. Subsequently, the material filament was introduced in the pelletizer Scheer SGS 50-E to obtain hybrid pellets.

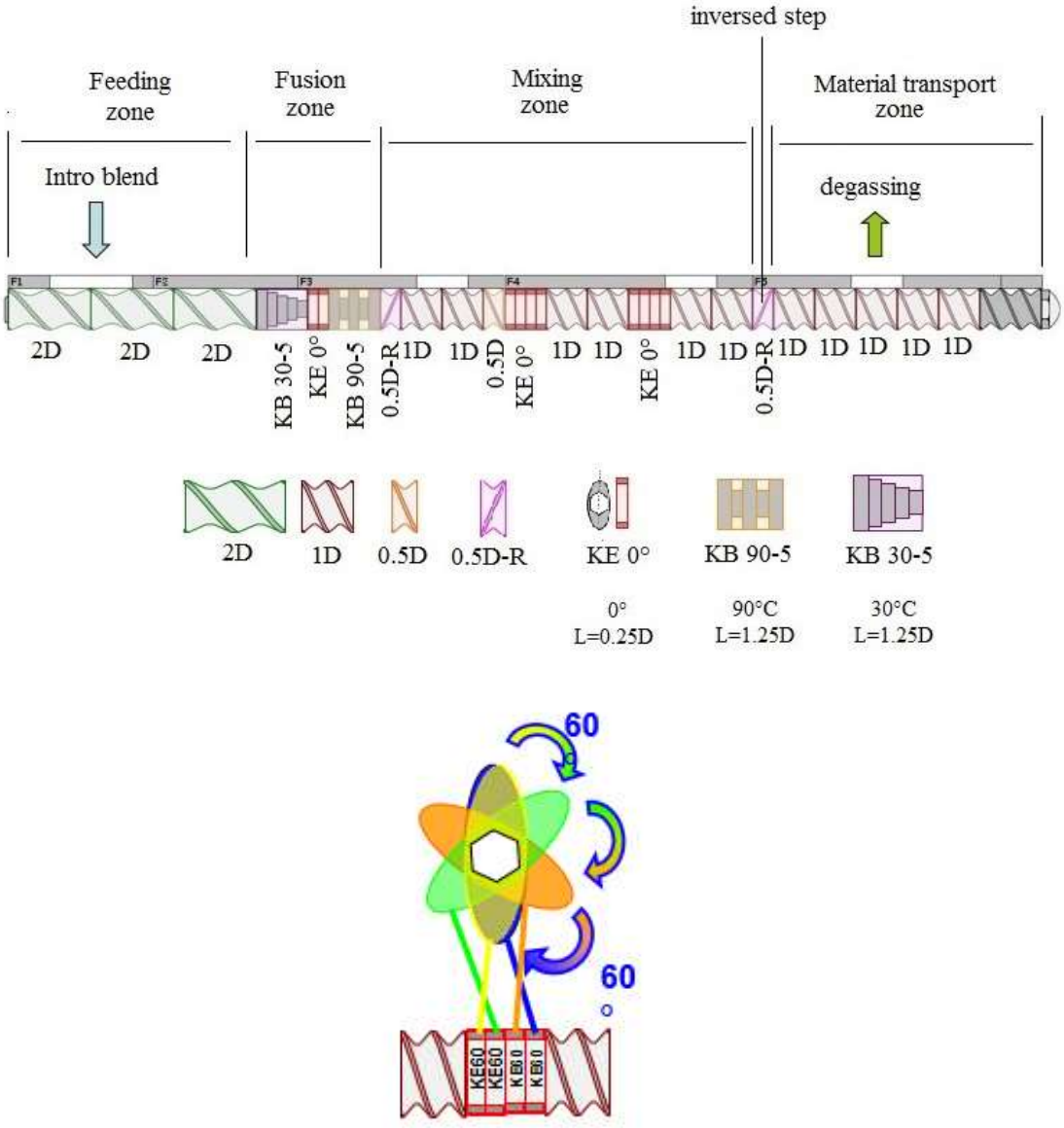


Figure 3. 5: Haake profile and its screw elements.

Two types of research were proposed to understand the influence of the glass content and the glass Tg in the hybrid and their direct effect in the application.

B) From hybrid pellets to hybrids powder

The hybrid pellets of each composition were ground in a ZM200 RETSCH laboratory high speed rotor mill grinder in the presence of liquid nitrogen to cool the polyamide below its glass transition temperature. Two runs were carried out. The first passage was done using a grill of 2 mm and at 6000 rpm of speed and the second one with a grill of 0.75 mm and at 14000 rpm. The powders were then sieved using a RETSCH AS 200 siever with a mesh of 355 µm. Hybrid powders were characterized using a Malvern Multisizer T laser diffraction (focal length 300 mm) granulometer measuring the particle size distribution. The last stage consisted in drying the powder for 10 hours at 80 °C. Coatings were then obtained by dipping in the fluid bed.

### 3.3.3 Preparation of hybrid coatings by Fluidized Bed Dipping

The procedure described in Figure 3.6 was used to obtain coatings of the new hybrid material. A reference PA11 matrix coating was routinely used as a comparative element. More information about this coating technique is in Appendix E.

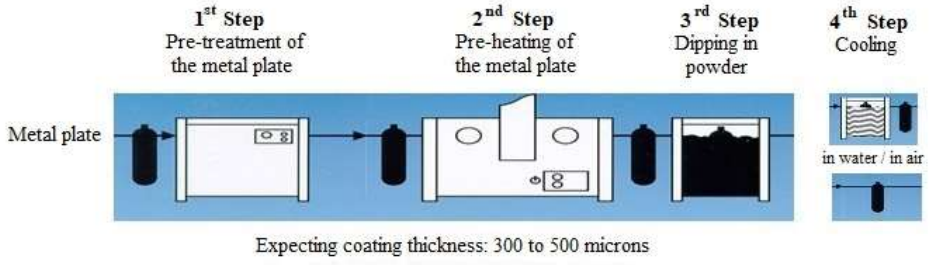


Figure 3. 6: Dipping in fluidized bed process.

The performance and durability of any coating are significantly affected by the surface preparation carried out. This is even more important in the case of steel structures, where the selection of the method of surface preparation is crucial in any corrosion treatment.

Different types of surface preparation can be selected depending upon the condition of the substrate, the coating system selected, the exposure and required durability of the coating, economic and environmental considerations. Some of the most common methods used are blast cleaning, hand and power tool cleaning, water jetting and degreasing.

The practical performance of the coatings is significantly affected by the condition of the surface prior to coating. The main relevant factors are presence of rust and mill scale, presence of contaminants (salts, dust, oil, and grease) and surface profile.

1st Step: surface preparation

Therefore, the first step in the dipping in fluidized bed process is to apply a pre-treatment to the metallic substrate. The metallic plates for coating evaluation were degreased and grit blasted with angular G17 cast iron hematite grit.

According to ISO 8501-1 each preparation grade is designated by the appropriate letters to indicate the type of cleaning method used and different numbers are attached to define the degree of cleanliness. Blast-cleaning is named as Sa and the degree of cleanliness used for surface treatment was defined as Sa 2 1/2. Sa 2 1/2 means very thorough blast-cleaning.

Measurements of surface roughness are expressed in terms of Ra, Rz or Rt, where Ra is the arithmetic mean deviation of the roughness profile. Rz is the maximum height of the roughness profile and Rt is total height of the roughness profile. These values include peak-to-valley profile measurement in combination with an assessment of the frequency of peaks within the sample area. The unit of surface roughness terms is μm.

2nd Step: preheating of the metal plate

The fluidized bath process involves bringing and maintain the workpiece at a specified temperature for a given period depending on its shape and mass, this uniform temperature exceeding the melting point of the Rilsan® powder. The oven temperatures can vary between 250 °C and 450 °C. In this research, the processing parameters for PA11 Rilsan were selected (10 min pre-heating time and 300 °C of temperature).

3rd Step: dipping in powder

The heated workpiece is then removed from the oven and soaked in a powder bath. The power bath is suspended or fluidized by a weak airflow diffused through a porous membrane at the bottom of the bath. The behaviour of the powder in suspension is identical to that of a fluid, so that the particles of powder are distributed perfectly on the surface of the parts, in the difficult to access corners too. In contact with the hot

surface, the particles melt to form a uniform layer with a coating thickness between 250 and 500 microns.

The dipping time usually ranges from two to four seconds and can be extended if it is necessary to obtain a thicker coating. A dipping time of 6 seconds was defined for this coating application.

4th Step: cooling

There are two type of cooling methods: in water and in air. Fast cooling in water was used to avoid the craters present in air cooling. The lack of anticrater additives in the hybrid formula can entail cratering on the coating if the cooling is too slow.

## 3.4 Characterization of the material

### 3.4.1 Density

The density of the glass melted at different melting conditions was measured, in order to check structural changes and establish glass stability. In the case of the hybrid, the influence of the glass content on the density was studied. The density of the samples was measured using a balance, SARTORIUS IAC 210P, according to the standards ISO 1183-1:2004 and ASTM D792:2008. So, the buoyancy method to determine the density of solids and liquids according to Archimedes' principle was used.

Archimedes' principle states that a body immersed partially or fully in fluid experiences a buoyant force acting upwards on it. The magnitude of this force is equivalent to the weight of fluid displaced by the body. The density measurement workflow is shown in Figure 3.7. The sample is weighed in air and then again in the auxiliary liquid with a known density. The auxiliary liquid was water. The density $(\rho)$ was calculated automatically from Equation 16:

$$\rho = \omega_a (\rho_a - \rho_w)/(\omega_a - \omega_w) \quad (16)$$

Where:

$\rho_a$ = sample density in air

$\rho_w$= sample density in water

$\omega_a$= sample mass (g) in air

$\omega_w$= sample mass (g) in water

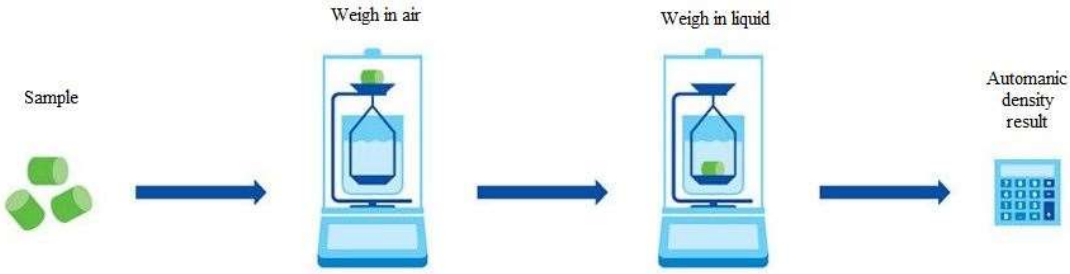


Figure 3. 7: The density measurement workflow using the vertical buoyancy method for solids and liquids according to Archimedes' principle.

## 3.4.2 Thermal properties

### 3.4.2.1 Differential Scanning calorimetry (DSC)

The thermal properties of PA11, TFP glass and hybrids composed by these two precursors were determined by differential scanning calorimetry (Netzsch F1ASC), according to the standards ISO 11357 and ASTM E 928-08. The tests were run from 20 °C to 300 °C at a heating rate of 2 °C/min twice to remove the effect of thermal history.

Differential scanning calorimetry measures the heat flow variations between the capsule that contains the sample for analysing and the empty capsule used as a reference. The DSC detects the heat variation in capacity of the material, at varying points of transition. By using this technique, it is possible to observe fusion and crystallization events as well as glass transition temperatures (Tg). The PA11 DSC curve is shown in Figure 3.8.

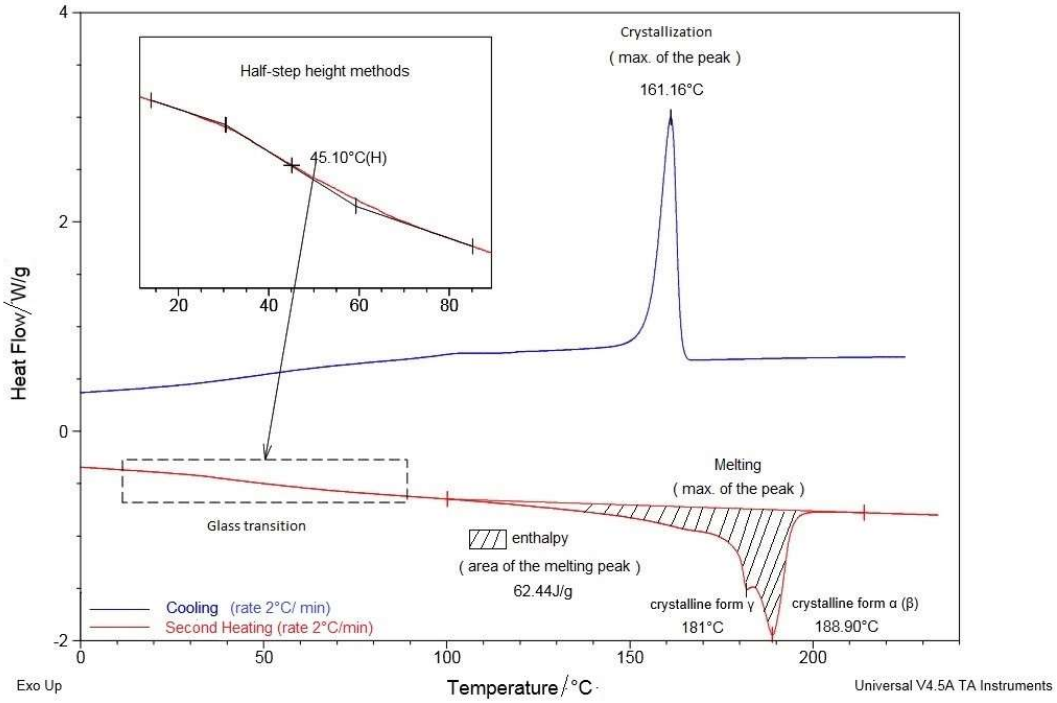


Figure 3. 8: Features of DSC PA 11 curve according to ISO 11357 :2-3.

One of the features that it is described in Figure 3.8 is the glass transition. The glass transition is a parameter to characterize a property of a polymeric material. The glass transition is the temperature where the polymer goes from a hard, glass like state to a rubber like state.

DSC defines the glass transition as a change in the heat capacity as the material goes from the glass state to the rubber state. This is a second order endothermic transition (requires heat to go through the transition) so in the DSC the transition appears as a step transition and not a peak such as might be seen with a melting transition.

DSC utilizes a heat flow technique and compares the amount of heat supplied to the test sample and a similarly heated "reference" to determine transition points. Tg is calculated by using a half-height technique in the transition region according to ISO 11357-2. The Tg was determined from the point of intersection of the tangents below and above the slope change, as shown in Figure 3.8.

The exothermic process shown by a peak may indicate a crystallization transition. The crystallization temperature ($T_c$) was calculated taking the maximum of the peak. The endothermic process indicates a melting transition and the melting temperature ($T_m$) was also obtained by the maximum of the peak. The degree of crystallinity, the

enthalpy of fusion, and enthalpy of crystallization of PA11 and different glass loading hybrids were also measured by DSC. The enthalpy of fusion ($\Delta H_f$) was determined by integrating the areas under the heating peaks and $\Delta H_f^0$ is the heat of fusion of 100% crystalline PA11 (which is tabulated as 189.05 J/g). The degree of crystallinity (Equation 17) was then determined using the following equation:

$$x_c = \Delta H_f / \Delta H_f^0 \quad (17)$$

In this research, the DSC was used for different approaches:

1. To measure the value of the Tg of the glass depending on the melting conditions and scaling up batches to verify their quality.
2. To detect Tg changes under thermal treatment effect at compounding conditions (5 minutes - 250 °C) and over time.
3. To measure thermal properties and crystallinity percentage of the reference and different hybrid compositions (miscibility).
4. To measure powder thermal properties for use in coating applications (adjust the process parameters).

#### 3.4.2.2 Thermogravimetric analysis (TGA)

TGA measures the amount of change in the mass of a sample as a function of temperature or time in a controlled atmosphere. The measurements are used primarily to determine the thermal and/or oxidative stabilities of materials as well as their compositional properties according to ISO 11358: 1997. The technique can analyse materials that exhibit either mass loss or gain due to decomposition, oxidation, or loss of volatiles (such as moisture) (Figure 3.9). TGA was used to characterise both the hybrids and precursors. The test was performed from 25 °C to 550 °C at a heating rate of 10 °C/min by using TG209 F1 Netzsch under nitrogen and air atmosphere depending on the material. The test identifies the degradation temperature, thermal stability, and moisture content. The thermograms of glass samples at different melting conditions ( melting temperature from 350 °C to 550 °C at 25 minutes of melting time and melting time from 15 to 45 minutes at 450 °C of melting temperature) and hybrids with 20 wt% and 40 wt% of glass, including PA11 processed at 250 °C, were collected and analysed. The results show the influence of the glass melting conditions on the glass properties and the effect of glass in the hybrids.

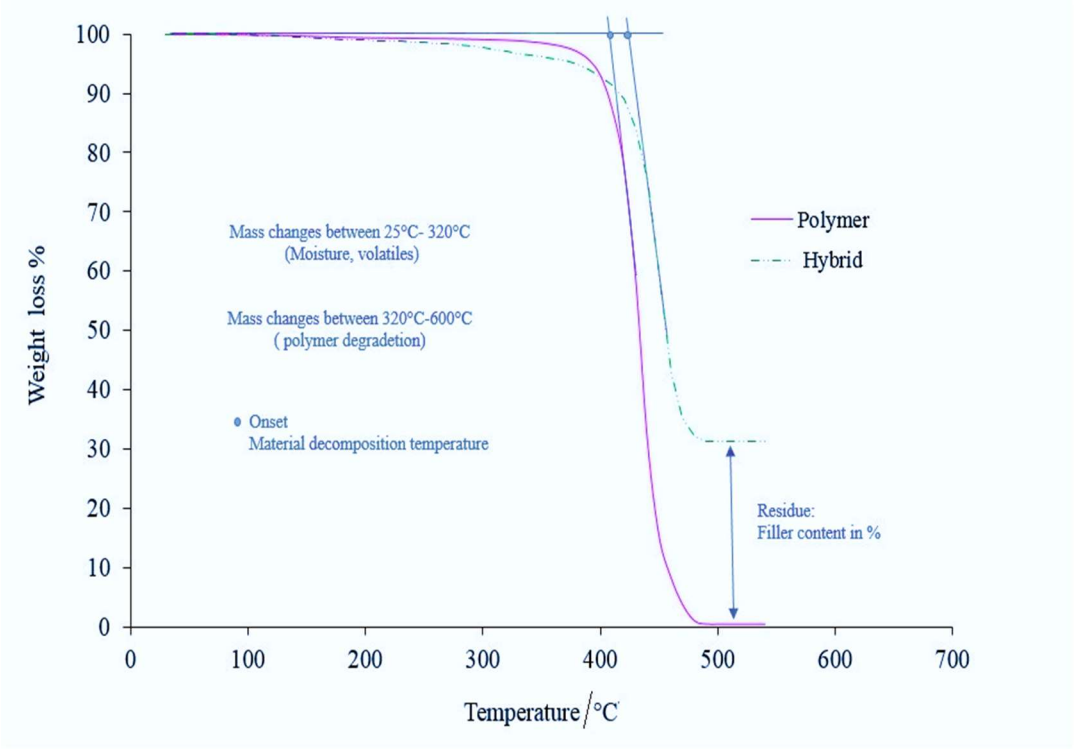


Figure 3. 9: Thermogravimetric analysis illustration according to ISO 11358.

### 3.4.2.3 Dynamic mechanical analysis (DMA)

To study the dynamic mechanical properties of PA11 and hybrids, a 242 Netzsch dynamic mechanical analyser was used to measure the storage modulus, loss modulus and the dissipation factor according to ISO 6721-1:2019. The test was conducted at a frequency of 1 Hz and 10-15 µm of amplitude. A ramp temperature of 2 °C/min was used and a range from -50 °C to 200 °C was examined. The laboratory scale sample test was carried out on dumb-bell samples (ISO 527 1BA), where the samples were dried at 80 °C for 24 hours in a vacuum oven. In the case of the hybrid powder for coating application, the DMA analysis was performed on dried powder samples pressed at 200 °C for 1 minute and 30 minutes. The storage modulus (E′) measures the stored energy, representing the elastic portion, and the loss modulus (E″) measures the energy dissipated as heat, representing the viscous portion. The tan delta is the dissipation factor.

Special attention was put on the analysis of the glass transition temperature of the materials, which were taken as the maximum in the dissipation factor versus temperature and on the storage modulus (Figure 3.10). The position, height and shape of the tan delta peak provides information about the amorphous content of the material

[1]. The goal was to evaluate the effect of using different contents of glass and different Tg glasses at the same composition on the hybrid.

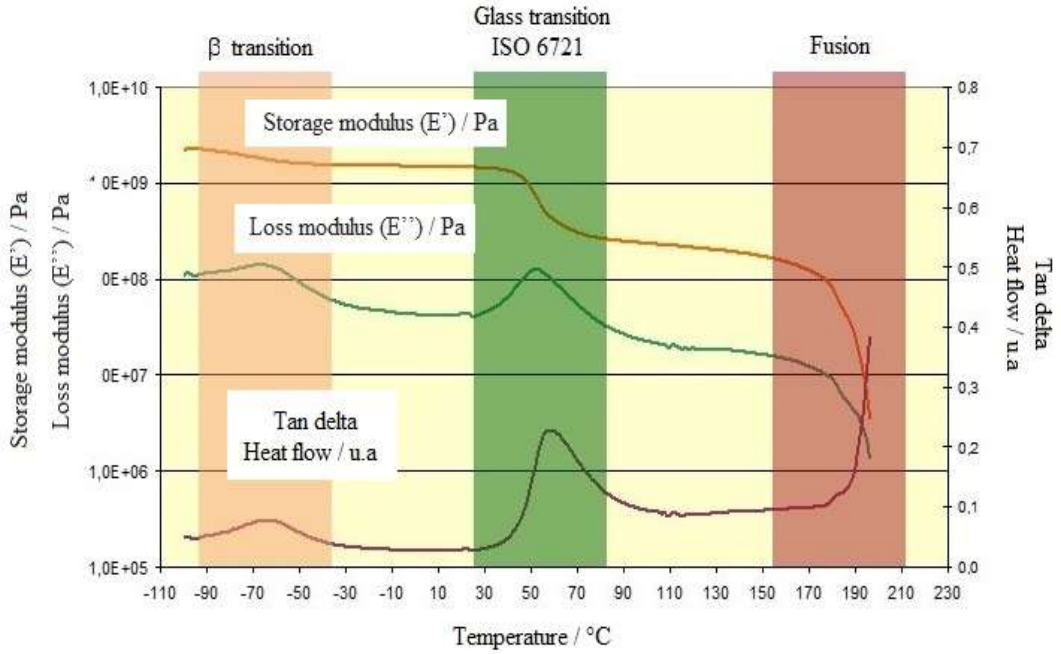


Figure 3. 10: A plot of the thermogram obtained from DMA test.

## 3.4.3 Melt Rheology study

### 3.4.3.1 Rotational rheometer

The rheological properties of the precursors alone and hybrids with different glass content were measured by a rotational rheometer (PHYSICA MCR 301) at temperatures of 230, 250 and 270 °C, respectively [146]. The testing was run using a parallel plate geometry and 1 Hz of frequency. Due to the high Tg of glass sample 6, the test was carried out at temperatures of 250, 270 and 290 °C.

Time dependant complex viscosity was plotted to evaluate the feasibility of TFP glass PA11 hybrid for powder coating application. The increase of viscosity during the coating application is key points to reach an industrial interest with good quality coating.

The relationship between rheology and flow activation energy was studied using Arrhenius equation. Viscosity is a measure of material's resistance to flow and deformation. The concept of the flow activation energy of materials describes the minimum energy barrier which material molecules must overcome for flow to occur

[147]. It can be used to differentiate and to characterize the thermal susceptibility of the materials [148]. The temperature dependence of the viscosity of material can be described by an Arrhenius equation (Equation 18).

$$\eta = A \exp^{(-Ea/RT)} \quad (18)$$

where A is a pre-exponential parameter, R is the universal gas constant (8.314 $J/(molK)$), Ea is the activation energy ($kJ/mol$), T temperature in degrees K, and $\eta$ is the complex viscosity at zero or low shear rate ($Pas$). The activation energy can be calculated based on known paired data of temperature and zero-shear or low-shear viscosity [149]. The low shear viscosity at 0.0135 $rad/s$ and high shear viscosity were used to calculate the activation energy and identify the trend at different shear rates.

## 3.4.4 Molecular weight measurement

Gel permeation chromatography (GPC) [150] was performed to detect any changes in the molecular weight of the PA11 that might suggest degradation due to glass. Glass content was also estimated from weight measurements after dissolution. The hybrid sample was dissolved in hexafluoro isopropanol (HFIP) +0,05 M potassium trifluoroacetate (KTFA) solvents over 24 hours at room temperature. A concentration of 1 $g/L$ of dissolution was used for the testing. The filtration was carried out with ACRODISC PTFE filter with diameter of 25 mm and porosity of 0,2 μm.

## 3.4.5 Structure study

The structural analysis of the glass and hybrid was carried out using two different spectroscopic techniques.

### 3.4.5.1 Fourier transform infrared spectroscopy (FTIR)

A VERTEX 70 Fourier transform infrared (FTIR) spectrometer was used to analyse the chemical structure of the hybrid and its components in the spectral range of 4000-400 $cm^{-1}$ wavenumber, in absorbance mode [151]. The samples in powder were deposited on the support. The infrared light penetrates the surface by 3 μm in order to provide readings. The inorganic material vibration is located at the low frequency vibration area.

#### 3.4.5.2 Raman spectroscopy

A Raman Bruckner Spectrometer was used to observe vibrational, rotational, and other low frequency modes in the hybrid material system [151]. Initial structures and degradation over time were measured. The wavenumber range of 4000 - 0 $cm^{-1}$ was checked for polyamide 11, tin fluoride phosphate glass and hybrids of both components.

### 3.4.6 Morphology analysis

#### 3.4.6.1 Scanning electron microscopy (SEM)

All the hybrid morphological evaluations were observed using scanning electron microscopy (SEM [152]) XL30 FEI. The samples were prepared by submersion in liquid nitrogen for 30 minutes and subjected to cryogenic fracture. The principal detector reveals the topography of the sample and the back scattered electron (BSE) detector is sensitive to the atomic weight of the elements. The colour range is white to black for heavy to light elements. The size of the particles was calculated by analysing the SEM images from an image of dark particles from a clear matrix.

#### 3.4.6.2 Transmission electron microscopy (TEM)

The detection of nanoparticles in the hybrid was analysed by transmission electron microscopy (TEM [153]) JOEL JEM 1230. The TEM analysis samples were prepared by cutting samples of approximately 40 nm thickness using an ultracryomicrotome LEICA EM FC6 at – 100 °C.

### 3.4.7 Mechanical properties

#### (a) Tensile Strength test

To assess the effects of TFP glass filler on static mechanical properties, tensile testing was performed on hybrids with different glass contents using as standard the neat polyamide 11 according to ASTM D638-14. The mechanical properties were measured in samples prepared using a DSM research 15 $cm^3$ micro compounder equipped with a DSM research laboratory injection moulding machine according to ISO 527-1BA. The test was carried out in a Zwick Material Testing Machine Z1455

machine with a cell of 10 kN and 25 mm/min of speed, at room temperature and 50% of humidity.

The elastic modulus of each hybrid ($E_i$) was calculated from the slope of the linear part of the stress-strain curve. The tensile strengths were extrapolated and calculated from the maximum of the curve and according to Equation 19:

$$\sigma_i = F/bd \tag{19}$$

where $\sigma_i$ is the tensile strengths of hybrid; b is the width of the rectangular cross section of the hybrid sample; d is the depth of the rectangular cross section of the hybrid sample.

### 3.4.8 Fire resistance

There are several applications where high pressures and temperatures dictate the use of fire-resistant material to mitigate the potential for dangerous and expensive fires. Fire retardants are chemical additives used in thermoplastics, thermoset, textiles, and coatings that inhibit or resist the spread of fire. They can be divided into these classes: Minerals (aluminium hydroxide (ATH) and magnesium hydroxide (MDM)), organohalogen compounds (organochlorines and chlorinated paraffin) and organophosphorus compounds (organophosphates, phosphonates and phosphinates).

It is worth studying the influence of phosphate on the fire-resistant property of polymeric materials. UL 94 [127] (Underwriters Laboratories test standard) is one of the most widely used flammability tests for determining relative flammability for plastic materials. It measures the ability of plastic part to extinguish the flame after ignition and its dripping behaviour in response to a small open flame or radiant heat source.

The tests results are intended to serve as a preliminary indication of the material's suitability with respect to flammability for a particular application, such as plastic materials used for parts in electronic devices and appliances. The flammability is influenced by several factors:

- Ease of ignition – how rapidly a material ignites
- Flame spread – how rapidly fire spreads across a polymer surface

- Fire endurance – how rapidly fire penetrates a wall or barrier
- Rate of heat release – how much heat is released and how quickly
- Ease of extinction – how rapidly the flame chemistry leads to extinction
- Smoke evolution
- Toxic gas generation

Hence, the study of how plastics burn has been, and continue to be, a major area of research to examine:

- The nature of the burning phenomenon in plastics
- Various methods to reduce plastics flammability, and
- Methods to test flammability

As these hybrids are composed of tin fluoride phosphate glass, it is interesting to carry out fire resistant tests according to a similar procedure to UL 94, the Standard for Safety of Flammability of Plastic Materials for Parts in Devices and Appliances testing [127], on hybrid samples containing 10, 20, 30, 40, 50, and 60 wt%. Note that it is a similar procedure to UL 94 due to the limited material quantity available to carry out a suitable testing. The test was done on micro DSM samples moulded according to ISO 527 BA. The processing parameters were:

- For extrusion compounding: 100 rpm of screw speed, 3-5 minutes of residence time and 250 °C of processing temperature
- For injection moulding: 250 °C barrel temperature and 40 °C of mould temperature

The test was performed according to the international standard EIC 60695-11 10: 1999, Fire Hazard testing and especially the test method B that consists of the vertical burning test. Figure 3.11 shows the test machine:

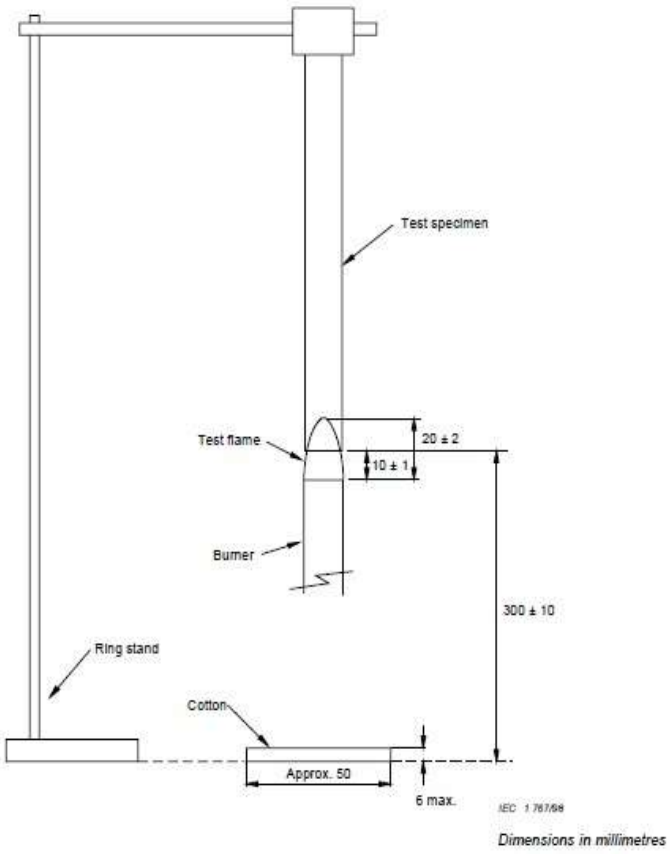


Figure 3. 11: Vertical burning test apparatus- method B according to EIC 60695-11.

Following the standard, for each set of five test specimens, the total after flame time for the set $t_f$, in seconds, is calculated according to Equation 20:

$$t_f = \sum_{i=1}^{5}(t_{1,i} + t_{2,i}) \quad (20)$$

Where, $t_f$ is the total after-flame time, in seconds ; $t_{1,i}$ is the first after-flame, in seconds, of the $i^{th}$ test; $t_{2,i}$: is the second after-flame, in seconds, of the $i^{th}$ test.

In this case, the test was adapted to one sample for each glass content. The bar specimen described by the standard is shown in Figure 3.12 and compared with our sample in Figure 3.13 to show the differences in dimension.

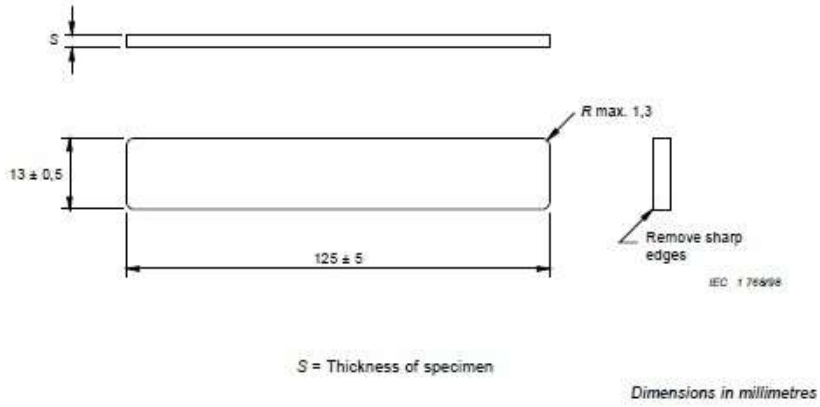


Figure 3. 12: Bar specimen according to standard.

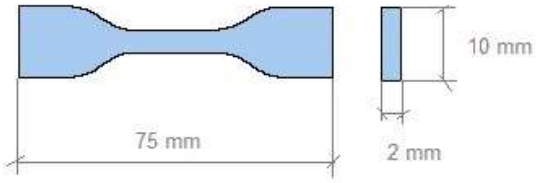


Figure 3. 13: Hybrid sample dimension.

The material shall be classified either V-0, V-1 or V-2 (V= vertical burning), in accordance with the criteria indicated in Table 3.5.

Table 3. 5: Vertical burning categories according to EIC 60695-11.

| Criteria | Category (see note) | | |
|---|---|---|---|
| | V-0 | V-1 | V-2 |
| Individual test specimen afterflame time ($t_1$ and $t_2$) | ≤10 s | ≤30 s | ≤30 s |
| Total set afterflame time $t_f$ for any conditioning | ≤50 s | ≤250 s | ≤250 s |
| Individual test specimen afterflame plus afterglow time after the second application ($t_2$ + $t_3$) | ≤30 s | ≤60 s | ≤60 s |
| Did the afterflame and/or afterglow progress up to the holding clamp ? | No | No | No |
| Was the cotton indicator pad ignited by flaming particles or drops? | No | No | Yes |
| NOTE If the test results are not in accordance with the specified criteria, the material cannot be categorized by this test method. Use the horizontal burning test method described in clause 8 to categorize the burning behaviour of the material. | | | |

## 3.5 Characterisation of the coatings

### 3.5.1. Adhesion

The metallic plates (100 mm x 100 mm x 3 mm) were degreased and grit blasted. Roughness after grit blasting is in accordance with Arkema recommendations (40 µm <Rz<80 µm). Dipping using the fluidized bed coating technique was used to perform coatings at the following processing conditions: the pre-heating time and temperature of 10 min at 300 °C; the dipping time of 6 seconds and fast cooling in water.

The coating thickness was measured on each coated plate at different locations before testing and average thickness in µm calculated. The measurements were taken by an Elcometer 456 giving a thickness of 350-450 µm. Initial and after water immersion adhesion measurements were carried out according to the Arkema method. The Arkema method consists of controlling adhesion by detachment. It is inspired by the standard norm NFT 58-112 for adhesion measurement. The test is described in Appendix F. This norm was cancelled in November 2011 and no substitute standard was published. The influence on the adhesion of the glass into PA11 was also evaluated by the Arkema method. The coated plates were immersed in a bath of water at 80 ±2°C during 24h and 48h. Afterwards, they were removed from the bath and tested.

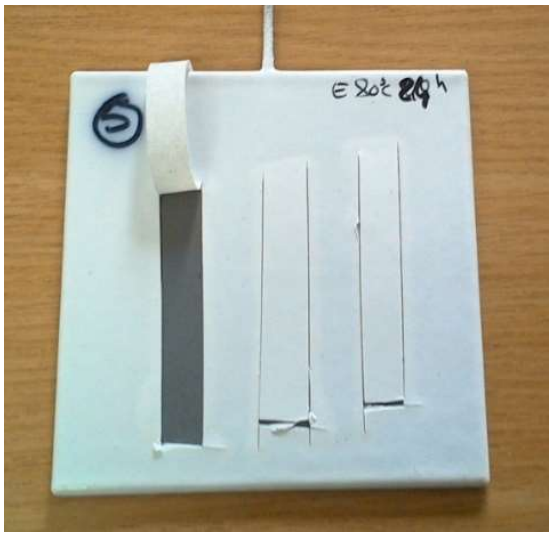

Figure 3. 14: Adhesion test by Arkema methods.

The objective of the test is to evaluate the adhesion of coatings applied onto a metallic surface. The test consists in detaching a sectioned band of the coating from the subtract (Figure 3.14). The coating is cut with a knife following two parallel lines separated by 10 mm along at least 30 mm to form a strip. A chisel knife (10 mm wide) or a penknife with a thin blade is inserted under one extremity of the strip that is pulled out. A grade from 0 to 4 is given:

0: no adhesion, the coating is detached from the substrate as soon as the knife is inserted

1: the coating is easily detached from the substrate with a low resistance to pulling out

2: similar to 1 but some strong anchor points exist

3: the detachment of the coating from the substrate is irregular; there is a strong adhesion on about 50% of the surface

4: high adhesion, no detachment of the coating; either the knife enables the detachment of the strip, but the strip breaks as soon as it is pulled out or the knife can just detach and cut some fragments of the coatings

### 3.5.2 Wear performance

Wear performance was assessed using a TABER 5130 abrasion machine with CS 17 wheel (ASTM D4060-90). CS17 wheel is a 1 kg mass abrasive roller applied for coarse abrasion. The measurement of reference and various hybrid composition (0-40 wt%) coatings were carried out according to ASTM D4060-90 (Standard Test Method for Abrasion Resistance of Organic Coatings by the Taber Abraser) in order to check the influence of the glass. This test method covers the determination of the resistance of organic coatings to abrasion produced by the Taber Abraser on coatings applied to a plane, rigid surface, such as a metal panel. The cylindrical steel plates (Figure 3.15) with specific dimension of 50 mm of diameter and 6 mm of thickness, were coated by dipping in fluidized bed with 10 minutes of pre-heating time and 300 °C of temperature, dipped for 6 seconds and cooled in water to avoid the presence of craters.

Figure 3. 15: Cylindrical steel plate for abrasion testing.

The loss of mass percentage was calculated from Equation 21:

$$\text{Loss of mass } \% = (\Delta m/m_1)100 = ((m_2 - m_1)/m_1)100 \qquad (21)$$

where Δm is mass variation, $m_1$ is the initial mass of the coated steel plate and $m_2$ is the final mass after 1000 cycles.

### 3.5.3 Hardness

The effect of the glass and ageing influence on coatings was checked measuring the Shore D Hardness (measure of the resistance of a material to penetration of a spring-loaded needle-like indenter [154]) with a HILDEBRAND 05-2 machine (Figure 3.16) according to ISO 868-2003. The required thickness of 4 mm was obtained piling up films of 0.5 mm. The samples were conditioned for 15 days at 23 °C and 50% HR before testing. Each sample was measured 5 times maintaining 6 mm of distance between each measurement. The penetration time was 15 s.


Figure 3. 16: Shore D HILDEBRAND 05-2.

The measured Shore D hardness on coatings was determined by the penetration depth of the indenter under the load. The indenter shapes are shown in Figure 3.17. Shore hardness values vary in the range from 0 to 100. Maximum penetration value is 2.5-2.54 mm, equivalent to minimum Shore D hardness equal to 0. Maximum hardness value 100 corresponds to zero penetration.

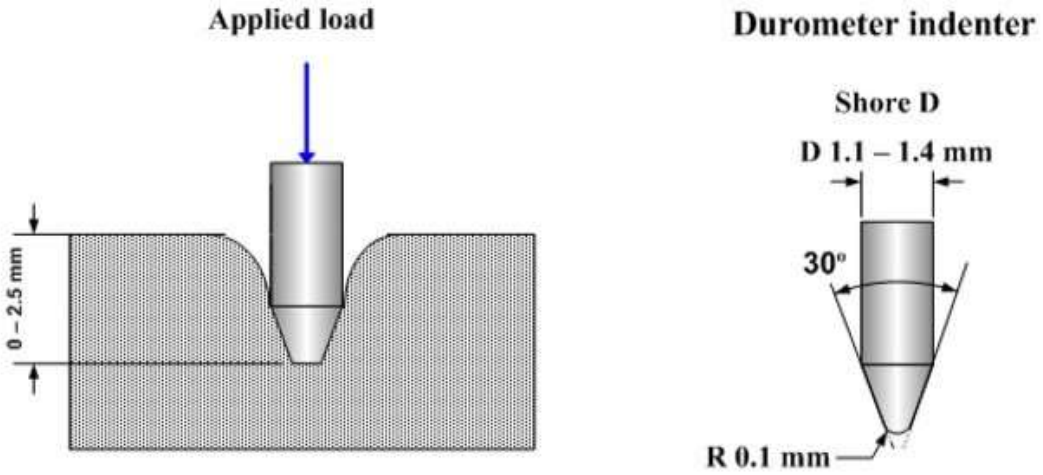


Figure 3. 17: Indenter shape and maximum penetration [ISO 868-2003].

### 3.5.4 Water absorption test

The influence of the glass in the water absorption process in PA11 films was investigated. The metallic substrates (dimension: (1000) x (100) x (3) $mm^3$) covered with silicon were dipped for 3 s at 300 °C. Silicon metallic substrates were used to facilitate the removing of the film from the metal. The reference and hybrid films containing 20, 30, 40 TFP glass by weight and using different glass transition temperature (Tg: 104, 125, 150 °C) were made for testing.

The water resistance test was carried out according to ISO 62. Before weighting the films to calculate the initial mass ($m_1$), they were dried for 24 hours at 50 °C in an oven and left cooling at room temperature into a desiccator. The film was then placed in a distilled water recipient at 23 °C. The films were immersed in water for 24 hours and dried with filter paper for measuring the final mass ($m_2$). The final mass was measured within a minute after which the film was taken out of the water. The water absorption percentage was calculated from the following Equation 22:

$$\text{Absorption } \% = (\Delta m/m_1)100 = ((m_2 - m_1)/m_1)100 \qquad (22)$$

where $\Delta m$ is a mass variation (final mass - initial mass), $m_1$ is the initial mass of the film and the $m_2$ is the final mass after immersion in water.

### 3.5.5 Tensiometer

To determine the surface energy, the contact angle method was used. This test consists in delicately depositing drops of liquid on a surface. The selected liquids were water, ethylene glycol and diiodomethane, water being the most polar and diiodomethane the most non-polar. Once these drops are set and after a waiting time defined by a standard (depending on the rate of spreading and the evaporation of the solvent) the angle formed by the drop is measured (Figure 3.18). All measurements are made at room temperature. To perform this test, the DGD fast / 60 contact angle meter GBX was used and the Owens-Wendt model for energy calculations was applied [130].

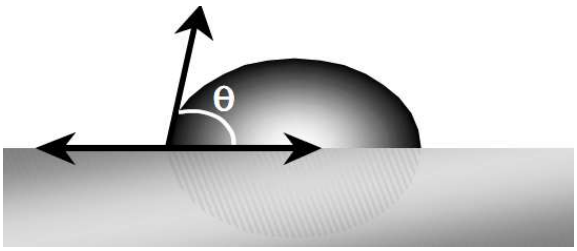


Figure 3. 18: Diagram of the contact angle (θ) between a drop of solvent and a substrate.

### 3.5.6 Impact test

The impact resistance of different glass content hybrids and reference were measured according to ASTM G14-04. The impact column is shown in Figure 3.19; the impact sphere diameter was 15.9 mm and it has 1 kg in mass. The (50mmx200mmx6mm) dimension metallic plates were dipped in fluidising bed powder to obtain a suitable coating for impact resistance measurement. The dipping parameters were defined as 13 second of dipping and 300 °C of preheating temperature. The samples were conditioned at 23 °C for 24 hours in 50% of humidity. The objective of the test is to evaluate the influence of the glass checking the resistance of the coating to cracking or delamination under the effect of mass impact under defined conditions. The minimum drop height was determined depending on the porosity or non-porous results shown by the coating after dropping the mass. Twenty mass droppings were carried out for each coating. The porosity is controlled using a Fischer poroscope H2D. Neat polyamide 11 and different hybrid composition coatings were tested.

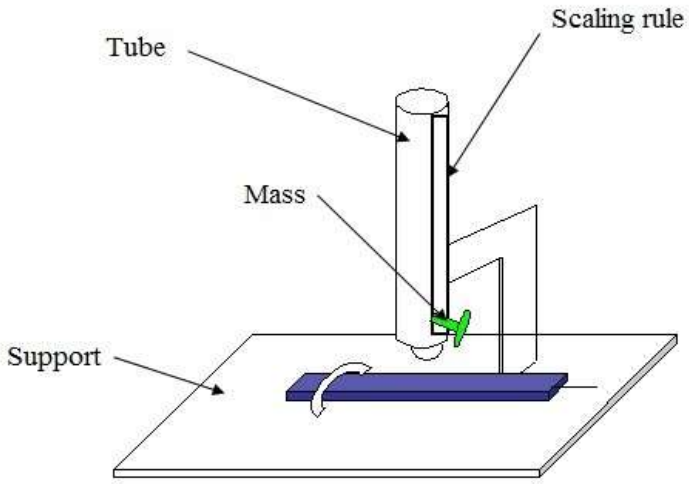


Figure 3. 19: Impact column according to ASTM G14-04.

The amount of energy required to cause the coating porosity is calculated by the average energy of impact. The results were expressed using the following Equation 23:

$$\bar{E_I} = \left(h_0 + d(A/N \pm 0.5)\right)F \qquad (23)$$

Where $\bar{E_I}$ is average energy of impact / Joules (Nm)

$h_0$ : minimum height to cause porosity (m)

d : increment in m

A : the sum of each non-porous height / m

N : the sum of each porous height / m

F : force due to gravity $= ma_g$ / N

m: mass / kg

$a_g$ : acceleration of gravity $9.8\ ms^{-2}$

± 0.5; +0.5 when it is non-porous,

-0.5 when it is porous

# Chapter 4 Influence of melting conditions on the structure and properties of tin fluoride phosphate glass

The hybridization of glass with PA 11 requires a sufficiently low glass transition temperature and softening point to allow the glass to be fluid in the same range of temperatures of the matrix, without significantly compromising the mechanical and chemical properties of the hybrids.

## 4.1 Melting conditions of the glass

The $50\%\ SnF_2\ + 20\%\ SnO\ + 30\%\ P_2O_5$ base composition was used as described in the design of experimentation. This glass is known to have a Tg of approximately 125 ˚C, a density of 3.75 $gcm^{-3}$, and an excellent water resistance [6]. The influence of the melting conditions on the glass properties was investigated in this chapter. In Table 4.1, the glass melting conditions are shown.

Table 4. 1: Glass melting conditions.

| Sample | Temperature / °C | Time / min |
|---|---|---|
| 1 | 450 | 15 |
| 2 | 450 | 20 |
| 3 | 450 | 25 |
| 4 | 450 | 30 |
| 5 | 450 | 35 |
| 6 | 450 | 40 |
| 7 | 450 | 45 |
| 8 | 350 | 25 |
| 9 | 400 | 25 |
| 10 | 500 | 25 |
| 11 | 550 | 25 |

## 4.2 Structural investigation of the glass– FTIR and Raman

The structure of glasses was studied using FTIR and Raman spectroscopy. The structural study began with the analysis of the chemical reagents used in the synthesis of the tin fluoride phosphate glasses and identification of their vibrational groups. These vibrational groups and data in the literature help in the interpretation of the glass vibrational group peaks. The melting conditions of the reference glass (melted at 450

°C for 25 minutes) having a molar composition of $50\%\,SnF_2 + 20\%\,SnO + 30\%\,P_2O_5$ were found in the literature [102-103]. This glass was selected due to its well-known affinity with polyamides [97]. Once the reference glass structure was identified, the study continued by analysing the effect of the glass melting conditions on the glass structure. Powder samples were observed in the region of 4000-400 $cm^{-1}$ by FTIR and in the region of 4000-0 $cm^{-1}$ by Raman spectroscopy using the absorbance mode.

Phosphate is based on corner-sharing $PO_4$ tetrahedral units. The tetrahedral units are classified according to their connectivity $Q^n$, where n (n=1,2,3,4) is the number of bridging oxygens per tetrahedron. Therefore, three spectral regions that are related to the activity can be roughly defined for the response of the phosphate network by Raman and FTIR spectrometry:

Deformation mode frequency~ 500 $cm^{-1}$
Bridging oxygen modes frequency region ~ 700-900 $cm^{-1}$
Non-bridging oxygen modes frequency region ~ 940-1380 $cm^{-1}$

To identify the structure of tin fluoride phosphate glass, the current understanding on the structure of phosphate glasses will be recapitulated. The content of $P_2O_5$ and the $PO_4$ tetrahedral connectivity will determine the structure of the phosphate glasses. In ultraphosphate glasses [$P_2O_5$] (>50 mol%), the structure is composed of $Q^3$ (three bridging oxygens (BO) and one non-bridging oxygen (NBO) bonded to the phosphorous atom by a double bond [104] and $Q^2$ (two BOs and two NBOs) tetrahedra. The $Q^3$ units form three-dimensional networks, while $Q^2$ units assist the chain formation. With $P_2O_5$ content up to [$P_2O_5$]=50 mol%, the structure of phosphate can be defined as metaphosphates, and the network is based mainly on $Q^2$ units and a few $Q^1$ end groups. Polyphosphate glasses are obtained with $P_2O_5$ contents of <50 mol%; in fact, polyphosphates are formed from the depolymerisation of the metaphosphate network resulting in shorter chains of $Q^2$ with end groups of $Q^1$ units. When $P_2O_5$ content is approximately 33 mol%, a pyrophosphate network is formed mainly by dimers of $Q^1$ units, and for [$P_2O_5$]<33 mol%, an orthophosphate is formed of mainly isolated $Q^0$ units. Figure 4.1 shows the different types of $PO_4$ tetrahedral connectivity related to the content of $P_2O_5$.

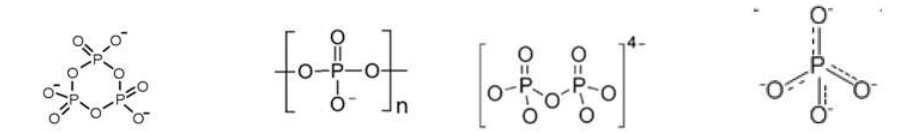


Figure 4. 1: Different types of - $PO_4$ tetrahedral connectivity.

### 4.2.1 Chemical reagents of tin fluoride phosphate glass

Three chemical reagents: $NH_4H_2PO_4$, SnO and $SnF_2$ were analysed using FTIR and Raman spectroscopy. The FTIR and Raman spectra of these chemical reagents are presented consecutively in Figure 4.2 and Figure 4.3. The characteristic peaks of these components are indexed in Table 4.1 and 4.2.

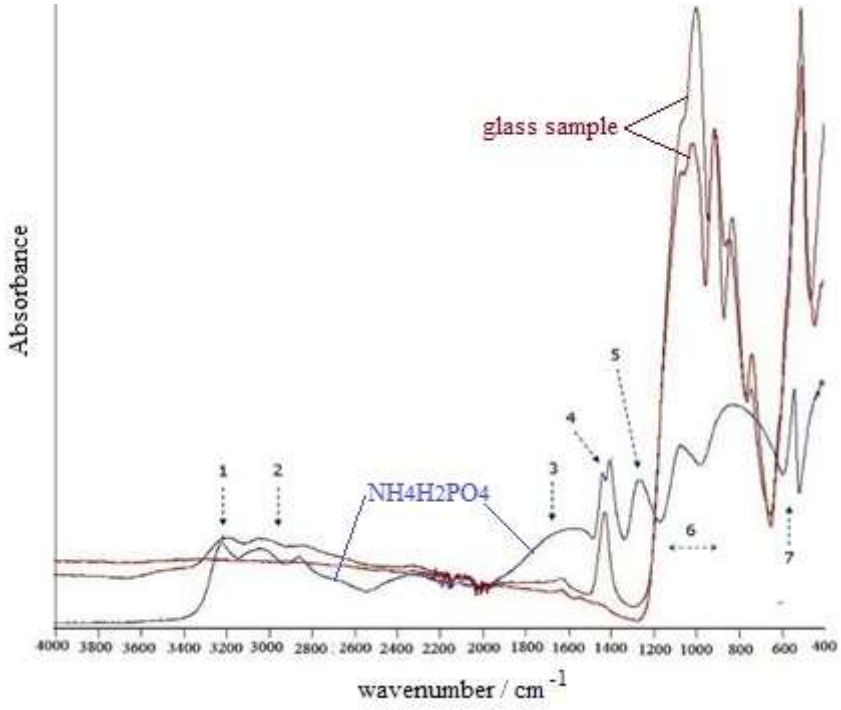


(a)

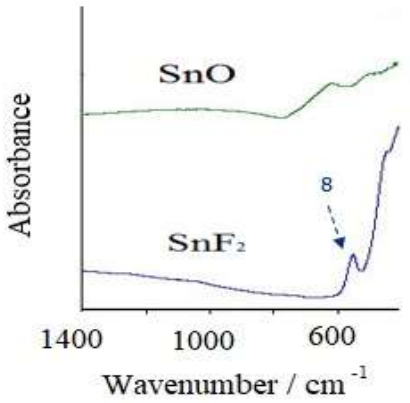


(b)

Figure 4. 2: FTIR spectra of glass chemical reagents: a) ammonium phosphate monobasic and reference glass; b) tin oxide and tin fluoride components.

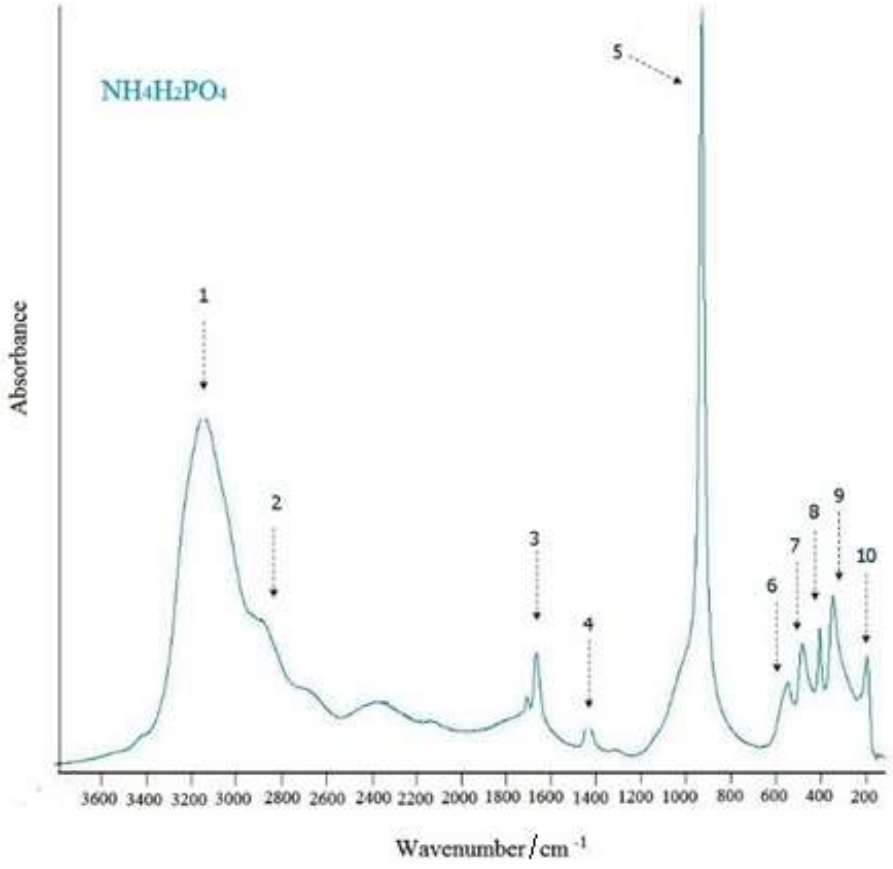


(a)

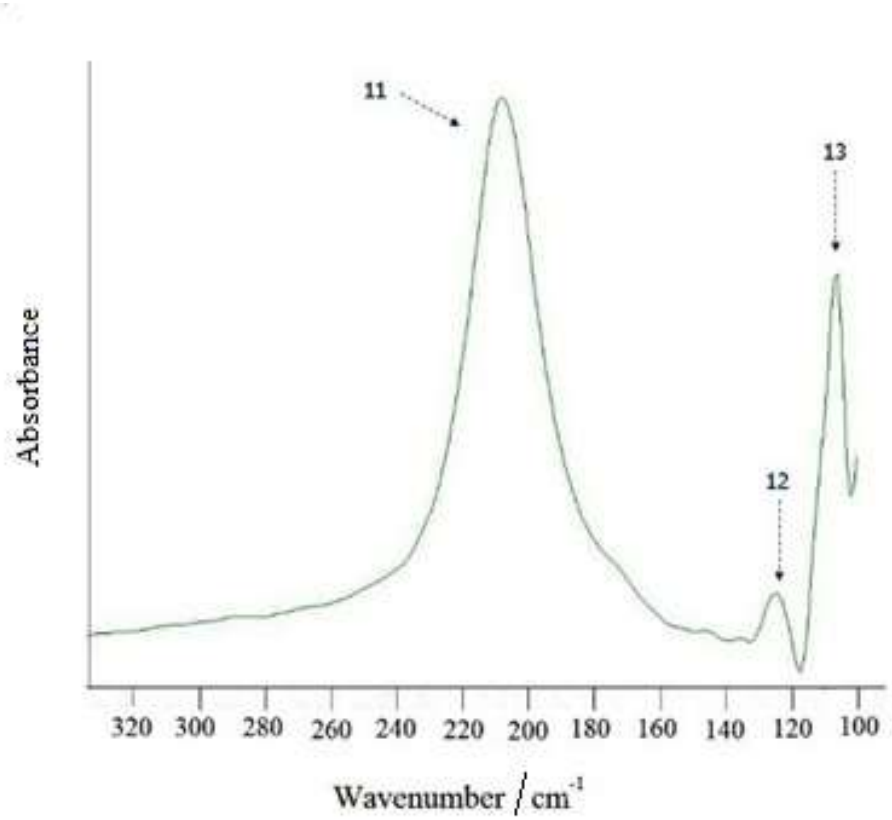


(b)

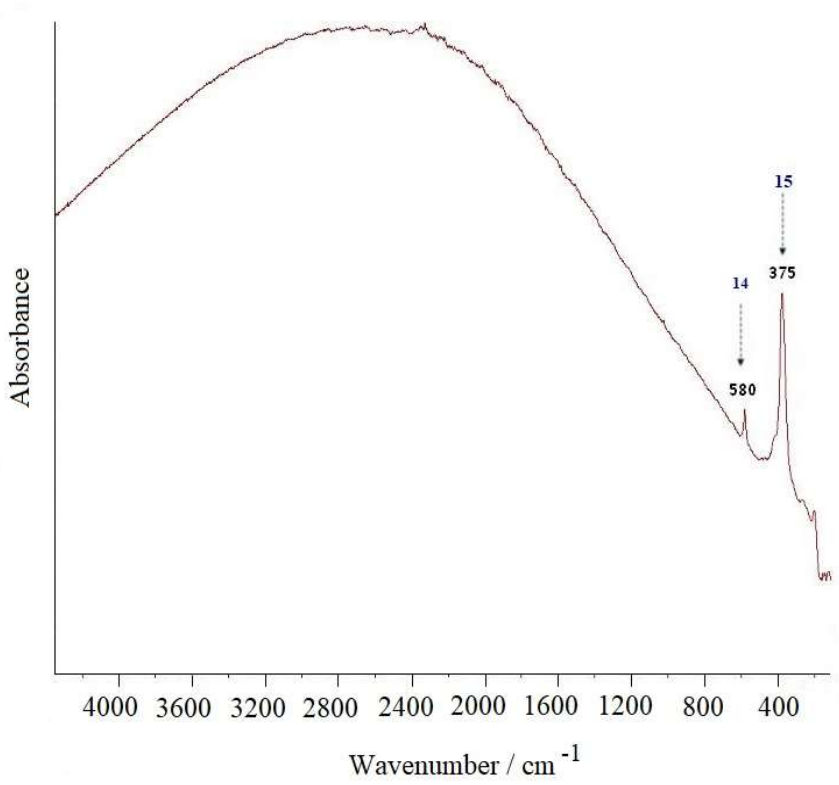


(c)

Figure 4. 3: Raman spectra of chemical reagents: a) ammonium phosphate monobasic; b) tin oxide; c) tin fluoride.

Table 4. 2: FTIR Characteristic absorption frequencies of various functional groups.

| No | Bond assignments | Wavenumber / $cm^{-1}$ |
|---|---|---|
| 1 | OH Stretching | 3249 |
| 2 | NH Stretching | 2874 |
| 3 | (P=O) | 1240 |
| 4 | Bond vibration of water | 1642 |
| 5 | Bond vibration of $NH_2$ | 1441-1408 |
| 6 | POH vibration | 990 |
| 7 | $PO_4$ vibration | 545- 439 |
| 8 | SnF | 540 |

Table 4. 3: Raman Characteristic absorption frequencies of various functional groups.

| No | Bond assignments | Wavenumber /$cm^{-1}$ |
|---|---|---|
| 1 | OH Stretching | 3144 |
| 2 | NH Stretching | 3050-2874 |
| 3 | Bond vibration of water | 1661 |
| 4 | Bond vibration of $NH_2$ | 1 440 |
| 5 | P-O-H vibration ($PO_4$) $Q^0$ | 1100-906 |
| 6-7 | Bending vibration (PO4) $Q^0$ | 545- 439 |
| 8 | | 398 |
| 9 | | 340 |
| 10 | | 187 |
| 11 | SnO | 208 |
| 12 | SnO | 125 |
| 13 | SnO | 106 |
| 14 | Sn F | 580 |
| 15 | Sn F | 375 |

The group frequency region was detected between 4000 and 1300 cm $^{-1}$, while the fingerprint region was detected between 1300-0 cm $^{-1}$. FTIR detects mainly ammonium phosphate monobasic vibrations (Figure 4.2a and Table 4.2). The vibration of the remaining two inorganic components (SnO and $SnF_2$) are located below 400 $cm^{-1}$ (Figure 4.2b and Table 4.2). Raman characterization of the components shows better the spectrometric vibrations of all components.

In FTIR, the broad band in the higher energy region is related to $O-H$ stretching vibration of the phosphate linked to OH and to the water [155]. The presence of water is supported by the peak at around 1660 $cm^{-1}$ , which is the bending vibration of the OH groups of water. The presence of $NH_4$ in the amonioum phosphate monobasic is also corroborated. The band around 2855 $cm^{-1}$ can be atributed to NH stretching vibration and at around 1420 to a bond vibration of $NH_2$ ( number 2 and 4 in Figure 4.2a). The strong absorption observed in the range of 1300-600 $cm^{-1}$, is due to the phosphate molecule. The peak at 1245 $cm^{-1}$ (number 5 in Figure 4.2a) is the stretching vibration of the P=O funtional group [104]. The vibration occurring between 1100-906 $cm^{-1}$ (number 6 in Figure 4.2a) is the vibration of the $P-OH$ group [155]. The peak at 510 $cm^{-1}$ (number 7 in Figure 4.2a) is attributed to $PO_4$ vibration. Regarding the Raman spectrum (Figure 4.3) and the assignments (Table 4.3) of ammonium phosphate monobasic the same bond vibrations were detected. There are three additional small peaks on Raman spectrum at low wavenumber that cannot be identified at this stage.

The vibrations found in $NH_4H_2PO_4$ spectra are in concordance with its structure. The structure of the amonium phosphate monobasic is shown in Figure 4.4.

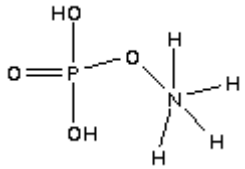


Figure 4. 4: The structure of the ammonium phosphate monobasic [155].

Regarding peak 8 for $SnF_2$ of the FTIR (Figure 4.2b), the kind of vibration is not known, as is also the case for peak numbers 14 and 15 of the Raman spectra in Figure 4.3c. The relevant point is that these peaks are related to $NH_4H_2PO_4$, $SnO$ and $SnF_2$ reagents of TFP glass and hence could be useful for the identification of the glass structure.

The FTIR pattern of tin oxide generally shows the presence of stretching vibration bands at 663 and 565 $cm^{-1}$. In the FTIR spectrum of $SnO$ (Figure 4.2b), there is evidence of vibrations at these wave numbers but their presence is slight and so they are not included in Table 4.2. On the other hand, well defined peaks for $SnO$ are shown

in the Raman spectrum of Figure 4.3b. The strong peak is likely to be related to the stretching vibrational mode, but no confirmatory evidence was found in the literature.

### 4.2.2 Tin Fluoride Phosphate glass

The structure of the tin fluoride phosphate reference glass (melted at 450 °C, 25 minutes) was identified by FTIR and Raman spectrscopy. Figure 4.5a shows the FTIR absorbance spectrum of the tin fluoride phosphate reference glass with the molar composition of $50\%SnF_2 + 20\%SnO + 30\%P_2O_5$ for frequencies between 3500 and 400 $cm^{-1}$. Table 4.4 summarizes the features and assigments.

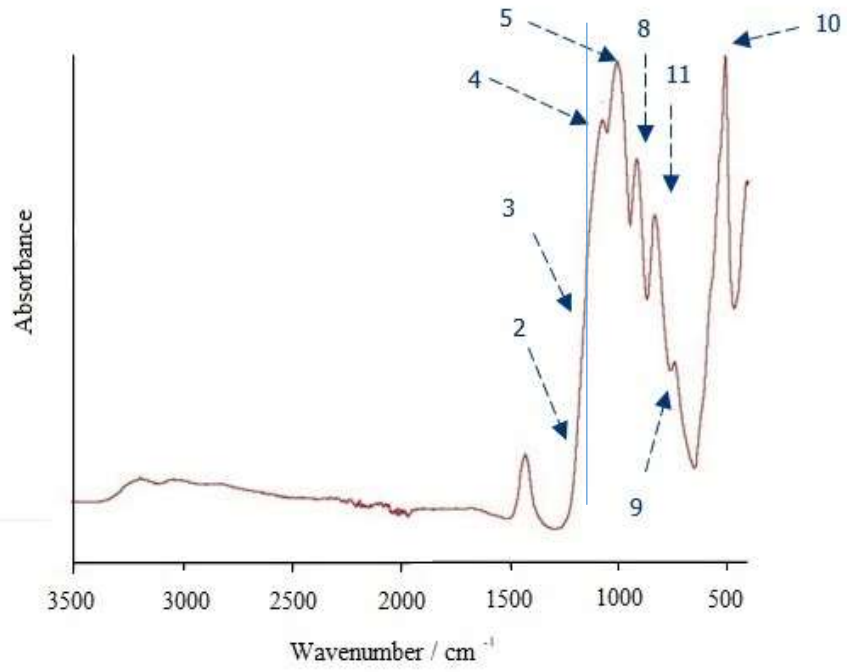


(a)

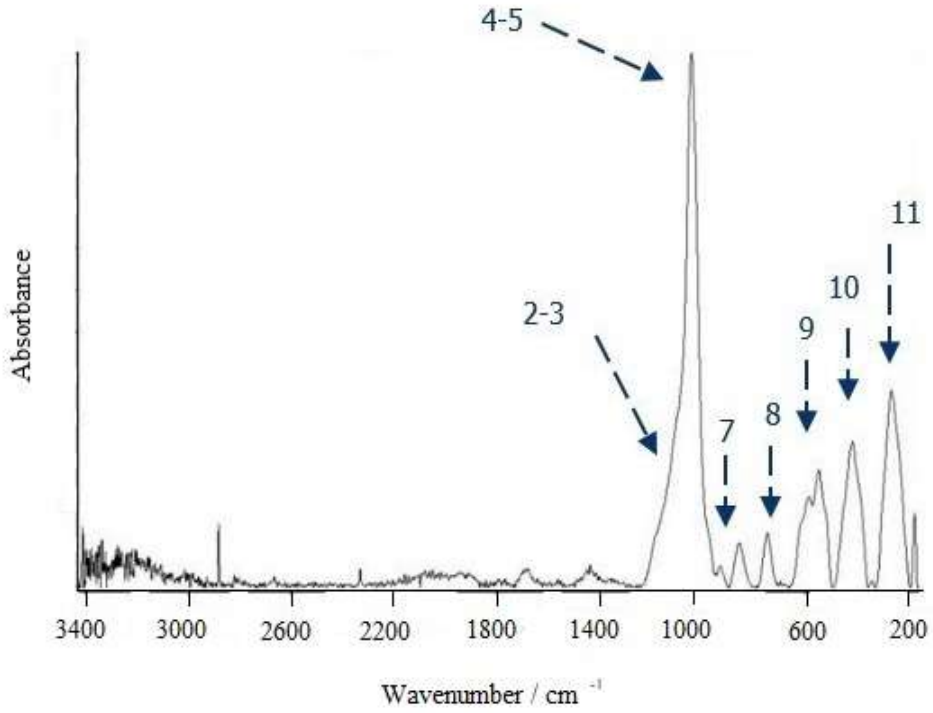


(b)

Figure 4. 5: Spectroscopy of the reference glass (25 min at 450 °C): (a) FTIR spectrum; (b) Raman spectrum.

Table 4. 4: The FTIR features observed in tin fluoride phosphate glass and their assignments.

| | Vibration mode | Bond | Assignments | Wavenumber/ $cm^{-1}$ |
|---|---|---|---|---|
| 1 | $\gamma_s$ | (P=O) | $Q^3$, superposed by $\gamma_{asy}$ ($PO_2$) | 1240 |
| 2 | $\gamma_{asy}$ | ($PO_2$) | $Q^2$ | 1240 |
| 3 | $\gamma_s$ | ($PO_2$) | $Q^2$ | 1150 |
| 4 | Stretching | ($PO^-$) | $Q^1$, end groups | 1100 |
| 5 | Vibration | (SnOP) | , SnPOF glasses | < 1100 |
| 6 | Stretching | ($PO_3^{2-}$) | $Q^1$ | 1040 |
| 7 | $\gamma_s$ | ($PO_4^{3-}$) | $Q^0$ | 985-990 |
| 8 | $\gamma_s$ | (POP) | $Q^2$ | 910-925 |
| 9 | $\gamma_{asy}$ | (POP) | $Q^2$ | 740 |
| 10 | Deformation | ($PO^-$) | , and SnF | 510-520 |
| 11 | Vibration | PF | | 845-850 |

Table 4. 5: The Raman features observed in tin fluoride phosphate glass and their assignments.

| n° | Vibration mode | Bond | Assignments | Wavenumber /cm$^{-1}$ |
|---|---|---|---|---|
| 1 | $\gamma_s$ | (P=O) | $Q^3$ | 1250-1390 |
| 2 | $\gamma_{asy}$ | ($PO_2$) | $Q^2$ | 1240-1278 |
| 3 | $\gamma_s$ | ($PO_2$) | $Q^2$ | 1130-1220 |
| 4 | $\gamma_{asy}$ | (PO3) | $Q^1$ | 1055-1074 |
| 5 | $\gamma_s$ | ($PO_3^{2-}$) | $Q^1$ | 1020-1050 |
| 6 | $\gamma_s$ | ($PO_4^{3-}$) | $Q^0$ | 950-960 |
| 7 | Stretching | (POP) | Q2 -$Q^1$ dominated; low content of $P_2O_5$ <30%; Short phosphate chains | 740 |
| 8 | Stretching | (POP) | $Q^1$-$Q^2$ dominated; relatively large content anions of $P_2O_5$ >30% | 693 |
| 9 | | | | 650-550 |
| 10 | | | SnF vibration | 395 (450-375) |
| 11 | | SnO | SnO vibration | 242 (300-100) |

Regarding the FTIR spectrum (Figure 4.5a), the asymmetric vibration of $PO_2$ groups are located near 1240 cm$^{-1}$ and the symmetric vibration near 1150 cm$^{-1}$. The frequency equivalent to $Q^2$ sites is characteristic of $PO_2$ groups in the phosphate chain. The absorption band at 1070 cm$^{-1}$, corresponding to the $P-O^-$ strechting mode (equivalent to $Q^1$ sites) is observed in the spectrum and it is suggest that the $Sn-O-P$ band vibration is located at 1100 cm$^{-1}$. The absorption band associated with the $PO_3$ end groups that is equivalent to $Q^1$ sites is observed around 1000 cm$^{-1}$. The peak at 907 cm$^{-1}$ is attributed to the asymetric stretching mode of the $P-O-P$ linkanges, while the band at 736 cm$^{-1}$ is assigned to the symetric stretching of $P-O-P$ groups. The peak at 830 cm$^{-1}$ is attributed to a stretching mode of $P-F$ bonds. This peak provides evidence that the $P-F$ bond exists in the glass structure. The peak at 506 cm$^{-1}$ is assigned to the deformation mode of $PO^-$ groups.

Figure. 4.5 b and Table 4.5 show spectrometry results obtained for the reference glass by Raman spectroscopy in the region between 4000 and 0 cm$^{-1}$. These results were used to corroborate and complete the structural study of the glass. Due to the asymmetric shape of the strongest peak, it defined the vibration of $PO_2$ equivalent to $Q^2$ in the range between 1200 and 1100 cm$^{-1}$ and the asymmetric vibration of $PO_3$ equivalent to $Q^1$ at around 1090 cm$^{-1}$. The strong peak with an asymmetry in one side is $PO_3$ symmetric stretching vibration of $Q^1$and it is located at 1020 cm$^{-1}$.The presence of stretching vibration of $P-O-P$ linkages at 740 cm$^{-1}$ and not at 693 cm$^{-1}$ confirms

that the structure is dominated by $Q^1$ sites more than $Q^2$ sites. The peak at 395 $cm^{-1}$ is attributed to SnF bonds corroborating its attribution by the peak of SnF vibration at 375 $cm^{-1}$, present in the $SnF_2$ chemical reagent spectrum. The peak at 242 $cm^{-1}$ is attributed to SnO bonds.

Both FTIR and Raman spectroscopy results identify the reference glass structure as pyrophosphate, mainly built by dimers ($Q^1$ end groups) with low presence of $Q^2$ polymeric chains. The high content of fluoride in the composition favour the network depolymerisation: F breaks the $P-O-P$ bonds to form monofluorophosphate ($PO_3F$) $Q^1$ units. A high presence of fluorine species into the phosphate decreases the average length of phosphates chains and successive conversion leads to pyrophosphate dimers. The process can be detected by a Raman peak at 1020 $cm^{-1}$ which is attributed to the symmetric stretching vibration of $(PO_3^{2-})$ equivalent to $Q^1$. This peak is clearly present in the Raman spectra of reference glass.

The pyrophosphate structure with high ratio of dimers is not the expected structure. The $P_2O_5$ content of this tin fluoride phosphate glass is 30 % mol, and according to the literature, the structure should be a polyphosphate glass (polymeric phosphate glass) with dominant $Q^2$ sites and some $Q^1$ end groups. The pyrophosphate structure is generally obtained for lower $P_2O_5$ contents.

A possible explanation for the existence of the pyrophosphate rather than the polyphosphate may lie in the interpretation of the spectra, particularly FTIR, in which some vibrations have not been identified. One is a band in the range of 3400-2700 attributed to the stretching vibration of NH and the other one is a peak at 1430 $cm^{-1}$ equivalent to the bending vibration of NH. These vibrations are not new as they were already observed in the ammonium phosphate monobasic reagent spectrum (Figure 4.2a). As mentioned before, these vibrations are typical in molecules containing $NH_4$. During the processing of the phosphate glass (composition $50\%SnF_2 + 20\%SnO + 30\%P_2O_5$), $NH_4H_2PO_4$ was used to form $P_2O_5$ molecules. Equation 24 shows the equilibrium reaction.

$$2NH_4H_2PO_4 \leftrightarrow P_2O_5 + 2NH_3 + 3H_2O \qquad (24)$$

Theoretically, if the reaction goes 100 % to completion, all the $NH_4H_2PO_4$ will be completely converted. However, in this case, the spectrometry results show that this

might not be the case. The presence of $NH_4$ in the final glass structure suggests that there could be some unreacted $NH_4H_2PO_4$ at the reference melting conditions (25 minutes at 450 °C). The unreacted $NH_4H_2PO_4$ can be detected by a FTIR peak at 990 $cm^{-1}$ or by a Raman peak at 950 $cm^{-1}$, which is attributed to the symmetric stretching vibration of $PO_4^{3-}$ equivalent to $Q^0$. The FTIR peak at almost 1000 $cm^{-1}$ suggests a transition from $Q^0$ to $Q^1$ where both are still present. The low intensity Raman peak at 950 $cm^{-1}$ means that the transition is dominated by $Q^1$. $NH_4$ and $Q^0$ identification in the spectra confirm the presence of unreacted $NH_4H_2PO_4$ in the final glass structure. This means that the extent of the chemical reaction is not 100 % and the final glass has fewer $P_2O_5$ molecules than expected (30 % mol). The equilibrium of the chemical reaction is not stable.

The stability of the precursors is essential for the development of a nanostructured polymer-glass hybrid. Thus, it is important to research how to synthesize stable tin fluoride phosphate glass. The fact that there are still some unreacted reagents in the glass may be possibly due to insufficient melting time or temperature. Therefore, a systematic investigation on glass melting conditions and its effect on the structure and properties of the glasses was carried out to improve the stability of the glass.

## 4.3 Influence of melting conditions on the structure of the tin fluoride phosphate glass – FTIR and Raman

The evolution of the glass structure depending on the melting conditions of the glass was studied. Seven samples were first synthesised at a fixed 450 °C using different melting times from 15 to 45 minutes and then 5 samples were synthesized at a fixed time of 25 minutes varying melting temperatures from 350 to 550 °C to identify the optimal melting conditions.

### 4.3.1 Influence of the melting time

The influence of the melting conditions on the structural changes of the glass was first investigated by varying the melting time from 15 to 45 minutes at a fixed melting temperature of 450 °C. The structure variation of the glasses produced under these conditions was analysed using FTIR and Raman spectroscopy (Figure 4.6).

FTIR spectra have been divided in two regions according to wavenumbers: functional group zone 4000-1300 $cm^{-1}$ (Figure 4.6a) and fingerprint zone 1300-400 $cm^{-1}$ (Figure 4.6b). The presence of $NH_4$ was detected in the functional group zone of the glass (Figure 4.6a). The steady reduction of $NH_4$ with the increase of the melting time is observed. The presence of $NH_4$ and the stretching vibration of $PO_4^{3-}$ equivalent to $Q^0$ will determine the suitable melting time, and it is noted that no $NH_4$ and no $Q^0$ were detected from 40 minutes melting at 450 °C glass samples. Figure 4.6 (a2) shows infrared absorption spectra of TFP glass at different melting times in the fingerprint zone. A peak observed around 950 $cm^{-1}$, which correspond to POH bond vibration, is only present for the 15 minutes melting glass. In Raman spectra (Figure 4.6b), the same POH vibration was observed as a peak at 924 $cm^{-1}$ for 15 minutes melting and one more at around 970 $cm^{-1}$ that is characteristic of $PO_4^{3-}$ symmetric stretching vibration equivalent to the $Q^0$ unit. These peaks were present in ammonium phosphate monobasic spectrum. The spectrum suggests that the chemical reagents are closer to the initial state (not reacted) than to develop into a stable glass structure. This means that the melting time of 15 minutes is insufficient for a complete conversion of $NH_4H_2PO_4$ into $P_2O_5$. The fact that $NH_4H_2PO_4$ is present in the final glass means the glass is unstable with less content of $P_2O_5$ in its composition. The variation in the composition can have a high impact in the structure and properties. The calculation of the content of $NH_4H_2PO_4$ necessary to obtain 30 % mol $P_2O_5$ during the synthesis was carried out using Equation 24, assuming chemical reaction reactivity 100 %. Phosphate glasses with less than 30 % mol of $P_2O_5$ are considered orthophosphate mainly isolated $Q^0$ units. Spectrometry results confirm the considerations.

The nature of the phosphate anion that constitutes the glass structure changes with the melting conditions of the glass. The fingerprint zone of the glasses shows different vibrational patterns and suggests an evolution of the structure depending on the melting conditions. The evolution of the structure is detected by identifying the $PO_4$ tetrahedral connectivity ($Q^n$) vibration peaks in the spectra. FTIR and Raman spectra (Figure 4.6) indicate that phosphate tetrahedral units undergo a transition from $Q^0$ to $Q^1$ sites as melting time increase. The structural changes or evolution of the structure take place at shorter melting times.

Although the glass composition is formulated to achieve polyphosphate networks, spectrometry shows that for the glass melted for 15 minutes at fixed 450 °C its network is orthophosphate. Increasing the melting time to 20 minutes, the FTIR spectrum of the glass shows a vibrational peak between the vibration of $Q^0$ (970 $cm^{-1}$) and the vibration of $Q^1$ (1040 $cm^{-1}$), suggesting the transition from $Q^0$ to $Q^1$ had taken place. In this case, Raman spectroscopy provides higher resolution for vibrational identification. The low absorbance of the peak at 970 $cm^{-1}$ attributed to $Q^0$ reveals lower content of $Q^0$ sites than that in glass melting time of 15 minutes. The peak at 1020 $cm^{-1}$ is attributed to pyrophosphate ($Q^1$ units) with three NBO. The band between 1240-1160 $cm^{-1}$ that makes the peak at 1020 $cm^{-1}$ asymmetric indicates the presence of $PO_2$ symmetric stretching vibration equivalent to $Q^2$.

It is noted that once the melting time reached the reference (25 minutes) the vibrations within fingerprint zone are almost equal for all melting times (Figure 4.6 a). But the transition from $Q^0$ to $Q^1$ is finished in the 40 minutes sample with no $NH_4$, no $Q^0$, and complete conversion of $NH_4H_2PO_4$ into $P_2O_5$. This structure was identified in the reference glass structure identification section. A small difference exists in FTIR spectra related to the peak intensity at 1100 $cm^{-1}$. The intensity of the peak/band determines the magnitude of the presence of this vibrational group in the structure of the material; strong peak intensity, higher content of the vibrational group in the structure and shows the evolution of the structure. The FTIR peak at 1100 $cm^{-1}$, as mentioned before, is attributed to POSn bonds equivalent to $Q^2$ and shows the transition from $Q^1$ into $Q^2$ of the glass structure depending the melting conditions.

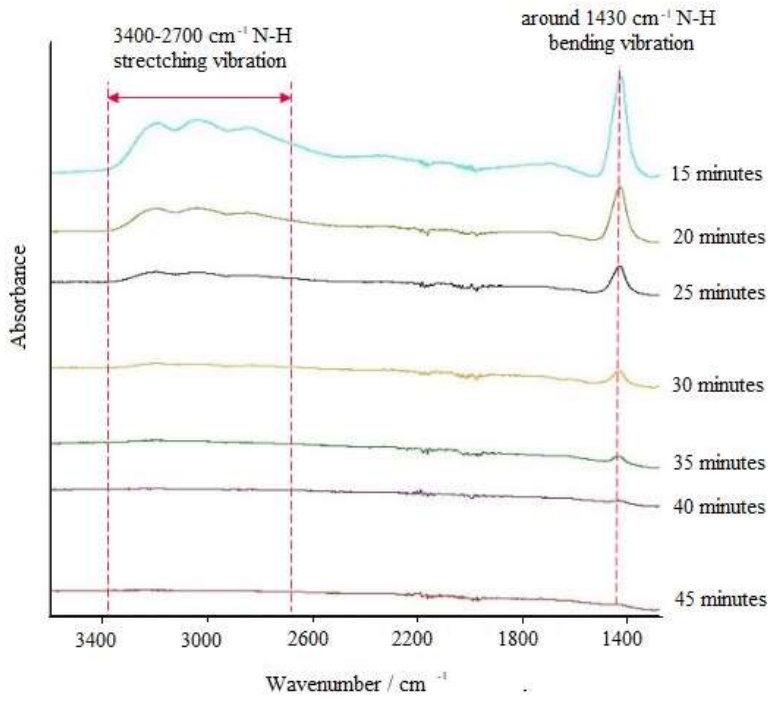
3400-2700 cm⁻¹ N-H
strectching vibration
around 1430 cm⁻¹ N-H
bending vibration
15 minutes
20 minutes
25 minutes
30 minutes
35 minutes
40 minutes
45 minutes
Absorbance
3400
3000
2600
2200
1800
1400
Wavenumber / cm ⁻¹

(a1)

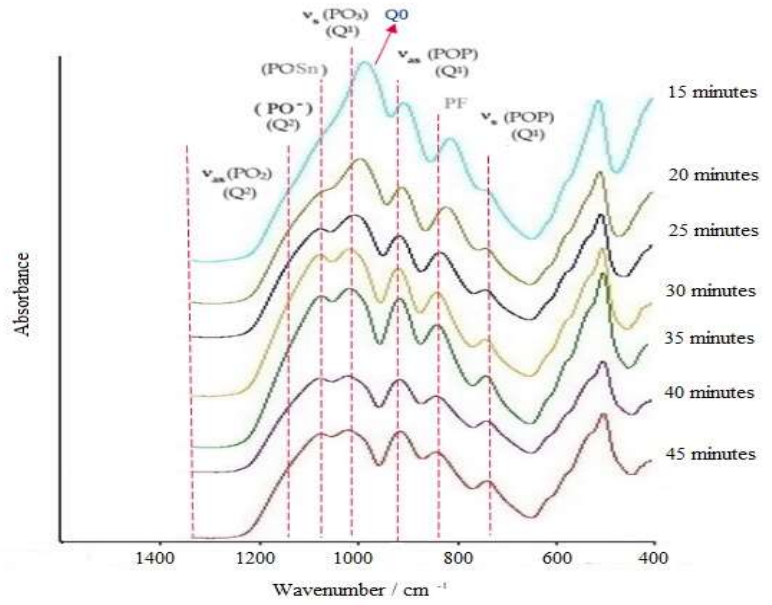
Q0
(POSn)
PF
15 minutes
20 minutes
25 minutes
30 minutes
35 minutes
40 minutes
45 minutes
Absorbance
1400
1200
1000
800
600
400
Wavenumber / cm ⁻¹

(a2)

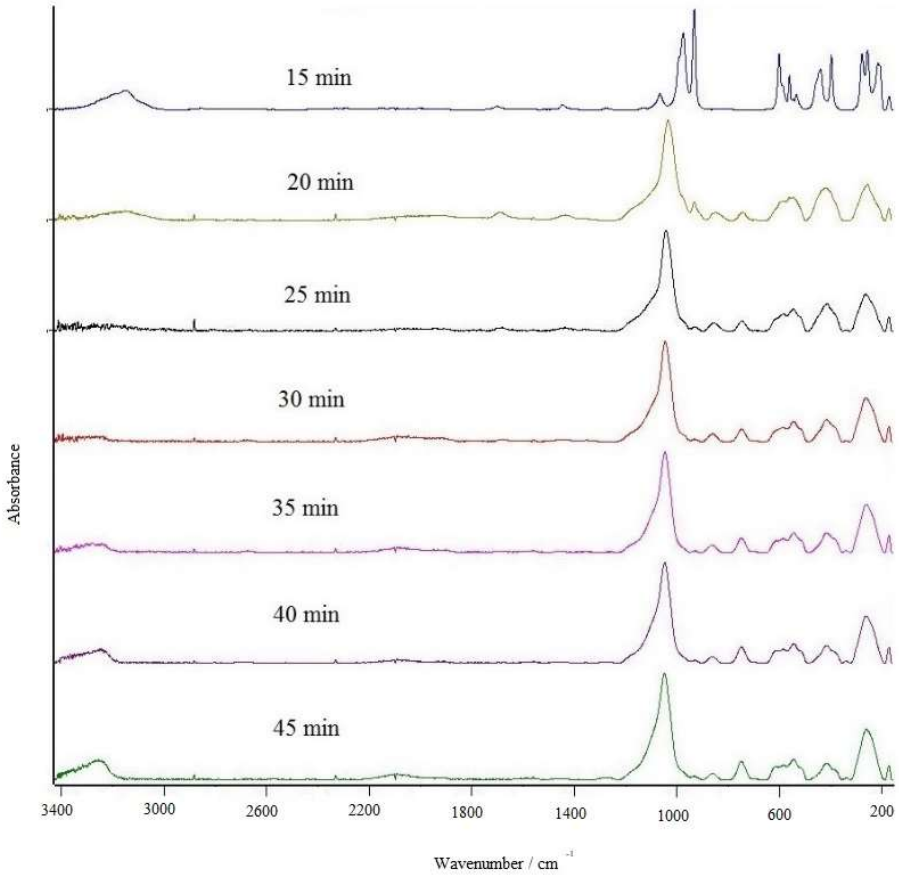


(b)

Figure 4. 6: Spectroscopy of the glass samples from 1 to 7 (melting time from 15 to 45 minutes at fixed 450 °C): (a) FTIR spectra: (a1) zone 3400- 1400 $cm^{-1}$, (a2) zone 1400-400 $cm^{-1}$; (b) Raman spectra.

## 4.3.2 Influence of the melting temperature

The influence of the melting temperature on the structure of the glass was investigated by varying the melting temperature from 350 to 550 °C at a fixed melting time of 25 minutes. The glasses produced under these conditions were analysed using FTIR and Raman spectroscopy (Figure 4.7).

Infrared absorption spectra of functional group zone 4000-1300 $cm^{-1}$ of TFP glass at different melting temperature are shown in Figure 4.7 (a1). The NH vibration between 3400-2800 $cm^{-1}$ suggests unreacted $NH_4H_2PO_4$ in the glass structure for melting temperatures of 350 °C and 400 °C. This is corroborated in Figure 4.7 (a2) by the peak at 970 $cm^{-1}$, equivalent to $Q^0$ in the case of glass melted at 350 °C for 25 minutes and by the peak at 1000 $cm^{-1}$, transition from $Q^0$ into $Q^1$ , in the case of glass melted at

400 °C. Glasses melted at 350 °C and 400 °C, are unstable glasses for the same reason of low melting time glasses, the degree of reactivity of phosphate molecule forming reaction, Equation 24. Both these temperatures are insufficient to complete conversion from $NH_4H_2PO_4$ into $P_2O_5$.

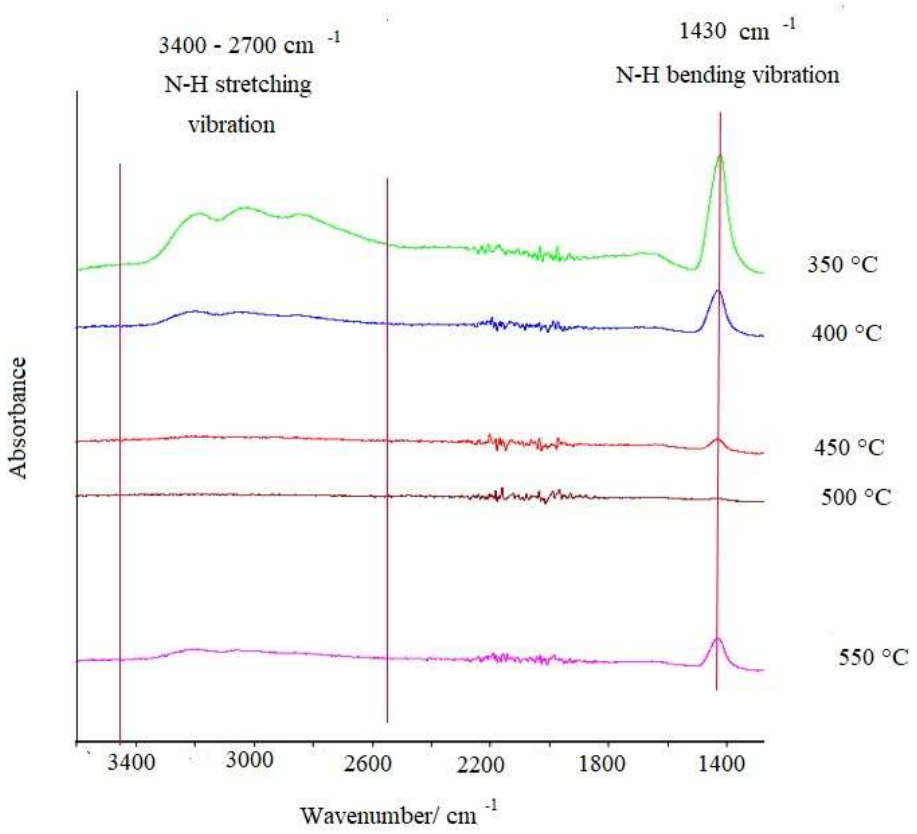


(a1)

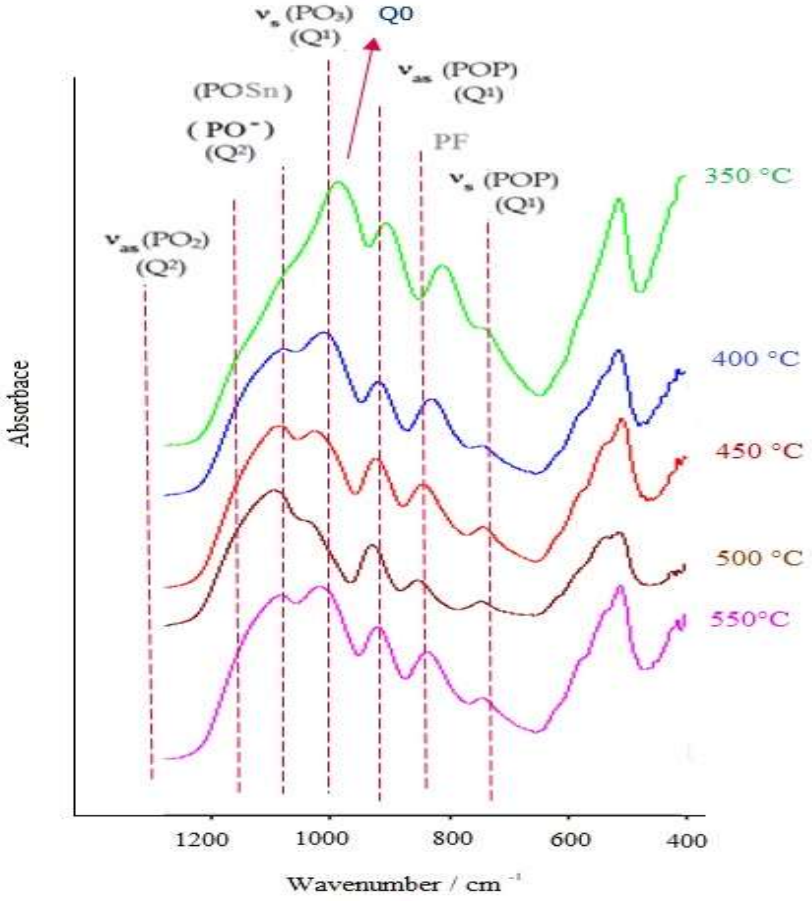


(a2)

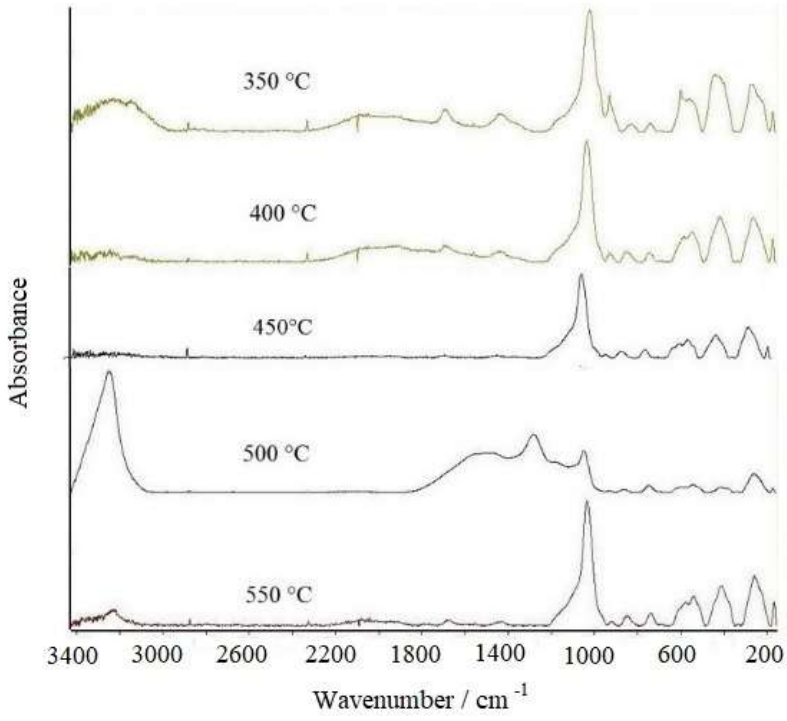


(b)

Figure 4. 7: Spectroscopy of the glass samples melted for 25 minutes from 350 to 550 °C: (a) FTIR spectra: (a1) zone 3000-1400 cm$^{-1}$, (a2) zone 1400-400 cm$^{-1}$; (b) Raman spectra.

The glass sample melted at 500 °C for a fixed 25 minutes shows interesting spectrometry results. The FTIR spectrum of this sample (Figure 4.7 (a1) and (a2)) shows that 100% reactivity is achieved because there is no presence of $NH_4$ and $Q^0$ sites. The decrease of the peak at 1040 $cm^{-1}$ (stretching of $PO_3^{2-}$ equivalent to $Q^1$) and the pronounced and slide shift of the peak at 1100 $cm^{-1}$ (stretching of POSn equivalent to $Q^2$ ) to 1150 $cm^{-1}$ suggest the polyphosphate structure where $Q^2$ sites are predominant. The Raman spectrum (Figure 4.7b) shows the $PO_2$ vibration with a peak at 1270 $cm^{-1}$ equivalent to $Q^2$ and $PO_3^{2-}$ vibration with a peak at 1020 $cm^{-1}$ equivalent to $Q^1$ that corroborate the polyphosphate connectivity of the glass. The vibrations higher than 1400 $cm^{-1}$ were due to fluorescence effects.

The evolution of the structure was converted in reversion at 550 °C. The spectrum of sample melted at 550 °C (Figure 4.7b) is similar to the spectrum of sample melted at 400 °C.

## 4.4 Effect of melting conditions on the density of tin fluoride phosphate glass

The density of the glasses produced at 450 °C for seven different melting times, from 15 minutes to 45 minutes, was measured and the results are given in Figure 4.8 a. It shows that the density of the ternary stannous fluorophosphates glasses increases with increased melting time. The increment slows down and reaches to an almost constant value at 25 minutes, suggesting a stable structure. The effect of melting temperature (at a fixed time of 25 minutes) on the density values are shown in Figure 4.8 b. The density of the glasses from 350 °C to 550 °C (at a fixed time of 25 minutes), including the reference (25 minutes and 450 °C), give the highest density value at 450 °C and a value close to this for the sample at 500 °C. At 550 °C, the density reduces significantly. The results confirm that the density of the material is dependent on the melting conditions.

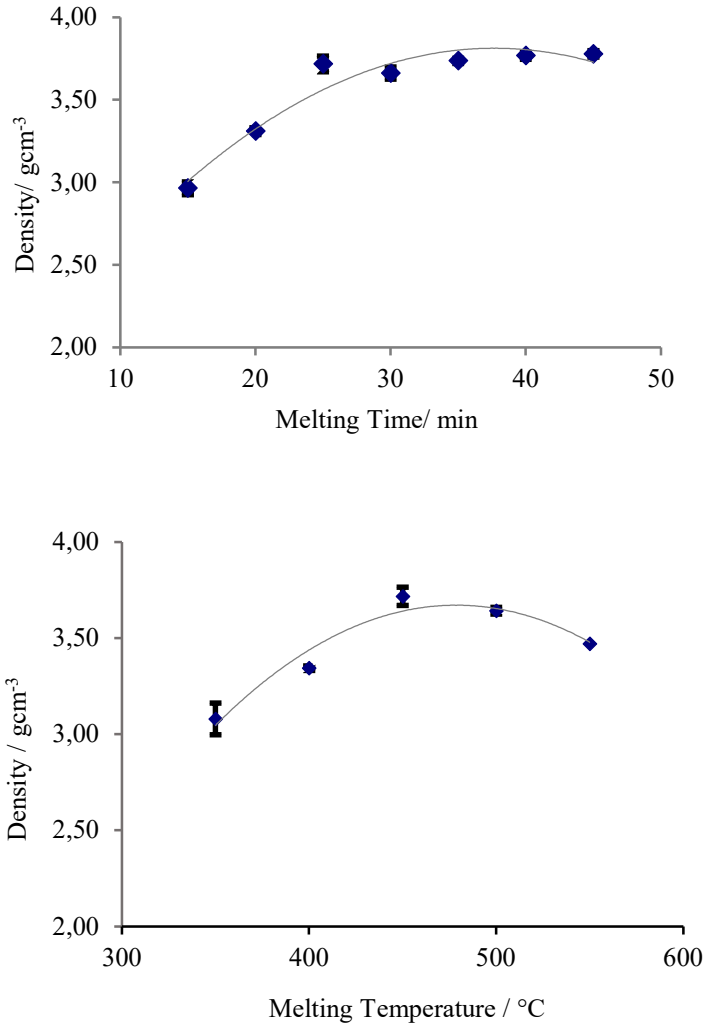


Figure 4. 8: Measured densities of TFP glass melted at: a) 450 °C for different times; b) different temperatures for 25 minutes.

## 4.5 Glass transition temperature

The effect of melting time on the glass transition temperature (Tg) of the glasses (at a fixed temperature of 450 °C) is shown in Figure 4.9 (a) and the effect of temperature of melting (at a fixed time of 25 minutes) on the Tg values in Figure 4.9 (b). Different melting conditions have resulted in a large variation of the Tg values of the glasses. The increase of the melting time and the temperature results in a higher Tg value. For example, as the melting time is increased from 15 to 45 minutes for an identical melting temperature (450 °C), the glass transition temperature increases from 95 to 161 °C. The increase in Tg values was also observed with increased melting temperature up to 500 °C using the same melting time of 25 minutes. However, the glass produced at 550 °C (sample 11) gives a Tg value of around 100 °C. This glass

also loses its transparency. The results suggest a different glass structure may be formed at this temperature. The changes of the Tg value of the glass could be explained as a possible change in the glass composition/structure caused by different melting conditions and discussed by the structural characterization of the glass in Section 4.3.

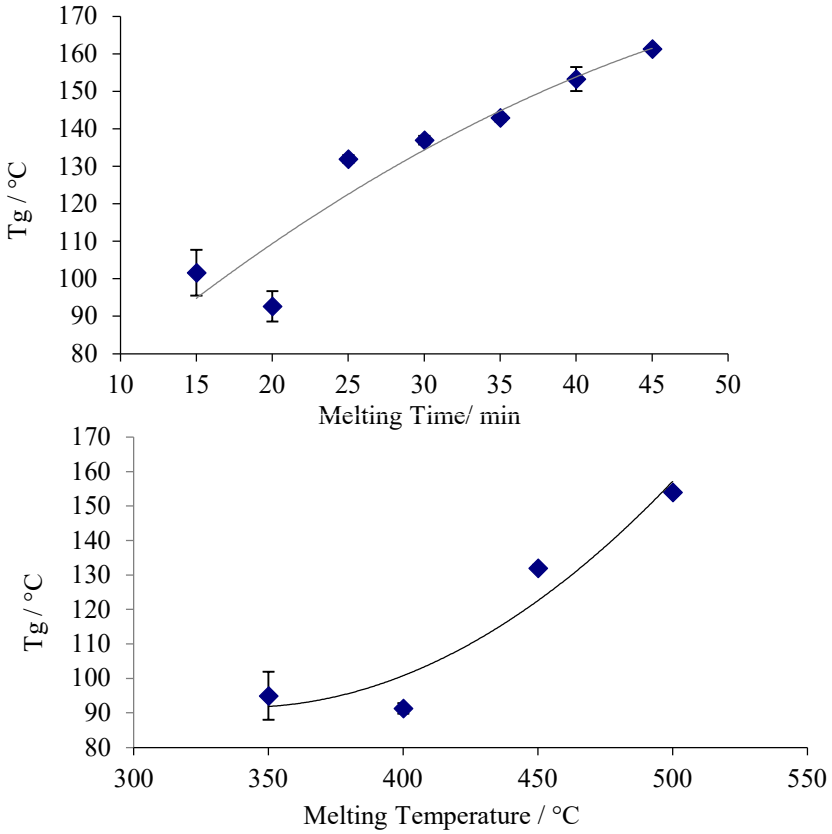


Figure 4. 9: The effect of melting conditions on the Tg of TFP glass melted at: a) 450 °C for different melting times; b) different melting temperatures for 25 minutes.

Values of density and glass transition temperature at each melting condition are summarized in Table 4.6. An increase of more than 30 °C of the glass transition temperature was detected between 20 and 25 minutes and 400 and 450 °C. The fact that density and the Tg at low melting conditions are reduced is related to the degree of reactivity of the phosphate molecule forming reaction (Equation 24).

In the section on the structural characterization of the glass, low melting conditions glasses were determined to be unstable due to the presence of unreacted $NH_4H_2PO_4$ in the synthetized glass structure. The presence of unreacted $NH_4H_2PO_4$ affects the reactivity degree of the phosphate molecule forming reaction and the reactivity degree is influenced by the composition of the glass and its structure.

The $NH_4H_2PO_4$ content is calculated by Equation 24 to obtain 30% mol of $P_2O_5$ assuming 100% chemical reaction reactivity. However, the presence of unreacted $NH_4H_2PO_4$ in the synthetized glass means that low melting conditions are insufficient for a complete conversion of $NH_4H_2PO_4$ into $P_2O_5$. As a consequence, the $P_2O_5$ content is less than 30% mol and the phosphate structure is formed with predominant weak linkages such as $F-Sn-F$, $Sn-P-F$, $F-P-F$.

The reference sample will be the limit for both melting conditions, relating to the major increase of Tg and the density to strong linkages predominant in the phosphate structure. The structure characterization of different melting conditions by FTIR showed a peak at 1100 $cm^{-1}$ that appears for the first time at the reference melting conditions (where Tg showed a high increase) and increases its intensity at higher melting conditions, like the Tg of the glass. The peak at 1100 $cm^{-1}$ is attributed to $Sn-O-P$ linkages.

At reference glass melting conditions, the divalent tin ($Sn^{2+}$) acts as a network former, in tetrahedral coordination, bonding with phosphorus via oxygen. The replacement of $P-O-P$ bonds by $Sn-O-P$ bonds increases the connectivity of the network together with the Tg and decreases glass susceptibility to attack by water. The intensity showed by the peak at 1020 $cm^{-1}$ ($P-O-P$ bond) and the peak at 1100 $cm^{-1}$ ($Sn-O-P$) gave information about the evolution of the replacement and which one is predominant in each condition.

Table 4. 6: Density and glass transition temperature of the glasses.

| Samples | Temperature /°C | Time /min | Density / $gcm^{-3}$ | Tg / °C |
|---|---|---|---|---|
| 1 | 450 | 15 | 2.96±0.04 | 102±6 |
| 2 | 450 | 20 | 3.31±0.02 | 93±4 |
| 3 | 450 | 25 | 3.71±0.05 | 132±1 |
| 4 | 450 | 30 | 3.69±0.04 | 137±1 |
| 5 | 450 | 35 | 3.73±0.02 | 143±1 |
| 6 | 450 | 40 | 3.76±0.02 | 153±3 |
| 7 | 450 | 45 | 3.77±0.02 | 161±0.5 |
| 8 | 350 | 25 | 3.08±0.08 | 95±7 |
| 9 | 400 | 25 | 3.34±0.01 | 91±1.5 |
| 10 | 500 | 25 | 3.64±0.02 | 154±1 |
| 11 | 550 | 25 | 3.47±0.04 | 105±1 |

## 4.6 Thermal stability

The thermal stability, the degradation temperature, and volatiles of tin fluoride phosphate glass at different melting conditions have been investigated by thermogravimetric analysis (TGA). Figure 4.10(a) and 4.10(b) show, respectively, the influence of the melting time and temperature on the thermal stability of the glass. The mass changes during heating are described in Table 4.7. The onset of decomposition (significant weight loss with decomposition temperature) gradually increases with increasing both the melting time and temperature, except for the sample melted at 550 °C. By increasing the melting time from 15 to 45 minutes, the onset temperature increases from 206 °C to 364 °C and increasing the melting temperature (350 to 500 °C) from 241 to 359 °C. The value obtained for sample 12 melted at 550 °C was 311 °C. The optimum thermal properties and decomposition temperature of 365 °C was obtained for the glass processed at 450 °C for 45 minutes. This suggests a stronger phosphate structure than those under other melting conditions. The higher content of volatiles (Table 4.7) and loss of weight suggest unstable glass. The increase of onset temperature at high melting conditions is due to the replacement of $P-O-P$ bonds by $Sn-O-P$ bonds that increases the connectivity of the network and improves the thermal stability of the glass.

a)

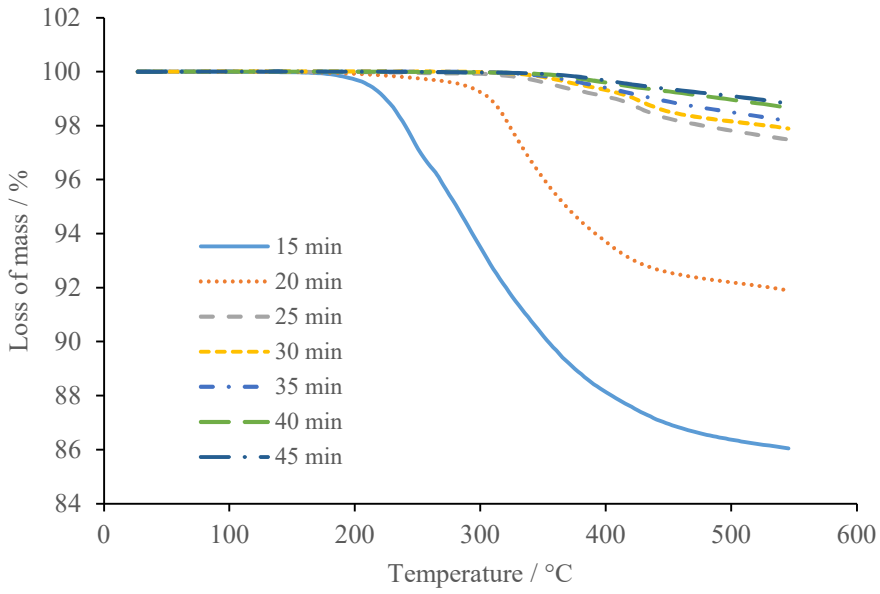

b)

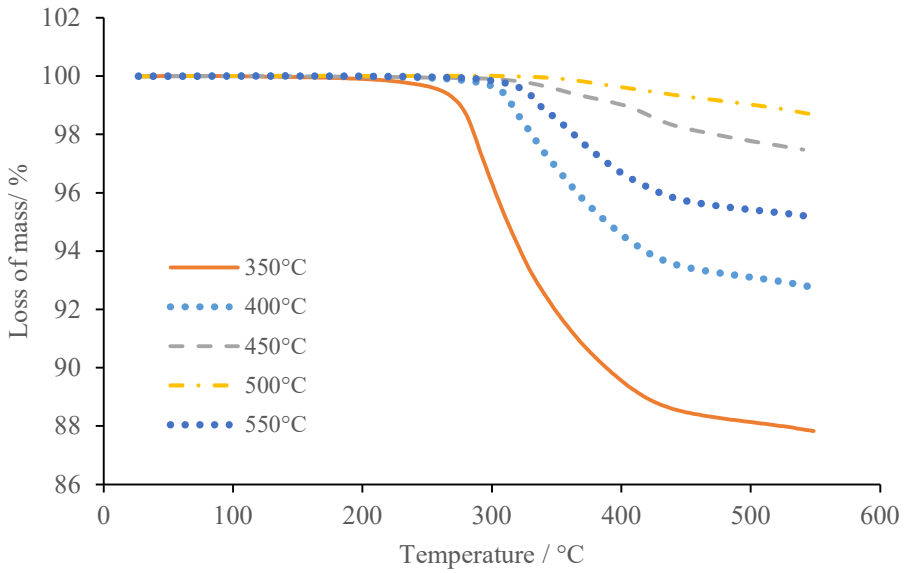


Figure 4. 10: The effect of melting conditions on the thermal stability of tin fluoride phosphate glass melted at: a) 450 °C for different melting time; b) different melting temperature for 25 minutes.

Table 4. 7: Mass changes versus temperature to define the glass degradation onset in tin fluoride phosphate glasses melted at different melting conditions.

| | Mass change 25 to 300°C | Mass change 300 to 550°C | |
|---|---|---|---|
| | Moisture / volatiles | Glass degradation | |
| | Step (%) | Step (%) | Onset ( °C) |
| 15 min | 6,53 | 7,42 | 206 |
| 20 min | 0,77 | 7,33 | 220 |
| 25 min | 0,02 | 3,45 | 323 |
| 30 min | 0,08 | 2,43 | 332 |
| 35 min | 0,01 | 1,78 | 344 |
| 40 min | 0,03 | 1,31 | 357 |
| 45 min | 0,03 | 1,15 | 364 |
| 350°C | 3,69 | 8,82 | 241 |
| 400°C | 0,32 | 7,11 | 273 |
| 500°C | 0,02 | 1,31 | 359 |
| 550°C | 0,14 | 5,04 | 311 |

## 4.7 Thermal treatment

In order to show the effect of the thermal conditions on different glass melting conditions, low melting conditions glass samples (20 minutes and 450 °C) and high

melting conditions glass (35 minutes and 450 °C) were re-heated at 250 °C for 10 minutes and their Tg measured by DSC.

The low melting conditions samples (20 minutes and 450 °C) had an initial Tg value of approximately 90-100 °C which was substantially affected by the thermal treatment. The Tg value decreases below 75 °C suggesting decomposition and structural changes.

The high melting conditions sample processed at 450 °C for 35 minutes suffered no changes and maintained its structure after re-heating. This means that these thermal conditions affected only the unstable tin fluoride phosphate glasses, which had been synthesized at low melting conditions.

## 4.8 Chemical durability

It was observed that the glasses processed at low temperature (lower than 450 °C) and for a shorter time (less than 25 minutes) were attacked by atmospheric moisture indicating a lack of chemical durability. White spots on the low melting glass surfaces were detected within seven days - this reaction did not appear in the glasses with higher melting conditions. Thus, the structural change of the glass over time was determined by Raman spectroscopy.

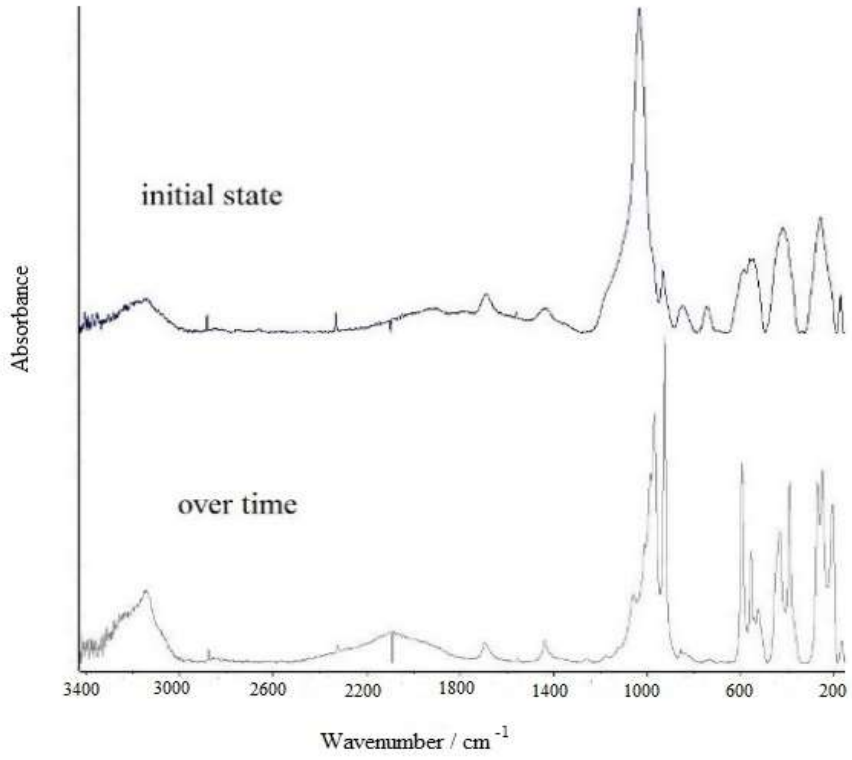


(a)

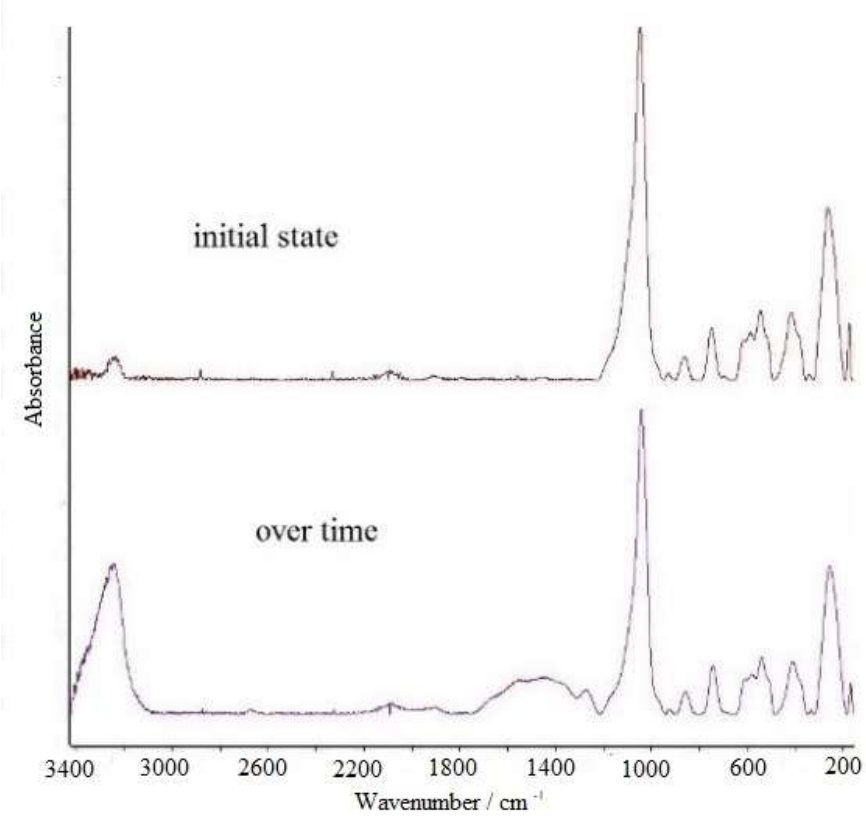


b)

Figure 4. 11: Raman spectra at initial state and over time: a) Sample 2 (20 minutes 450 °C); b) Sample 5 (40 minutes 450 °C).

Structural changes of the glass were detected for low melting conditions glasses over time. In Figure 4.11 (a), the spectra of sample 2 (20 minutes and 450 °C) shows decomposition and degradation with large structural changes over time.

The presence of unreacted $NH_4H_2PO_4$ in low melting conditions glasses implies that the low melting conditions are insufficient for a complete conversion of $NH_4H_2PO_4$ into $P_2O_5$. As a consequence, $P_2O_5$ content is less than 30% mol and the phosphate structure is formed with predominant weak linkages such as $F-Sn-F$, $Sn-P-F$, $F-P-F$. These types of bonds are easily attacked by water and provide weak points in the network, degrading it easily over time.

The low absorbance of the peak at 970 $cm^{-1}$ reveals $Q^0$ sites. The peak at 1020 $cm^{-1}$ is attributed to pyrophosphate ($Q^1$ units) with three NBO. The band between 1240-1160 $cm^{-1}$ that makes the peak at 1020 $cm^{-1}$ asymmetric indicates the presence of $PO_2$ the symmetric stretching vibration equivalent to $Q^2$.

Sample 5 (35 minutes and 450 °C) suffers no structural changes but absorbs water (typical behaviour of glasses) and needs to be dried before mixing with hydroscopic materials.

In order to explore possible new applications for the glass-polymer system that related to water contact, a water resistance test was carried out by immersing samples in ionised water for 48 hours at 80 °C using a laboratory test tube. Table 4.8 shows the results obtained for the glass samples. The variation of the volume (Δv) for 3 samples per each melting condition was calculated using the following Equation 25:

$$\Delta v = ((v) - v_0/v_0)(100) \quad (25)$$

Where $v_0$ is the initial volume of the glass and v is the volume of the glass after immersion in ionised water for 48 hours at 80 °C.

Table 4. 8: Glass after immersion in ionised water for 48 hours at 80 °C.

| Samples | Density / gcm $^{-3}$ | Δv variation of the volume / % |
|---|---|---|
| 1 | 2.9 | - |
| 2 | 3.3 | - |
| 3 | 3.7 | -3.7 ±2.3 |
| 4 | 3.6 | -1.2 ±0.3 |
| 5 | 3.7 | 0.4 ±0.2 |
| 6 | 3.7 | -0.02 ±0.6 |
| 7 | 3.7 | 0.39 ±0.1 |
| 8 | 3.0 | - |
| 9 | 3.3 | - |
| 10 | 3.6 | 0.18 ±0.9 |
| 11 | 3.4 | -23 ±7.6 |

The test revealed no resistance to water for low melting time and temperature, such as samples 1 2, 8 and 9. Due to their short melting time, the chemicals in these sample did not have time to form a glass network. The water attack occurred before corroborated observation of the samples at room temperature. Samples 1, 2, 8 and 9 initially suffered moisture attack as shown by clear white areas on the glass surface. Further immersion in water resulted in more decomposition as shown by white, chalk-like small debris particles floating on the water.

Increasing the melting time of the glass from 20 to 25 minutes, the water resistance of the glass was improved, losing only 4% of glass volume at 25 minutes. Raising the

melting time to 30 minutes resulted in a further improvement of water resistance as indicated by a 1.2% glass volume variation. In the case of the melting temperature, the improvement is evident at 500 °C obtaining a value of 0.18% of volume variation. At 550 °C, the loss of volume is high compared with the others, 23%, and it suggests a change of structure.

These results are directly related to the presence of ammonium in the glasses as detected by FTIR. The results show that to obtain sufficient $P_2O_5$ from $NH_4H_2PO_4$, the glass needs to be melted for at least 35 minutes at 450 °C or 500 °C for 25 minutes to reach the complete reaction and conversion to $P_2O_5$. The presence of $NH_4$ in the glass results in a reduced water resistance of the glass.

## 4.9 Rheological properties

The rheological properties have been investigated by the rotational rheometer for glass processed at 450 °C for 25 minutes. The tests were carried out at three different temperatures: 230 °C, 250 °C and 270 °C, respectively. These three temperatures were selected to simulate the glass behaviour by extrusion processing that would be applied for hybridization with PA11. The three temperature are recommended extrusion process temperatures for PA11. Figure 4.12 shows the measured time independent of complex viscosity at three temperatures, which reveals a linear viscoelastic behaviour indicating that the glass behaves as a Newtonian fluid at these temperatures. To evaluate the impact of TFP glass on the time dependant nature of PA11, the majority of the viscosity graphics were plotted versus time.

This is because one of the important goals of this research is to develop new materials for coating applications for which the variation of viscosity with time is important. For coating applications, it is desirable that the material flows sufficiently to enable it to run into the contours of the neighbouring surfaces in order to minimize voids and then quickly regain a high viscosity towards the end of deposition. Figure 4.13 shows the effect of temperature of the glass fluid on the viscosity.

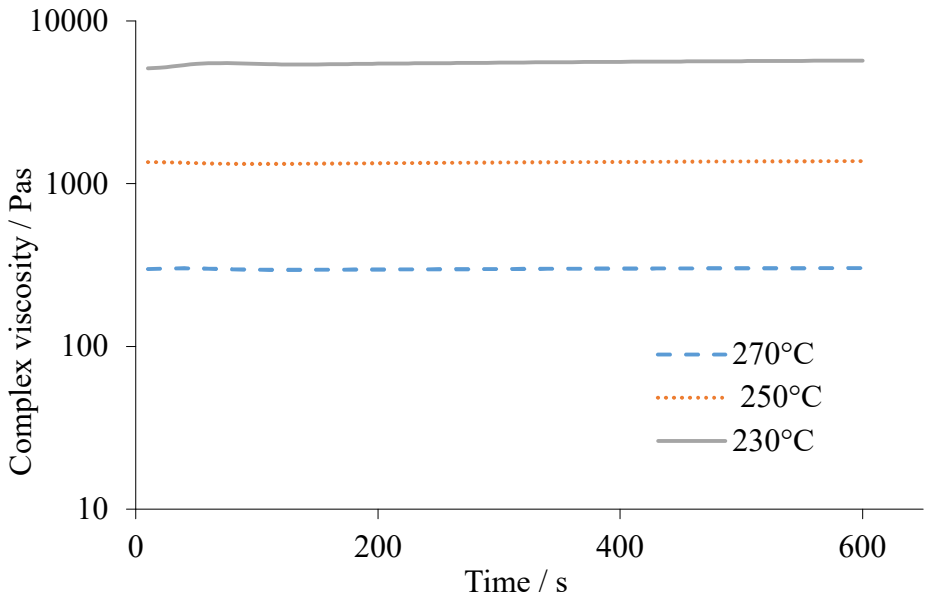


Figure 4. 12: Measured complex viscosity of tin fluoride phosphate glass at different temperatures against time.

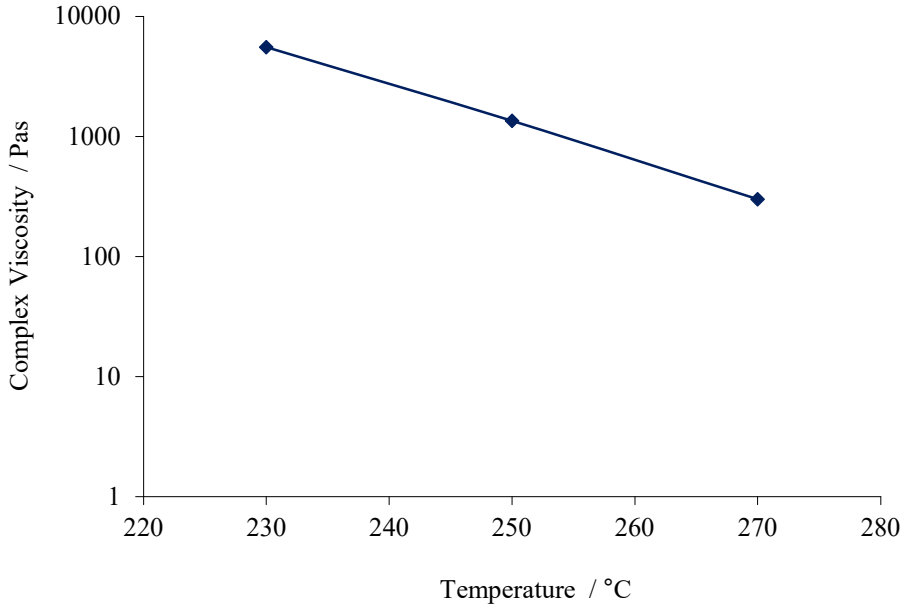


Figure 4. 13: The effect of temperature on the complex viscosity of tin fluoride phosphate glass.

The major decrease of η*(complex viscosity) against temperature (Figure 4.13) is an important factor for hybrid morphology development under thermal and shearing conditions representative of compounding.

Using the complex viscosity data, the activation energy of flow can be determined for the glass using an Arrhenius equation (Equation 18).

In this equation, η is the steady shear viscosity at a given shear rate, A is a preexponential constant, Ea is the activation energy for viscous flow, R is the universal gas constant, and T is the absolute temperature. Ea can be calculated from the slope of a plot of the log η versus 1/T. This equation strictly requires a steady shear viscosity, but it is possible to use the complex viscosity if it is assumed that the Cox–Merz rule applies to these materials. The Ea was calculated at low frequency, 0.1 $rads^{-1}$, and the results of the slope is shown in Figure 4.14 [156-157].

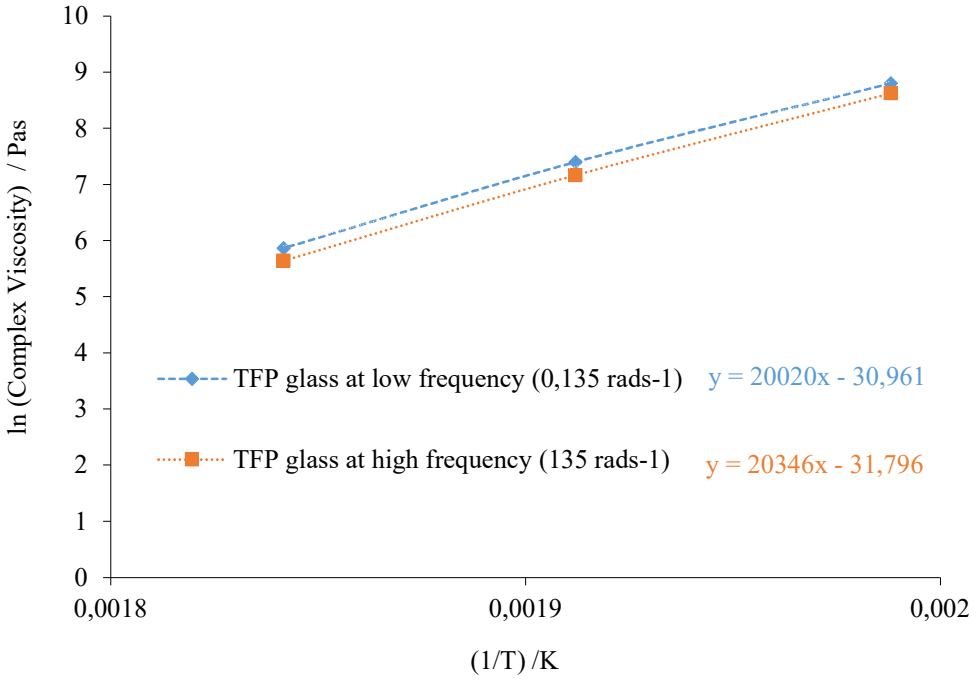


Figure 4. 14: Ln of the complex viscosity as a function of (1/T) in kelvin with the slope equation to calculated activation energy of TFP glass.

The activation energy (Ea) of TFP glass was calculated from the slope of the plot at two different frequencies, low 0.135 $rads^{-1}$ and high 135 $rads^{-1}$. At low frequencies, the value is 166 KJ/mol and 169 KJ/mol at high frequencies. In both cases, similar values were obtained. Urman et al. studied [111] the activation energy of the pure components (TFP glass; PA12) and hybrids with different glass content. In this study the activation energy was calculated at two different frequencies, 0.5 and 50 $rads^{-1}$, and the results showed a value around 160 KJ/mol of P glass. In both studies, similar activation energy (Ea) results of the glasses were found at both frequencies.

As phosphate glasses are considered as polymers, the increase in Tg can be related to the glass molecular weight. The polymers are formed with molecules that reach different polymerization degrees and, therefore, different molecular weights. The same principle applies to phosphate glasses. In the case of synthetic polymers from chain polymerization, the length of the chain will be determined by the time that the chain is growing. So, it is suggested that the glass is increasing its chain size by adding repeating units over time. Longer melting time shows higher molecular weight and as consequence, higher Tg values. This is confirmed by the increase in viscosity obtained for the glass sample with Tg 150 °C (Figure 4.15).

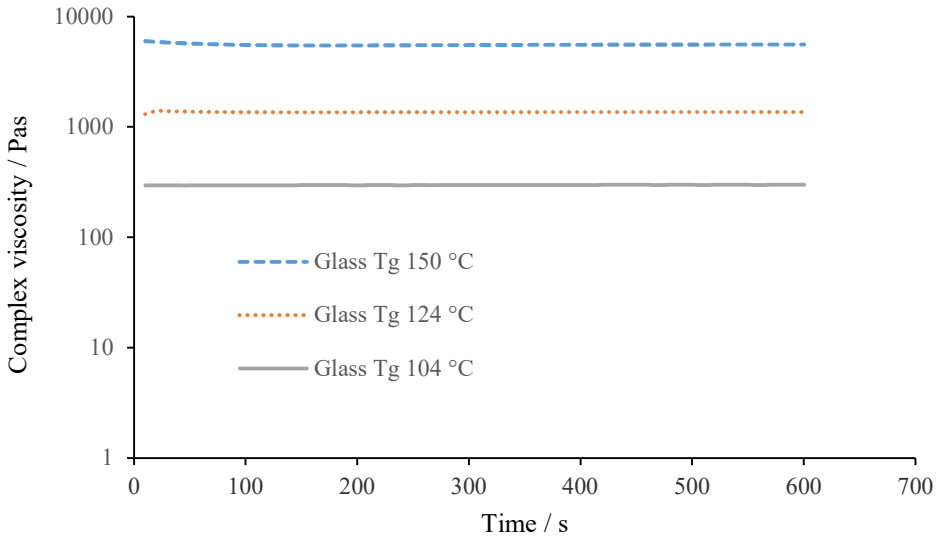


Figure 4. 15: The effect of the Tg on the complex viscosity against time of tin fluoride phosphate glass at 250 °C of processing temperature.

Hence, the Tg variation of the glass at different melting conditions is related to the molecular weight and influences the other glass properties. As in polymers, the molecular weight is important because it determines many physical properties, for example mechanical properties such as stiffness, strength, viscoelasticity, toughness, and viscosity. A lower molecular weight results in lower Tg values and inferior mechanical properties.

## 4.10 Final remarks

This research reveals the important role of melting conditions on the structure and properties of the glass. The study demonstrates an eminent evolution of the glass

structure according to melting time and temperature and shows how these structural changes affect the properties of the glass. Structural identification is achieved by $Q^n$ units. The transitions of $Q^n$ units depend on the chemical composition of the glass and the $P_2O_5$ content Another influencing parameter is the behaviour of oxides; they are either a network former or modifier. The divalent tin started to act as network former at reference melting conditions (25 minutes 450 °C) replacing P-O-P by P-O-Sn bonds and elaborated a stronger network. Even the reference glass is not stable due to incomplete conversion from $NH_4H_2PO_4$ to $P_2O_5$, the reference glass shows a large improvement relative to lower melting conditions. The presence of $NH_4$ was found in the final glass structure, which confirms the presence of some unreacted $NH_4H_2PO_4$ at the reference melting conditions (25 minutes at 450°C). The measured properties were much better than those at lower melting conditions, which is consistent with the achievement of a strong glass network at the reference conditions. Control of melting conditions enabled the glass to replace weak linkages with strong ones and the replacement continues with increasing melting conditions (longer melting time and higher temperature). The reactivity degree of the glass forming chemical reaction is the cause of the property variability and is directly related to the melting conditions.

With increasing melting conditions, the spectra show a systematic structural evolution from orthophosphate to pyrophosphate in the case of melting time and orthophosphate-pyrophosphate-polyphosphate-pyrophosphate in the case of melting temperature. The structural evolution (transition changes) stopped at certain melting conditions. Melting time structural evolution stopped when $NH_4$ and $Q^0$ sites disappear delimitating the suitable melting time to synthesize glass with a stable structure at 40 minutes and then maintain it constant. Melting temperature structural evolution did not stop, it was a succession of $Q^n$ sites achieving a polyphosphate at 500 °C with optimal properties. At higher temperature (550 °C), the structure suffers a reversion giving structural properties similar to the sample melted at 400 °C.

Possible solutions to the $NH_4H_2PO_4$ to $P_2O_5$ conversion, and the resulting structural instability of the glass, would be using a pure $P_2O_5$ or using two step synthesis for reagents like ammonium phosphate glass.

Summary of results.

1. Evidence of a P-F bond is found in the glass structure.

2. The reference glass was identified as pyrophosphate mainly built up from dimers ($Q^1$ end groups) with a smaller presence of $Q^2$ polymeric chains.

3. The high fluoride content of the reference glass induces network depolymerisation in which the F breaks the P-O-P bonds to form monofluorophosphate $PO_3F$ $Q^1$units. This reduces the average length of the phosphate chains and leads to pyrophosphate dimers.

4. A pyrophosphate glass was formed from the reference glass (50 % $SnF_2$ + 20 % SnO + 30 % $P_2O_5$) rather than polyphosphate as expected from the literature. The polyphosphate is generally formed at lower $P_2O_5$ contents.

5. The formation of the pyrophosphate is attributed to the incomplete conversion of the precursor $NH_4H_2PO_4$ during melting, which produces a reduced amount of $P_2O_5$ for subsequent glass formation.

6. Optimum times and temperatures during the melting process were found to be necessary to ensure the complete conversion of $NH_4H_2PO_4$ to $P_2O_5$.

7. Results on properties (like density, Tg, decomposition temperature, chemical durability and rheological) provided in this chapter showed the same trend across the different melting conditions. The higher the melting temperature and time, the better are the properties. In the case of melting temperature, the glass research allowed to set up the recommendation not to exceed a temperature of 550 °C. At this temperature, the glass structure suffered a regression with worse properties.

# Chapter 5 Effect of the processing conditions on TFP glass – PA11 hybrids

A key factor for the improvement of the coating and its overall performance is adhesion. Adhesion is influenced by the morphology, thermal and rheological behaviour of hybrid precursors. The protective performance of the hybrid powder coatings depends on two types of adhesion. One is the adhesion between the surface of the metal substrate and the deposited hybrid material while the other is the interaction between the inorganic and organic phases of the hybrid. This chapter is addressed at the analysis of the important parameters of the hybrid such us processing history, rheological and thermal behavior, chemical composition and mechanical properties performance. These parameters also influence the second type of adhesion (glass – polymer adhesion).

The aim of this chapter is to investigate laboratory-scale processing of materials in order to understand the evolution of hybrid coatings and their properties. The correlation between the hybrid compositions and their properties will provide valuable information on their possible application. As a result, novel hybrids of tin fluoride phosphate (TFP) glass (composition of $50\%\,SnF_2 + 20\%\,SnO + 30\%\,P_2O_5$ were synthesized with polyamide 11 and their morphology, thermal, rheological properties as well as mechanical properties investigated.

Hybridization was achieved by melt blending up to 60 wt% of glass using different compounding conditions (temperature, screw speed and residence time) at a laboratory scale. Scanning electron microscopy showed that the two-phase morphology was greatly influenced by the extrusion temperature profile and the glass content. In addition, transmission electron microscopy was undertaken, and the studies revealed nanoparticles of 40nm.

In order to determine the existence of miscibility between the hybrid components, measurement of the loss tangent, was carried out. The presence of two transition peaks of the loss tangent using Dynamic Mechanical Analysis (DMA) in the hybrid containing high wt% tin fluoride phosphate glass implied an immiscible system showing heterogeneously distributed regions of very different molecular

motilities. The measurements of mechanical properties by DMA showed a reinforcement effect of the glass in the polymer as was reflected by the increase of storage modulus (E') at low and high temperatures in hybrids containing 40, 50 and 60 wt% tin fluoride phosphate glasses. This enabled the achievement of the highest value at 50 wt%. These tensile test studies revealed important results in terms of a mechanical transition from ductile to brittle behaviour at high glass contents.

## 5.1 Processing conditions of the hybrid

Powdered glass samples sieved at 100 µm and the PA11 polymer were used to produce a series of hybrids with different glass and different processing conditions to verify the effect of glass content and processing parameters on the hybridization. The hybrid compositions and processing conditions are listed in Table 5.1.

Table 5. 1: Testing samples composition and compounding conditions.

| Condition | Glass/ wt% | Glass/ vol% | T/ C° | Screw Speed / rpm | Residence Time / s |
|---|---|---|---|---|---|
| 1 | 20 | 8 | 200 | 50 | 5 |
| 2 | 20 | 8 | 200 | 100 | 5 |
| 3 | 20 | 8 | 200 | 200 | 5 |
| 4 | 20 | 8 | 220 | 100 | 5 |
| 5 | 20 | 8 | 240 | 100 | 5 |
| 6 | 20 | 8 | 260 | 100 | 5 |
| 7 | 20 | 8 | 300 | 100 | 5 |
| 8 | 20 | 8 | 250 | 100 | 2 |
| 9 | 20 | 8 | 250 | 100 | 5 |
| 10 | 20 | 8 | 250 | 100 | 7 |
| 11 | 20 | 8 | 250 | 100 | 10 |
| 12 | 10 | 4 | 200 | 100 | 5 |
| 13 | 10 | 4 | 250 | 100 | 5 |
| 14 | 20 | 8 | 200 | 100 | 5 |
| 15 | 20 | 8 | 250 | 100 | 5 |
| 16 | 30 | 13 | 200 | 100 | 5 |
| 17 | 30 | 13 | 250 | 100 | 5 |
| 18 | 40 | 18 | 200 | 100 | 5 |
| 19 | 40 | 18 | 250 | 100 | 5 |
| 20 | 50 | 25 | 200 | 100 | 5 |
| 21 | 50 | 25 | 250 | 100 | 5 |
| 22 | 60 | 34 | 200 | 100 | 5 |
| 23 | 60 | 34 | 250 | 100 | 5 |
| 24 | 0 | 0 | 250 | 100 | 5 |
| 25 | 10 | 4 | 250 | 100 | 5 |
| 26 | 20 | 8 | 250 | 100 | 5 |
| 27 | 30 | 13 | 250 | 100 | 5 |
| 28 | 40 | 18 | 250 | 100 | 5 |
| 29 | 50 | 25 | 250 | 100 | 5 |
| 30 | 60 | 34 | 250 | 100 | 5 |

An important issue with regards to the manufacturing of phosphate glass/polyamide hybrids is the processability of the hybrids during the blending process. The processability of a polymer blend is defined as the ease at which the blend components

can be hot-melt-extruded to deliver a high quality extrudate, free of contamination or defects such as bubbles or unmelted polymer and with high smoothness. The nature of the blend phases played a huge role in determining the processability and the quality of the final extrudate as changes in the processing conditions (screw speed, temperature and residence time) and content of the glass could affect the morphology of the hybrid. Morphology variation can result in change of properties.

Scanning electron microscopy was used to observe the morphology obtained through different processing conditions and glass content in order to choose the optimal composition and processing parameters for the scaling-up of the hybrid.

Due to the low quantity of glass available, different glass batches were used for the morphology experimental work. Morphology of the glass observed by SEM in Chapter 4 is key to understand the development of the morphology.

## 5.2 Glass-polymer morphology

### 5.2.1 Influence of melting procedure of glass

Scanning electron microscopy was used to observe the morphology obtained through different manufacturing processes of glass. Three different manufacturing processes were defined. The detailed description of each process is given below:

1st Process

It is a two-step process, first $P_2O_5$ plus SnO is synthesized at high temperature and then the temperature decreased to add $SnF_2$.

- $NH_4H_2PO_4$+SnO at 900 °C for 30 min
- Add $SnF_2$ at 300 °C, maintain for 30 minutes
- Cool down to room temperature

2nd Process

It is the same process as the first one, except that in this case $SnF_2$ is incorporated like an additive to tin phosphate glass.

- $NH_4H_2PO_4$+SnO at 900 °C for 30 min
- Cool down to 700 °C and stir wasted material
- Grind the glass manually
- Ground glass+$SnF_2$ at 500 °C for 30 min
- Cool down to room temperature

3rd Process

It is one step process with all chemicals synthesized together at low temperature.

- $NH_4H_2PO_4$ + SnO + $SnF_2$ at 450 °C for 25 min
- Cool down to room temperature


Figure 5. 1: Visual aspect of the glass.

The visual aspect of the glass in each process is shown in Figure 5.1. The white colour of the glass from 1st process is due to $SnF_2$ chemicals that remains on the glass surface. The temperature designed for the second step (300 °C) is not enough to mix tin phosphate glass with $SnF_2$. The first process glass was discarded for further studies.

The images (Figure 5.2) revealed different surface aspect and morphology of the glass depending on the melting procedure. The 3rd process glass presented in Figure 5.2d, 5.2e and 5.2f at different magnification (d x800; e x3200; f x12800) showed higher homogeneous dispersion with angular faces. The 2nd process glass presented in Figure 5.2a, 5.2b and 5.2c at different magnification (a x800; b x3200; c x12800) revealed round and porous morphology. This shows evidence of the influence of glass processing conditions on the glass morphology. The round and porous morphology could be the consequence of a premature moisture attack.

Therefore, the 3rd process was selected to carry out the research. It has a simple one step and low temperature manufacturing process that is important from an industrial aspect. The appearance of the glass was satisfactory but, in some cases, small back impurities were detected inside the glass. It is possible these were due to the low quality of the crucibles.

The particle size of the selected 3rd process glass was only measured after it was sieved at 100 µm. The values were between 1 µm and 190 µm. The maximal particle size was bigger than the mesh size due to its rectangular shape. If a rectangle shaped glass

particle has one side smaller than 100 µm and the other one bigger than 100 µm, it can pass through the 100 µm mesh during the sieving.

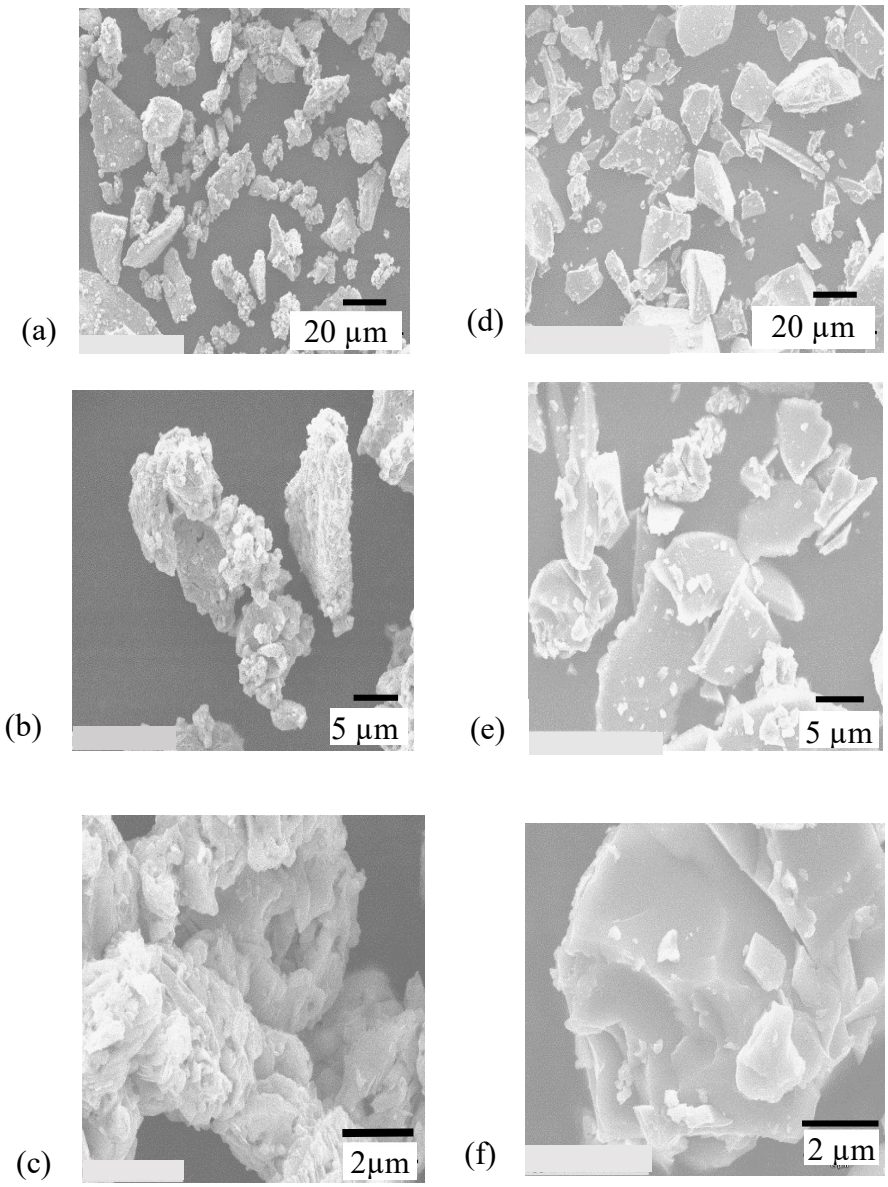


Figure 5. 2: SEM surface aspect micrographs of TFP glass manufactured with different processes. The 2nd process glass morphology at different magnifications: a) x800; b) x3200; c) x12800. The 3rd process glass morphology at different magnifications: d) x800; e) x3200; f) x12800.

A SEM equipped with a microanalysis X detector was used to detect the composition of some black spots present in the glass batches (Figure 5.3). Carbon, oxygen, and fluorine elements were present at a higher rate in the black spots than in the surrounding glass matrix. The presence of C in the black spots suggested residual carbon burned off during the melting in the air.

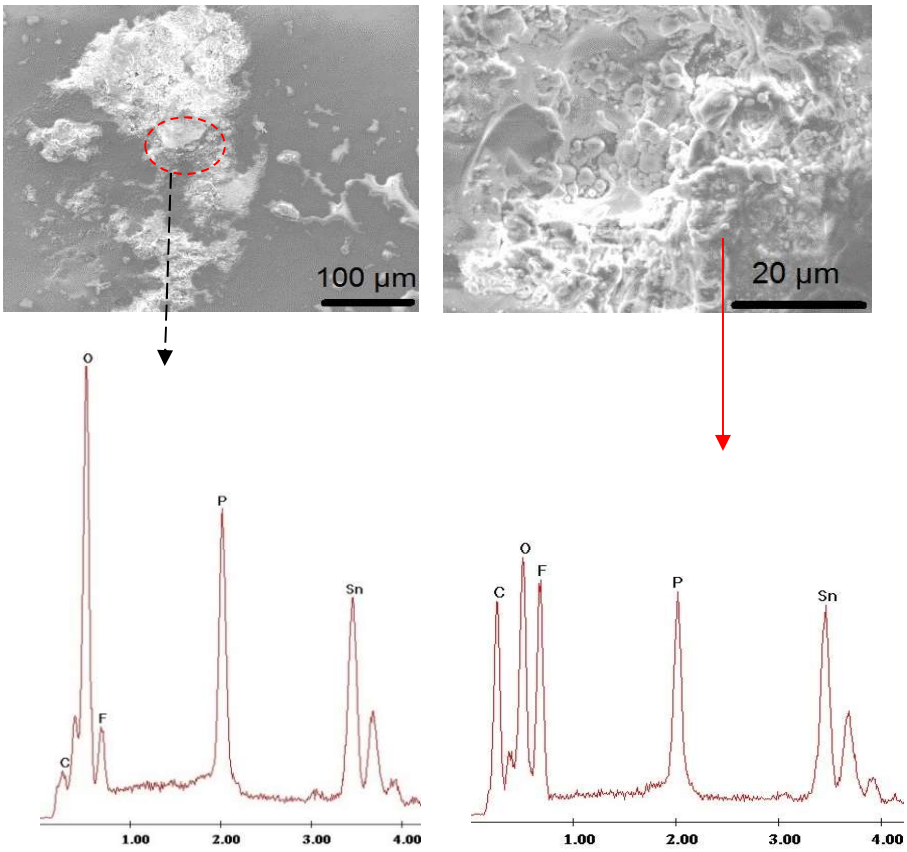


Figure 5. 3: Composition analysis of 3rd process glass by EDX analyser.

### 5.2.2 Influence of extrusion processing parameters on the morphology of hybrid

During the mixing of the blends by the extrusion process, different effects could take place, such as chemical reaction, break-up of the droplets, coalescence and dispersion of the filler that could be homogeneous or heterogeneous. The influential parameters of the extrusion process are analysed below.

*A) Screw Speed- shear rate*

The screw speed is the rotation of the screw measured by rpm (revolution per minute). This parameter is related to the shear rate, which has great influence on the development of the blend morphology. Figure 5.4 shows SEM images for the 20 wt% glass hybrids extruded at 250 °C, 5 minutes of residence time and 50, 100 and 200 rpm of screw speed.

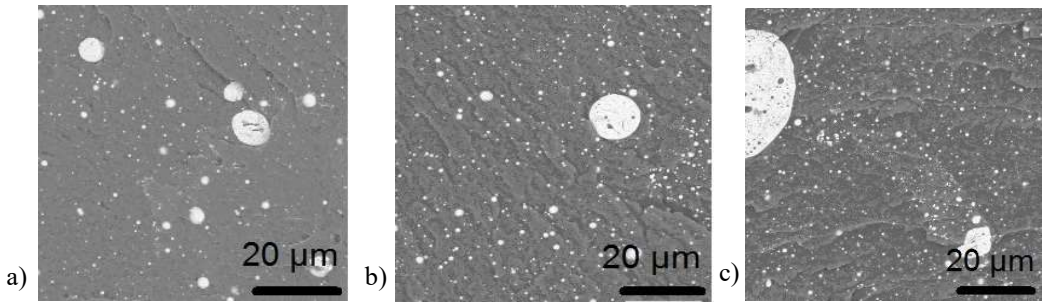

Figure 5. 4: Influence of the screw speed on the hybrid morphology: a) 50 rpm; b) 100 rpm; c) 200 rpm.

Comparative observations of the three trials (Figure 5.4) indicated that at higher screw speed the dispersion is improved, however coarse particles remain in the sample. At a speed of 50 rpm, the presence of a few coarse particles was noted, the largest one measures 90 µm. These coarse particles became less but larger at higher screw speed. At a speed of 200 rpm, particle size reached to about 160 µm.

The initial shape of the glass before compounding is sharp and rectangular and it is shown in Figure 5.2 (e). It is mentioned in section 5.2.1 that the particle size of the glass before compounding is between 1-190µm. At all three screw speed conditions, coarse particles get broken as their size is smaller after compounding.

The coarse particles are due to the heterogeneous dispersion of the filler in the matrix. Micrographs with complete area of the hybrid extrude were added in Figure 5.5 to show the heterogeneity of all samples.

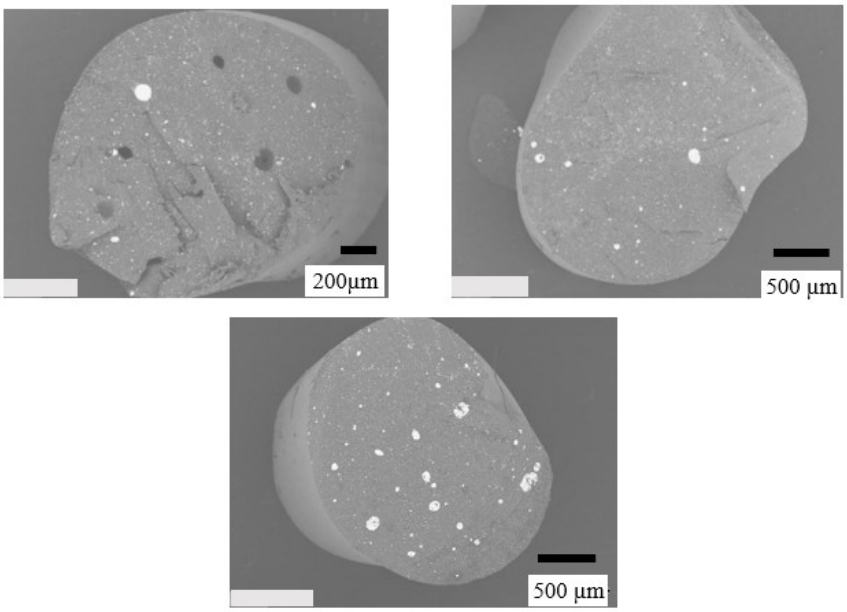

Figure 5. 5: Micrographs of complete surface area of the hybrid at different screw speed: a) 50 rpm; b) 100 rpm; c) 200 rpm.

The Tg of the glass samples used to compound hybrids at different screw speed were measured by DSC. The results showed a Tg of the glass around 145 °C. Therefore, the presence of no broken coarse particles in the hybrids can be explained by an increase of the glass viscosity. The effect of the glass Tg on the complex viscosity of TFP glass was represented in Figure 4.15. The viscosity results were obtained for TFP glass samples with Tg of 104 °C, 125 °C and 150 °C. The coarse particles were related to glass sample viscosity rather than to the screw speed. 100 rpm was chosen as the screw speed for the trials. The screw speed is associated with the shear stress applied and residence time of the composite melt during compounding in extruder. The increase of screw speed causes two different effects:

(1) produces higher shear stress on the melt and thus promotes better distribution of the filler within the polymer matrix resulting in improved mechanical properties.
(2) reduces the residence time of the melt in the extruder causing incomplete melt compounding.

*B) Temperature*

The extrusion processing temperature refers to the temperature of the extruder barrel. Thus, the influence of the temperature on the morphology of hybrids was investigated for hybrids containing 20 wt% glass, extruded at 100 rpm speed, 5 minutes of residence time and varying processing temperatures of 220, 240, 260 and 300 °C, respectively. Figure 5.6 shows SEM micrographs of each condition.

Comparative observations of the four trials indicated that the lower the temperature, the more undesirable and heterogeneous the dispersion becomes. The particle size distribution in the matrix of the hybrid was measured by analysing SEM images from dark particles in the clear matrix. Before calculating the size, the image is thresholded and binarized.

At the extrusion processing temperature of 300 °C, it is observed that a very fine glass dispersion with a particle size ranging from about 0. 17 µm to over 1 µm was achieved. At 260 °C, the dispersion remains relatively fine and particles reach approximately from 0.17 to 4.4 µm in size. The particle size range measured at 240 °C and 220 °C reaches approximately from 0.17 to 30 µm and 0.17 to 60 µm, respectively.

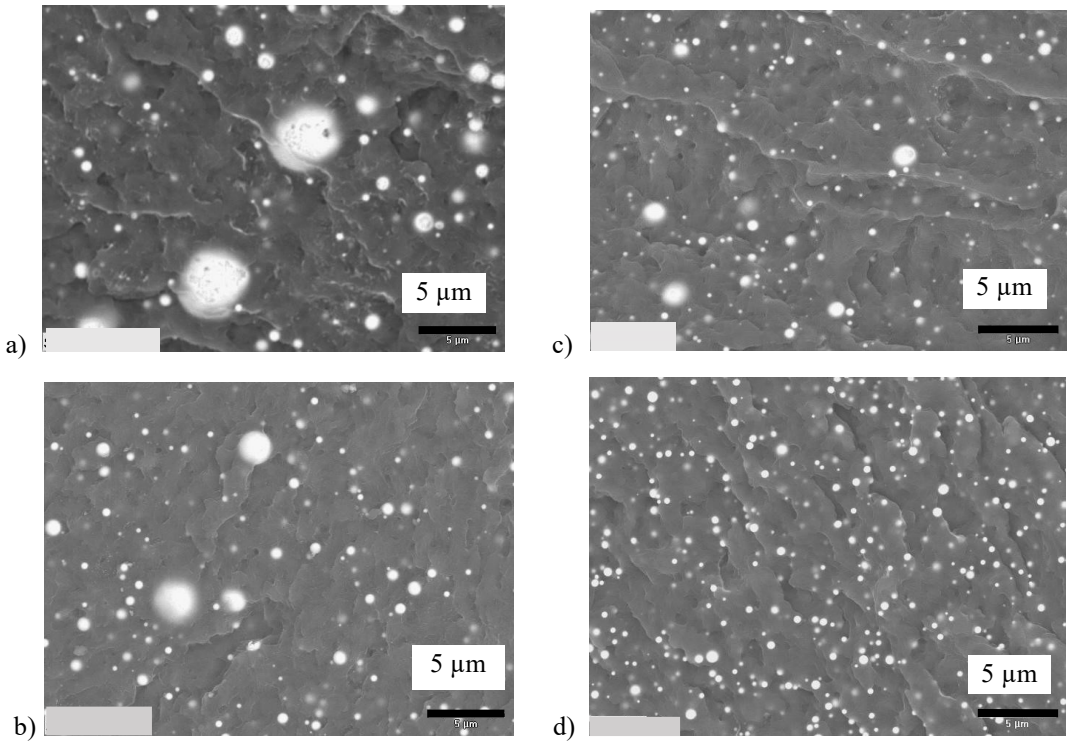


Figure 5. 6: The influence of extrusion processing temperature on the hybrid morphology analysed by SEM micrographs: a) 220 °C; b) 240 °C; c) 260 °C; d) 300 °C.

Large particle size ranges were present in the micrographs of the hybrids for almost all testing conditions, so it was not easy to work with them. In order to interpret and understand the mechanism behind the development of the particle size, the presence of two populations of particles in the hybrids was considered. The micrographs show a bimodal distribution for all hybrids, each hybrid has a very fine particle distribution together with a very coarse one. For easier interpretation, a range for each distribution was quoted. Particle size between 0-900 nm was considered as fine particle distribution and all sizes above 900 nm, coarse particle distribution.

The particle size distribution of different processing temperatures was plotted in Figure 5.7 to identify the trend of the morphology mechanism. One temperature per graphic was presented.

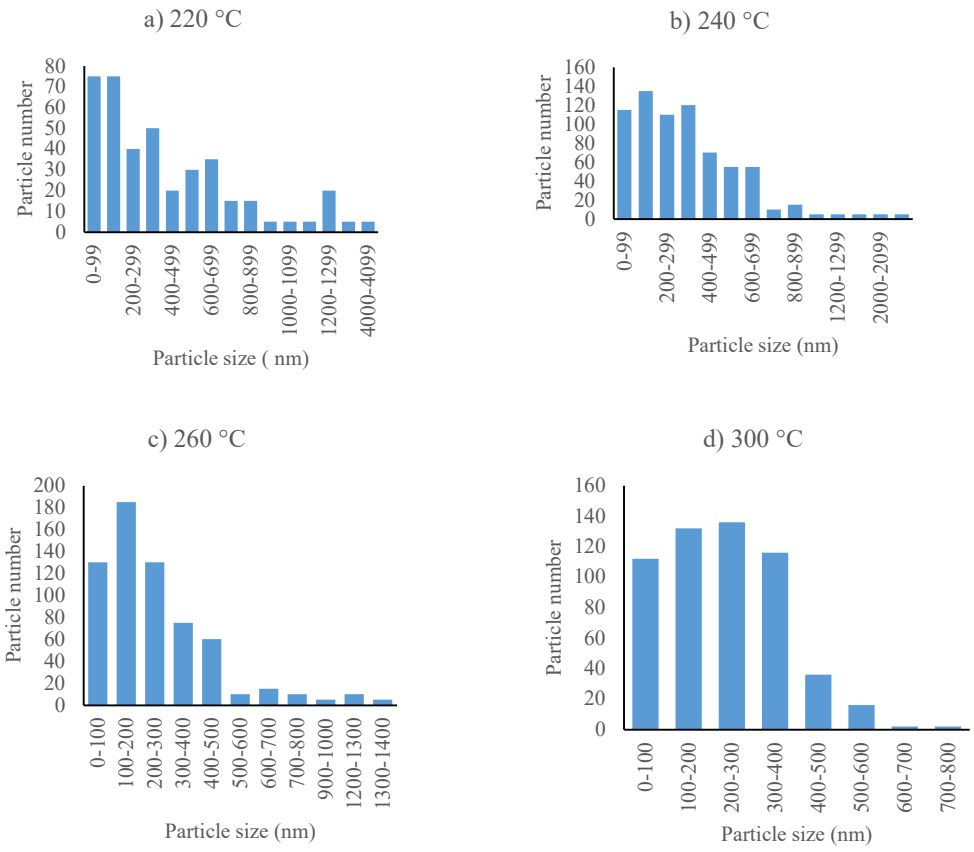


Figure 5. 7: Number frequency histograms showing bimodal particle size distribution of TFP glass-PA11 hybrids processed at different processing temperatures: a) 220 °C; b) 240 °C; c) 260 °C; d) 300 °C. The particle size data is based on the image analysis of more than 500 particles.

Transmission electron microscopy (TEM) was carried out to observe the size of the glass particles in the matrix at a smaller scale and to study the nanoscale structure of the hybrid. The sample used for TEM was extruded at 300 °C processing temperature and its structure is shown in Figure 5.8. Figure 5.9 shows a TEM micrograph for polyamide 6-TFP glass reported in the literature [6]. Both hybrids show a two-phase microstructure morphology, where glass is distributed in droplets. The smallest observed particle in PA 11 matrix was 40 nm and 70 nm in PA6 matrix. The smaller nanoparticles in the PA11 matrix are attributed to their higher processing temperature. The spherulitic structure was observed in the matrices of both PA 11 and PA6. The difference between the two materials is due to the higher degree of crystallinity and glass content of PA 6.

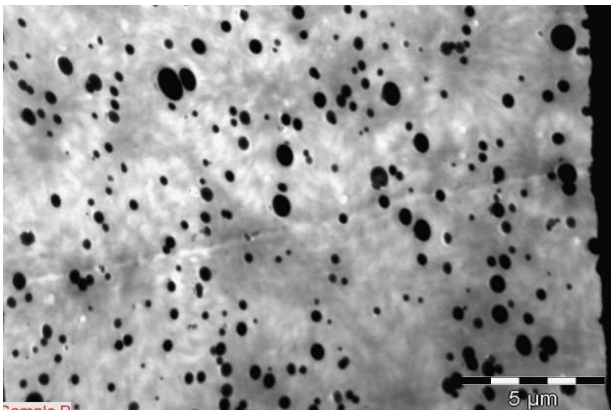


Figure 5. 8: TEM micrograph of dispersed glass particles in polyamide 11 hybrid indicating the presence of sub-100 nm particles of 20% (6 vol%) TFP glass- polyamide 11 hybrids.

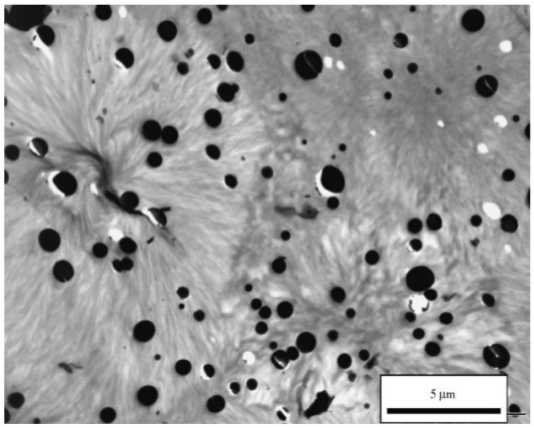


Figure 5. 9: TEM micrograph of 10 vol% P glass- Polyamide 6 hybrid [6].

*C) Residence time*

The residence time is the average length of time during which the material is under compounding. The influence of the residence time on the morphology of the hybrids was investigated for 20 wt% glass hybrids. The samples were extruded at 100 rpm, and 250 °C of processing temperature using 2\5\7 and 10 minutes of residence time. Figure 5.10 shows the micrographs and Table 5.2 shows the particle size measured for each condition. How the particle size was determined is explained in Chapter 3 (Section 3.4.6.1).

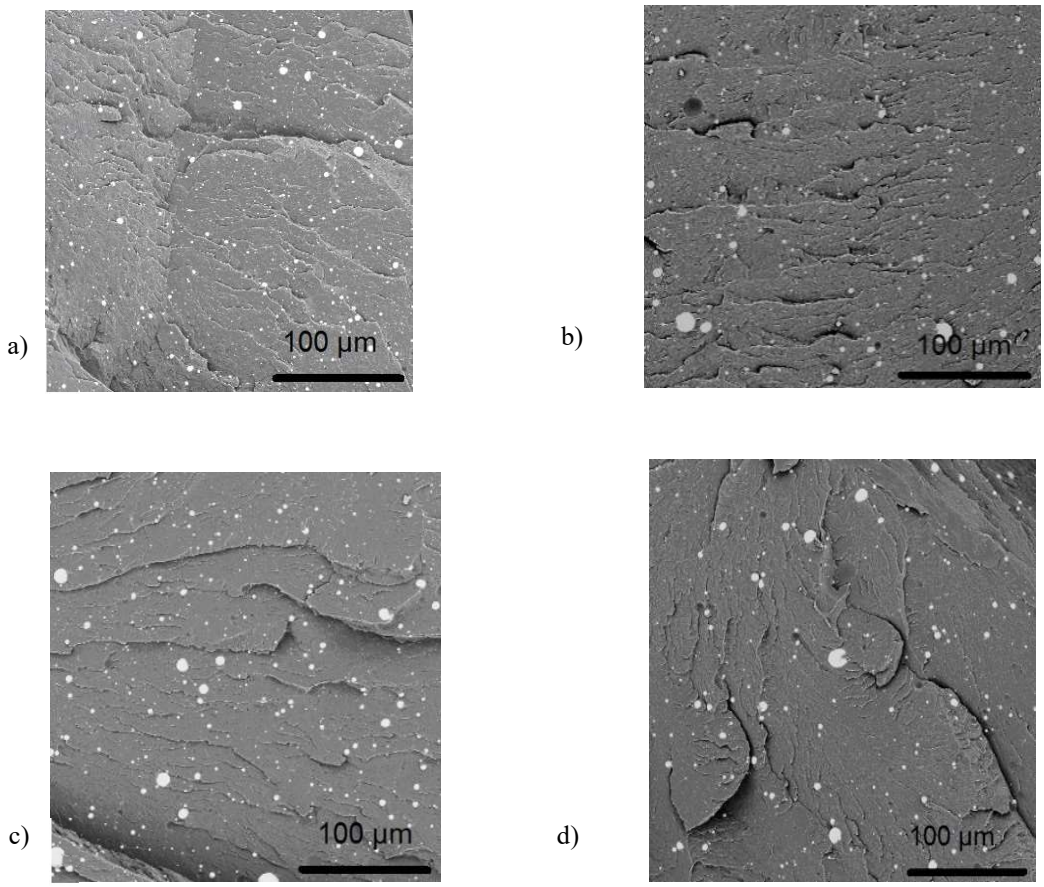


Figure 5. 10: The influence of residence time on the morphology of the hybrid analysed by SEM micrographs: a) 2 minutes; b) 5 minutes; c) 7 minutes; d) 10 minutes.

The comparative observations of tests at different residence time showed similar dispersion. Slightly finer and more homogeneous dispersion was obtained for shorter residence times (2 and 5 minutes), but no specific trend was found. Whatever the residence time was, coarse particles were present in the hybrids. The presence of coarse particles can be explained by the heterogeneous dispersion of the filler. The powder was sieved with 100 µm mesh. The coarse particles were smaller than the mesh size. The size of the glass particles is between 1 µm and 190 µm and they have a sharp and rectangle shape. They have not been broken down, rather than they have grown. They have softened because they now have a round shape. A value of 5 minutes residence time was fixed for the following testing after no specific trend was found. According to these results the residence time does not have any influence on the morphology development of the hybrid.

Table 5. 2: Glass particle size of different residence time hybrids measured by SEM image analysis.

| Residence time /min | Particle size / μm |
|---|---|
| 2 | 0.4- 13 |
| 5 | 0.4 – 44 |
| 7 | 0.7- 16 |
| 10 | 0.6- 30 |

The research of the effect of extrusion processing parameters on the morphology showed that the processing temperature was the most influential parameter. The great influence of the temperature on the morphology will have a high impact on the final properties of the material. It is known too that the filler content is a key parameter for the final properties of the new material and the processing conditions of the mixture. Thus, it is necessary to investigate more in depth, firstly the effect of the temperature and glass content on the morphology of the hybrids and then to evaluate material properties such as Tg, mechanical properties, thermal properties, fire resistance and rheological properties to analyse the processability of the material. These properties are important for further understanding of the hybrid behaviour in the coating application.

### 5.2.3 Influence of the processing temperature and glass content

The influence of the glass content at two different temperatures on the morphology of the hybrids was investigated for hybrid compositions containing 10/ 20/ 30/40/ 50 and 60 wt% glass. All compositions were extruded at a screw speed of 100 rpm and a residence time of 5 minutes. The micrographs for each condition are shown in Figure 5.11.

Initially, the processing temperature was set as 200 °C (all the micrographs placed on the left-hand side of Figure 5.11) Comparative tests at different contents of glass showed heterogeneous dispersions for low contents at 10 and 20 wt% TFP glass (Figure 5.11a and 5.11b on the left-hand side). For 30 and 40 wt% P glass content (Figure 5.11c and 5.11d on the left-hand side) the dispersion was refined even if it still remained heterogeneous. The dispersion at 50 wt% P glass (Figure 5.11e placed on the left-hand side) became very fine with a few large particles. Thus, it was suggested that at 50 wt% P glass, the fine and homogeneous morphology was attributed to processing parameters variability, such as higher processing temperature during compounding. In

contrast for 60 wt% P glass (Figure 5.11f placed on the left-hand side) the dispersion was very rough. The micrographs of SEM at 200 °C of processing parameters revealed optimum dispersion at 50 wt% glass. But the morphology becomes finer after 30 wt % P glass. It was observed that holes were present at low and high content of glass. This phenomenon was no longer observed at a content of 50%. This could include interaction between components at 50 wt % P glass.

A higher temperature of 250 °C was then selected for processing the hybrid, 250 °C is the usual processing temperature for PA 11. The comparative observations at different content of glass using a processing temperature of 250 °C (all the micrographs placed on the right-hand side of Figure 5.11) showed relatively coarse dispersions for low glass content, (10 and 20 wt %, Figure 5.11a and 5.11b on the right-hand side), which were then refined from 30 and 40 wt% (Figure 5.11c and 5.11d on the right-hand side). The finest morphology was observed at 50 wt% (Figure 5.11e placed on the right-hand side) as well as 60 wt% (Figure 5.10f placed on the right-hand side). These dispersions are significantly finer than those observed previously at a processing temperature of 200 °C. For contents from 10% to 40% (Figure 5.11a, 5.11b 5.11c and 5.11d), it was noticed that particle sizes > 1 µm were of irregular shape while those < 1µm were perfectly spherical. However, due to the excessive different sizes, image analysis does not provide an accurate measurement for small particles. The average values of bimodal particle size distribution are shown in Table 5.4, where lower size particles are obtained at 250 °C for all compositions as it was shown in micrographs. To interpret better the influence of the processing temperature and glass content on the morphology, Figure 5. 12 was plotted.

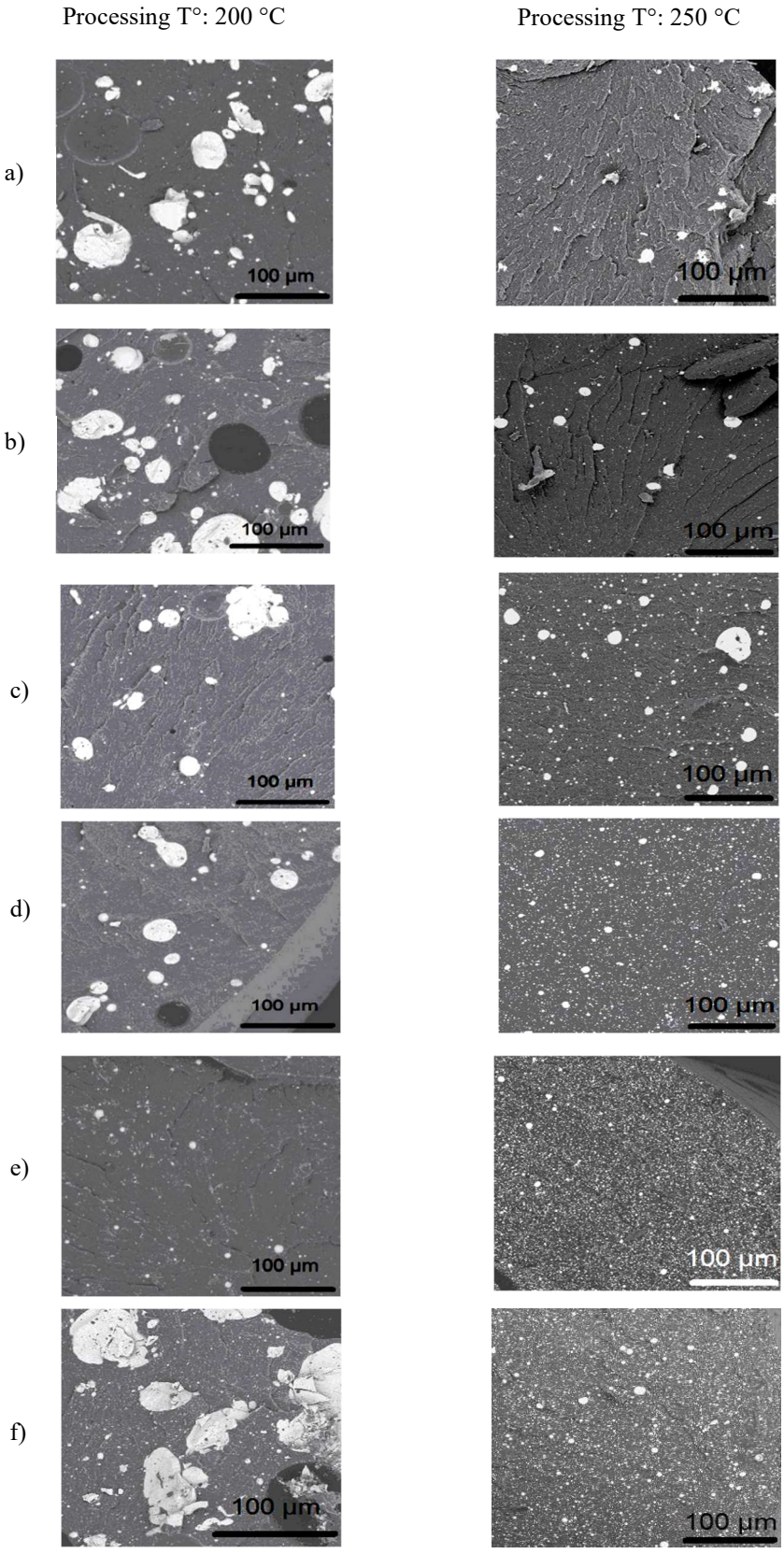


Figure 5. 11: The influence of the processing parameters and glass content on the morphology of the hybrid processed at 100 rpm and 2-5 minutes loading up to 60 wt% TFP glass at 200 °C and 250 °C, a) 10wt%; b) 20wt%; c) 30wt%; d) 40wt%; e) 50wt%; f) 60wt%.

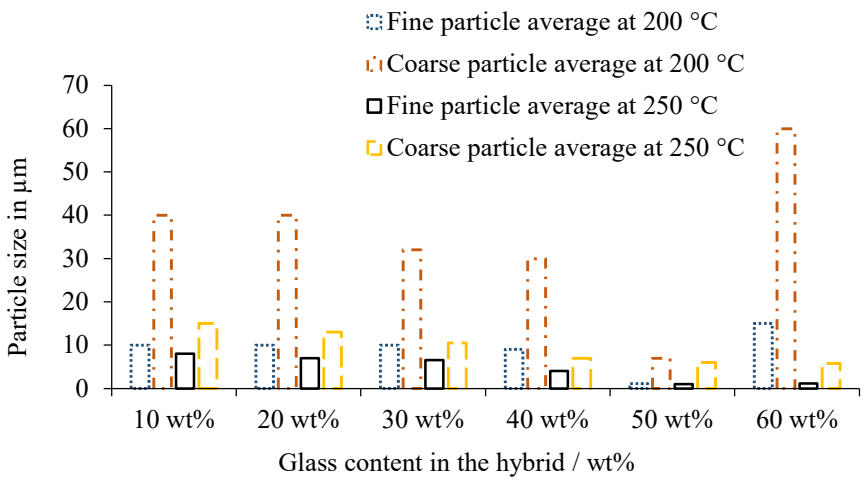


Figure 5. 12: Particle size distribution graphics at different processing temperatures and glass content.

The adherence between glass particles and polyamide matrix was investigated for the hybrid filled with 0-60 wt% glass extruded at 250 °C to find evidence of interaction. Polymer-glass adherence at almost all contents of P glass with fracture of the glass particles was noted (Figure 5.13). Some glass particles suffered fracture, whilst other particles were pulled-off from matrix.

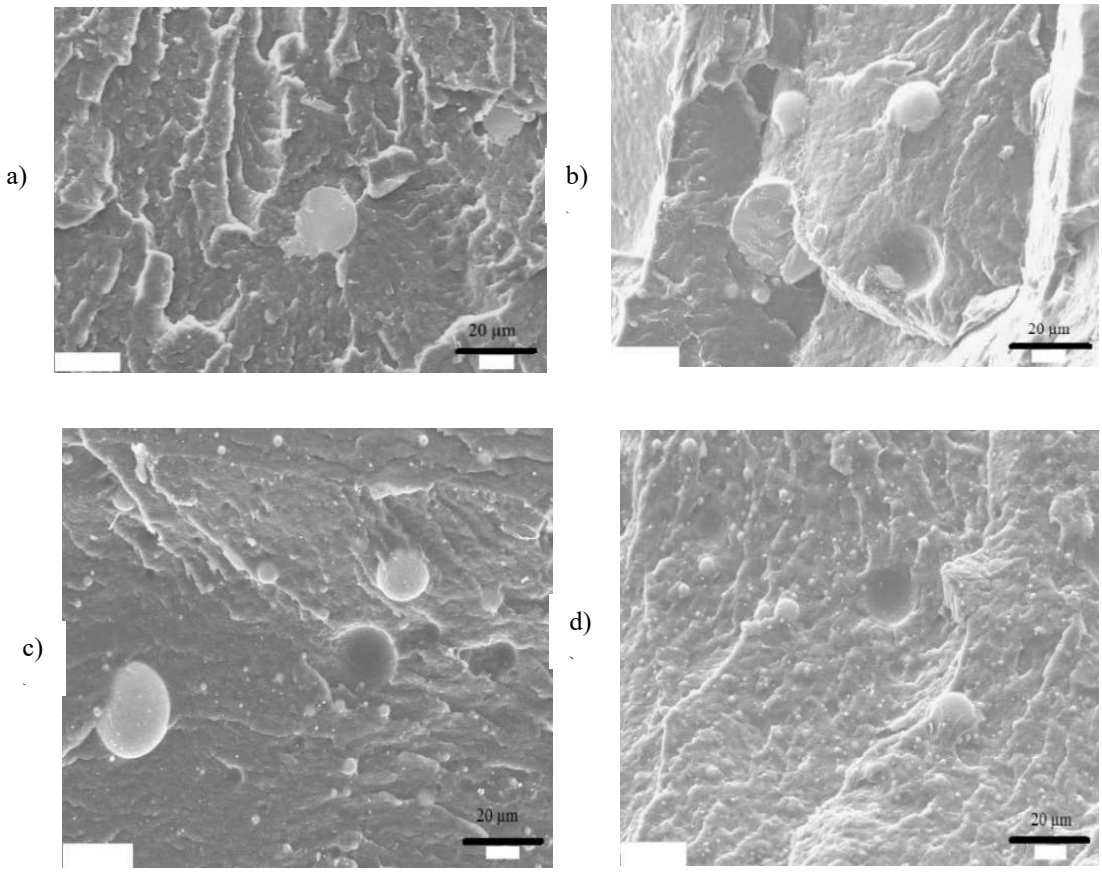

e)

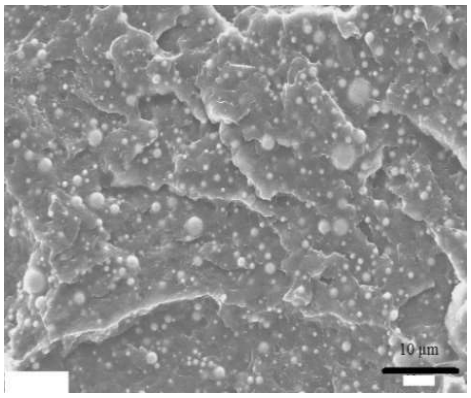


f)

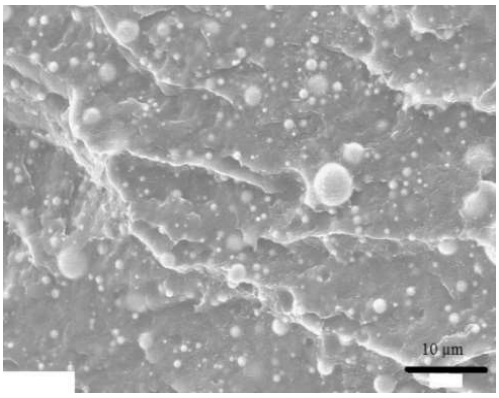


Figure 5. 13: Evaluation of TFP glass particles adherence to PA11 matrix by SEM in hybrids processed at 250 °C of processing temperature, 100 rpm of screw speed and 5 minutes of residence time with different glass content: a) 10 wt%; b) 20 wt%; c) 30 wt%; d) 40 wt%; e) 50 wt%; f) 60 wt %.

Considering processing temperatures of 200 °C and 250° C, better dispersion at higher temperature was obtained, achieving the best in both cases at 50% of glass in weight. The glass morphology changes from original angular particles to smaller and rounded particles in the polymer matrix, which is governed by the viscosity ratio of glass to polymer**.** The microstructural changes result from the break-up of the particles under the influence of thermal and shearing compounding conditions. The viscosity, the shear rate and interfacial tension have a great influence on the morphology. The underlying mechanism which influences glass content is currently unclear. However, by increasing processing temperature from 200 °C to 250 °C, the viscosity of the glass melt is expected to reduce significantly. The viscosity of the glass at 200 °C was not measured, but the effect of the temperature on the rheological properties of TFP glass was already studied in Chapter 4, section 4.9. In figure 4.13, a major decrease of complex viscosity against the temperature was described as an important factor for hybrid morphology development under thermal and shearing conditions. This favour the breakdown of the droplets and improves the homogeneity of glass dispersion.

## 5.3 Glass transition temperature of the hybrid

Dynamic mechanical analysis (DMA) measures the cyclic response of a material as a function of the temperature. Figure 5.14 shows a graph of the loss modulus of different glass content hybrids and its individual components against temperature. The curves of loss modulus give information about the Tg of material (Section 3.4.2.3). The Tg results of tested materials were summarized in Table 5.3. It is evident in these curves

that as TFP glass is added to the polyamide 11, the Tg of the polyamide 11 suffers a decrease. It appears that the glass is acting as a plasticizer. The Tg of PA11 in hybrids decreases, by a maximum of 10 °C, for low glass content (≤ 40 wt%) or remained almost unchanged as in the case of the hybrids containing high glass content, 50-60 wt% P glass. Additionally, the glass transition peak is observed for the pure glass component in the hybrid for high glass content, ≥ 30 wt% glass, which appears between 140 °C and 155 °C. The chain mobility becomes more pronounced by increasing weight % P glass.

There are some types of phosphates like phosphate esters that are used as plasticizers for several polymers [93]. Phosphates are usually small molecules. Although the initially TFP glass was considered as a polymer, the study carried out about glass melting conditions shows that TFP glass has a structure composed of almost dimers.

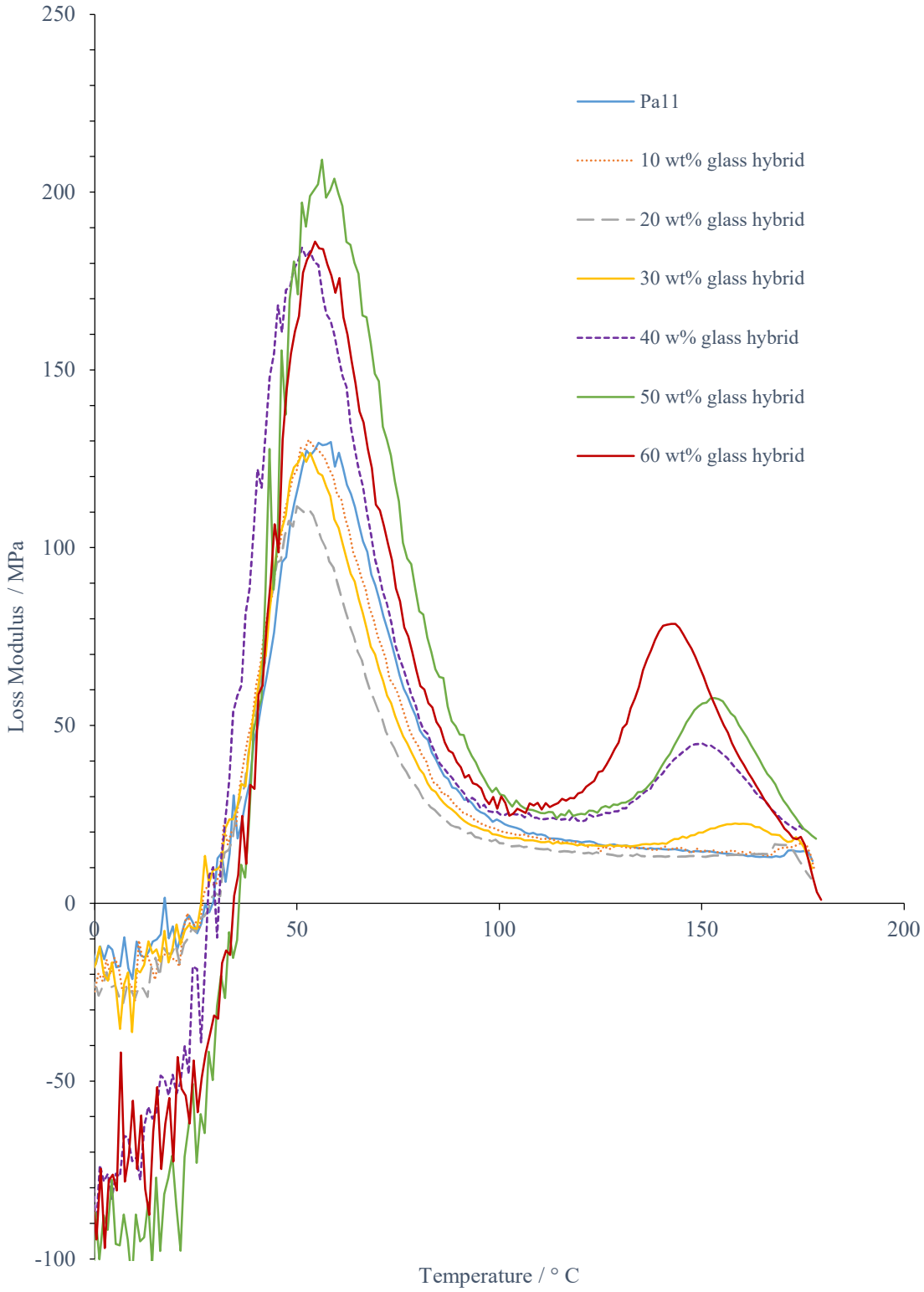


Figure 5. 14: Loss Modulus versus temperature from dynamic mechanical analysis for different glass content hybrids.

Table 5. 3: Glass transition temperature of the hybrid materials resulting from DMA.

| Glass / wt% | Glass / vol% | PA11 Tg / °C | TFP glass Tg / °C |
|---|---|---|---|
| 0 | 0 | 58 | - |
| 10 | 4 | 53 | - |
| 20 | 8 | 48 | - |
| 30 | 13 | 51 | - |
| 40 | 18 | 51 | 152 |
| 50 | 25 | 56 | 153 |
| 60 | 34 | 56 | 142 |

The appearance of two transitions is the result of the heterogeneously distributed region of very different molecular mobility. As the two peaks could be associated with the two hybrid components, the DMA results showed an immiscible hybrid system at high TFP glass filler loading of more than 40 wt%. A partially miscible hybrid system for all other P glass ratio was conjectured. The literature shows some evidence of the failure of general polymer blend miscibility rules- such as Fox and Gordon Taylor equations for hybrid materials [6]. These equations predict a glass transition temperature value that is between the glass transition temperatures of the individual components. Urman and Otaigbe demonstrated, by studying P glass/ polyamide 6 hybrids, evidence of miscibility between hybrid components, showing that, even the Tg of polyamide 6 decreases in DMA results, Figure 5.15 [6]. Although the blend system does not follow the general polymer prediction, systems at loadings ≤ 20 wt% show an approximately linear decrease in Tg. Thus, they might follow the common relation for polymer-plasticizer blends [6]. The second Tg is not in the literature because the highest glass loading is less than 13 vol% (30 wt%) and the second Tg appeared after 30-40 wt% glass. Figure 5.14 shows the same behaviour as described in the literature (Figure 5.15) up to 13 vol% (30 wt%) glass content. The first Tg assigned to PA 11 decreased from 58 to 48 °C with a loading of 20 wt% of TFP glass.

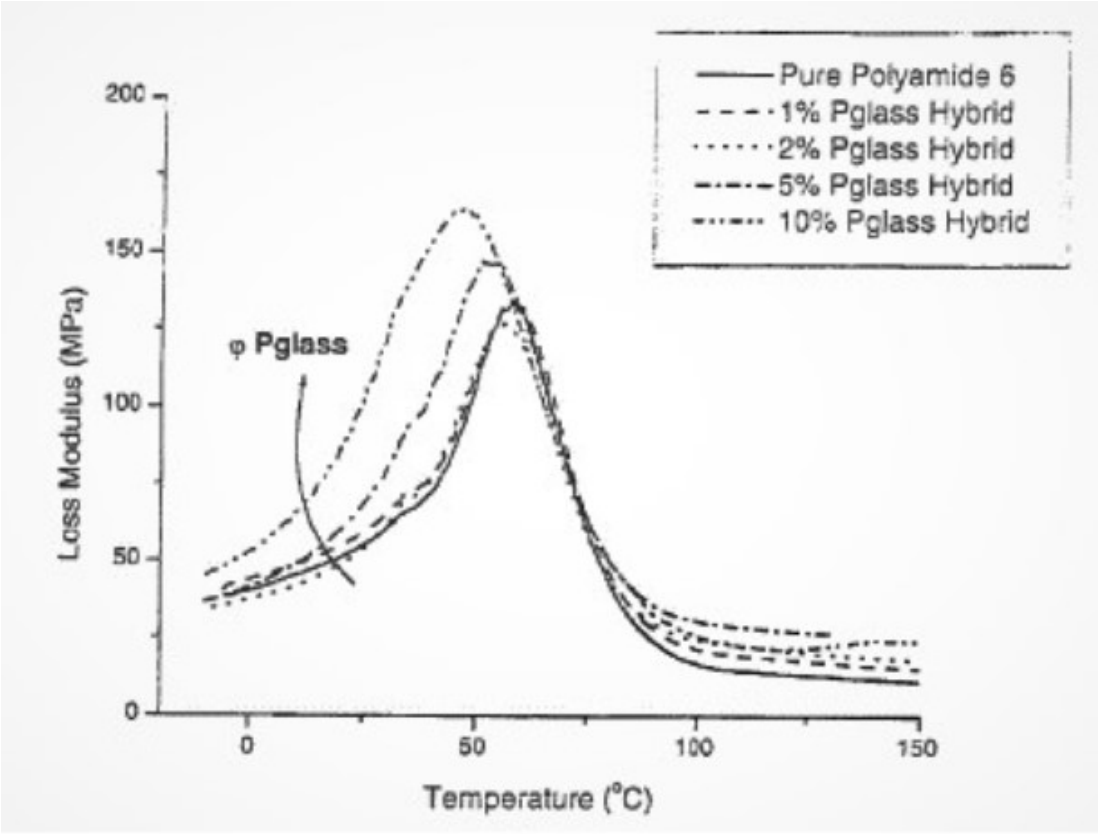


Figure 5. 15: Torsional DMA results of loss modulus versus temperature for the P glass- PA6 hybrid materials with indicated P glass content [93].

Since it was impossible to produce glass samples for DMA, the first conjectures were done comparing DMA to DSC results, a partially miscible system for < 30 wt% P glass and immiscible system for > 30 wt% P glass showing two Tg-s. A missing interpretation of the system for > 30 wt% P glass was found as the shift of the Tg of the individual components could not be determined accurately. The shift of the glass Tg at lower or higher temperatures could suggest interaction between components and a partially miscible system. The Tg of the hybrid measured by DMA has higher value than those measured by DSC (PA 11 Tg 48 °C and glass Tg 125 °C). There is a frequency effect which puts the mechanical (ca. 1 Hz) Tg about 17°C higher than that for a DSC measurement (ca. 0.0001 Hz) and assumed activation energy of 400 kJ/mole (typical for polymer Tg).

## 5.4 Mechanical properties

### 5.4.1 Dynamic mechanical properties

The dynamic storage modulus E' was calculated to measure the change in stiffness of the samples as reported in Section 3.4.2.3. The samples were tested at a temperature range of -50 to 200 ˚C and at a frequency rate of 1 Hz.

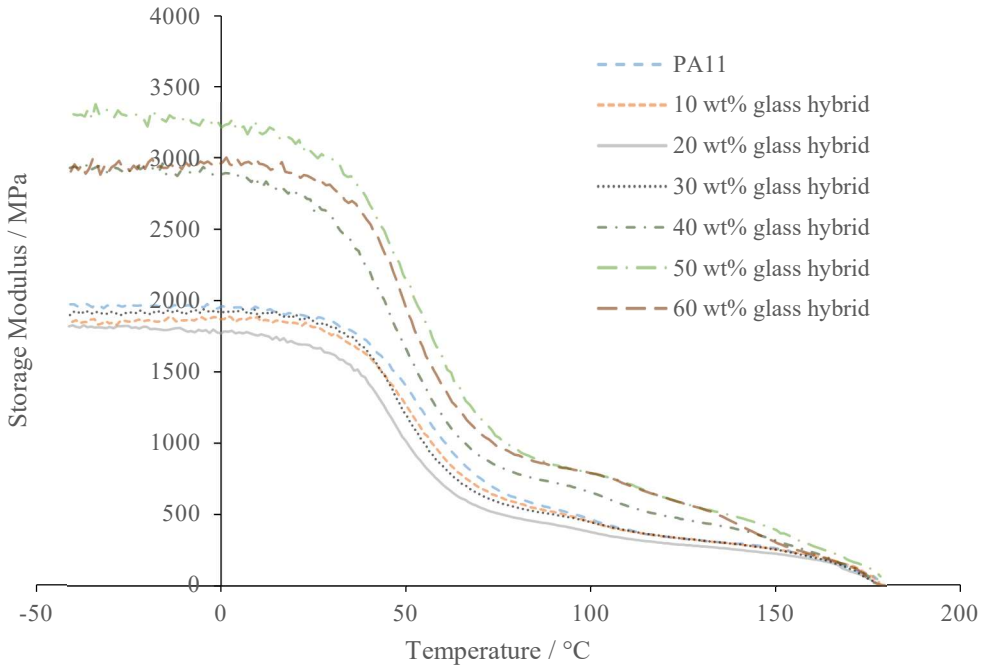


Figure 5. 16: E' (Storage modulus) results of TFP glass- PA11 hybrids with different glass weight percent.

The dynamic mechanical analysis was carried out on dumbbell samples (ISO 527 ABA) containing different amounts of glass (Table 5.1, condition 24 to 30). The storage modulus data (E') of the hybrids is plotted in Figure 5.16. The substantial peak at around 140-150 °C seen in Figure 5.14 does not present itself in Figure 5.16 because different things are plotted in these graphics. In Figure 5.14, the loss modulus is plotted that is related to the chain movement giving information about the Tg of the material. In case of Figure 5.16, the storage modulus is plotted that is related to the elastic modulus of the material. The storage modulus, either E' or G', is the measure of the sample's elastic behaviour. In general, the incorporation of rigid filler particles to the neat polymer matrix should result in a reinforcement effect. An increase of storage

modulus (E') in a wide range of test temperatures describes the existence of a reinforcement effect in the composite.

The pure polyamide 11 and 10, 20, 30 wt% TFP glass hybrids have essentially the same or very similar storage modulus values. An increase of E' at several temperatures after 40 wt% P glass can be distinguished recording the maximum value at 50 wt% P glass. Figure 5.17 summarizes the storage modulus (E') data of the hybrids collected at 23 °C and 150 °C. The standard deviation of measured values was ±0.9.

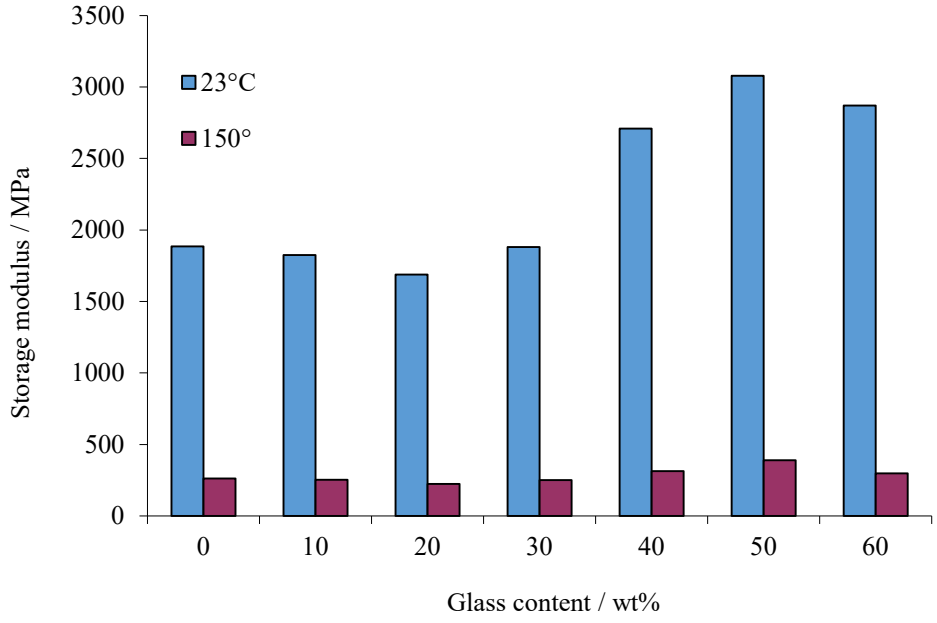


Figure 5. 17: Storage modulus versus different TFP glass content hybrid materials at two temperatures, 23 °C and 150 °C, from DMA.

Results at both temperatures, low and high, show the same evolution of E' values against the glass content. The phenomena responsible for the increase of E' of the hybrid could be chemical or physical. The chemical interaction may result in bonding by chemical reaction of the hybrid components obtaining a new structure and, therefore, new properties in the material. The physical interaction is related to particle ordering in the polymer matrix called agglomeration or percolation. The glass forms a network in the matrix increasing stiffness of the material. It is common that high filler loading composites processed by melt mixing method, using conventional processing techniques, suffer a particle agglomeration or percolation effect.

## 5.4.2 Static mechanical properties

The stress strain values of the hybrids are shown in Table 5.4 and the typical Stress-Strain curve of hybrids in Figure 5.18. Three samples of each condition were tested.

Table 5. 4: Stress and strain values of hybrids.

| Glass content / wt% | Glass content / vol% | Elastic Modulus / MPa | Tensile Stress / MPa | Deformation at break / % |
|---|---|---|---|---|
| 0 | 0 | 1007 ± 37 | 34 ± 1 | 319 ±31 |
| 20 | 8 | 1056 ± 21 | 34.8 ± 0.1 | 290±41 |
| 50 | 34 | 1086 ± 208 | 36.9 ± 0.8 | 53±28 |

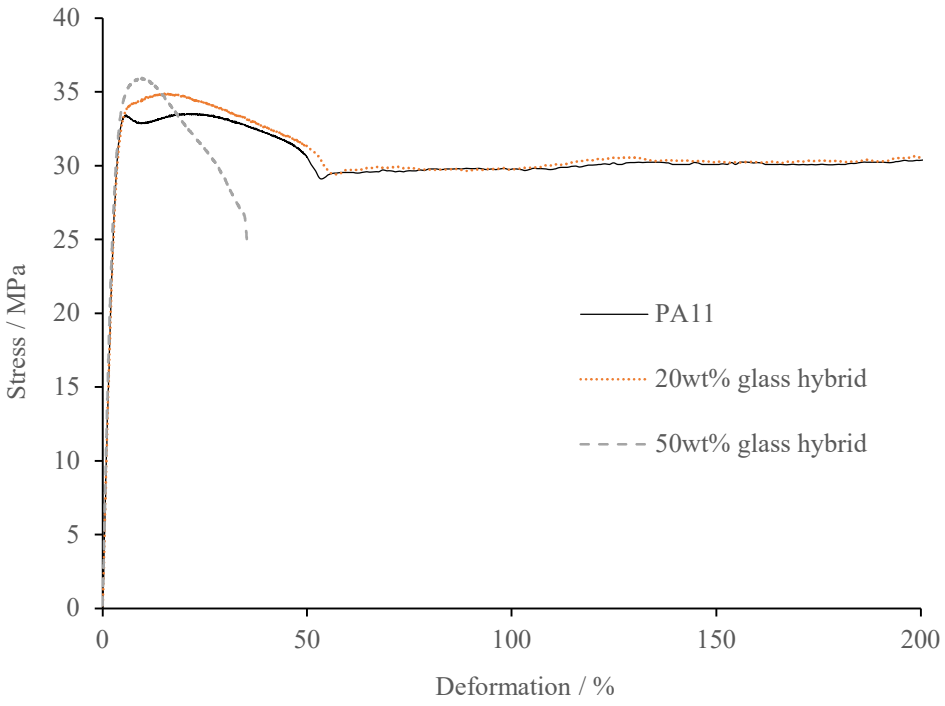


Figure 5. 18: Stress/ Strain curves of TFP glass - polyamide 11 hybrids.

The stress strain curve shows that the glass influences the mechanical properties of the hybrid. At 50 wt% glass content the hybrid changes its behaviour suffering a pronounced decrease of material ductility. Moreover, with the 20 wt% of glass hybrid the change is slight; this is similar to the pure polymer. The curve of pure polyamide 11 is consistent with the behaviour of a pseudo ductile material showing clear evidence of yield stress, followed by a slight monotonic increase in stress with increasing strain

as the material approaches failure. The elastic modulus is similar in the three cases. TFP glass does not appear to influence the elastic modulus or the stiffness of the material.

In contrast to results shown in the literature, the research reveals a different effect of the glass in the polymer matrix. Further, a slight reinforcement effect of glass was found in the polyamide 11. In the case of the polyamide 6 a plasticiser effect was described. Figure 5.19 shows the typical stress strain curves of TFP glass and polyamide 6 hybrids [6].

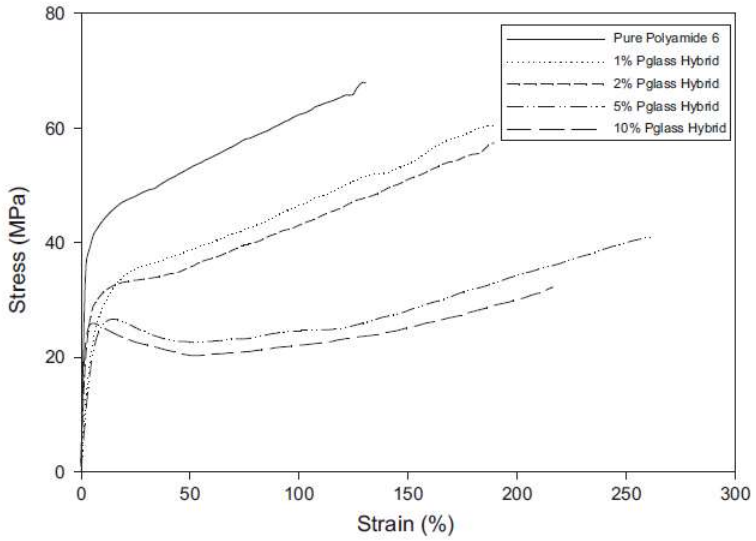


Figure 5. 19: The typical Stress/Strain curves of P glass- PA 6 hybrids [6].

The pure polyamide 6 and the hybrid with less than 2% in volume of glass (~10 wt%) present a typical curve of viscoelastic materials, being concave to the strain axis and showing no clear evidence of yield stress. The curve shows typical plasticized polymer behaviour after 2% in volume of glass. The hybrids behave as pseudo ductile materials with clear evidence of yield stress. There are two main points that can explain the difference between the current research results and those from the literature:

1. The increase of the viscosity over time of PA 11 (influence of the catalysis).
2. Different values of viscosity for the same glass (Figure 5.20- 5.21). In the literature, the complex viscosity is between $10^1$-$10^2$ and in this study between $10^2$-$10^3$. As shown in Chapter 4, this suggests that these glasses have different structures and so the final products could have substantially different properties.

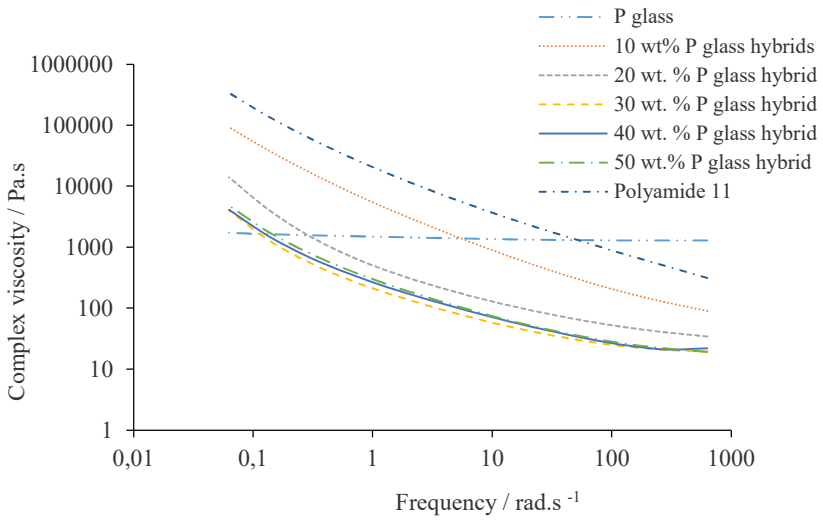


Figure 5. 20: Frequency dependence of the complex viscosity of PA11 hybrids at 250 °C.

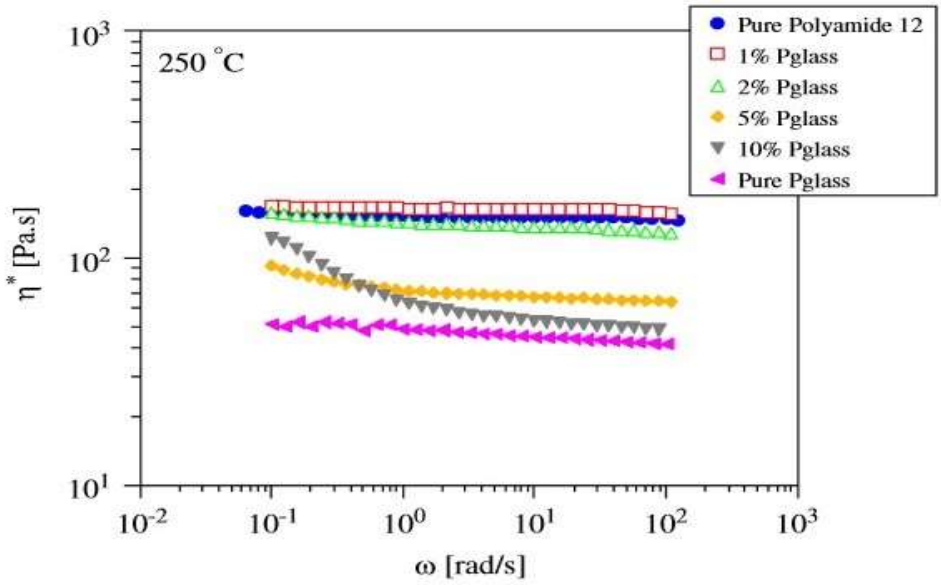


Figure 5. 21: Frequency dependence of the complex viscosity of polyamide 12 hybrids at 250 °C [3].

## 5.5 Thermal properties

The thermal stability of neat polyamide 11 and tin fluoride phosphate glass hybrids has been investigated by TGA under nitrogen using the heating rate of 10°C/min as shown in Figure 5.22. The onset is gradually improved with the concentration of TFP glass. The best thermal properties and decomposition temperature were obtained for the hybrid containing 40 wt%, Figure 5.23. Different content of TFP glass was detected before (wt%) and after (volatiles % + degradation step % + residue %) extrusion

processing. The residue% is representative of inorganic material and after extrusion process, the test showed less glass than before processing.

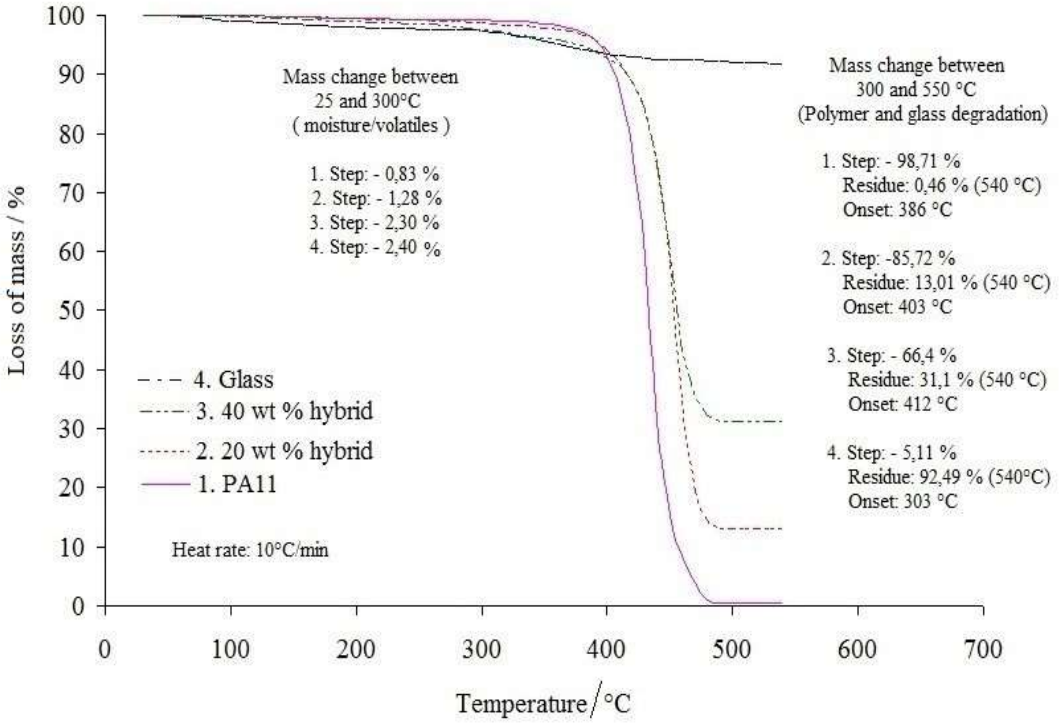


Figure 5. 22: Thermogravimetric analysis of PA11, TFP glass and 20, 40 wt% glass hybrids in nitrogen flow at 10 °C /min heating rate.

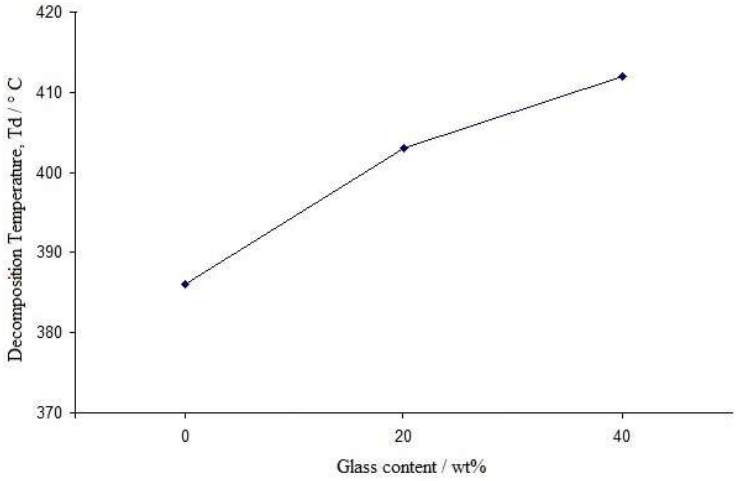


Figure 5. 23: Thermal stability characterized by decomposition temperature as a function of TFP glass concentration.

The thermal properties of the glass are greatly influencing the final properties of the hybrid. The improvement of thermal stability of PA11 by incorporating TFP glass is

probably due to the superior thermal stability of glass particles, which promotes the stability of the polymer matrix via the formation of protecting layers or chars during decomposition process [93]. But it could be also due to the interaction between components.

## 5.6 Fire resistance

The fire resistance test according to UL 94 was performed on PA11 and hybrids filled 0-60 wt% glass. The test results shall be classified either V-0, V-1 or V-2 (V= vertical burning), in accordance with the criteria indicated in Chapter 3 - Table 3.5. Note that it is a similar procedure to UL 94 due to the limited material quantity available. The test was carried out on five dumb-bell samples according to ISO 527 BA. It is known that some phosphate glasses have excellent flame resistance as was mentioned in the literature review. Some phosphate glasses behave as fire retardants. Thus, they can be use in thermoplastics, thermosets, textiles, and coatings to inhibit or resist the spread of fire. The improvement of fire resistance could be advantageously exploited in coating applications. There are several applications where high pressures and temperatures dictate the use of fire-resistant material to mitigate the potential for dangerous and expensive fires.

Interesting behaviour was noticed during the tests. The hybrid samples did not ignite. It was also observed that the product (TFP glass hybrid) flowed rapidly with many drops. Cotton placed at the bottom of the test burned for hybrids filled with 10 and 20 wt% glass. In the case of 30, 40, 50 and 60 wt% glass hybrids, there were drops but there was no combustion of the cotton. The vertical burning test classification results are shown in Table 5.5.

Table 5. 5: The vertical burning test classification results of PA11 and hybrids filled 0-60 wt% glass.

| Hybrid glass/ wt% | Vertical burning test classification |
|---|---|
| 0 | V2 |
| 10 | V2 |
| 20 | V2-V1 |
| 30 | V0 |
| 40 | V0 |
| 50 | V0 |
| 60 | V0 |

Results showed that the glass loadings of 10 and 20 wt% were insufficient to achieve a V0 rating for these hybrids. However, glass loadings of 30, 40, 50 and 60 wt% did achieve the UL94 V0 rating. In conclusion, a major improvement in fire resistance was found in hybrids with 30-60 wt% glass. This has substantial potential for industrial applications.

## 5.7 Rheological properties

The rheological properties of a polymer blend play an important role in determining its final morphology. This morphology along with some other parameters, would determine the final properties of the product, classifying the product suitable or not for the selected application, in this case powder coating. Rheology is also important in determining the processability of both polymer blends and composites [158].

The rheology of blends reveals useful information regarding the changes in fluidity, morphology, viscoelasticity, molecular orientation, thermal and melt stability. Through an understanding of these concepts and how the properties of the blends are affected by particular thermal, temporal, and shear conditions, one can manufacture materials with desired properties suitable for industrial applications [159, 160].

The rheological experiments of the hybrids were also restricted to 230, 250 and 270 °C as in rheological experiments of the glass in chapter 4- section 4.9. Typical melt processing temperatures of PA 11 were selected to develop an understanding of hybrid processing technology.

The observations showed that PA11 was thermally unstable under test conditions, while glass is stable. The pure TFP glass behaves like a Newtonian fluid, whilst PA11 behaves as a non-Newtonian material, increasing its viscosity over time and in both cases having the same behaviour over the whole range of tested temperature (Figure 5.24 and Figure 5.25). The fact that the viscosity of the PA11 increases is due to the catalysis, and the viscosity of the glass decreases over the temperature might result in an interesting morphology. For coating application is desirable that the material flows sufficiently fast to form a uniform layer and quickly regain high viscosity.

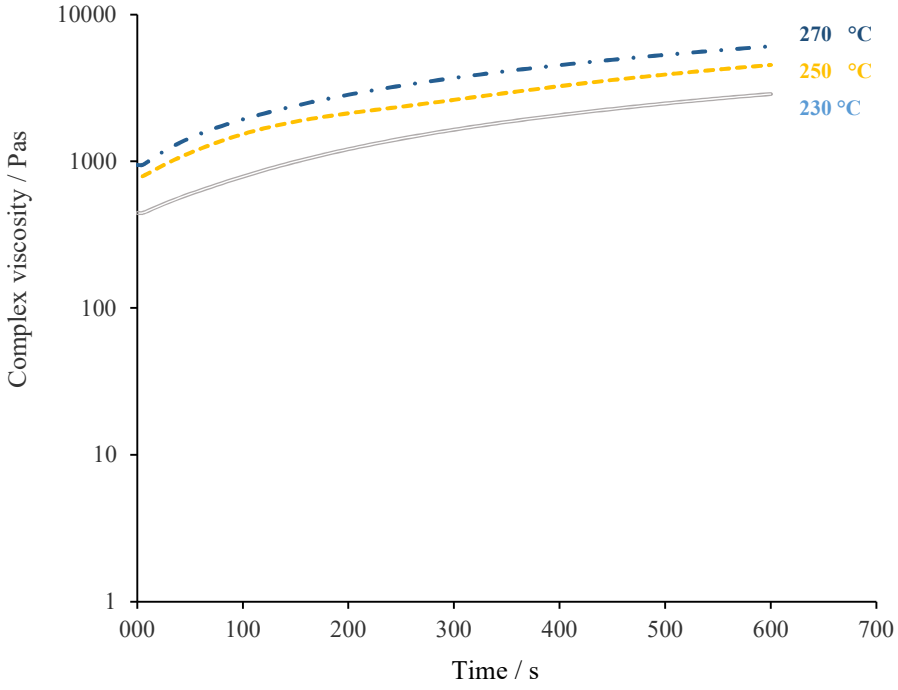


Figure 5. 24: Time dependence of the complex viscosity of PA11 at 230, 250 and 270 °C.

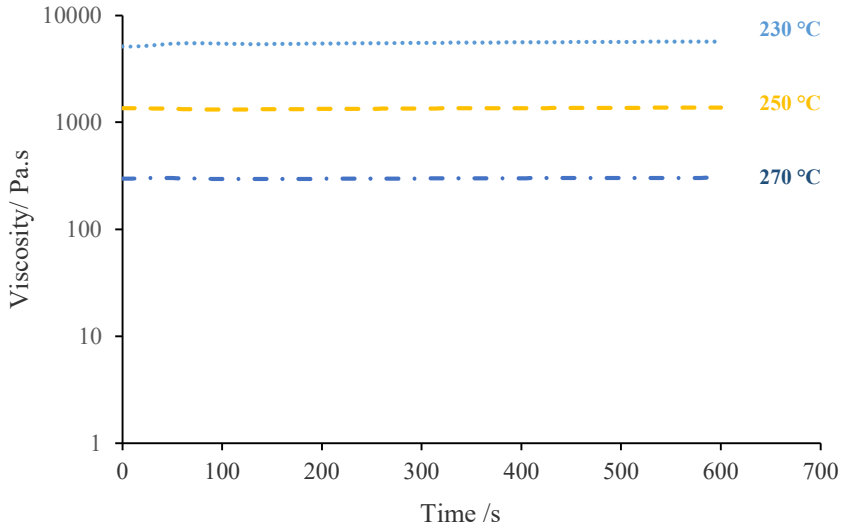


Figure 5. 25: Time dependence of the complex viscosity of TFP glass at 230, 250 and 270 °C.

Time dependence of the complex viscosity of 20 and 40 wt% glass - PA11 hybrids at 230, 250, 270 °C are shown in Figure 5.26 and 5.27. The curves show an increase of the viscosity along time depending on the glass content. It seems that the Newtonian behaviour of the glass is more dominant than the pseudoplastic one at 230 °C, giving a stable viscosity along time. At temperatures of 250 and 270 °C the non-Newtonian behaviour is predominant.

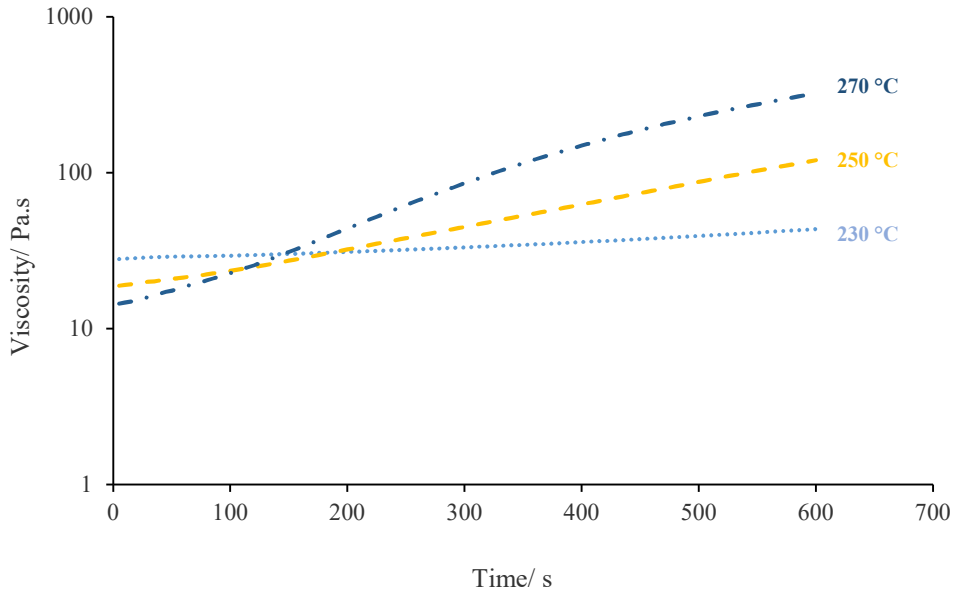


Figure 5. 26: Time dependence of the complex viscosity of 20 wt% TFP glass- PA11 hybrid at 230, 250 and 270° C.

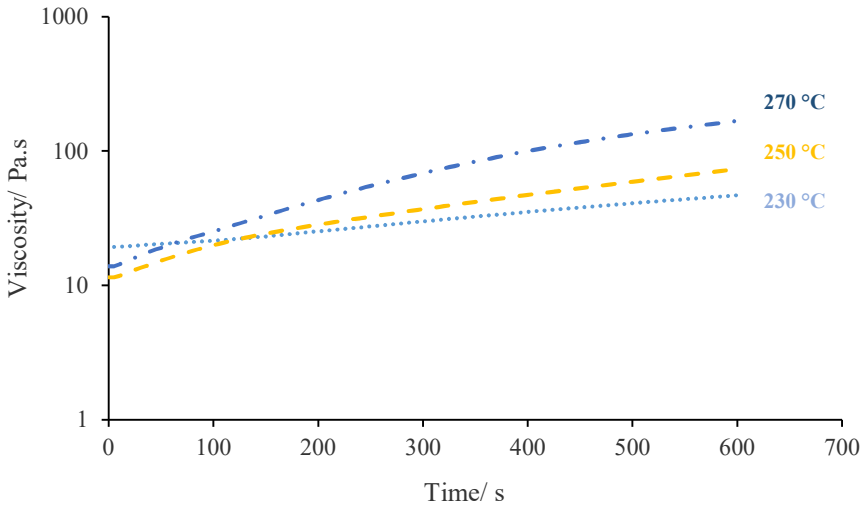


Figure 5. 27: Time dependence of the complex viscosity of 40 wt% TFP glass-PA11 hybrid at 230, 250 and 270 °C.

It was noticed that a large decrease of viscosity took place by the addition of glass. The decrease of viscosity might display desirable interactions that are beneficial in a number of applications as reported in the first rheological study of TFP glass/polymer hybrid as performed on PA12/ P glass [6]. The large decrease of viscosity is expected to benefit good processability and enable higher glass contents to be incorporated in the hybrids.

## 5.8 Final remarks

(a) Overview

The research carried out in this chapter provides substantial information defining the most influential processing parameters. The morphology of the hybrid was observed under extrusion processing parameters, such as screw speed (shear rate), temperature, residence time and glass content. The characterization to determine the optimal extrusion processing parameters of the hybrid at laboratory-scale was done by microscopy. Morphologies using different glass contents and processing parameters were compared and properties such as Tg (by DMA), rheological, mechanical (DMA and Tensile test), thermal (TGA) and fire resistance measured. The major effect was shown by two parameters (temperature and glass content) on the development of the hybrid morphology.

The optimum processing temperature for the development of P glass/polyamide 11 hybrid is calculated in Chapter 6 using the rheological properties of the individual components of the hybrid measured here, from a Newtonian – non-Newtonian (increase of viscosity over time) system. However, the characterization results show that > 30 wt% P glass content is necessary to obtain an improvement in the properties over PA11 matrix.

(b) Summary of Chapter 5

1. Tin fluoride phosphate glass with the molar composition of 50% $SnF_2$ + 20 % SnO + 30 $P_2O_5$ was synthesized with polyamide 11 by melt blending up to 60 wt% of glass by changing the glass content and compounding conditions. Widely different morphologies were produced because of the possible interaction among the components.
2. SEM analysis of the hybrids revealed a major influence of extrusion processing temperature and glass content on the morphology. Evidence of compatibility and adherence between the hybrid components was found resulting from the reduction of the phase dispersed due to possible interaction.
3. Better homogeneity and dispersion of particles in the hybrids were detected at high temperatures and high glass loadings. The optimum conditions will be identified in the next chapter.

4. The glass transition temperature characterization by DMA showed an immiscible hybrid system in the hybrid loaded with 60 wt% tin fluoride phosphate glass. The appearance of two transition peaks is the result of heterogeneously distributed regions of very different molecular mobilities. A clear phase separation of the hybrid components was found at this glass content.

5. An increase in the storage modulus (E') measured by DMA at low and high temperatures was found at hybrid loadings of 40, 50 and 60 wt% tin fluoride phosphate glass and revealed a reinforcement effect related to physical or chemical interactions between the hybrid components.

6. Tensile testing showed that the elongation at break was reduced as the glass content increased, something that is generally observed in glass-reinforced polymers. The reinforcement effect found in the DMA testing was not evident in the tensile test results due the variation of elastic modulus in the samples.

# Chapter 6 Morphology development of TFP glass- PA11 hybrids

## 6.1 Morphology considerations

The morphology is the study of form and structure of materials. In the specific case of polymer morphology, it could be defined as the study of order within macromolecular solids.

There are several ways to produce nanostructured material, some of them are sol-gel, coupling agents and reactive compounding. During this study, a new way to produce nanostructured material composed of phosphate glasses and polymers was studied. The objective was to mix glass macroscopic fillers into polymeric matrix by the melt mixing technique and obtain well-dispersed particles. Thermal-shearing conditions of the extrusion compounding and reported affinity between TFP glass and PA11 were key considerations in this objective. The viscosity and interfacial tension of hybrid components are expected to be influential parameters in explaining the mechanism of nanoparticle formation and determining the optimal conditions.

Some theoretical approaches have been carried out to identify the morphology development mechanism for TFP glass/ PA11 hybrid. Firstly, the two steps of the mechanism were observed by scanning electron microscopy. The first step is the obtaining of microparticles from the macroscopic ones and the second one is from microparticles to nanoparticles. The interfacial tension was then calculated to define Ca (Capillary number) and, together with viscosity ratio, used to examine the type of droplets breakup mode during extrusion. The glass Tg and the processing temperature of the hybrid are two parameters that can be controlled in the system. These two parameters have a great influence on the viscosity, which is one of the key parameters for morphology development. Finally, a diagram was developed, to define the optimal processing temperature for obtaining a nanostructured morphology between P glasses and polymers. SEM images of the morphology of the hybrid have been shown in Chapter 5.

The morphology with nanosized particles was observed. As phosphate glass is considered polymeric in nature, this was expected to aid making an immiscible polymer blend. The morphology development of immiscible polymer blends during processing is well documented, especially in the case of dilute blends with Newtonian components and subjected to shear flow. In Chapter 5, rheological results show a non-Newtonian behaviour for PA11 matrix and Newtonian behaviour for glass. Newtonian droplets in a viscoelastic matrix has been studied since the pioneering studies of Flumerfelt. It is reported [135] that the critical capillary number and the break-up time increased with increasing elasticity of the matrix fluid. The challenge is to demonstrate that due to the peculiar characteristics of phosphate glass- polyamide 11 hybrids, it is possible to predict the morphology of the hybrid using the deformation and break-up of single Newtonian droplets in a Newtonian medium as tackled theoretically and experimentally by Taylor and Grace [135].

This type of blend represents an out of equilibrium situation and its morphology depends strongly on particular processing conditions. Therefore, a new method to predict the morphology of nanostructured material composed of phosphate glasses and polymers is developed. Thermal-shearing conditions of the extrusion compounding, different (low-high) Mw components and reported affinity between TFP glass and PA11 are key points in the process.

## 6.2 Homogeneity of the dispersion of the glass in melt mixing

A requirement in material development is to predict how additives affect the performance of the material and it is of crucial importance the way these additives are distributed inside the material. In formulating the polymer blend (nanocomposites) the challenge is to control the blend morphology. This section is focused on developing a method to predict P glass- polymer system morphology.

Homogeneity of the dispersion of the glass during processing is governed by the viscosity ratio, that is the ratio between the dispersed phase viscosity and matrix viscosity. The viscosity of each component at different temperature has already been analysed in chapter 5.

The morphology of this kind of system is highly dependent on the processing conditions and the properties of both components. The homogeneity of the dispersion

of the glass is highly dependent on the viscosity of the components. If the processing conditions and the properties that influence viscosity can be identified, it might be possible to build up a diagram that will allow the prediction of morphology.

The effect of the processing conditions on the properties of tin fluoride phosphate glass-PA11 hybrids was studied in Chapter 5. The results reveal that the viscosity of the components is highly influenced by processing temperature. Rheological measurements were undertaken at 210, 230, 250, 270 and 290 °C to check behavioural changes in the viscosity. These changes have impact on the morphology as will be shown later by SEM micrographs at different processing temperature.

The effect of the properties of hybrid precursors on the viscosity has been studied. Two main properties were identified, the Tg of the glass and polyamide 11 grade. Chapter 4 shows how the Tg of the glass varies considerably depending on the melting conditions of the glass and the changes in the Tg of the glass affect values of viscosity. The viscosity against the temperature of three glasses with different Tg (Glass 1: Tg 104 °C, Glass 2: Tg 124 °C, Glass 3: Tg 150 °C) and three different polyamide 11 grades (LMNO Grade 1: PA 11 without catalysis, BMNO grade 2: PA11 with catalysis and T Nat B grade 3: PA 11 for coating application) are selected to evaluate the influence of the components viscosity in the hybrid morphology evolution. The only difference between these grades is the catalysis of the PA11. Higher viscosities are shown by glasses with higher Tg. The difference on the viscosity of polyamide 11 grades is due to the use of a catalyser for synthetizing the polymer. It is fundamental to understand the mechanism of the morphology development under the parameters that have effect on the viscosity to choose a suitable processing temperature and appropriate properties of the components in each case. Figure 6.1 gives a diagram that provides the key to achieve homogeneous and fine morphologies. This can include nanosized particle formation and could help later to interpret material characterization results.

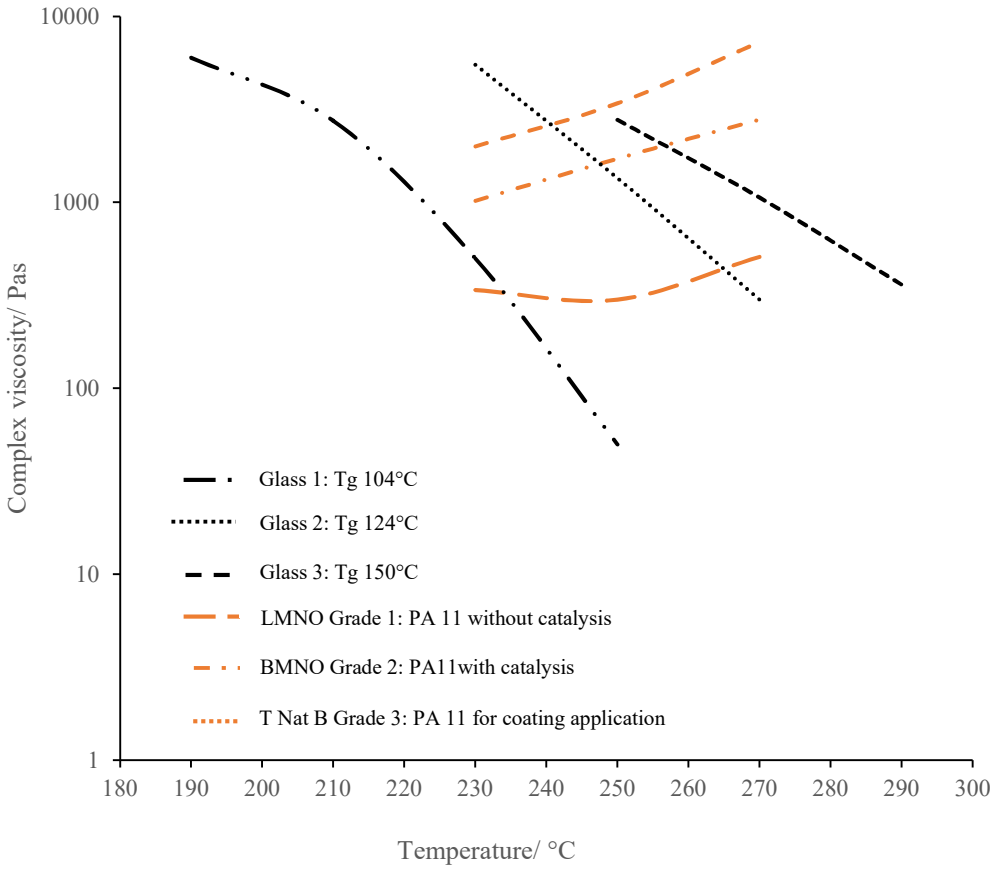


Figure 6. 1: Viscosity versus processing temperature of hybrid individual components. Morphological behaviour diagram.

For example, a polymer with complex viscosity of 50 Pas, liquid at 250 °C, will be an effective choice for TFP glass with Tg 104 °C. The hybrid system would be likely to provide a nanostructured hybrid material under suitable processing conditions. The glass with Tg 124 °C will leave the vitreous-fluid state approximately at processing temperature of 290 °C and the glass with Tg 150 °C at temperatures higher than 300 °C. These two are a good combination to obtain homogeneous morphology.

BMNO grade 3 polyamide 11 and TFP glass with Tg 124 °C were selected to check the veracity of the method by observing the hybrid morphology by SEM at different conditions. This type of unstable system greatly depends on the morphology of the dispersed phase, which is controlled by the viscosity ratio during processing. Three possible conditions for viscosity ratio with their respective processing temperature can be described from Figure 6.1.

The first condition was defined as $\eta\ (\eta_d/\eta_m) \gg 1$, and can give a heterogeneous dispersion with large particles at hybrid processing temperature < 245 °C. The second condition is $\eta = \eta_d = \eta_m = 1$. At this condition, a homogenous and fine dispersion can be achieved, and nanoparticles could appear. The hybrid processing temperature is between 245 °C- 255 °C, the crossing point of both components. The third one is $\eta\ (\eta_d/\eta_m) \ll 1$, where coalescence can be reached at hybrid processing temperature >255 °C.

One temperature for each condition that has viscosity data of the matrix and the dispersed phase was then chosen. Viscosity ratio$(\eta_d/\eta_m)$ at these temperatures was calculated and is shown in Table 6.1.

Table 6. 1: Viscosity ratio of TFP glass-PA11 hybrids at different temperatures.

| | Viscosity /Pas | | |
|---|---|---|---|
| Temperature | Glass Tg 124 °C | PA11 BMNO | Ratio |
| 230 | 5545 | 1020 | 5.44 |
| 250 | 1600 | 1600 | 1.00 |
| 270 | 300 | 2780 | 0.11 |

Finally, the morphology of the hybrid BMNO PA11 grade 2 - TFP glass (Tg 124 °C) at these three conditions was evaluated by SEM (Figure 6.2). PA11 filled 30 wt% TFP glass hybrid samples were extruded by 150 rpm screw speed and 5 minutes of residence time at temperatures of 230 °C, 250 °C and 270 °C.

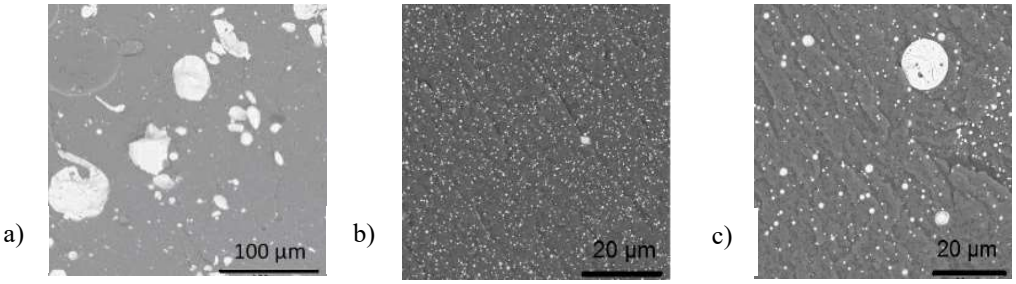


Figure 6. 2: SEM micrographs of hybrid extruded by 150 rpm of screw speed, 5 minutes of residence time and at different processing temperature: a) 230 °C; b) 250 °C; c) 270 °C.

The feasibility of the diagram to predict the morphology of polymer- low Tg phosphate glass hybrid system was checked by SEM micrographs in Figure 6.2. When the viscosity ratio is higher $\eta\ (\eta_d/\eta_m) \gg 1$, or lower $\eta\ (\eta_d/\eta_m) \ll 1$, then one heterogeneous dispersion was obtained and will affect the final hybrid product. In

blends, often a close viscosity between the dispersed phase and matrix is researched to achieve homogeneous dispersion, like in this case, where the best dispersion is obtained when $\eta = \eta_d = \eta_m = 1$ (Figure 6.2 b). The dispersed phase is fragmented in small spherical droplets, with regular form and homogenous dispersion. At this point, there is a possibility of forming nanoparticles in the polymer matrix, as both materials are fluid. However, this is not enough, because materials with viscosity higher than 50 Pas are in vitreous state. This means that for developing nanoparticles in the polymeric matrix, it is necessary to choose hybrid precursors with reported affinity between them. The diagram in Figure 6.1 increases the possibility of nanoparticle formation by describing the optimal processing conditions for each polymer glass combinations. For example, the optimal processing conditions for glass with Tg 124 °C (melted at 450 °C for 25 minutes) and BMNO grade PA11 were found to be approximately 250±5 °C of processing temperature. For BMNO- glass with Tg 150 °C at 257±5 °C and for BMNO- glass with Tg 100 ° C at 225±5 °C. Other possible combinations for $\eta = \eta_d = \eta_m = 1$ (Figure 6.1) are:

- LMNO Grade 1: PA 11 without catalysis - Glass 1: Tg 104 °C using processing T 235 ±5°C
- LMNO Grade 1: PA 11 without catalysis - Glass 2: Tg 124 °C using processing T 265±5 °C
- T Nat B Grade 3: PA 11 for coating application - Glass 1: Tg 104 °C using processing T 217±5 °C
- T Nat B Grade 3: PA 11 for coating application - Glass 2: Tg 124 °C using processing T 240±5 °C
- T Nat B Grade 3: PA 11 for coating application - Glass 3: Tg 150 °C using processing T 250±5 °C

## 6.3 Interactions in polymer – low Tg phosphate glass blends

The viscosity of the components, as explained in the above section, is a fundamental parameter on the polymeric blends' morphology development at thermal and shearing conditions, where macro to micro size particles are formed. But the localization of the nanoparticles in the matrix is linked to the balance of interactions between components. Interactions occur when the components are compatible, or they have affinity. Choosing precursors with low interfacial tension will promote the interactions. The

first conclusive evidence of intimate mixing of the TFP glass-polyamide 6 (PA6) hybrid components by melt blending had been characterized by 1H-31P solid-state nuclear magnetic resonance (NMR) [136]. Thus, synthesizing a glass-polymer hybrid with phosphate glasses and highly interacting commodity resins, as a polyamide, is aimed at improving an interaction between both [5]. The Tg of phosphate glasses are the one key advantage, which is low enough to allow melt processing with engineering thermoplastics to afford composite hybrid systems. The interaction between polyamides and phosphate glasses is well documented in the literature. There is mentioned an exceptional physicomechanical interaction between the components. The absorption of ammonia to the phosphate glass surface is one suggested classical interaction of these hybrid components [6]. The hybrid components have a high degree of interaction, which contributes towards the miscibility in the melt and polymer-glass adhesion in the solid state [5] and could result in dissolution of particles achieving nanometric scale morphology. As a result, TFP glass- polyamide 11 components should provide interesting melt properties and a compatible hybrid material.

### 6.3.1 Theoretical interfacial tension of the hybrid

The surface energy is an essential parameter to consider in blend development. The diminution of the surface energy needs the use of an interfacial agent that has good affinity with both components. The interfacial agents are placed between the two components and decrease the surface energy. In general, this surfactant molecule is a block copolymer formed in-situ by coupling or grafting. The objective of this research is to create the interface agent between TFP glass and PA11 during the processing without any external additives. The key points to achieve the interphase agent between tin fluoride phosphate glass and polyamide 11 are explained below.

In principle, the interfacial tension of polymer/filler should be sufficient to anticipate the morphology. It is almost impossible to find experimental data for the polymer/filler interphase. Usually, theoretical models like Owens-Wendt, Girifalco-Good or Wu equations [131,132,133, 134] are applied to calculate it (Equations 26, 27, 28, 29):

$$\gamma_{12} = \gamma_1 + \gamma_2 - [2\ (\gamma^d_1\gamma^d_2) + [\ (\gamma^p_1)^{1/2} - (\gamma^p_2)^{1/2}]^2 \quad (26)$$

$$\gamma_{12} = \gamma_1 + \gamma_2 - 2\ \sqrt{}\ (\gamma^d_1\gamma^d_2) - 2\ \sqrt{}(\gamma^p_1\gamma^p_2) \quad (27)$$

$$\gamma_{12} = \gamma_1 + \gamma_2 - 2\sqrt{(\gamma_1\gamma_2)} \quad (28)$$

$$\gamma_{12} = \gamma_1 + \gamma_2 - (4\gamma_1\gamma_2)/(\gamma_1 + \gamma_2) \quad (29)$$

where $\gamma^d$ is the dispersion component in mN/m, $\gamma^p$ the polar component in mN/m and $\gamma$ interfacial tension in mN/m.

In this study, the interfacial tension of each component was then calculated experimentally using the contact angle method by measuring the contact angle Θ (Figure 6.3) between the solid (glass and polymer) and the liquid (the pendant drop). Drops of solvent were gently deposited on the surface: water, ethylene glycol and diiodomethane were used, the water being the most polar and the diiodomethane the most apolar. Once these drops are laid and after a waiting time defined by a standard (depending on the rate of spreading and the evaporation of the solvent) the angle formed by the drop is measured. All measurements were performed at room temperature. $\gamma_{solid\text{-}air}$ (Equation 30) is representative of cohesive/interaction forces in the material and is expressed by Young's equation [161-162].

$$\gamma_{solid\text{-}air} = \gamma_{solid\text{-}liquid} + \gamma_{liquid\text{-}air} \cos\theta \quad (30)$$

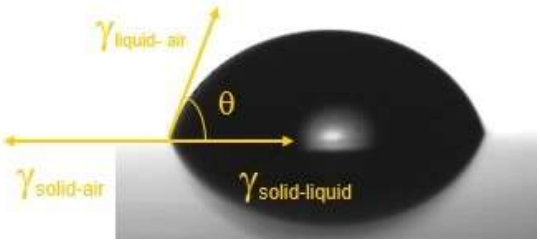


Figure 6. 3: Contact angle method.

The Owens & Wendt equation was selected to calculate the surface energy because it is typically applicable to surfaces with moderate polarity such as polyamides, polyvinyl chloride, polyurethanes, polyesters, polyacrylates, and polycarbonates. The Owens-Wendt concept considers that both dispersion and hydrogen bonding forces may operate. The surface energy (**γ**) is divided into two components (Equation 31):

$$\gamma = \gamma^{d}_{solid\text{-}air} + \gamma^{p}_{solid\text{-}air} \quad (31)$$

The dispersion component ($\gamma^d$) denotes London dispersion forces, a type of force acting between atoms and molecules. London dispersion forces operate between all materials (in polar and apolar materials). They are part of the van der Waals forces. London forces are exhibited by apolar molecules as correlated movements of the electrons in interacting molecules. The polar component ($\gamma^p$) denotes the component of surface tension due to both hydrogen bonding and dipole-dipole interactions (Debye- Keeson Van der Waals forces).

The contact angle of each solid (polyamide 11 and TFP glass) was measured using three measuring liquids with known surface energy, polar, dispersion and a midway one. The dispersive and polar components of the hybrid and glass were then calculated. The theoretical interfacial tension of the hybrid was obtained from extended equations. The results are summarized in Table 6.2.

Table 6. 2: The interfacial tension of the components and hybrid.

| | $\gamma^d$ | $\gamma^p$ | $\gamma$ / mN/m |
|---|---|---|---|
| Glass | 26.4 | 21.7 | 48.1 |
| PA11 | 33.9 | 10.4 | 44.3 |
| Owens-Wendt | | | 2.54 |
| Girifalco-Good | | | 0.08 |
| Wu | | | 0.16 |

It is important to point out that these theoretical interfacial tension values were calculated at room temperature and that the melt surface tension of components can be different from the solid one. The interfacial tension will be much lower during processing. Thus, the low value of solid surface tension at room temperature suggests great affinity between components during processing.

## 6.3.2 Thermal characterization of the hybrid

The compatibility and phase behaviour of polymer blends can be studied by many techniques. Calorimetric approaches have been largely applied and Differential Scanning Calorimetry is often used for the task. In this section, DSC was selected to evaluate the thermal properties of the hybrids, such as Tg, enthalpy of crystallization and fusion, temperatures of crystallization and melting. The changes in these properties of the hybrids can reveal information on phase behaviour, which can help

determining the type of phase separation [163]. The glass, PA11 and different glass content (0-60 wt%) hybrids were extruded at 250 °C, 150 rpm of screw speed and 5 minutes of residence time.

Figure 6.4 shows a DSC thermogram of the TFP glass melted at 450 °C for 20 minutes, where the glass transition of the glass was obtained at 101 °C in the second heating. No presence of other transitions define the glass as an amorphous material, which has no organization in the solid state. The transparency that glass has, among other properties, is due to this random organisation. Figure 6.5 presents DSC thermograms of polyamide 11 and hybrids with different glass content, where the thermal properties such as the glass transition, entalpy of fusion and the melting temperature were calculated. The thermal properties of TFP glass- polyamide 11 hybrids are summarized in Table 6.3.

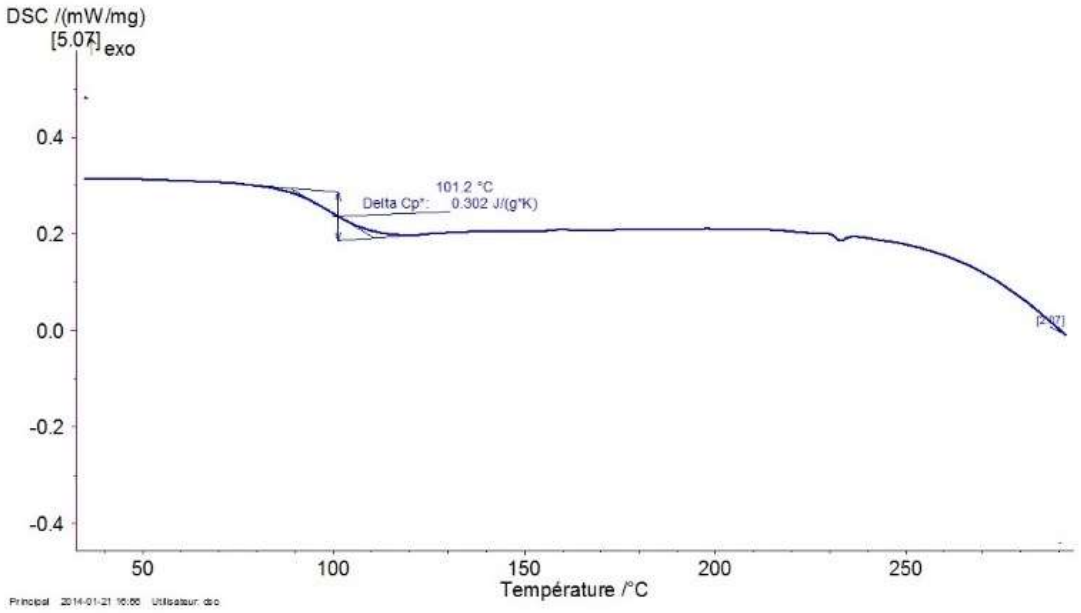


Figure 6. 4: DSC thermogram of tin fluoride phosphate glass.

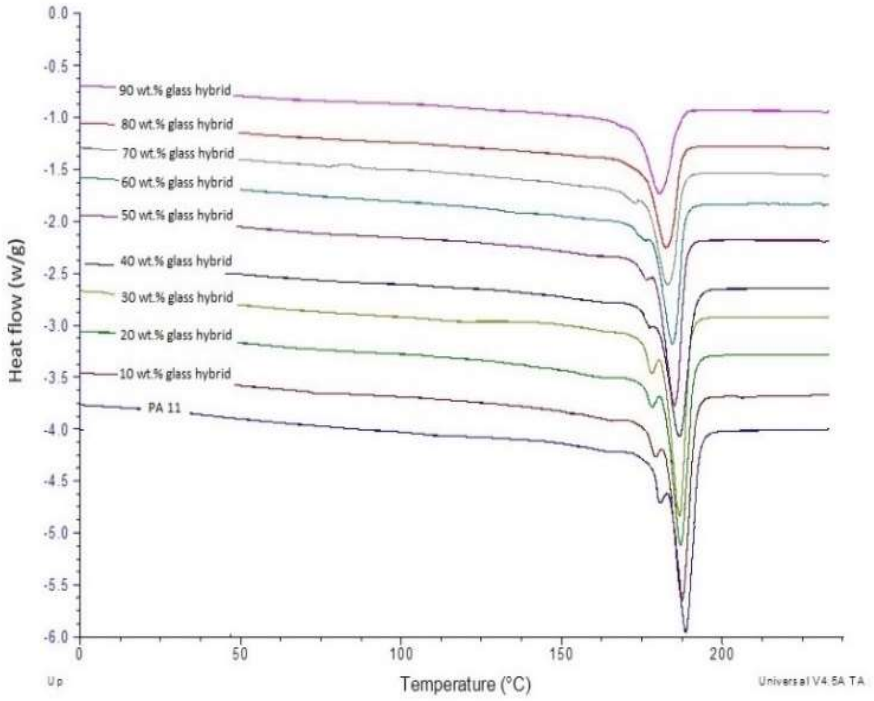


Figure 6. 5: Melting temperature of polyamide 11 and different glass content (0-90 wt%) hybrids by DSC.

The crystallinity percentage of the materials was estimated by Equation 32, where w is the weight percentage of PA11, the only crystallisable component of the hybrid. $\Delta H_f$ is the heat of fusion measured by DSC and $\Delta H^0_f$ the standard heat of fusion of 100% crystalline PA11, its value being 230 J/g.

$$x_c = w\Delta H_f/\Delta H_f^0 \quad (32)$$

Table 6. 3: Thermal properties of TFP glass- PA11 hybrids.

| Glass content wt% | Crystallinity / % | Tc / °C | Tg / °C | Tm / °C |
|---|---|---|---|---|
| PA11 | 30 | 164 | - | 189 |
| 10% Glass hybrid | 26 | 164 | - | 187 |
| 20% Glass hybrid | 20 | 163 | - | 187 |
| 30% Glass hybrid | 15 | 163 | - | 186 |
| 40% Glass hybrid | 13 | 162 | - | 186 |
| 50% Glass hybrid | 10 | 161 | - | 185 |
| 60% Glass hybrid | 8 | 159 | - | 184 |
| 70% Glass hybrid | 5 | 159 | - | 183 |
| 80% Glass hybrid | 3 | 157 | - | 182 |
| 90% Glass hybrid | 1 | 158 | - | 180 |
| Glass | | | 104 | |

It was noted that a decrease of the melting temperature and crystallization temperature, and a consistent decrease of the percent crystallinity with addition of TFP glass to the system, took place. Substantial diminution on the melting peaks with increasing glass content are visible in Figure 6.5. The loss of half crystallinity already at 30 wt% glass content indicates that TFP glass hinders the crystallization of polyamide 11 in the blends. This is a typical characteristic of amorphous-semi-crystalline miscible polymer blends where the glass transition temperature of the semi-crystalline polymer is lower than that of amorphous component (Tg PA11 48 °C, Tg TFP glass 101 °C). Crystallization difficulties may suggest that glass (solvent plasticizer) dissolves the polymer. However, more work is needed for substantiation.

When setting design and processing parameters for specific polymers, it is important to know the temperature where segmental molecular motion begins. The DMA loss modulus, E", is very useful in this respect because it is a measure of the viscous nature of polymeric materials. The peak maximum of E" corresponds to the beginning of significant segmental motion of the polymer chains. Thus, the mechanical energy input is dispersed as heat by the internal friction caused by chain motion, which characterizes the phenomenon called damping. Loss modulus (E") is a sensitive indicator of molecular differences.

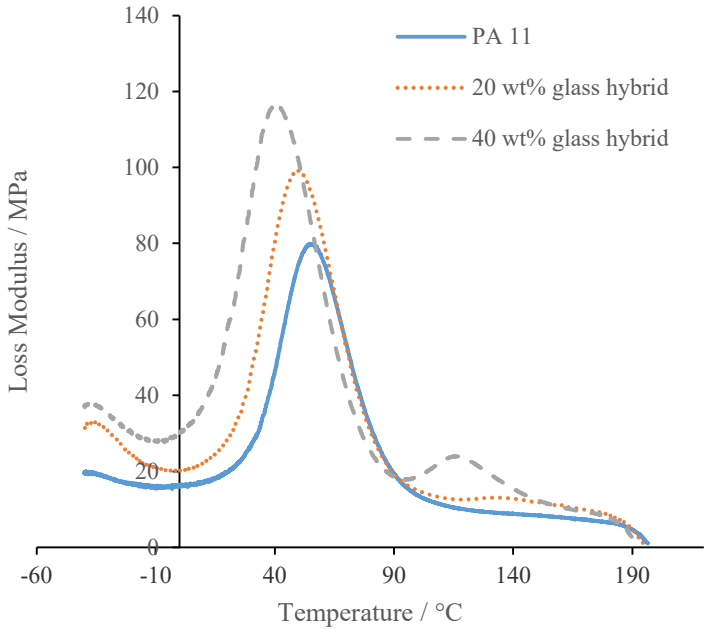


Figure 6. 6: Loss modulus versus temperature of PA11 and different glass content (0-20-40 wt%) hybrids.

The Tg of polyamide 11 and hybrids with 20-40 wt% glass was measured by DMA (Figure 6.6) instead of using DSC. It is observed in Figure 6.6 that the Tg peak of the hybrids became broader and heightened and decreased in temperature with increasing the glass content. The relative homogeneity or miscibility of the system can be reflected by the width and height of the glass transition peak. A broader and higher Tg peak implies less dense structure with more free volume. It showed less resistance to motion at the onset of Tg, which strongly suggested a "looser" internal structure and/or the presence of plasticizers that led to larger rotational freedom. DMA results suggest that glass is acting as plasticizer.

The material transition measurements define glass behaviour as an external primary plasticizer, which enters both the crystalline and the amorphous regions. As external primary solvent plasticiser, the glass will have the potential to dissolve polyamide and create an intermediate phase that might have properties of both extreme cases.

When the polymer is heated the movements of the main chain sets in, becoming maximum at Tg, at which losses occur corresponding to α-relaxation. This relaxation corresponding to Tg, may also be understood by free volume theory [135], in which the molecular mobility (and consequently the relaxation time) near Tg depends mainly on free volume. The free volume theory was not calculated in this research, but interesting further work can be done around this subject.

### 6.3.3 Molecular weight

Polymers consist of repeat units (monomers) chemically bonded into long chains. Understanding the physical properties of a polymer (such as mechanical strength, solubility, and brittleness) requires knowledge of the length of the polymer chains. Chain length is often expressed in terms of the molecular weight of the polymer chain, related to the relative molecular mass of the monomers and the number of monomers connected in the chain. However, all synthetic polymers are polydisperse in that they contain polymer chains of unequal length, and so the molecular weight is not a single value - the polymer exists as a distribution of chain lengths and molecular weights. The molecular weight of a polymer must therefore be described as some average molecular weight calculated from the molecular weights of all the chains in the sample. The molecular weight averages can be determined by gel permeation chromatography

(GPC) [164] and size exclusion chromatography (SEC) [164]. The number average molecular weight is the statistical average molecular weight of all the polymer chains in the sample, and is defined by Equation 33:

$$Mn = \Sigma N_i M_i / \Sigma N_i \quad (33)$$

where $M_i$ is the molecular weight of a chain and $N_i$ is the number of chains of that molecular weight. Mn can be predicted by polymerization mechanisms and is measured by methods that determine the number of molecules in a sample of a given weight; for example, colligative methods such as end-group assay [165]. If Mn is quoted for a molecular weight distribution, there are equal numbers of molecules on either side of Mn in the distribution. The weight average molecular weight is defined by Equation 34:

$$Mw = \Sigma N_i M_i^2 / N_i M_i \quad (34)$$

Compared to Mn, Mw considers the molecular weight of a chain in determining contributions to the molecular weight average. The more massive the chain, the more the chain contributes to Mw. Mw is determined by methods that are sensitive to the molecular size rather than just their number, such as light scattering techniques [165]. If Mw is quoted for a molecular weight distribution, there is an equal weight of molecules on either side of Mw in the distribution.

The polydispersity index (Equation 35) is used as a measure of the broadness of a molecular weight distribution of a polymer, and is defined by:

$$\text{Polydispersity index} = Mw / Mn \quad (35)$$

The larger the polydispersity index, the broader the molecular weight. A monodisperse polymer where all the chain lengths are equal (such as a protein) has an Mw/Mn = 1. The best controlled synthetic polymers (narrow polymers used for calibrations) have Mw/Mn of 1.02 to 1.10. Step polymerization reactions typically yield values of Mw/Mn of around 2.0, whereas chain reactions yield Mw/Mn values between 1.5 and 20.

The molecular weight measurements and rheological experiments were restricted to PA 11 - Glass (Tg: 104 °C) to explain more in detail the role of the glass in the hybrid

system. The large decrease of viscosity by adding glass has been previously reported in Chapter 5.

Gel permeation chromatography (GPC) was carried out for samples filled with (0-60) wt% glass to calculate the final glass content in the hybrid after compounding and the effect of the glass in the molecular weight. The hybrid samples (extruded at 250 °C, 150 rpm and for 5 minutes) were dissolved in hexafluoroisopropanol (HFIP) +0,05 M potassium triofluoroacetate (KTFA) solvents during 24 hours at room temperature. A concentration of 1 g/L of dissolution was used for the testing. The filtration was carried out using an ACRODISC PTFE filter with diameter of 25 mm and porosity of 0.2 µm. The results from the gel permeation chromatography (GPC) are summarized in Table 6.4:

Table 6. 4: GPC measurements of TFP glass-PA11 hybrids mixed at 250 °C of extrusion processing temperature.

| Samples | Mn | Mw | Polydispersity Mw/Mn | Insoluble (%) |
|---|---|---|---|---|
| PA11 100% | 27800 | 53900 | 1.9 | - |
| PA11 + 10%Glass | 21900 | 44600 | 2.0 | 3.8% +/- 0.2% |
| PA11 + 20%Glass | 22400 | 42000 | 1.9 | 12.4% +/- 0.6% |
| PA11 + 30%Glass | 20500 | 39700 | 1.9 | 17.8% +/- 0.9% |
| PA11 + 40%Glass | 19500 | 37200 | 1.9 | 27.1% +/- 1.4% |
| PA11 + 50%Glass | 20000 | 37200 | 1.9 | 35.9% +/- 1.8% |
| PA11 + 60%Glass | 18100 | 33300 | 1.8 | 41.9% +/- 2.1% |

The decrease of the Mw for increasing TFP glass content could have two explanations:

1) thermo-hydro degradation (hydrolysis) due to the TPF glass
2) Dissolution of the PA11

Due to the plasticizer behaviour detected on the DMA analysis shown in section 6.3.2 for TFP glass with Tg around 125°C, and the diminution of TFP glass content after compounding, it is suggested that interaction occurs because glass dissolves PA11. The polydispersity of about 2.0 for all hybrid blends suggests that the chain-transfer

reactions take place at the same rate as ring-opening reactions, and thermodynamic equilibrium is achieved. The polymerization is thermoneutral. To understand the great decrease of viscosity, rheological experiments of PA11/ glass (Tg 104 °C) hybrid filled at 0-50 wt.% glass were carried out. The samples were processed at 250 °C, 150 rpm and 5 minutes using a DSM research 15 $cm^3$ micro compounder equipped with an injection moulding machine. The rheological test was carried out at 250 °C. The results are shown in Figure 6.7.

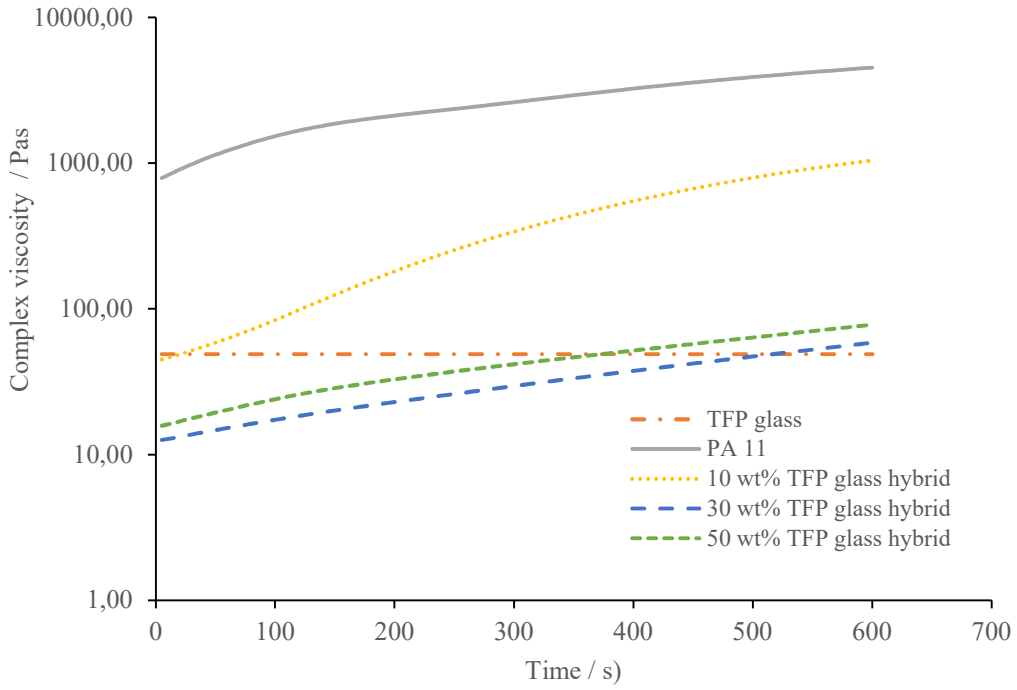


Figure 6. 7: Complex viscosity versus time of PA11 and different glass content (0 to 50 wt%) hybrids processed at 250 °C of processing temperature,150 rpm of screw speed and 5 minutes of residence time.

The decrease of the viscosity of the hybrid is due, firstly, to the loss of molecular weight due to plasticizer interaction during processing. GPC results show a loss of 17-31% of PA11 Mw for the hybrid with 10-50 wt% glass (Table 6.5). Secondly, melt rheology results of hybrid blends filled at 10, 30, 50 wt% glass corroborated that glass is a molecular liquid (viscosity lower than 50 Pas) that is composed of molecules that do not form a covalent network but interact only through weak van der Waals forces or through transient hydrogen bonds. Many molecular liquids can be super-cooled into glass.

Table 6. 5: GPC measurements of TFP glass- PA11 hybrids.

| Glass content /% | Loss of PA11 Mw /% |
|---|---|
| 10 | 17 |
| 20 | 22 |
| 30 | 26 |
| 40 | 31 |
| 50 | 31 |

FTIR results (Figure 6.8) for hybrids processed with different glass Tg (104 °C and 125 °C) suggested the absence of chemical reactions (covalent bonds), as no new peaks were detected. However, well-defined, and intense phosphate peak around 1000 $cm^{-1}$ obtained for the hybrid with 104 °C Tg glass revealed a higher interaction-plasticiser effect.

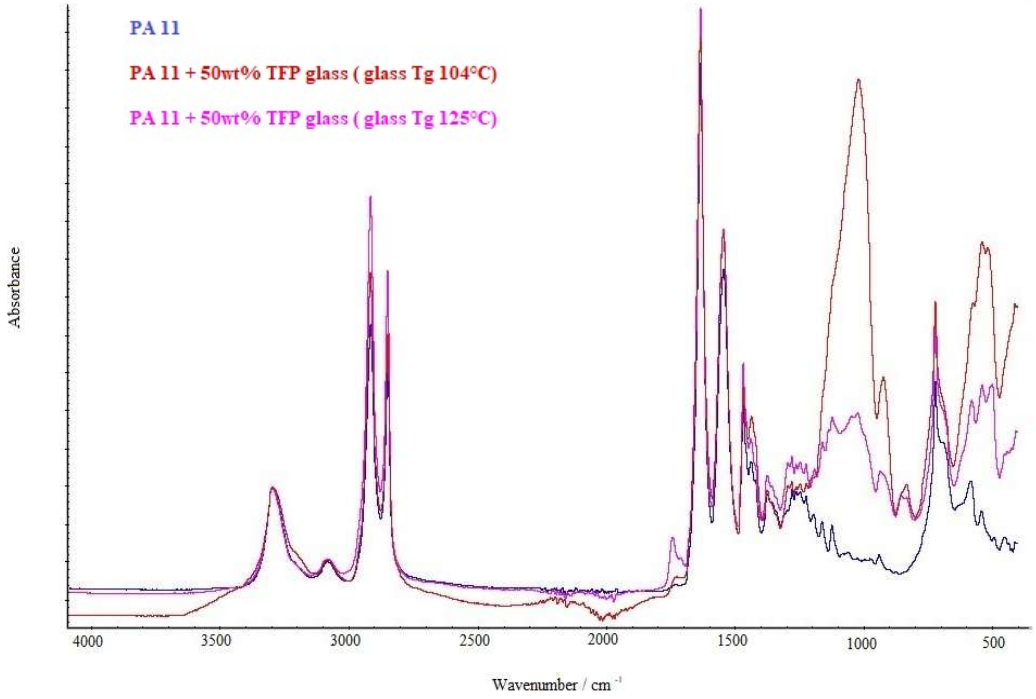


Figure 6. 8: FTIR spectra of PA11 and different Tg glass hybrids.

## 6.4 Morphology development mechanism

The hybrid components and the processing conditions have a primordial role in the nanoparticle's formation mechanism. SEM analysis, where the influence of glass content and temperature on the hybrid morphology was described in Chapter 5,

showed that particles > 1μm, microstructure physical-mechanical process ( droplet break-up in a shear flow), have irregular shape, while those < 1 μm, submicron-nanostructure-physicochemical process (interactions between components), were perfectly spherical. The hypothetical mechanism for morphology development of PA11/TFP glass hybrid is based on two steps as described below.

### 6.4.1 From macro to microstructural changes

It was considered that the initial macroscopic glass filler first suffers microstructural changes during the process. The microstructural changes are defined as droplet break-up in a shear flow (Figure 6.9). The droplets break up occurs under favourable conditions converting the dispersed phase particles to smaller size, for example, like in this case from macroscopic glass particles to microscopic ones. The viscosity, the shear rate and interfacial tension have great influence on the microstructural changes mechanism. Thus, the morphology generation from first angular glass particles to smaller and a round dispersed phase in the blend is governed, firstly, by the viscosity ratio, the viscosity of the droplet phase ($\eta_d$) divided by the viscosity of the matrix phase ($\eta_m$). During flow, the inclusions of a liquid/liquid dispersion are deformed and oriented by hydrodynamic forces, but it can also lead to droplet break-up. The latter occurs at a critical value of capillary number. Thus, the second parameter influencing the morphology is capillary number (Ca, Equation 36) that can characterize where droplet break-up takes place (Figure 6.9-6.10) and coalescence (Figure 6.11) [135]. Both parameters are adimensional for simple blends with viscoelastic components in simple shear and extensional flows.

$$Ca = (\eta_m \dot{\gamma} R)/\sigma \qquad (36)$$

Where $\eta_m$ is the viscosity of the matrix; $\dot{\gamma}$ is the shear rate; R is the droplet radius and σ the interfacial tension.

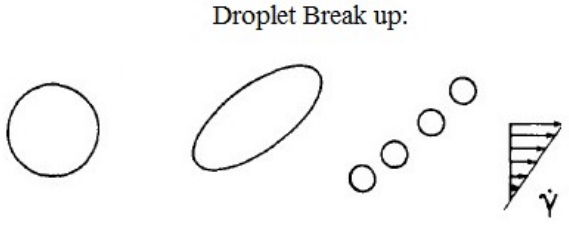


Figure 6. 9: Droplet break-up in a shear flow [135].

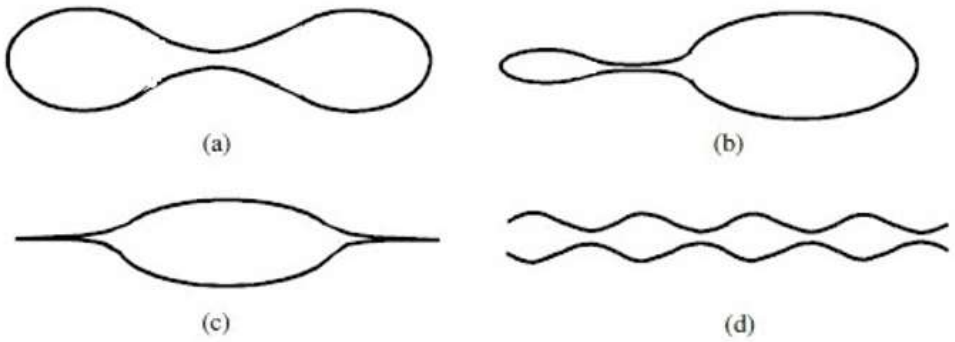


Figure 6. 10: Different modes of particle break up in extensional flow and morphology generation [135]: a) Simple breakup by waist-thinning occurs when Ca > Ca $_{cr}$; b) Asymmetric breakup by waist-thinning, probably requires a minimum of surfactant; c) Tip streaming, requires a minimum of surfactant; d) Capillary breakup occurs when Ca > > $Ca_{cr}$.

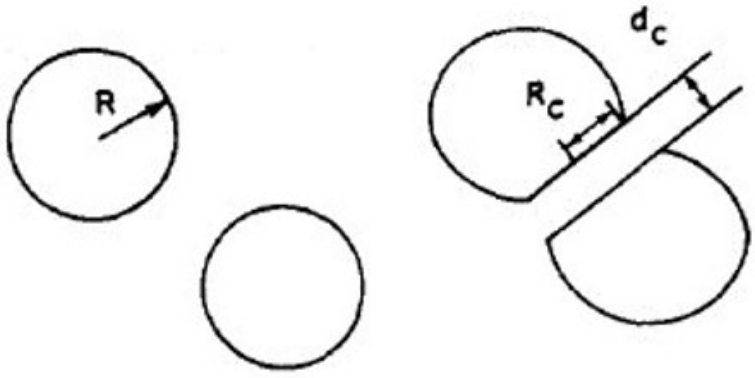


Figure 6. 11: Droplet coalescence on the morphology generation [135]. R is the droplet radius; $R_c$ is the contact radius; $d_c$ is the matrix film thickness.

Systematic data of critical capillarity number ($Ca_{cr}$) as a function of viscosity ratio in simple shear and extensional flow provided by Grace [135] will give simply the chance to determine the modes of particle break-up of the hybrid under the influence of processing conditions. Capillary number for this specific case is calculated following Equation 36. From different options, a value of matrix viscosity was defined at viscosity ratio equal 1 (1600 Pas). The shear rate in the DSM twin-screw extruder (Taylor-Couette geometry) is estimated by maximum shear rate at clearance, Equation 37 [166]:

$$\dot{\gamma} = \frac{\pi D_2^2 N}{15\,(D_2^2 - D_1^2)} \tag{37}$$

where $D_2$ is the barrel diameter, $D_1$ the screw diameter and N is rpm. For a 15cc barrel, the shear rate is :

$$\dot{\gamma} = 15.7\ N$$

Hybrid compounding was done at 150 rpm, so the shear rate is 2355 $s^{-1}$. The droplet radius of 1.04 µm and the interfacial tension of 2.5 mN/m were calculated before. So, Capillary number is 1.5072 and viscosity ratio is 1 at optimal temperature of 247 °C, Figure 6.12.

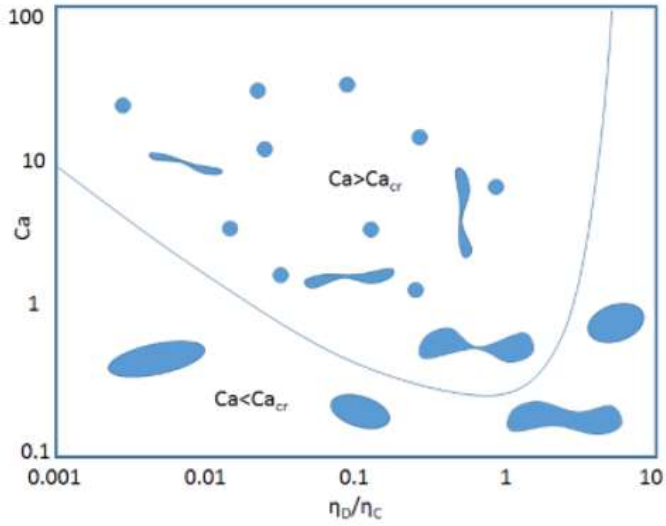


Figure 6. 12: Representation of the different deformation and break-up in a biphasic liquid/liquid polymeric blend in shear flow [135].

Microstructural changes from macroscopic glass filler to micron particles in the matrix are shown in Figure 6.13.

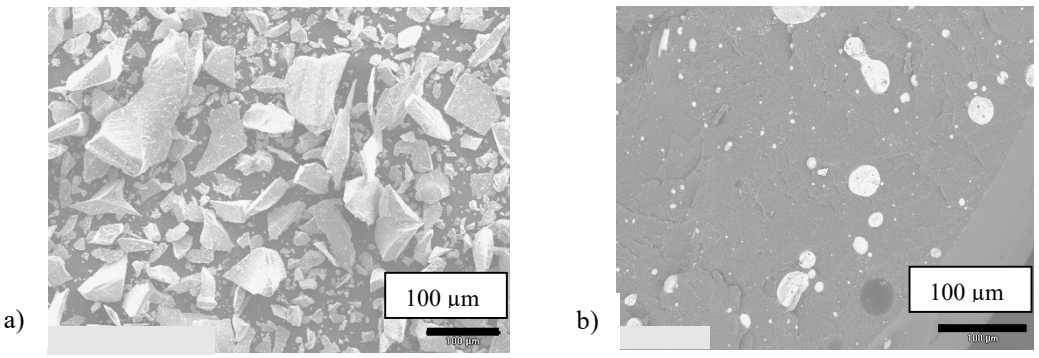


Figure 6. 13: TFP glass hybrid morphology development: a) TFP glass morphology; b) Droplet break-up of PA 11- TFP glass hybrid in shear flow.

The dispersed phase is fragmented in small spherical droplets, with regular form, where the droplet radius is written by the ratio between hydrodynamic stresses ($\eta\dot{\gamma}$) where $\eta = \eta_d = \eta_m = 1$ and $\dot{\gamma}$ shear rate) and the interfacial stresses ($\gamma_{AB}/R$) where $\gamma_{AB}$ is the interfacial tension). It can be used to calculate the droplets radius from Equation 38. The equation indicates that it is necessary to increase the shear rate and decrease surface energy for obtaining a homogeneous and fine dispersion. The surface energy is a key point for morphology development of the blends.

$$R \sim \frac{\gamma_{AB}}{\eta\dot{\gamma}} \tag{38}$$

Using Equation 4, it was possible to calculate the droplets radius for the PA 11- P glass hybrid. Interfacial tension was taken from Table 6.2 using Owens-Wendt equation (condition $\eta = \eta_d = \eta_m$). The shear rate of the extruder at 150 rpm is equal to 1500 $s^{-1}$. So, droplet radius achieved under shear and thermal compounding conditions:

R= 1.04 μm at processing temperature of 247 °C

Figure 6.14 presents the submicron particles or nanoparticles obtained in the morphology. These micrographs corroborate the hypothetical thinking. This is the second step of the morphology development mechanism.

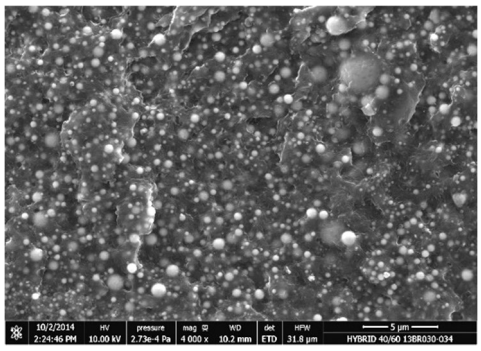


Figure 6. 14: 40 wt% glass hybrid morphology to show the presence of nanoparticles and dispersion. The hybrid was synthetized using PA11 BMNO and glass with 124°C Tg. The processing conditions were: 250 °C of processing temperature, 150 rpm and 5 minutes of residence time.

## 6.4.2 From micron to Nano particles

To obtain submicron particles-nanoparticles, a chemical reaction or interaction between components should take place. Figure 6.15 shows the explanatory scheme

where an interlayer composed of two components is developed. There are two mechanisms to form the interlayer that can lead the glass from micro particles to submicron ones. One is when the polymer preferentially interacts with the filler. The polymer nucleates onto filler particles. This nucleation modifies the local composition and thus modifies the phase separation creating an interlayer between the two components. The second option is the dissolution of the filler in the polymeric matrix that leads to in an interlayer too. In both cases, the interlayer consists of a phase whose composition and structure depend on the respective interactions of both the polymer and the filler [167].

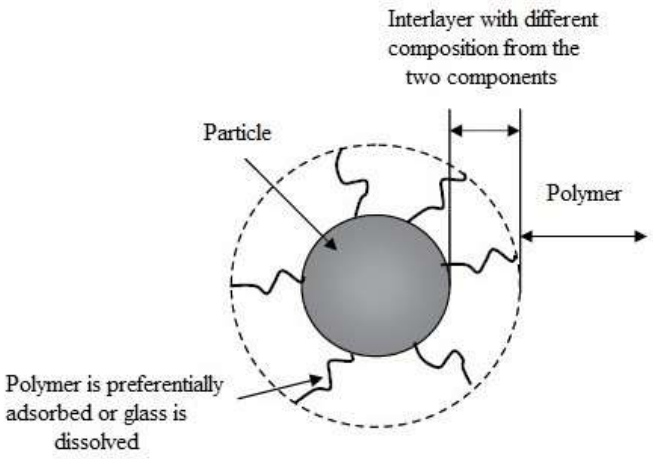


Figure 6. 15: Scheme of a filled partially miscible blend in which the interlayer composed of both components might be due to polymer nucleating or glass dissolution [168].

Regarding the adhesion between of TFP glass and PA11, it is well known that this is a complex system but there is still a need to develop an appreciation of the underlying mechanisms. Models of adhesion have been studied over many years including mechanical interlocking, physico-chemical anchoring, hydrogen and van der Waals bonding. Scanning and transmission electron microscopy of polyamide 11 and TFP glass interfaces provided good evidence of strong adhesion particularly in the 20 and 50 wt% glass hybrids processed at 250°C, 150 rpm and 5 minutes of residence time. The microscopy revealed the absence of voids at the interfaces and well-coated glass particles (Figure 6.14, 6.16 and 6.17). There is also some evidence of glass particle dissolution at the particle boundaries. A glass plasticiser effect has also been reported in the literature [5,6] with different polymer matrices. The interaction between glass and PA 6 and PA 12 is well documented.

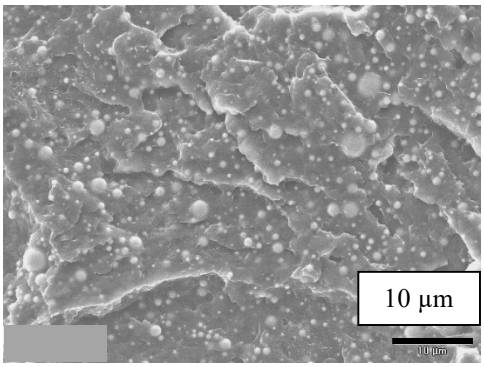


Figure 6. 16: 50 wt% glass hybrids processed at 250°C, 150 rpm and 5 minutes of residence time micrograph.

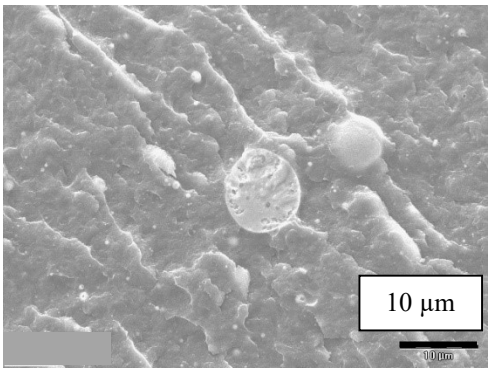


Figure 6. 17: 20 wt% glass hybrids processed at 250°C, 150 rpm and 5 minutes of residence time micrograph.

In addition to the work in the literature on the plasticiser effect, the dissolution of the glass into the PA11 matrix was also suggested by this research on hybrid characterization. This work is reported below.

- The improvement of material flow adding glass by reducing polymer melt viscosity is presented in section 6.3.3, in Figure 6.7. The wetting effect improves mechanical bonding
- A broader and higher Tg peak at lower T° in Figure 6.6 - DMA results- implies less dense structure with more free volume. It showed less resistance to motion at the onset of Tg, which strongly suggested the presence of plasticizers that led to larger rotational freedom.
- The decrease of the molecular weight and the loss of a % of glass in GPC results follows the behaviour of the other two tests.

## 6.5 Final remarks

(a) Overview

This research is the result of studies conducted in Chapters 4 and 5. It shows strong influence of the properties of the precursors on the morphology. Glass at different melting conditions ( Glass 1: Tg 104 °C; Glass 2: 124 °C; Glass 3: Tg 150 °C) and different PA11 degrees and three different polyamide 11 grades (LMNO Grade 1: PA 11 without catalysis, BMNO grade 2: PA11 with catalysis and T Nat B grade 3: PA 11 for coating application) were observed under different processing T°( 230 °C, 250 °C, 270 °C). To determine the optimal processing temperature at each case, a diagram of complex viscosity against temperature was plotted. Only one condition (glass 2: 124 °C + BMNO grade 2) was observed by SEM. The micrographs corroborated the diagram at least under this condition. The diagram enables customizing homogeneous and submicron hybridization with respect to thermal and shearing conditions.

The nanostructures are linked to the balance of interactions between components. The evidence of nanoparticles in TFP glass- PA11 hybrids is shown in Chapter 5 (section 5.2.2-Figure 5.6). Thus, in this study, the interfacial tension, thermal properties, and the molecular weight were characterized in order to find evidence of possible interaction and be able to explain the evolution of the hybrid morphology. A plasticiser effect was found and supported by work in the literature [5,6]. Moreover, the effect was also supported by research in this experimental study on rheological and DMA behaviour. In addition, the decrease of glass content in GPC measurements suggest a dissolution of the glass.

# Chapter 7 Deposition process and properties of TFP glass – PA11 hybrid coatings on stainless steel by fluidized bed dipping

P glass based organic–inorganic hybrid coatings have been developed for achieving primeless PA11 coatings on stainless steel by fluidized bed dipping coating technique. Hybridization of the powder coating was achieved by melt blending up to 40 wt% of glass using different melting conditions of the tin fluoride phosphate glass. Such prepared hybrid coatings were found to be relatively dense, uniform, and macro defect free at same processing conditions as PA11 powder. A micro-meso-nanostructured hybrids morphology with interesting properties have been achieved.

However, the morphology responsible for these interesting properties also can cause difficulties in the deposition of coatings by fluidized bed dipping. This research studies the industrial applicability of these novel type of hybrid morphologies for the powder coating market and the influence of the addition of TFP glass on the structure and properties of fluidized bed dipping coatings. The industrial feasibility of the hybrid powder coating was characterized by rheological properties, density, inherent viscosity, particle size distribution and morphology. The performance of the resulting coatings was evaluated by thickness, corrosion resistance- barrier properties- adhesion, mechanical properties, and morphology of the hybrid coatings.

The morphological behaviour diagram shown in Chapter 6- section 6.2- Figure 6.1 was developed to predict the most suitable processing temperature to achieve homogeneous and nanostructured morphology. The diagram was applied to hybrid composed by different grade of polyamide 11 and glass synthetized at different melting conditions. The diagram helps to interpret better the hybrid coating characterization results and overcome the difficulties during the first attempt to the scaling-up caused by the variability on the glass properties at large batches. The effect of melting conditions during synthesis on the structure and properties of TFP glass are well documented in Chapter 4. No academic work has been reported for these hybrids for powder coating applications to date. This represents a gap in academic knowledge as well as many potential industrial applications.

## 7.1 Processing conditions of the coating

Six different hybrid powders were prepared to evaluate coating properties. To compound these blends different melting condition glasses were used to check the influence. The precursors were blended in an industrial twin screw extruder and pelletized using the composition and extrusion conditions shown in Table 7.1. These pellets were ground into powder and sieved to obtain suitable particle size distribution for fluidized bed dipping powder coating application. This powder was then applied onto the metal surface by fluidized bed dipping.

Table 7. 1: Composition and extrusion conditions of hybrid preparation.

| Composition | PA11 / wt % | TFP glass /wt % | Tg glass / °C | Screw speed /rpm | Temperature / °C |
|---|---|---|---|---|---|
| 1 | 100 | 0 | | 150 | 250 |
| 2 | 80 | 20 | 96 | 150 | 250 |
| 3 | 60 | 40 | 96 | 150 | 250 |
| 4 | 70 | 30 | 104 | 150 | 250 |
| 5 | 70 | 30 | 124 | 150 | 250 |
| 6 | 70 | 30 | 150 | 150 | 200 |

## 7.2 Powder characterization

As it was mentioned in the literature, section 2.3.4, the fluidisation properties have great importance in fluidized bed dipping coating process. The main parameters related to the fluidification properties are the mean particle size, density, and viscosity. Thus, these three parameters have been evaluated to determine the applicability of novel hybrid powder. The morphology of the hybrid powder was observed by SEM. The dispersion and the size of the glass particles in the powder particles were evaluated to compare and analyse after with the hybrid coating morphology.

### 7.2.1 Mean particle size and density

The mean particle size (Dv50) and the density have been used to predict the fluidisation type by Geralt chart [137,138]. Hybrid powders were characterized using a Malvern Multisizer T laser diffraction (focal 300 mm) granulometer [169]. The mean particle size value (Dv50) of compositions from Table 7.1 are summarized in Table

7.2. The standard deviation (SD) was calculated according to n (number of tested samples) equal to 6.

Table 7. 2: Mean particle size values of PA11 and hybrid powders.

| Composition | Dv 50 /µm | SD |
|---|---|---|
| 1 – PA11 | 206 | 3 |
| 2- 20wt% hybrid | 264 | 6 |
| 3- 40 wt% hybrid | 302 | 5 |
| 4- 30 wt% hybrid | 290 | 3 |
| 5- 30 wt% hybrid | 293 | 3 |
| 6- 30 wt% hybrid | 293 | 2 |
| Rilsan powder | 100 | 2 |

The mean particle size (Dv50) of the hybrid powder with 40 wt% glass is 3 times bigger than the Rilsan® powder in the case of 40 wt% glass and almost 3 times in the case of 30 wt% glass.

Densities of TFP glass – PA11 hybrids were measured by Archimedes method and the results are shown in Figure 7.1.

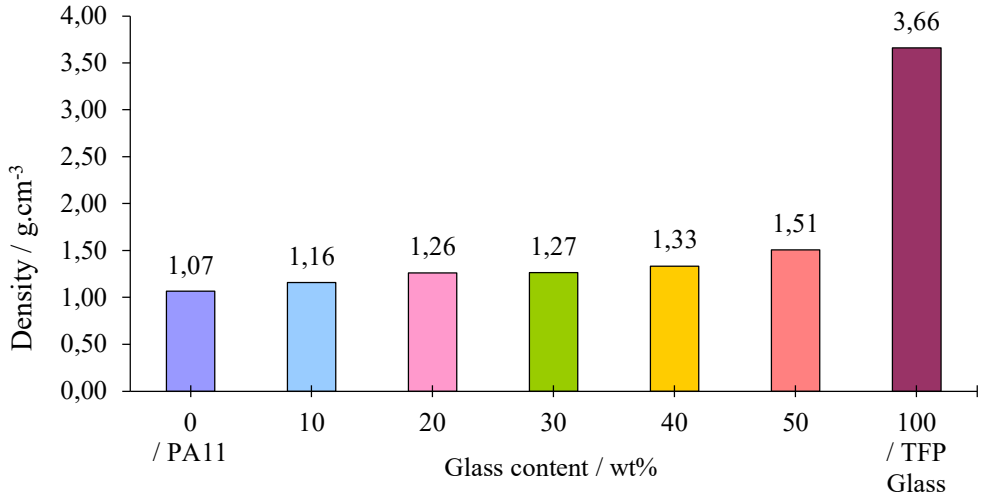


Figure 7. 1: Density of different glass content hybrid.

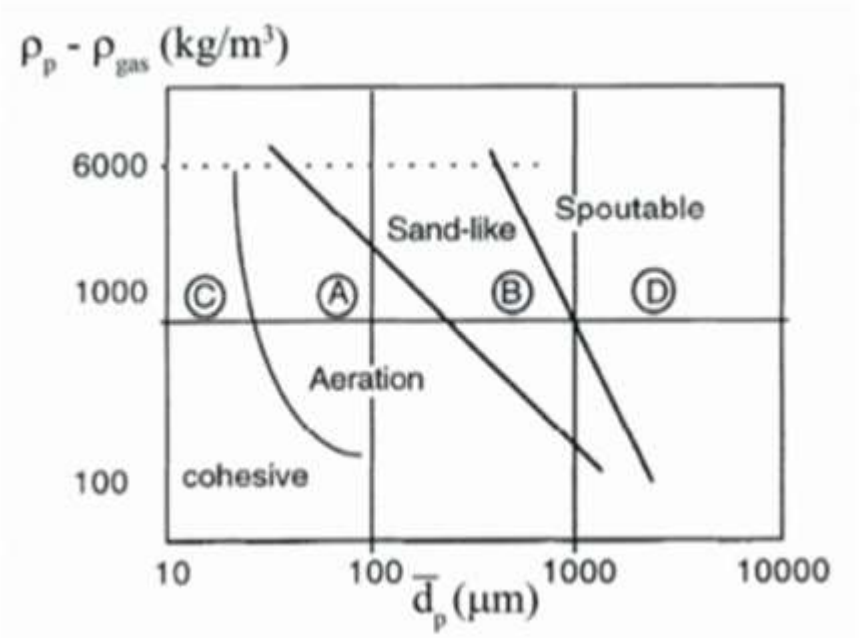


Figure 7. 2: Geldart chart of fluidisation modes, Groups C, A, B and D [137].

Table 7. 3: Geldart classification model for PA11 and hybrids with 20,30,40 wt% glass.

| Composition | Density / $gcm^{-3}$ | Mean particle size / μm | Group classification |
|---|---|---|---|
| PA 11 | 1.07 | 207 | A |
| 20 wt% glass hybrids | 1.26 | 264 | A |
| 40 wt% glass hybrids | 1.33 | 302 | A |
| 30 wt% glass hybrids | 1.27 | 297 | A |

Classification of materials according to their fluidization behavior are represented in Figure 7.2 by Geldart chart. Geldart provides convenient criteria for predicting the fluidization behavior based on the mean particle size and particle density. Geldart defined four types of materials which differ by the cohesion forces between particles [170]. Based on these parameters, particles are classified into four groups: C, A, B, and D (note that Figure 7.2 applies only at ambient temperature and pressures).

Group A particles are easy to fluidize. The dense phase of these materials expands stably before bubbling commences. These materials have a small mean particle size range from 30 μm to 125 μm and/or density less than 1,400 $kgm^{-3}$. Indeed, most particles used in fluidised beds are Group A powders.

Geldart Group B particles have a particle size range of 150 μm to 1,000 μm and densities 1,400 and 4000 $kgm^{-3}$. Group B particles tend not to undergo a smooth fluidization, and bubbles form at the onset of fluidization. Thus, the minimum fluidization velocity and the minimum bubbling velocity are similar. Group B powders fluidize easily and are used in a wide range of fluidized unit operations with few difficulties. Typical example of Group B material is sand.

Geldart Group C powders are typically less than 30 μm and are the most difficult to fluidize. These particles are considered cohesive and almost always experience significant issues during fluidization. In fact, particles this small tend to behave more as particular clusters than single, independent particles [171]. Nano particles fall into this classification. To limit this effect, Group C powders are usually fluidized with the aid of baffles, microjets, pulsing, and/or mechanical vibration. But they are difficult and often impossible to fluidize because of large surface (cohesive) forces holding particles together. Flour is an example of these type of materials.

The largest particles fall into the Geldart Group D classification. The gas requirements for fluidizing Group D powder are large. During fluidization of Group D powders, the bubbles formed are enormous and slugging can be observed even in large fluidized bed [172].

Geldart group classification assigned to PA11 and 20, 30, 40 wt% TFP glass hybrids were summarized in Table 7.3. Group A fluidization modes was predicted based on the mean particle size and particle density results, present also in Table 7.3.

The PA11 processed for industrialization trials is rougher than commercial one but still is grouped into Group A (small mean particle size and/or density less than 1.4 $g/cm^3$ are ideal for coating purpose). The Group B particles have mean particle diameters roughly between 40 microns and 500 microns and density between 1.4 and 4 $g/cm^3$. The fluidization mode of this type of particles is highly affected by the formation of gas bubbles in the bed but particles often fluidize well. According Geldart materials with viscosity less than 1.4 $g/cm^3$ can consider into group A. Thus, all the compositions are suitable for coating application. However, due to a variable and rough particle size ranging from a few μm to about 600 μm of the hybrid powder and the density value close to the maximum limit, hybrid powders can be considered as

Group B materials. Group B powders tend to allow to the formation of large bubbles (on the order of meters in tall bed), so slugging can occur in even some large units.

Slugging occurs when the walls of the fluidized bed stabilize the bubble such that the bubble push the solid upward in the unit. Bubble size larger than two-thirds the diameter of the bed can cause slugging. Particle size range of the hybrid powder was measured by SEM.

### 7.2.2 Viscosity characterisation

The ability of the coating to flow is important in their preparation, storage, and application. Thus, rheological properties were analysed for the sixth different compositions. One of the important rheological parameters is the viscosity of the coating and its thixotropic recovery. The complex viscosity against time plot can be used to evaluated them.

The key parameter in rheological properties, viscosity, of the hybrids at three different processing temperature and different glass wt% were analysed in Chapter 5 (section 5.7) to interpret their rheological behavior.

The rheological behaviour of the material is highly considered for understanding the morphology development of hybrid materials in Chapter 6 (section 6.3.3) and determining the feasibility of one new material for powder coating application. One way to improve wetting improving mechanical bonding is to improve material flow by reducing polymer melt viscosity. The balancing act to achieve lower viscosity while not sacrificing other properties is another requirement that the novel hybrid system has to overcome.

However, for coating application feasibility, it is desirable to decrease the viscosity but at the same time to have an increase of the viscosity during the application is important too. In the literature [5,6], it was reported the reducing polymer melt viscosity evidence between TFP glass and PA, but no system has been evidenced that meets the two requirements to date. So, a time dependant viscosity matrix, already functional for coating applications as PA11was selected to achieve the 3 requirements together (decrease viscosity, increase viscosity and improve properties).

Figure 5.24, 5.25, 5.26 and 5.27 in Chapter 5 have confirmed the increase of viscosity effect over the time in the hybrids sought for the coating process application. Figure 6.7 showed reducing polymer melt viscosity represented by the complex viscosity versus time of PA11 and different glass content (0 to 50 wt%) hybrids processed at 250 °C of processing temperature,150 rpm of screw speed and 5 minutes residence time. Finally, the improvement evidence of thermal and mechanical properties in Chapter 5, such as in Figure 5. 17, the increase of the Storage Modulus versus different TFP glass content hybrid materials at two temperatures, 23 °C and 150 °C, from DMA and in Figure 5.23, increase of the thermal stability characterized by decomposition temperature as a function of TFP glass concentration by TGA, might suggest the improvement of some mechanical properties of the hybrid coating such as hardness, abrasion, impact, etc.

The inherent viscosity of the hybrid powders with variable glass content wt% was measured to monitor the progress of the reaction in relation of hybrid molecular weight (Table 7.4). The specific range to avoid coating applicability problem, low or high viscosity issues, for PA11 is 1.0 -1.1. The results are in concordance with PA11, so no applicability issues were expected regarding the viscosity.

Table 7. 4: Inherent viscosity of TPF glass PA11 hybrid using different glass content wt%.

| Glass content / wt% | Inherent viscosity of the hybrid / adimensional |
|---|---|
| 0 | 1.08 |
| 10 | 1.04 |
| 30 | 1.03 |
| 50 | 1.12 |

### 7.2.3 Morphology of the hybrid powder

Powder morphology of the hybrid with 30 wt% of glass is shown in Figure 7.3. Rough dispersion with particle size between 0.4 and 20 µm together with fine dispersion with particles size smaller than 0.5 µm was observed. A variable and rough particle sizes ranging from a few µm to about 600 µm of the hybrid powder were measured by SEM

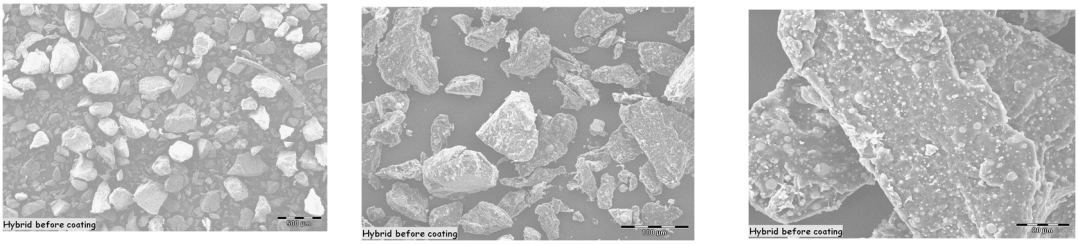


Figure 7. 3: Powder morphology of the hybrid with 30 wt% glass (composition 3) at different magnification. Scale bar: a) 500 µm; b) 100 µm; c) 20 µm.

## 7.3 Coating characterization

There are plenty of coating characterization techniques in the market. Some of them are listed in section 2.4. The properties of the coating to characterise depend on the final application of the coating. The most common areas to test for basic powder coating functionality are film thickness, uniformity/proper curing, adhesion, and appearance. The thickness, bond strength, and porosity of a coating directly affect its protective properties for a metal.

In this research, film thickness, adhesion, barrier properties, mechanical properties and morphology of the coating were evaluated to characterize the novel TFP glass - PA11 hybrid coating.

### 7.3.1 Thickness of the coating

A film thickness test determines the thickness of the powder on the part once it has been applied. The coating thickness was measured on each coated plate at different locations before testing and average thickness in µm calculated. The measurements were taken by an Elcometer 456 giving a thickness between 350-450 µm. Figure 7.4 shows the thickness value of Rilsan® fine powder in µm for different powder coating techniques mastered by Arkema coating division and available in the market. Fluidized bed dipping technique was selected to perform the first feasibility trials of the novel hybrid powder coatings. The thicker and broader thickness range of dipping application made possible to perform coating characterization testing.

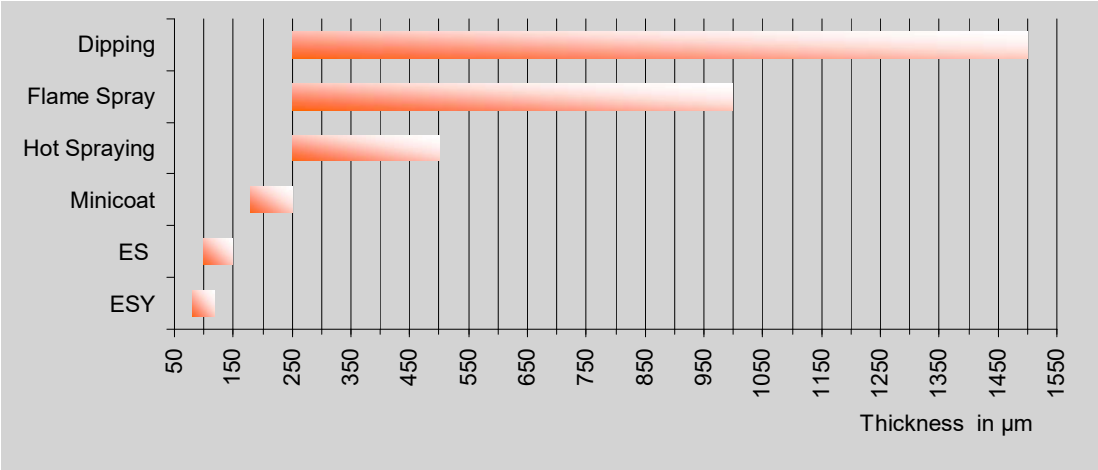


Figure 7. 4: Coating thickness regarding the powder coating applications technique[173].

The typical film thickness of Rilsan® fine powder applied by fluidized bed dipping is 350 µm, powder particle size distribution is between 0-250 µm and powder mean particle size is 100 µm.

The mean particle size for 20, 30, 40 wt% glass hybrids is presented in Table 7.2 and it is around 300 µm. The approximative value for powder particles size distribution observed by SEM, as commented in section 7.2.3, is 0-600 µm. These values suggest a high thickness variability onto coated plates for characterization testing. Some of the hybrid coating properties might be affected, for example, the impact resistance. The average impact energy increases rapidly with the thickness of the coating. It is therefore essential to have similar thicknesses between the coated plates tested to ensure good reproducibility.

Other issues can appear if the film thickness is either too low/ thin or too high/ thick. The low film thickness issues are substrate show through, grainy flow finish, orange peel, uneven film thickness and poor hiding. The high film thickness issues are uneven surface, orange peel, wavy flow appearance, pinholes, and back ionization.

### 7.3.2 Adhesion

The bond strength between the coating and the metal matrix is directly related to the roughness and the chemical energy of the metal surface and the adhesion of the coating. The improvement and the performance of the coating depend on the adhesion.

Coated samples with thickness between 360-460 µm were tested according to the method based on the norm NF EN10310. This method is explained in Appendix F. The objective is to check the influence of phosphate glass in the PA11 matrix on adhesion. Initial and aged (80±2 °C, 24 hours immersed in water) coated plates of PA11 and hybrids with 20, 30 and 40 wt% glass were examined. Complementary testing such as glass water resistance, roughness and SEM was carried out in order to help interpret and discuss the results.

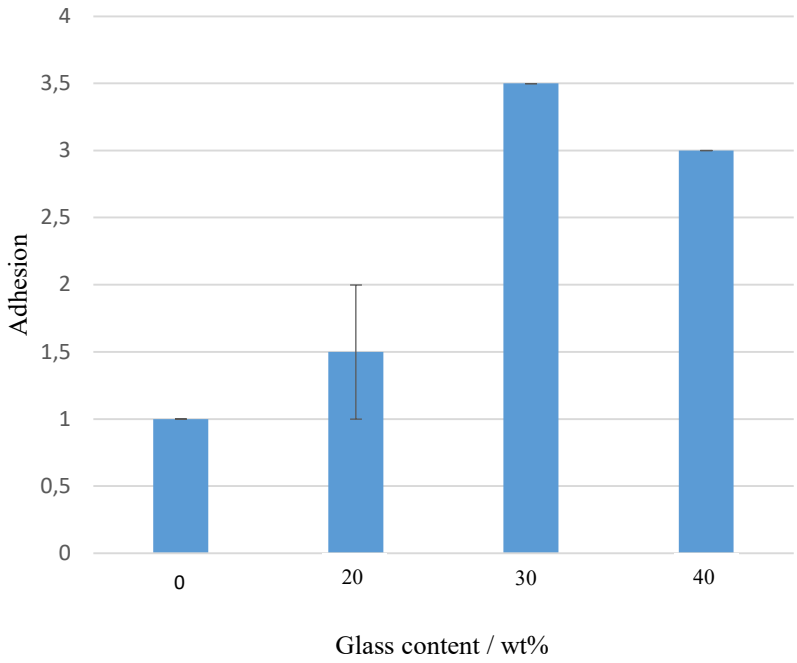


Figure 7. 5: Effect of glass content on the adhesion of TFP glass-polyamide 11 coatings at room temperature.

The adhesion values plotted in Figure 7.5 were measured cutting the coating with a knife following two parallel lines separated by 10 mm along at least 30 mm to form a strip. A chisel knife (10 mm wide) or a penknife with a thin blade is inserted under one extremity of the strip that is pulled out. The results are evaluated by a grade from 0 to 4. Each grade is a description of the coating state. Non- integer values can be used to describe the coating state between two grades.

Figure 7.5 showed an improvement of the adhesion by adding TFP glass to PA11 matrix. The results of 20 wt% glass hybrid show large standard deviation, so the interpretation was done accordingly. The variability on the results at 20 wt% glass, did not allow to determine the trend of the hybrid adhesion at low loadings. In the other

hand, a substantial increase in metal coating adhesion at high glass loadings was present in Figure 7.5. There is an optimum value in adhesion which is more than three times higher comparing with PA11 matrix at a glass content of approximately 30 wt%. Adhesion of 40 wt% glass hybrids were also largely better than the matrix. Nevertheless, it was lower than 30 wt% glass hybrids. The increase of adhesion at room temperature suggests a reinforcement effect of the glass and the fact that lower glass content hybrid has better adhesion can suggest an interaction at this glass content. According to these first results at room temperature, an improvement of adhesion can appear after passing the requirements of the water immersion test.

Unfortunately, the results of water immersion test did not meet expectations. The results were not plotted due to the lack of material for further testing. Few plates were tested, and the results of the test was quotation or grade 0. According to these tested samples, the hybrid had loosened adherence after being immersed 24h in water at 80 °C.

Figure 7.6 and 7.7 are illustrative pictures of adhesion tested metal coating plates. They showed the adhesion test cutting method and the appearance of the metal coating after the test. Figure 7.6 shows PA 11 and 40 wt% glass hybrid metal coating plates after Arkema method adhesion test at room temperature. Three cuts, one V cut and two detachment, were made in order to measure the adhesion of PA11 and hybrids. Although, the results have to be determined after doing the test, the adhesion improvement is appreciable in the pictures. Figure 7.6 a) showed a grade 1 value for PA11 - the coating separates easily but with little resistance to tearing force; while the hybrid picture in Figure 7.6 b), can be defined as Grade 3 - the coating separates irregularly: there is a perfect connection on about 50% of the surface.

a)  b) 

Figure 7. 6: Adhesion test at room temperature; cutting method and the appearance of metal coating: a) PA11; b) 40 wt% glass hybrid coating.

a)  b) 

Figure 7. 7: Adhesion test - immersed in water test (24h 80 °C); cutting method and appearance of the metal coating: a) PA11; b) 40 wt% glass hybrid coating.

For samples pictured in Figure 7.7, three detachments cuts were made to evaluate the coating adhesion after immersion test in water. The aspect of both coatings, PA11 and 40 wt% glass hybrids, revealed grade 0 value - no adhesion, the separation of the coating is done as soon as the tool passes. These unexpected results can be attributed to diverse causes and make difficult the interpretation of the material results.

The hygroscopic character of the glass can be one of the causes of the poor results of the adhesion in water. The glass shows hygroscopic behavior at room temperature for low temperature and short melting time melting conditions. In Chapter 4, in the glass research about glass melting conditions, it was observed that low melting conditions glasses were attacked by atmospheric moisture indicating a lack of chemical durability (section 4.8). A structural change of these glasses over the time was also identified.

The hybridization of PA 11 and TFP glass to process hybrid coating powder materials were done by low melting conditions glass batches, their Tg was 104 °C measured by DSC. So, the glass batches used for developing the tested hybrid coatings, were immersed 24h in water at 80°C, and water contact impact on the glass was evaluated visually. High and low melting conditions glass pieces with similar mass were immersed in water using laboratory testing tubes. The tubes were placed at 80 °C in an oven for 24 h. Pictures in Figure 7.8 were the results of the test. Picture 7.8 a) were glasses synthetized at high melting conditions and 7.8 b) at low melting conditions. The opacity of the water in the tube in the case of low melting conditions glasses, means that glass was dissolved in the water, decomposition of the glass took place during the test.

a)  b) 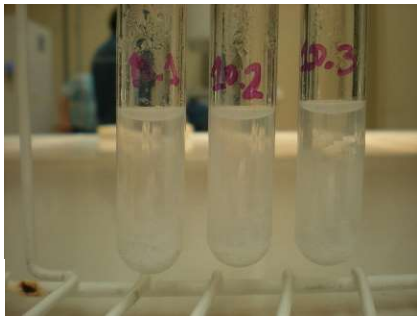

Figure 7. 8: TFP glass after 24 h immersed in water at 80 °C: a) high melting conditions glasses; b) low melting conditions glasses -These glass batches were selected to hybridize with PA11 and produce hybrid powder for coating samples to use in adhesion testing.

The presence of higher metal oxidation was detected in aged hybrid coated plates rather than in aged PA11 coated plates. To discard evidence of any chemical reaction between hybrids and metal that can damage the substrate surface, a roughness test was carried out on steel plates. The standard deviation (SD) was calculated according to n (number of tested samples) equal to 5.

Table 7. 5 : Roughness results of initial steel plate, PA11 and hybrids coated steel plate.

| | | $R_{max}$ /µm | SD | $R_z$ /µm | SD | $R_a$ /µm | SD | $R_t$ /µm | SD |
|---|---|---|---|---|---|---|---|---|---|
| Initial Steel plate | | 75 | 14 | 58 | 7 | 8 | 0,67 | 81 | 13 |
| after 24h 80°C immersed in water | PA11 | 73 | 3 | 57 | 2 | 8 | 0,5 | 75 | 5 |
| | 40 wt% hybrid coating | 63 | 6 | 50 | 1 | 7 | 0,6 | 67 | 5 |

The roughness results are shown in Table 7.5 where $R_a$ is the arithmetic mean deviation of the roughness profile in µm. $R_z$ is the maximum height of the roughness profile in µm. $R_{max}$ is the maximum peak-to-valley height of a base length of the roughness profile in µm and $R_t$ is total height of the roughness profile in µm.

The changes are not enough to indicate any chemical abrasion on the metal surface. They can be related to more prolonged metal water contact. This suggests a higher permeability to the water of hybrid coatings compared to PA11 coatings. To test this hypothesis, which is not in accordance with the theoretical hypotheses made at first (tortuous path - lower permeability of hybrid due to glass nodes in the matrix), two different water resistance tests were carried out.

### 7.3.3 Barrier properties

To corroborate the faster contact of the water with the surface of the substrate in the case of hybrid coatings, water vapour barrier properties were first evaluated for PA11 and 20, 40 wt% glass hybrid coatings. The results are shown in Table 7.6. The barrier properties were expressed in gmm /$m^2$24h, that means a quantity of mass (g) that has diffused for a time (24 h) through a membrane of surface S ($m^2$) and thickness e (mm). The results show that the test value increased after adding the glass, obtaining lower barrier properties for any glass content hybrids. The standard deviation (SD) was calculated according to n (number of tested samples) equal to 5.

Table 7. 6: Water vapour barrier properties of PA11 and TFP glass-PA11 coatings.

| | Thickness of coating/ µm | SD | gmm/$m^2$.24h | SD |
|---|---|---|---|---|
| PA11 | 386 | 5,9 | 1 | 0,04 |
| 20 wt% TFP glass- PA11 hybrid | 364 | 20 | 1,2 | 0,12 |
| 40 wt% TFP glass- PA11 hybrid | 364 | 6,5 | 1,3 | 0,12 |

These results are consistent with those suggested by the roughness measurements, but the coatings were checked by SEM (Figure 7.9) in order to interpret and understand the results better.

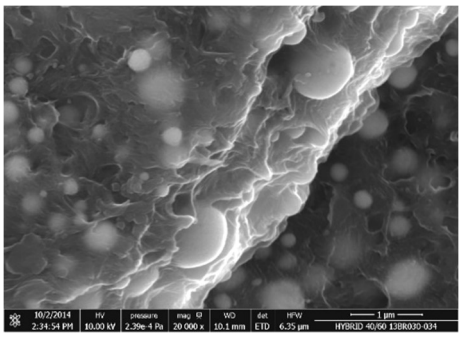

Figure 7. 9: Scanning electron micrographs of glass dispersion on TFP glass-PA11 coatings with glass content of 40 wt% processed at 250 °C, 150 rpm and 5 minutes.

Even if the lower barrier properties could be related to the hydroscopic behaviour of the glass, they might also be related to a heterogeneous dispersion or poor particle/matrix adhesion. Thus, a second water resistance test, the water absorption test, was carried out according to ISO 62. Figure 7.10 shows the water absorption data for

the pure polyamide 11 and 20, 30,40 wt% glass-filled polyamide deposits. The PA11 coating exhibits a high-water permeability due to its affinity with the water. The presence of the glass reduces the amount of water absorption by almost a half and shows a minimum in the absorption percentage at a glass content of approximately 30 wt%. This is the same content, at which the hybrid exhibits the maximum adhesion as shown in Figure 7.5.

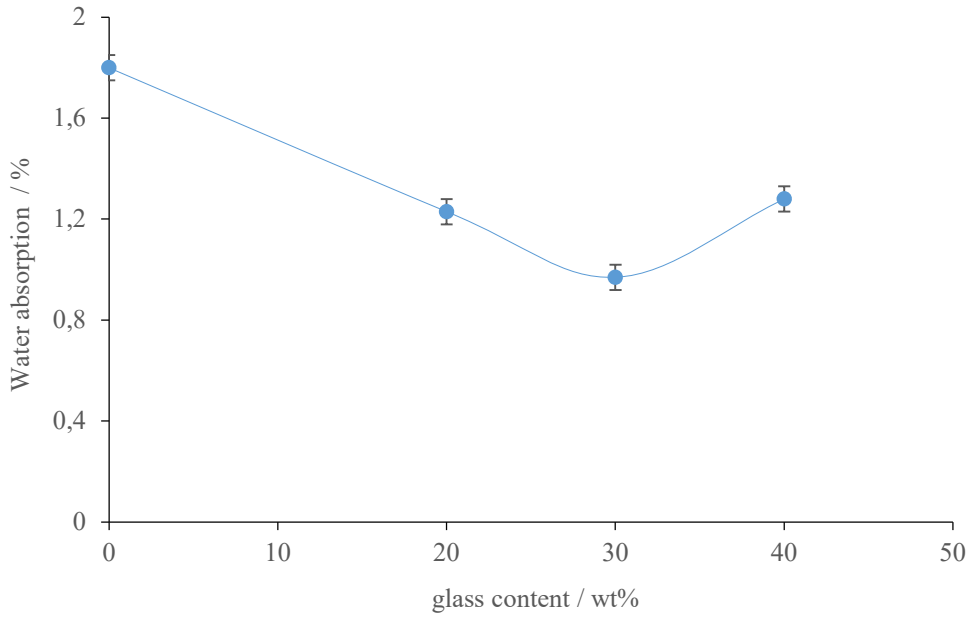


Figure 7. 10: Effect of the glass content on the water absorption of TFP glass-polyamide 11 coatings.

## 7.3.4 Mechanical properties of the coating

### 7.3.4.1 Hardness

The mechanical property hardness is the ability of the material to resist indentation, scratching, abrasion, cutting, and penetration. This property may be important for structural materials that require a high resistance to indentation or abrasion. The hardness of a polymer reflects such other qualities as resilience, durability, uniformity, strength, and abrasion resistance [174].

The hardness of the coatings was measured by the Shore D method. Figure 7.11 shows the influence of the glass content on the hardness for PA11 and glass-filled PA11. Increasing the glass content resulted in an increase in the hardness of the composite,

which indicated that a reinforcement effect was taking place. There is not an optimum value as the theoretical modulus of the glass is higher than the polymer.

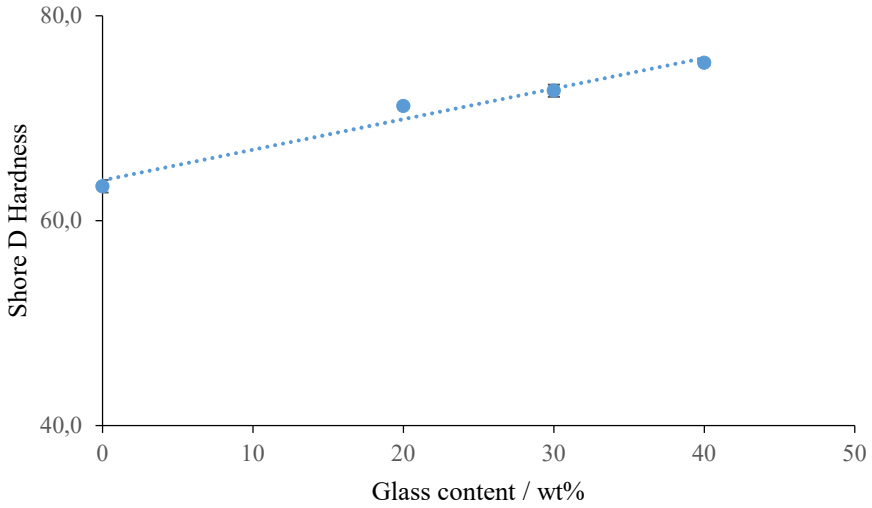


Figure 7. 11: Effect of glass content on the hardness of TFP glass-polyamide 11 coatings.

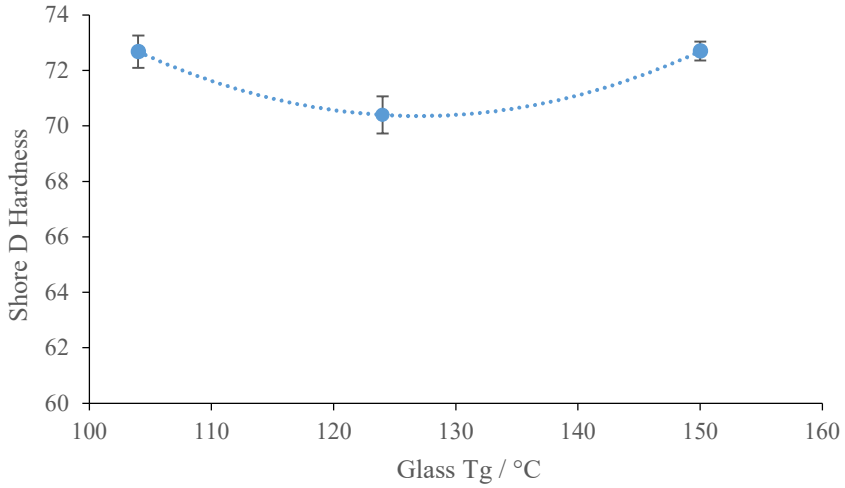


Figure 7. 12: Effect of glass Tg on the hardness of 30 wt% TFP glass-polyamide 11 coatings.

Figure 7.12 shows the influence of the glass Tg on the hardness of the coating. A lower value for the glass with Tg 104 °C was expected as its modulus is also lower. Obtaining such as high hardness value suggests an interaction between filler and matrix as noted before in the DMA results. However, this interaction is not visible in abrasion resistance.

### 7.3.4.2 Abrasion resistance

The abrasion resistance according to ASTM D4060 was measured for PA11 and 20, 30, 40 wt% hybrid deposits. Figure 7.13 shows abrasion data depending on the glass content for the pure polyamide and different compositions of TFP glass-PA11 hybrid coatings. The graphic shows a tendency for an increase of loss of mass percentage with increasing glass content. The increase of loss of mass percentage is proportional to the abrasion resistance decrease. Adding glass is giving worse abrasion resistance of the material, except in the case of 30 wt% glass content. As noted in the laboratory scale research, the 30 wt% glass-PA11 hybrid is not following the trend of the other glass contents, even not in coatings. There were improvements of properties at 30 wt% glass content at laboratory scale and in the application. This suggests something different might be happening at 30 wt% glass content and this is a contributor to the establishment of an optimum glass content. Subsequently, it was interesting to analyse some coating properties such as abrasion, hardness and impact resistance using 30 wt% glass and different Tg glass batches. This will reinforce the research on glass melting conditions justifying the influence of glass melting conditions on the final application.

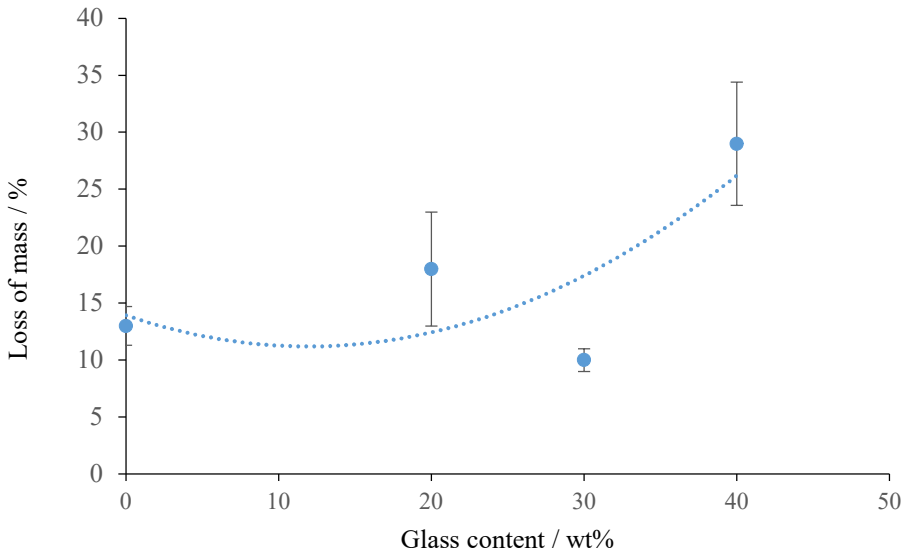


Figure 7. 13: Effect of glass content on the abrasion resistance of TFP glass-PA11 coatings.

Figure 7.14 shows the mass loss obtained in the abrasion resistance test for 30 wt% glass-filled polyamide deposits using three types of glasses. The peculiarity of these glasses is that they have different Tg values of 104 °C, 124 °C and 150 °C, all of them

measured by DSC. The slight decrease of mass loss percentage suggests a better abrasion resistance at higher glass Tg value.

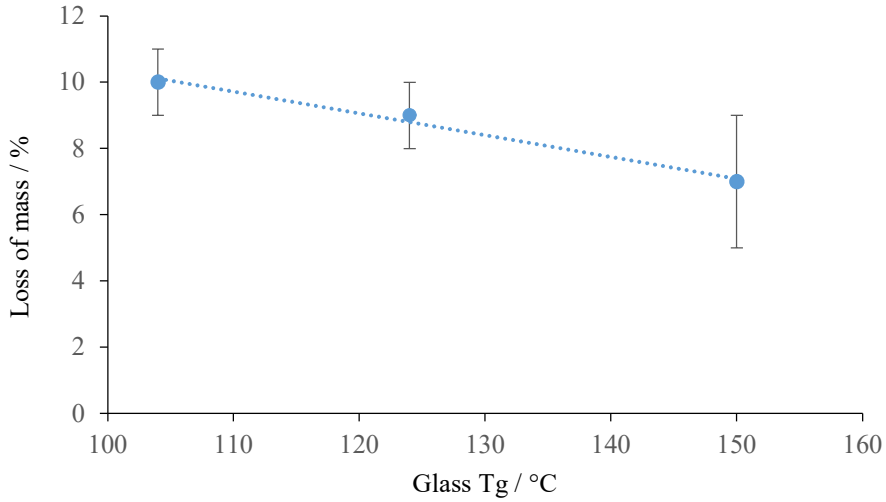


Figure 7. 14: Effect of glass Tg on the abrasion resistance of 30 wt% TFP glass-PA11 coatings.

### 7.3.4.3 Impact resistance

The results obtained during an ASTM G14 test is influenced by various external factors which are difficult to control:

 The thickness of the coating: The average impact energy increases rapidly with the thickness of the coating. It is therefore essential to have similar thicknesses between the plates tested to ensure good reproducibility.

 The viscosity: The viscosity of the powder also has an important influence on the coating behavior. Too low a viscosity results in the film shattering on impact.

Impact resistance of PA11 and hybrids filled with 20,30,40 wt.% glass were measured according to ASTM G14-04. The results plotted in Figure 7.15 show no influence of the glass in the hybrid for impact resistance.

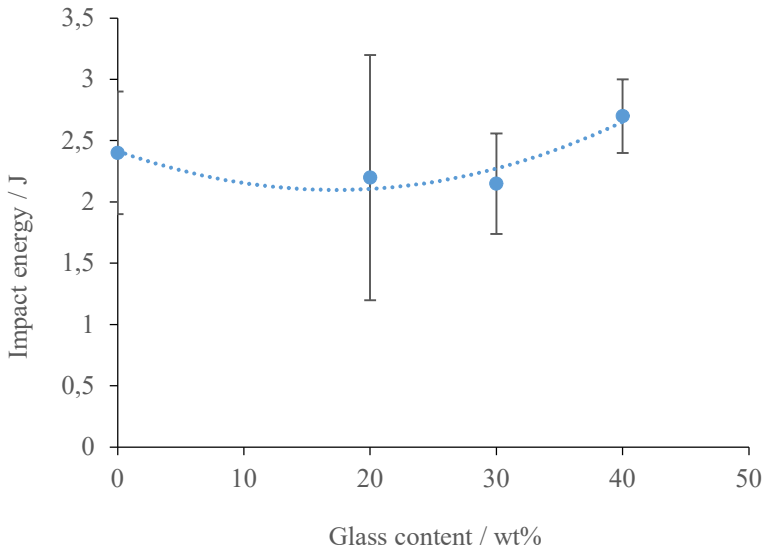


Figure 7. 15: Effect of glass content on the impact resistance of TFP glass-PA11 coatings.

### 7.3.5 Morphology of the hybrid coating

The morphology of the hybrid coating was checked by SEM (Figure 7.16 and 7.17). The presence of pinholes with deepness that can reach to 40 µm were observed on the coating surface. A pinhole is a pore-like penetration that is present in paints and coatings due to the entrapment of moisture, air, solvents, or other fluids. The presence of pinholes increases the corrosion rate experienced on a surface due to the moisture pockets that cause crevice corrosion, pitting and increased redox reactions. In fluidized bed dipping, the pinholes results from insufficient shaking during immersion, too low preheating temperature or too short dipping time. For further work in this subject, it is noted the need to improve shaking and use higher preheating temperature and longer dipping time to avoid pinholes. A research study about the influence of dipping processing parameters on the hybrid coating could be interesting. The hybrid coatings were applied at 300 °C of preheating time and 6 s of dipping time.

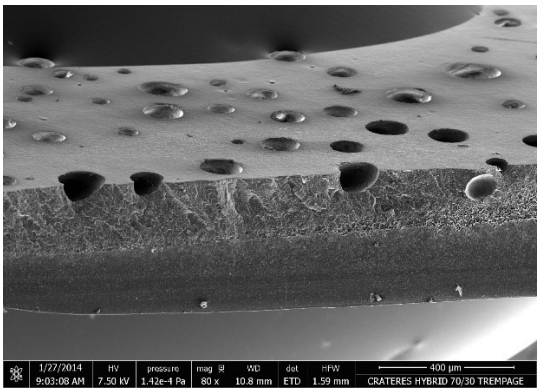


Figure 7. 16: Presence of pinholes on the hybrid coating surface.

The pinhole defect is a key factor to interpret coating characterization results. Thus, the objective is to identify the origin of these pinholes on the hybrid coating. For this, experiments were carried out jointly by microscopy and infrared spectrometry.

To attain the identification of the pinholes origin microscopic observations were focused on the coating surface. Two different areas were selected for analysis of the surface morphology and the composition.

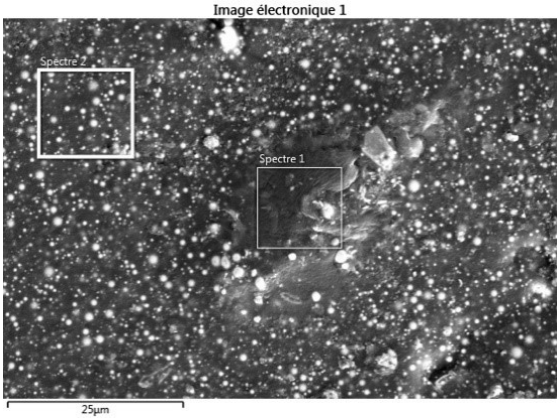


Figure 7. 17: Micrograph of hybrid coating surface area definition for the morphological and compositional analysis to determine the origin of the pinholes. Spectra 1- pinhole deep surface and Spectra 2 – defect free surface.

The surface observation at the bottom of the pinhole shows an area of different morphology from the surrounding matrix, it seems that there are less glass particles here (Figure 7.17). This is confirmed in Figure 7.18 by comparative X-ray microanalysis between the two surface areas. A weaker signal from phosphorus and tin was detected in the spectra 1 and suggest less presence of glass particles.

Spectra 1: pinhole deep surface

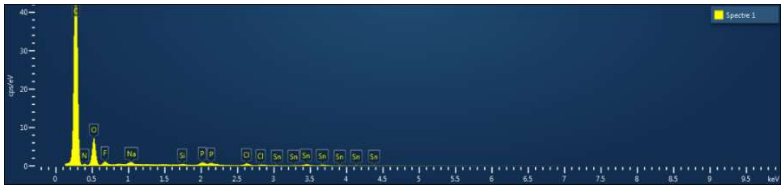

Spectra 2: defect free surface

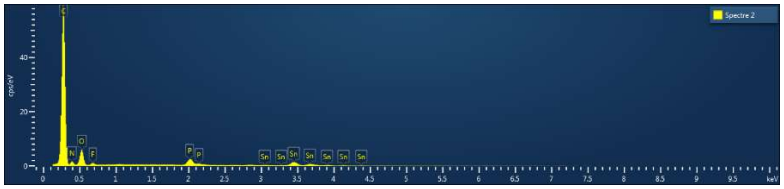

Figure 7. 18: The compositional results of the surface area of spectra 1 (pinhole deep surface) and spectra 2 (defect free surface) by comparative X-ray microanalysis.

The pinhole surface area as well as the surrounding matrix surface area were then analysed by infrared spectrometry (Figure 7.19). Both pinhole and matrix spectra show the characteristic bands of a polyamide (N- H stretching vibration band at 3300 $cm^{-1}$, amide I, C=O stretching vibration at 1650 $cm^{-1}$ and amide II, C-N stretching at 1560 $cm^{-1}$). In addition, a band at 1740 $cm^{-1}$ is observed on both, corresponding to the presence of C = O function, which was not clearly attributed till now. The presence of the broad band around 1020 $cm^{-1}$, with higher or lower absorbance depending on the spectrum sample, is attributed to the tetrahedral phosphate anion vibrations. So, the variation in absorbance of phosphate peak can be related to the quantity of the glass particles present in the surface area. Both SEM and FTIR tests reach to the same conclusion: pinhole defects result in less glass particle surfaces area onto the coating surface.

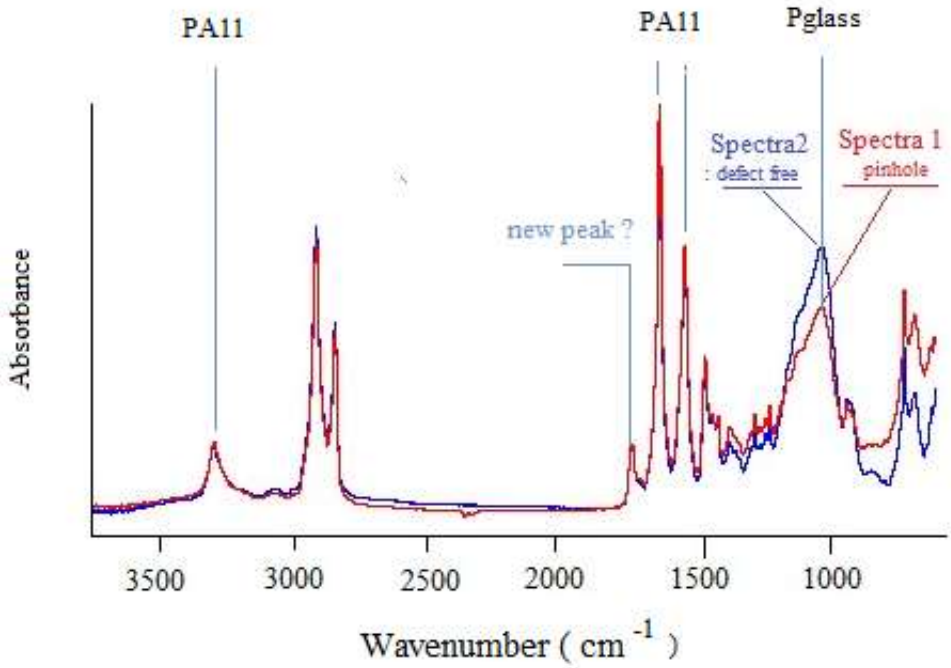


Figure 7. 19: Hybrid coating structural differences between Spectra 1 (pinhole defect surface area) and Spectra 2 (defect free surface area).

The thickness of this hybrid coating was observed by SEM after the cryogenic fracture to evaluate the morphology. Hybrid powder (Figure 7.20) and hybrid coating (Figure 7.21) morphology was compared to evaluate the influence of the dipping technique onto the TFP glass- PA 11 hybrid.

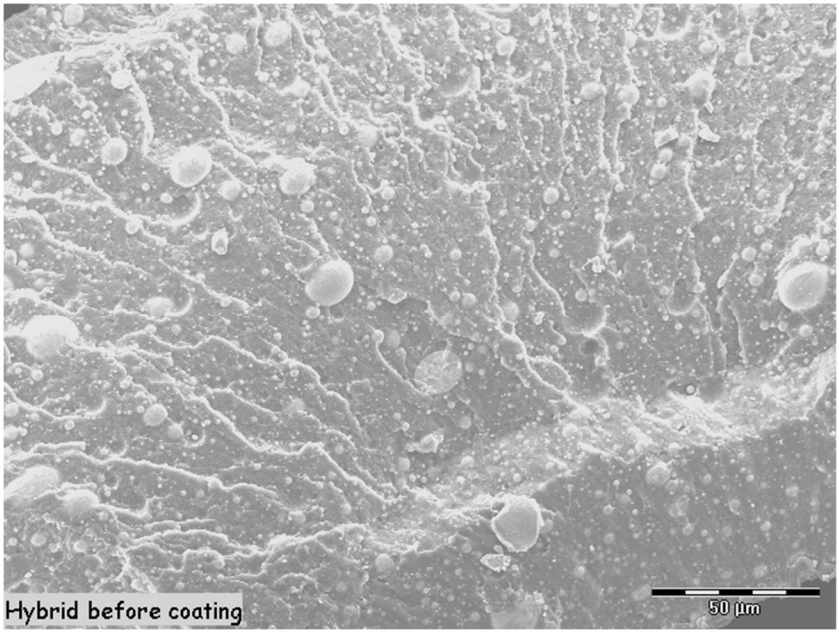


Figure 7. 20: 30 wt% glass hybrid powder morphology.

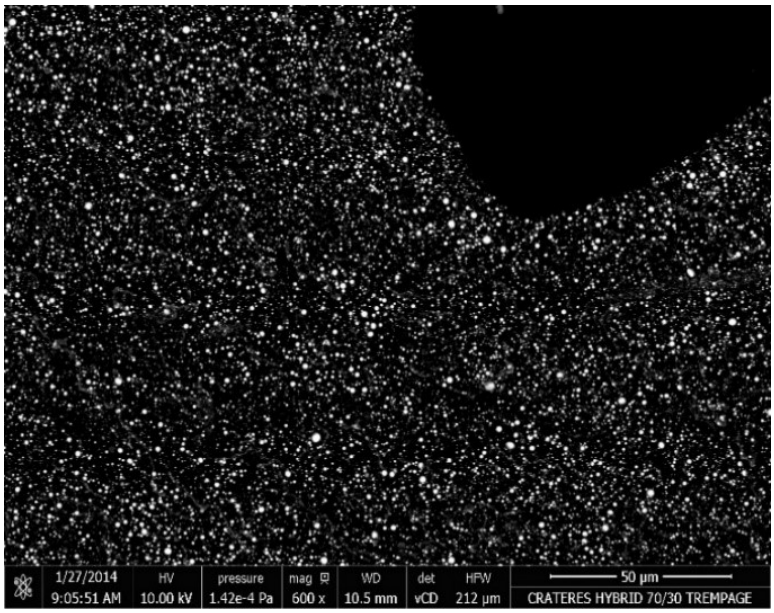


Figure 7. 21: 30 wt% glass hybrid coating morphology.

A major influence of the coating application in the hybrid morphology was observed. In the hybrid coating morphology, the glass particles were dispersed in a fine and homogeneous manner throughout the coating thickness. No problems of aggregation of the glass particles were observed. On the other hand, hybrid powder morphology presents a heterogeneous dispersion and rough particle size range as almost throughout all the morphological results in the thesis.

It was an interesting challenge to work on reaching a state in which both reactants and products are present in concentrations which have no or very little further tendency to change with time, so that there is no observable change in the properties of the system [175] , considering the hygroscopic character of both precursors (sensible to hydrolysis), the unstable composition of glass melts related to glass melting conditions and catalysed PA11 matrix where fluid takes a finite time to attain equilibrium viscosity. The catalyst is for coating application.

The equilibrium state results when the forward reaction proceeds at the same rate as the reverse reaction. The reaction rates of the forward and backward reactions are generally not zero, but equal. Thus, there are no net changes in the concentrations of the reactants and products. This state is known as dynamic equilibrium. Tin fluoride phosphate glass – PA11 hybrid system has hydrolysis reversible reactions, weak bonds

as hydrocarbons that can initiate the chain reaction by the rupture of a free radical bond, highly reactive radicals $PO^{\cdot}$ and $HO^{\cdot}$. So, there are many possible routes to reach the equilibrium state [175].

Without incorporating any additional additives (no antioxidants and no coupling agents) TFP glass – Polyamide 11 hybrid was challenged to identify the mechanism to attain a similar stable state that was close to the dynamic equilibrium.

Finally, the stabilization of TFP glass into the PA 11 matrix was achieved with the fluidised bed dipping coating. This stable state of the hybrid coating morphology is due to an interaction between PA 11 and TFP glass. The achievement of this type of morphology is a substantial advance towards the main goal of the thesis and nanostructured polymer- glass hybrid coatings in general.

The identification of the new peak detected during the analysis of pinhole defects in the hybrid coating FTIR spectrum can provide new insights into the understanding of the interaction between hybrid precursors. The spectra of hybrid precursors were first shown in Figure 7.22 (PA 11) and 7.23 (TFP) glass. Vibrational bonds and their assigments were summarized in Table 7.7 (PA11) and in Table 7.8 (TFP glass).

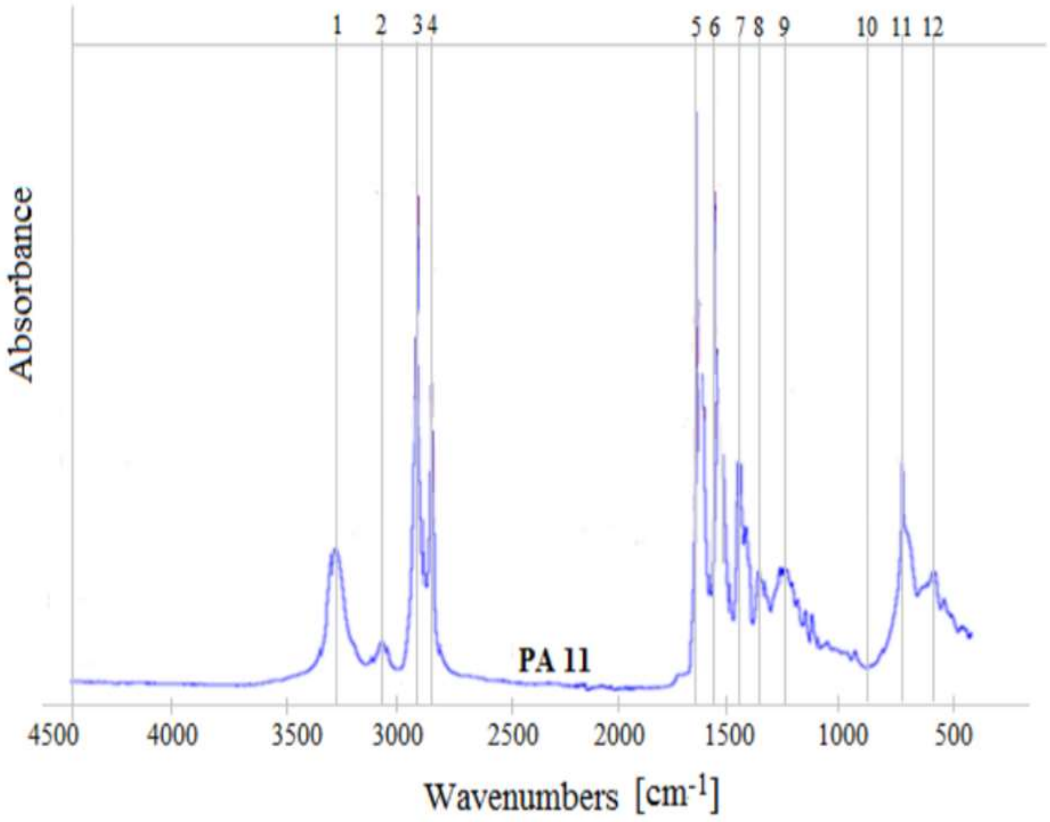


Figure 7. 22: FTIR spectrum of PA 11.

Table 7. 7: The FTIR features observed in PA 11.

| Peak | Wavenumber / $cm^{-1}$ | Assignment / Bonds |
|---|---|---|
| 1 | 3300 | hydrogen-bonded and N–H stretching vibration |
| 2 | 3050 | C=C Cyclic alkene |
| 3 | 2918 | Asymmetric stretching of $CH_2$ |
| 4 | 2848 | Symmetric stretching of $CH_2$ |
| 6 | 1634 | amide I, C=O stretching vibration |
| 7 | 1541 | amide II, C–N stretching |
| 8 | 1466 | CO–N–H bending vibration |
| 9 | 1161 | Interaction between (δ)NH and (ν)O=C-N stretching |
| 10 | 937 | amide IV, (δ)CONH stretching vibration |
| 11 | 721 | CH2 wagging (rocking) |
| 12 | 688 | amide V, N–H out-of-plane bending vibration |

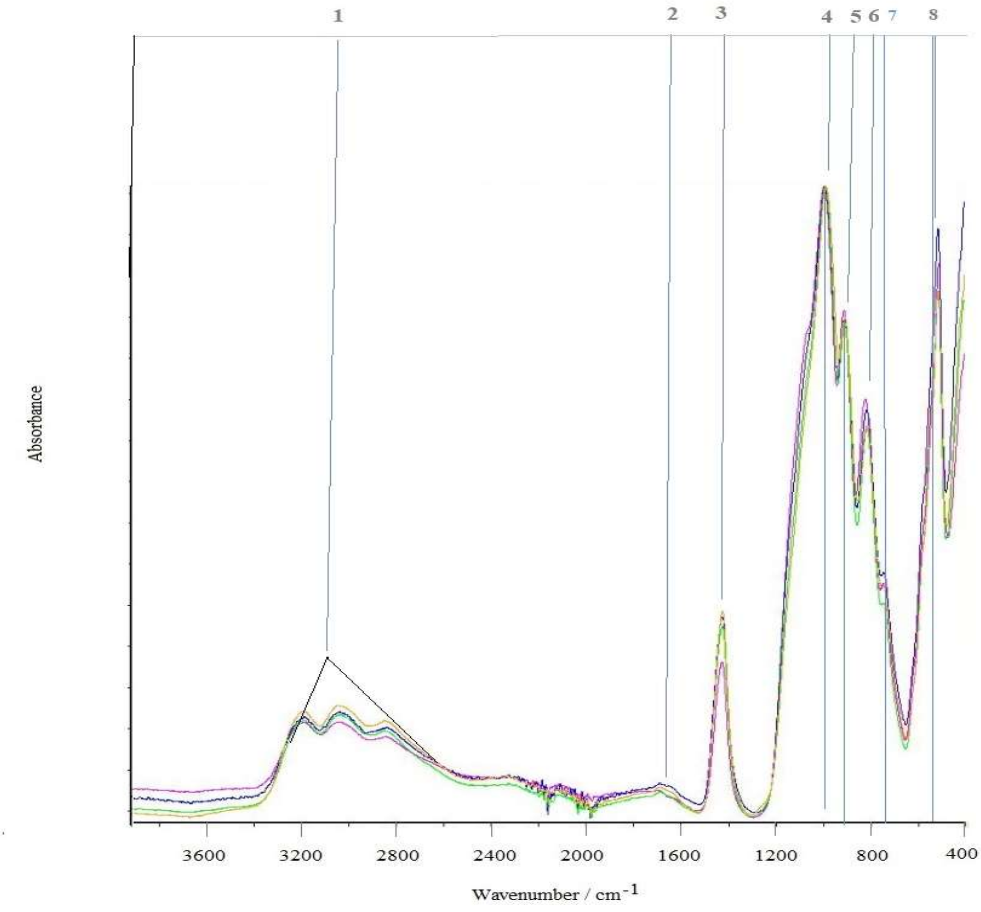


Figure 7. 23: Infrared spectrum of TGP glass scaled- up by GTS glass company.

$NH_4H_2PO_4$ was used to form $P_2O_5$ molecules. Equation 24 shows the equilibrium reaction. The glass was melted using lower parameters than optimal melting condition, furthermore, unreacted $NH_4H_2PO_4$ was present in the spectra. The water detected in the glass can activated the hydrolysis reaction during the melt mixing of the hybrid in any hydrolysable functional group.

Table 7. 8: The FTIR features observed in PA 11.

| Peak | Wavenumber / $cm^{-1}$ | Assigments / Bonds |
|---|---|---|
| 1 | 3249-2874 | Stretching vibration OH- NH |
| 1 | 1642 | Bond vibration of water |
| 3 | 1441- 1408 | Bond vibration of $NH_2$ |
| 3 to 4 | 1240 | (P=O), $Q^3$, superposed by $\gamma_{asy}$ ($PO_2$) |
| 3 to 4 | < 1100 | Vibration, (SnOP), SnPOF glasses |
| 3 to 4 | 1100 | ($PO^-$) $Q^1$, end groups |
| 4 | 1040 | Stretching ($PO_3^{2-}$), $Q^1$ |
| | 990 | POH vibration |
| | 985-990 | ($PO_4^{3-}$), $Q^0$ |
| 5 | 910-925 | (POP), $Q^2$ |
| 6 | 845-850 | PF |
| 7 | 740 | Stretching (POP), Q2 -$Q^1$ dominated; low content of $P_2O_5$ <30%; Short phosphate chains |
| 8 | 545- 439 | Deformation $PO_4$ and vibration SnF vibration |

Spectra superposition of PA 11, hybrid powder and hybrid coating were represented to detect any new peaks, changes of intensity of the peaks, location shift or shape of the peak variability Figure 7.24. Vibrational phenomena associated to provide new structural approach of the Tin fluoride phosphate glass – Polyamide 11 is summarized in Table 7.9.

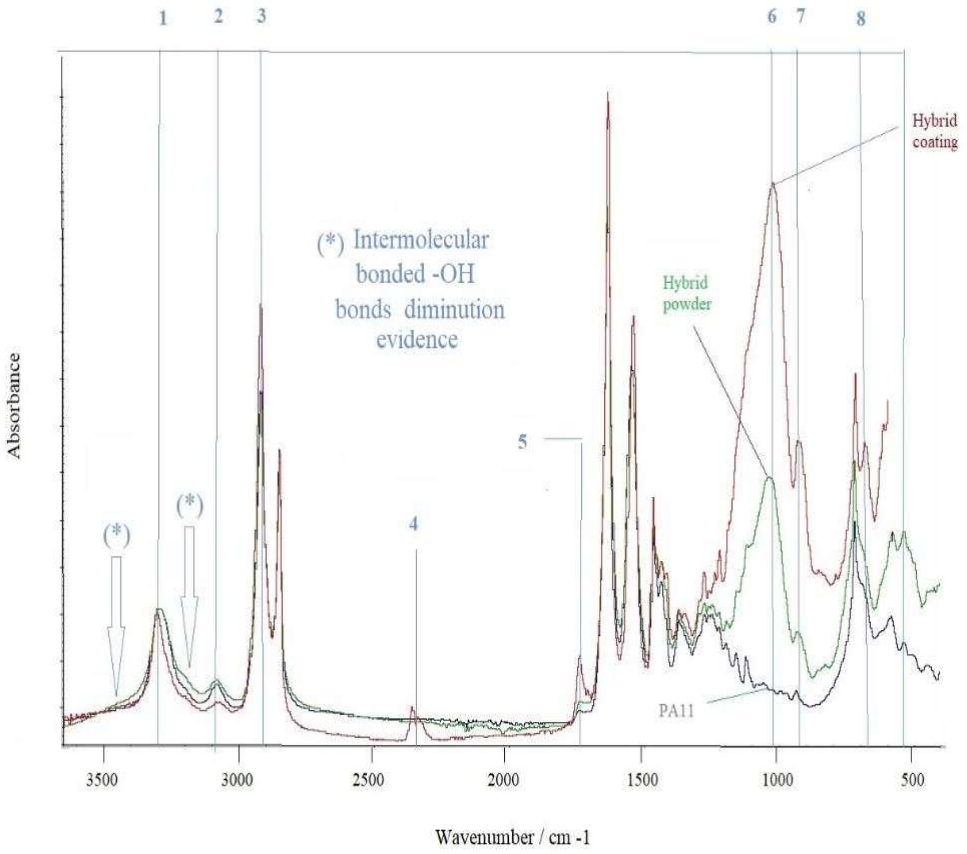


Figure 7. 24: FTIR spectrum of superposed PA11, hybrid powder and hybrid coating.

There is evidence of changes happening during the fluidized bed dipping process as the hybrid coating spectrum shows new phenomena compared with the hybrid powder results. The powder spectrum is the usual result obtained for these materials. The new phenomena are summarized in Table 7.9.

Table 7. 9: The FTIR features observed in TFP glass- PA 11 hybrid coating.

| Peak | Wavenumber / cm $^{-1}$ | Assigments Bonds |
|---|---|---|
| (*) | 3550-3200 | Diminution of intermolecular bonded – OH |
| 1 | 3300 | Amine II, N–H stretching vibration peak upshift |
| 2 | 3050 | Diminution of C- C double bonds ( cyclic alkene) |
| 3 | 2918 | Increase stretching of $CH_2$ ( alkyl) |
| 4 | 2440 -2350 | P-H, impurities |
| 5 | 1750 | New peak of C=O ester ( aliphatic) |
| 6 | 1020 | New peaks P – O – C and ester C-O Phosphate Stretching ($PO_3^{2-}$), $Q^1$ |
| 7 | 910 | (POP), $Q^2$ |
| 8 | 650 | New peak of P- C (aliphatic) |

A common example of ammonolysis is the reaction of a primary amine or secondary amine with a carboxylic acid or with a carboxylic acid derivative to form an amide. In some cases, high temperatures (>200 °C) can overcome salt formation by driving off water, without the need for "activation" of the carboxyl group. The downside to this simple reaction is that the compounds may decompose at these elevated temperatures.

The carboxylic acid derivatives can be esters, anhydrides, acid halides or any other activated species. Depolymerization of the polyamide by hydrolysis (carboxylic acid + amine) give the opportunity to new linkages. The diminution of bonded -OH and shape change, and upshifted secondary amine peak suggest that they are part of the new bonding. A carboxylic acid reacts with the alcohol and is derived in the ester which provides the possibility of forming where after its acyl phosphate [176-177].

A phosphodiester bond occurs when exactly two of the hydroxyl groups in phosphoric acid react with hydroxyl groups on other molecules to form two ester bonds [176]. When a single phosphate or two phosphates known as pyrophosphates break away and catalyse the reaction, the phosphodiester bond can be formed. The decrease of the C=C bonds at 3050 $cm^{-1}$ can be considered as a change of cyclic polymer to linear chains. The cyclic chain opening can be the key for forming small molecule of phosphate ester that link the polyamide 11 with TFP glass [176-177].

## 7.4 Final remarks

Summary of Chapter 7:

(1) Phosphate glass based organic–inorganic hybrid coatings were successfully prepared by reactive extrusion and fluidized bed dipping. The coatings were uniform, macro defect-free and dense.
(2) The results demonstrated that the hybrid coatings were promising surface treatment systems and provided improved adhesion. The increase in adhesion was associated with a reinforcement effect of the glass. The improved adhesion could be attributed to the formation of chemical bonding at the interface.
(3) Hardness tests demonstrated enhanced mechanical properties compared with PA 11 coatings. The hardness and the associated reinforcement were found to increase with glass content.

(4) There were improvements in properties at 30 wt% glass content at the laboratory scale and in the application compared with the PA11 coating. The results indicated that there was an optimum in mechanical properties at 30 wt% glass content.

(5) The analysis of coating properties such as hardness and abrasion, using 30 wt% glass and different Tg glass batches reinforced the research on glass melting conditions and confirmed their influence on practical applications. The results on hardness and DMA suggest there is a significant interaction between the glass phase and the matrix.

# Chapter 8 Contribution to Original Knowledge

## 8.1 Major contribution

This work comprises different findings that contribute original knowledge to the field of developing TFP glass/ PA polymer hybrid coatings.

### 8.1.1 Effects of glass melting process on the structure and properties

The design of phosphate glass/PA hybrids with different glass content for coating application has not been previously attempted. The successful achievement of this project has enabled the establishment of the effect of processing parameters and glass content on properties of hybrids as well as the interactions between the glass and polyamide.

Thirteen low Tg TFP glasses were developed by slightly changing the melting conditions from reference glass (composition: $30P_2O_5$-$50SnF_2$-20SnO and melting conditions: temperature 450°C and 25 minutes). The reference glass was identified as having pyrophosphate $Q^1$ end groups with a smaller presence of $Q^2$ polymeric chains. A pyrophosphate glass was formed from the reference glass rather than polyphosphate as expected from the literature. The reason for these results was the high fluoride content. This induced network depolymerisation in which the F breaks the P-O-P chains and leads to pyrophosphate dimers. Evidence of P-F bonds was found also in the glass structure.

In addition to the above results, it was also found that the formation of the pyrophosphate was attributed to the incomplete conversion of the precursor $NH_4H_2PO_4$ during melting, which produces unreacted $P_2O_5$ for subsequent glass formation. This research established the optimum times and temperatures during the melting process to ensure the complete conversion of $NH_4H_2PO_4$ reagent powder to $P_2O_5$ glass structure.

### 8.1.2 Laboratory-scale and scaling-up methodology for synthesizing phosphate glass/polyamide 11 hybrids for scaling up and manufacturing coatings

Polyamide PA 11 – TFP glass hybrids were prepared for the first time in coating deposition. An important contribution was the finding that the process parameters played an important role on the definition of the morphology of TFP glass/PA 11 hybrids.

The morphology of the hybrid was observed under extrusion processing parameters. SEM micrographs were used to identify the two most influential processing parameters for morphology development: temperature and glass content. Better homogeneity and dispersion of the particles were detected at high glass loadings.

By increasing processing temperature and glass content in the hybrids, the viscosity of the hybrids decreased, which made it possible to improve the processability during extrusion and to manufacture high quality extrudates with enhanced thermo-mechanical properties. The hybrids obtained with higher amount of glass and higher temperature had better properties, in terms of microstructure, fire resistance, thermal, mechanical, and chemical properties.

### 8.1.3 Precursors compatibility approach diagram (Complex viscosity vs Temperature)

One of the major contributions of this thesis was determining the theoretical processing temperature necessary to reach miscibility in the synthesis of glass polymer morphologies (Chapter 6). A plot of complex viscosity against temperature of the precursors can be used to define a suitable processing temperature to produce a homogeneous dispersion and improved properties.

### 8.1.4 First TFP glass/ PA11 hybrid coating produced by dipping in fluid bed

In this research project a method to successfully manufacture phosphate glass/polyamide 11 hybrid coatings by dipping in a fluidized bed was developed. In

the traditional phosphate glass/polyamide hybrids, the base composition $30P_2O_5$-$50SnF_2$-20SnO was always kept constant. In the research by Urman et al. [6], interacting TFP glass/polyamide hybrids were developed. However, no study is available in the literature on the influence of glass melting conditions, glass content and hybridization processing conditions on the hybrid coatings and the hybrid coating properties.

This project successfully developed TFP glass/PA11 hybrids. These materials showed improved fire resistance and adhesion properties over conventional PA11 coatings.

# Chapter 9 Conclusions

## 9.1 Glass

1. Low melting point tin fluoride phosphate glasses have been prepared with glass transition temperature Tg between 97-160 °C. The effect of glass melting conditions on the properties and structure of tin fluoride phosphate glass has been studied.

2. FTIR and RAMAN spectra show different phosphate environments depending on the melting conditions, pyrophosphate species (dimers) being predominant in all of them.

3. The FTIR and Raman spectra peaks of reference glass (melted at 450 °C for 25 minutes) show the presence of P-F and $Q^1$, $Q^2$ phosphate sites confirming the proposed structure. A high content of $Q^1$ sites (corroborated by the peak at 1020 $cm^{-1}$ in Raman spectra) suggest a short chain with mainly $PO_3F$ end groups. The almost disappearance of $NH_4$ confirms the achievement of glass stability at reference glass melting conditions.

4. Divalent tin ($Sn^{2+}$) plays the role of a network former, in tetrahedral coordination, bonding with phosphorus via oxygen (Sn-0-P). A FTIR peak at 1100 $cm^{-1}$ reveals that Sn enters the glass network under reference glass melting conditions, resulting in the formation Sn-O-P linkages. The replacement of P-O-P bonds by Sn-O-P bonds increases the connectivity of the network and decreases it susceptibility to attack by water. Hence an improved chemical durability and thermal stability, as well as an increase in Tg and glass density, was achieved.

5. The glass melted at 550 °C exhibited a decrease in quality comparable with those glasses synthesized at low melting conditions. In both cases, a similar structure of the glass was obtained.

6. The melt rheology of a low Tg tin fluoride phosphate glass was studied and used to guide the selection of optimum processing temperatures with thermoplastic polymers. The influence of the complex viscosity against

temperature was studied. A large decrease of glass viscosity was detected when increasing the temperature making the glass fluid for several polymer processing temperatures. A Newtonian behaviour of the glass was identified at different temperatures.

7. The optimum melting conditions of the glass were identified for developing a nanostructured phosphate glass- polyamide 11 hybrids.

8. Low melting condition and high melting condition tin fluoride phosphate glasses were reheated at hybrid processing conditions in order to study their influence on the structure and properties. It was found that at low melting conditions, the heating atmosphere influenced the structure and showed evidence of structural changes. The structural changes were identified by spectrometry as phosphate sites changed from $Q^1$ to $Q^0$. The structural changes were corroborated by measuring Tg of the glass. A substantial decrease of the Tg was observed in the reheated glass. The structure determines the properties of the final glass, so a decrease of properties was expected. This will have direct negative consequences in hybrid compounding, greatly influencing the final properties of the hybrid.

## 9.2 Hybrids

1. Glass with a molar composition of $50\%\ SnF_2\ + 20\%\ SnO\ + 30\%\ P_2O_5$ was melt-blended with polyamide 11 under different conditions and the hybrids containing up to 60 wt% of glass were obtained. Scanning electron microscopy (SEM) showed affinity and adherence between the glass and the polyamide 11.

2. SEM analysis revealed a major influence of extrusion processing temperature and glass content on the morphology of hybrids. Better homogeneity and dispersion of glass particles in the hybrid were detected at higher process temperatures and higher glass content. The optimum conditions were identified to be 250 °C and higher content than 30 wt% glass.
3. Transmission electron microscopy (TEM) studies revealed nanoparticles of 40 nm in size were formed in the samples processed at a higher temperature of 250 °C. This implies a potential to produce nanostructured hybrids from

macroscopic glass fillers. A diagram of complex viscosity versus processing temperature was developed in order to explain the hybrid morphology formation

4. Dynamic mechanical analysis (DMA) showed two transition peaks in the hybrid loaded with 40 wt% TFP glass, suggesting that it forms a partially miscible system with clear phase separation. The existence of two phases in the hybrids was corroborated by FTIR spectra superposition.

5. An increase in the storage modulus (E') at 23 °C and 150 °C was found for the samples with glass content of 30 wt% with the glass Tg of 103 °C and 160 °C, respectively. This is most likely attributed to an interaction using glass with Tg 103 °C for developing the hybrid and to the higher stiffness of the glass phase in the case of using glass that has a Tg of 160 °C. The storage moduli (E') of the samples with lower glass content are almost the same as that of pure polyamide 11. Tensile testing showed a pronounced reduction in ductility for a high glass content (50 wt%).

6. The fire resistance test reveals a great improvement of fire resistance at high glass loading, after 30 wt % TFP glass.

## 9.3 Coatings

1. It was found that TFP glass-PA11 hybrid with different compositions (0-40 wt% TFP glass) are a suitable material to develop coatings by dipping in a fluidized bed. Coating morphology shows homogenous dispersion, good matrix/particle adhesion and particles between 70-950 nm.

2. An improved surface quality was obtained because the glass contributes to decreasing the viscosity of the hybrid. GPC and mass spectrometry link the decrease of the viscosity to a depolymerisation of the PA11 chain. A substantial decrease of Mw (GPC) was detected for increasing glass content in the hybrid. The sensitivity of PA11 and phosphate glasses to water, or the instability of the glass (reactive end groups), might be the cause of the depolymerisation of the PA11 chain.

3. Hybrid coatings with glass content 30 wt% show better thermal stability. An improved thermal and fire resistance may be useful in a coating application where higher temperature is required.

4. The addition of TFP glass to the PA11 matrix improved greatly the adherence to metal substrates. The origin of the improvement is related to the well-known affinity of the phosphate glasses to the metal. The improvement disappeared when the coating was immersed in heated water. The high sensitivity of P-O bonds to the water might be the cause. Adding conventional compositional modifiers to the initial glass composition may overcome this problem.

5. A reinforcement effect was found in hybrid coatings measured by SHORE D Hardness. Higher values of hardness were obtained with increasing glass content. Collateral effects were the decrease of impact and abrasion resistance.

# Chapter 10 Future works

The following work is proposed for future study.

**Background**. Mixing immiscible polymers in the liquid state may result in various phase morphologies, which can influence adhesion. These morphologies depend on the nature and the relative amounts of the polymers used and on the flow history of the sample. Immiscible polymers behave as different materials at different flow fields. The phase morphology is an important factor in the rheology of immiscible polymer blends. Most binary polymer blends are immiscible. To a large extent, the characteristics of these immiscible polymer blends are determined by the state of the interface between the components. The interaction of two melts at the interface is primarily represented by a quantity k, denoted the interfacial tension, which is the excess free energy caused by the existence of an interface across two dissimilar phases. In more detail, as described below, future work could involve the processing conditions, composition and additives, including compatibilizers.

**Proposed work on mixing sequences** involving compatibilized PLA/PA11 blends. Two different mixing approaches should be studied. The first approach considers one step blending, in which all components are mixed in the extruder simultaneously. The second approach consists of modifying PLA by premixing it with Joncryl in the extruder until an equilibrium state is reached and then adding PA11 by mixing for 3 minutes. Increasing melt strength and elasticity of PLA are expected to influence the compatibilization properties. As a result, blends obtained with the second route are designated “modified PLA/PA11 blends”.

For the PLA/PA11/Joncryl blends obtained with one-step mixing, the SEM micrographs presented in Figure 5 illustrate (i) a notable reduction of the average size of dispersed particles due to a lower interfacial tension; (ii) a significant narrowing of the size distribution of the dispersed phase; (iii) a remarkable decrease of voids at the interface and of empty cavities corresponding to extracted particles; (iv) a better dispersion and more spherical particles of the minor phase; and (v) the disappearance of the co-continuous structure for the 40/60 PLA/PA11 blend. The above structural characteristics and interactions between phases suggest that these factors significantly

affect the adhesion of the material systems and should be included as areas of future study.

**Work to understand the coating systems, adhesion, and properties.** Future work should include an investigation of the compounding process to control the dispersion and interaction of the multiphase materials.

The structure and interfaces of the materials should be investigated by scanning electron microscopy. The software analyses the data in order to carry out a comparative study between different processing conditions and materials. The measurements and the study should be first focused on calculating the particle size mean values. These values are the mean diameter in number (Dn), the mean diameter in volume (Dv) and, therefore, an approximate polydispersity index (Ip).

The work should be aimed at understanding how the processing parameters affect the structure, adhesion, and performance of the material coatings. One such performance parameter is impact resistance and the study should be aimed at providing an improved understanding of this parameter. There is currently no theory to predict the impact resistance of a charged polymer according to the characteristics and the amount of charges introduced. The proposed future work should be aimed at characterizing how the compounding conditions relate to the structure and interfaces, as well as developing an improved understanding of impact performance of this class of materials.

The results demonstrated that the hybrid coatings are promising surface treatment systems, which have the ability to substantially improve the coating adhesion. This enhancement of adhesion appears to be associated with glass reinforcement. Further work is proposed to confirm and understand the mechanisms involved.

# References

[1] M.L Zheludkevich, I.M Salvado, M.G.S Ferreira, Sol-gel coatings for corrosion protection of metals. *Journal of Materials Chemistry*, 15, (2005), 5099-5111.

[2] V.H.V. Sarmento, M.G. Schiavetto, P. Hammer, A.V. Benedetti, C.S. Fugivara, P.H. Suegama, S.H. Pulcinelli, C.V. Santilli, Corrosion protection of stainless steel by polysiloxane hybrid coatings prepared using the sol-gel process. *Surface and Coatings Technology*, 204, (2010), 2689-2701.

[3] B.A. Sunil, J.U. Otaigbe and J. Thalacken, Glass-polymer melt hybrids I: Viscoelastic properties of novel affordable organic-inorganic polymer hybrids. *Polymer Engineering and Science*, 41, (2001), 1055-1067.

[4] Y. Wang, G.P.P Bierwagen, A new acceleration factor for the testing of corrosion protective coatings: Flow-induced coating degradation. *Coatings Technology and Research*, 6, (2009), 429-436.

[5] K. Urman, J.U. Otaigbe, Novel phosphate glass/polyamide 6 hybrids: miscibility, crystallization kinetics, and mechanical properties. *Polymer Science Part B Polymer Physics*, 44, (2006), 441-450.

[6] K. Urman, J.U. Otaigbe, New phosphate glass/polymer hybrids— Current status and future prospects. *Progress in Polymer Science*, 32, (2007), 1462-1498.

[7] K. Urman, D. Iverson, J.U. Otaigbe, Study of the effects of melt blending speed on the structure and properties of phosphate glass/polyamide 12 hybrid materials. *Applied Polymer Science*, 105, (2007), 297-308.

[8] T.A Misev, R. van der Linde, Powder coatings technology: new developments at the turn of the century. *Progress in Organic Coatings*, 34, (1998), 160-168.

[9] L. Lin, G.S. Blackman, R.R. Matheson, A new approach to characterize scratch and mar resistance of automotive coatings. *Progress in Organic Coatings,* 40, (2000), 85-91.

[10] S. Rossi, M. Fedel, S. Petrolli, F. Deflorian, Accelerated weathering and chemical resistance of polyurethane powder coatings. *Journal of Coatings Technology and Research*, 13, (2006), 427-437.

[11] E. Dogan, A.E. Acar, The use of anhydride linkages to increase the glass transition temperatures of polymers containing carboxyl end groups: A perspective in powder coatings. *Progress in Organic Coatings*, 76, (2013), 513-518.

[12] B. Pilch-Pitera, Blocked polyisocyanates containing monofunctional polyhedral oligomeric silsesquioxane (POSS) as crosslinking agents for polyurethane powder coatings. *Progress in Organic Coatings*, 76, (2013), 33-41.

[13] V.A. Vasil'ev, I.V. Korolev, L.N. Mashlyakovskii, Effect of molecular structure of epoxy oligomers with perfluorinated fragments on hydrophobic properties of powder coatings. *Russian Journal of Applied Chemistry*, 87, (2014), 656-663.

[14] X. Jia, S. Zhang, R. Liu, Preparation and characterization of carboxyl-terminated poly (butadiene-co- acrylonitrile)-epoxy resin prepolymers for fusion-bonded-epoxy powder coating. *Journal of Wuhan University of Technology*, 27, (2012), 694-701.

[15] Q. Shi, W. Huang, Y. Zhang, Y. Zhang, Y. Xu, G. Guo, Curing of polyester powder coating modified with rutile nano-sized titanium dioxide studied by DSC and real-time FT-IR. *Journal of Thermal Analysis and Calorimetry*, 108, (2011), 1243-1249.

[16] B.S. Hadavand, M. Ataeefard, H.F. Bafghi, Preparation of modified nano ZnO /polyester/TGIC powder coating nanocomposite and evaluation of its antibacterial activity. *Composites Part B: Engineering*, 82, (2015), 190-195.

[17] E.C. Trottier, S. Affrossman, R.A. Pethrick, Dielectric studies of epoxy/polyester powder coatings containing titanium dioxide, silica, and zinc oxide pigments. *Journal of Coatings Technology and Research*, 9, (2012), 525-539.

[18] M. Puig, M.J. Gimeno, J.J. Gracenea, J.J. Suay, Anticorrosive properties enhancement in powder coating duplex systems by means of ZMP anticorrosive pigment. Assessment by electrochemical techniques. *Progress in Organic Coatings*, 77, (2014), 1993-1999.

[19] M.A.A. El-Ghaffar, N.A. Abdel-Wahab, M.A. Sanad, M.W. Sabaa, High performance anti-corrosive powder coatings based on phosphate pigments containing poly(o-aminophenol). *Progress in Organic Coatings*, 78, (2015), 42-48.

[20] A.Y. Grigoriev, I.N. Kavaliova, A.V. Kupreev, E.E. Dmitrichenko, Friction and wear of polyamide-6 powder coatings gradient-filled by metal nanofilms. *Journal of Friction and Wear*, 34, (2013), 107-113.

[21] M. Vähä-Nissi, Characterization of filled powders for powder coating of paper. *Powder Technology*, 279, (2015), 127-133.

[22] M. Kalaee, S. Akhlaghi, A. Nouri, Effect of nano-sized calcium carbonate on cure kinetics and properties of polyester/epoxy blend powder coatings. *Progress in Organic Coatings*, 71, (2011), 173-180.

[23] M. Zouari, M. Kharrat, M. Dammak, M. Barletta, Scratch resistance and tribological performance of thermosetting composite powder coatings system: A comparative evaluation. *Surface and Coatings Technology*, 263, (2015), 27-35.

[24] D. Piazza, N.P. Lorandi, C.I. Pasqual, L.C. Scienza, A. Zattera, Influence of a microcomposite and a nanocomposite on the properties of an epoxy-based powder coating. *Materials Science and Engineering: A*, 528, (2011), 6769-6775.

[25] S.M Mirabedini, A. Kiamanesh, The effect of micro and nano-sized particles on mechanical and adhesion properties of a clear polyester powder coating. *Progress in Organic Coatings*, 76, (2013), 1625-1632.

[26] M. Puig, L. Cabedo, J.J. Gracenea, A. Jiménez-Morales, J. Gámez-Pérez, J.J. Suay, Adhesion enhancement of powder coatings on galvanised steel by addition of organo-modified silica particles. *Progress in Organic Coatings*, 77, (2014), 1309-1315.

[27] A.N. Khramov, V.N. Balbyshev, N.N. Voevodin, M.S. Donley, Nanostructured sol-gel derived conversion coatings based on epoxy and amino silanes. *Progress in Organic Coatings*, 47, (2003), 207-213.

[28] W.J. van Ooij, D.Q. Zhu, G. Prasad, S. Jayaseelan, Y. Fu, and N. Teredesai, Silane based chromate replacements for corrosion control, paint adhesion, and rubber bonding. *Surface Engineering*, 16, (2000), 386-396.

[29] R.L. Parkhill, E.T. Knobbe, M.S. Donley, Application and evaluation of environmentally compliant spray-coated ormosil films as corrosion resistant treatments for aluminium 2024-T3. *Progress in Organic Coatings*, 41 (2001), 261-265.

[30] R. Kasemann, H. Schmidt, Coatings for Mechanical and Chemical Protection Based on Organic-Inorganic Sol-Gel Nanocomposites. First European Workshop on Hybrid Organic-Inorganic Materials, Chateau de Bierville, France, 8–10 November 1993, pp. 171-180.

[31] F. Yang, G.L. Nelson, PMMA/silica nanocomposite studies: Synthesis and properties. *Journal of Applied Polymer Science*, 91, (2004), 3844-3850.

[32] J.W. Gilman, Flammability and thermal stability of polymer layered silicate (clay) nanocomposites. *Applied Clay Science*, 15, (1999), 31-49.

[33] S. Wang, Y. Hu, R. Zong, Y. Tang, Z. Chen, W. Fan, Preparation and characterization of flame-retardant ABS/montmorillonite nanocomposite. *Applied Clay Science*, 25, (2004), 49-55.

[34] L. Jianguo, G. Gaoping, Y. Chuanwei, Enhancement of the erosion–corrosion resistance of Dacromet with hybrid SiO2 sol–gel. *Surface & Coatings Technology*, 200, (2006), 4967-4975.

[35] R. Zandi-zand, A. Ershad-langroudi, A. Rahimi, Silica based organic-inorganic hybrid nanocomposite coatings for corrosion protection. *Progress in Organic Coatings,* 53, (2005), 286-291.

[36] J. Gallardo, I. Garcia, L. Celis, M.A. Arenas, A. Conde, A. Duran, Effect of sintering temperature on the corrosion and wear behaviour of protective $SiO_2$-based Sol–gel coatings. *Journal of Sol-Gel Science and Technology*, 27, (2003), 175-183.

[37] C.J.T. Landry, B.K. Coltrain, B.K. Brady, In situ polymerization of tetraethoxysilane in poly (methyl methacrylate): Morphology and dynamic mechanical properties. *Polymer*, 33, (1991), 1486-1494.

[38] T. Humplik, J. Lee, S.C. O'Hern, B.A. Fellman, M.A. Baig, S.F. Hassan, M. A. Atieh, F. Rahman, T. Laoui, R. Karnik, E. N. Wang, Nanostructured materials for water desalination. *Nanotechnology*, 22, (2011), 292001.

[39] B. Ercan, E. Taylor, E. Alpaslan, T. J. Webster, Diameter of titanium nanotubes influences anti-bacterial efficacy. *Nanotechnology*, 22, (2011), 295102.

[40] R. Kochetov, A.V. Korobko, T. Andritsch, P.H.F. Morshuis, S.J. Picken, J.J. Smit, Modelling of the thermal conductivity in polymer nanocomposites and the impact of the interface between filler and matrix. *Journal of Physics D: Applied Physics*, 44, (2011), 395401.

[41] A. Okala, A. Usuki, The chemistry of polymer-clay hybrids. *Material Science and Engineering*, C3, (1995), 109-115.

[42] E. Reynaud, T. Jouen, C. Gauthier, G. Vigier, J. Varlrt, Nanofillers in polymeric matrix: a study on silica reinforced PA6. *Polymer*, 42, (2001), 8759-8768.

[43] E.D. Dumain, T. Agawa, S. Goel, A. Toman, A. S. Tse, Cure behaviour of polyester-acrylate hybrid powder coatings. *Journal of Coatings Technology*, 71, (1999), 69-75.

[44] G. Iwamura, T. Agawa, K. Maruyama, H. Takeda, A novel acrylic/polyester system for powder coatings. *Surface Coatings International*, 83, (2000), 285-288.

[45] A. Lafabrier, A. Fahs, G. Louarn, E. Aragon, J.F. Chailan, Experimental evidence of the interface/interphase formation between powder coating and composite material. *Progress in Organic Coatings*, 77, (2014), 1137-1144.

[46] S.R. Taylor, Coatings for corrosion protection: An overview. Encyclopedia of Materials: Science and Technology (second edition), 2001, Elsevier, Virginia, pp. 1274-1279.

[47] Y. Takeshita, T. Sawada, T. Handa, Y. Watanuki, T. Kudo, Influence of air-cooling time on physical properties of thermoplastic polyester powder coatings. *Progress in Organic Coatings*, 75, (2012), 584-589.

[48] V. Girard Amélioration d'un procédé propre de production de poudre de polyamide 11, PhD. Génie des procédés et des produits. Université de Nancy (France), 2011, p.216.

[49] J. Duszczyk, K. Siuzdak, T. Klimczuk, J. Strychalska-Nowak, A. Zaleska-Medynska, Manganese phosphatizing coatings: The effects of preparation conditions on surface properties. *Materials*, 11, (2018), Art.No. 2585: pp. 1-22.

[50] M. Hajisafari, A. Chakerizade, M. Fallah, G. Darband, Characterization of Zn–Mn phosphate coating deposited by cathodic electrochemical method. *Transactions of the Indian Institute of Metals*, 72, (2019), 307–317.

[51] K. Borko, F. Pastorek, J. M. Neslušan, S. Fintová, B. Hadzima, Effect of combined surface treatment on quality and electrochemical corrosion properties of manganese phosphate on HSLA steel domex 700. *Koroze a Ochrana Materialu*, 62, (2018), 45-53.

[52] M.R. Dayyari, A.A. Amadeh, S. Sadreddini, The influence of direct current density on microstructure and corrosion resistance of magnesium phosphate coating via cathodic electrochemical treatment. *Materials Chemistry and Physics,* 199, (2017), 537-542.

[53] P. Rodrigues, M. Terada, R. A. Junior, A. Costa, I. Costa, E. P. Banczek, Niobium pentoxide coating replacing zinc phosphate coating. *Matéria*, 19, (2014), 105-116.

[54] G.B. Darband, M. Aliofkhazraei, Electrochemical phosphate conversion coatings: A review. *Surface Review and Letters*, 24, (2017), Art. No. 1730003: pp.1-12.

[55] I. Zhang, H. Li, Influence of manganese phosphating on wear resistance of steel piston material under boundary lubrication condition. *Surface and Coatings Technology*, 304, (2016), 530-536.

[56] G. Darband, A. Afshar, M. Rabani, Effect of treatment time and temperature on microstructure and corrosion behavior of Zn–Ni electrophosphate coating. *Journal of Alloys and Compounds*, 688, (2016), 596-604.

[57] C. Galvan-Reyes, J.C. Fuentes-Aceituno, A. Salinas-Rodriguez, The role of alkalizing agent on the manganese phosphating of a high strength steel part 2: The combined effect of NaOH and the amino group ($NH_4OH$, mono-ethanolamine and $NH_4NO_3$) on the degradation stage of the phosphating mechanism. *Surface and Coatings Technology*, 299, (2016), 113-122.

[58] L. Ma, X. J. Yang, C. Peng, Q. Yang, Rapid electrochemical phosphating at room temperature. *Asian Journal of Chemistry*, 26, (2014), 5509-5512.

[59] C. Spagnol, E. do Prado Banczek, I. Costa, M. Taras Cunha, A. Lazarin Gallina, M. Tussolini, P. Rodrigues, Corrosion characterization of phosphated carbon steel treated with benzotriazole. *Anti-Corrosion Methods and Materials*, 62, (2015), 379-387.

[60] P. Pokorny, M. Novák, L. Mastny, P. Szelag, V. Brozek, Thermal stability of phosphate coatings on steel. *Metalurgija*, 54, (2015), 489-492.

[61] I. Sivakumaran, V. Alankaram, The wear characteristics of heat-treated manganese phosphate coating applied to AlSi D2 steel with oil lubricant. *Tribology in Industry*, 34, (2012), 247-254.

[62] R. Thomas, M.J. Umapathy, Nano silicon dioxide accelerated zinc phosphate conversion coating on mild steel using decyltriethylammonium bromide as an additive. *Silicon*, 7, (2015), 371-381.

[63] M.R. Dayyari, A. Amadeh, S. Sadreddini, Application of magnesium phosphate coating on low carbon steel via electrochemical cathodic method and investigation of its corrosion resistance. *Journal of Alloys and Compounds*, 647, (2015), 956-958.

[64] X. Zhang, G-Y. Xiao, B. Liu, C-C. Jiang, Y-P. Lu, Influence of time interval on the phase, microstructure and electrochemical properties of hopeite coating on stainless steel by chemical conversion method. *New Journal of Chemistry*, 39, (2015), 5813-5822.

[65] C. Galvan-Reyes, A. Salinas-Rodriguez, J.C. Fuentes-Aceituno, Degradation and crystalline reorganization of hureaulite crystals during the manganese phosphating of a high strength steel. *Surface and Coatings Technology*, 275, (2015), e10-e20.

[66] E. Matin, M.M. Attar, B. Ramezanzadeh, Evaluation of the anticorrosion and adhesion properties of an epoxy/polyamide coating applied on the steel surface treated by an ambient temperature zinc phosphate coating containing Ni 2+ cations. *Corrosion*, 71, (2015), 4-13.

[67] S. Shanmugam, K. Ravichandran, T.S.N. Sankara Narayanan, M.H Lee, A facile electrochemical approach for the deposition of iron-manganese phosphate composite coatings on aluminium. *RSC Advances*, 5, (2015), 988-1008.

[68] A. Nuran, C. Osman Nuri, G. Yapincak, Wear characteristics of traditional manganese phosphate and composite hBN coatings. *Tribology Transactions*, 56, (2013), 1109-1118.

[69] S. Shanmugam, K. Ravichandran, T.S.N. Sankara Narayanan, M. Marappan, Development of permanganate assisted manganese phosphate coating on mild steel. *Corrosion Engineering Science and Technology*, 49, (2014), 719-726.

[70] X-B. Chen, X. Zhou, T. Abbott, M. Easton, N. Birbilis, Double-layered manganese phosphate conversion coating on magnesium alloy AZ91D: Insights into coating formation, growth and corrosion resistance. *Surface and Coatings Technology*, 217, (2013), 147-155.

[71] A. Kumar, S.K. Bhola, J. Majumdar, Microstructural characterization and surface properties of zinc phosphated medium carbon low alloy steel. *Surface and Coatings Technology*, 206, (2012), 3693-3699.

[72] M. Fouladi, A. Amadeh, Comparative study between novel magnesium phosphate and traditional zinc phosphate coatings. *Materials Letters*, 98, (2013), 1-4.

[73] L. Fang, L-b. Xie, J. Hu, Y. Li, W-T. Zhang, Study on the growth and corrosion resistance of manganese phosphate coatings on 30CrMnMoTi alloy steel. *Physics Procedia*, 18, (2011), 227-233.

[74] A. A. Oskuie, A. Afshar, H. Hassannejad, Effect of current density on DC electrochemical phosphating of stainless steel 316. *Surface & Coatings Technology*, 205, (2010), 2302-2306.

[75] G. L. Song, An irreversible dipping sealing technique for anodized ZE41 Mg alloy. *Surface & Coatings Technology*, 203, (2009), 3618-3625.

[76] J.L. Stauffer, Finishing systems design and implementation: A guide for product parameters, coatings, process, and equipment, 1993, Society of Manufacturing Engineers, pp. 132-134.

[77] J. Edwards, Coating and surface treatment systems for metals, 1997, ASM International, Novelty, OH, pp. 214-217.

[78] R.D. Southwick, J. S. Wasylyk, G.L. Smay, J.B. Kepple, E.C. Smith, B.O. Augustsson, The mechanical properties of films for the protection of glass surfaces. *Thin Solid Films*, 77, (1981), 41-50.

[79] J.D.J. Jackson, B. Rand, H. Rawson, Glass surface coatings resistant to mechanical damage. *Thin Solid Films*, 77, (1981), 5-12.

[80] G. P. Halada, C. R. Clayton, The intersection of design, manufacturing, and surface engineering, Handbook of Environmental Degradation of Materials, second edition, Myer Kutz, 2012, pp. 321-344.

[81] T. P. Schuman, Protective coatings for aluminium alloys, Handbook of Environmental Degradation of Materials, 3rd edition, Myer Kutz, 2018, pp. 423-448.

[82] R.G. Buchheit, Corrosion resistant coatings and paints, Handbook of Environmental Degradation of Materials, Myer Kutz, 2005, pp. 367-385.

[83] H. Hosono, Y. Abe, Fast lithium conducting glass-ceramics in the $Li_2O$–CaO–$TiO_2$–$Al_2O_3$–$P_2O_5$ system. *Solid State Ionics*, 44, (1991), 293-297.

[84] H. Hosono, Y. Abe, Porous glass-ceramics with a skeleton of the fast-lithium-conducting crystal $Li_1+xTi_2-_xAl_x$ $(PO_4)_3$. *Journal of the American Ceramic Society*, 75, (1992), 2862-2864.

[85] B. K. Money, K. Hariharan, Lithium ion conduction in lithium metaphosphate-based systems. *Applied Physics A*, 88, (2007), 647-652.

[86] X. Xu, Z. Wen, X. Yang, J. Zhang, and Z. Gu, High lithium ion conductivity glass-ceramics in $Li_2O$-$Al_2O_3$-$TiO_2$-$P_2O_5$ from nano-scaled glassy powders by mechanical milling. *Solid State Ionics*, 177, (2006), 2611-2615.

[87] R. C. Lucacel, M. Maier, V. Simon, Structural and in vitro characterization of $TiO_2$-CaO-$P_2O_5$ bioglasses. *Journal of Non-Crystalline Solids*, 356, (2010), 2869-2874.

[88] N. A. Ghoneim, A. M. Abdelghany, S. M. Abo-Naf, F. A. Moustafa, K. M. Elbadry, Spectroscopic studies of lithium phosphate, lead phosphate and zinc phosphate glasses containing $TiO_2$: effect of gamma irradiation. *Journal of Molecular Structure*, 1035, (2013), 209-217.

[89] H. A. Elbatal, A. M. Abdelghany, F. H. Elbatal, K. M. Elbadry, F. A. Moustafa, UV-visible and infrared absorption spectra of gamma irradiated CuO-doped lithium phosphate, lead phosphate and zinc phosphate glasses: a comparative study. *Physica B: Condensed Matter*, 406, (2011), 3694-3703.

[90] Y. Daiko, H. Yajima, and T. Kasuga, Preparation of porous titanium phosphate glass-ceramics for $NH_3$ gas adsorption with self-cleaning ability. *Journal of the European Ceramic Society*, 28, (2008), 267-270.

[91] S. V. Dorozhkin, Amorphous calcium (ortho)phosphates. *Acta Biomaterialia*, 6, (2010), 4457-4475.

[92] J.Y. Ding, P.Y. Shih, S.W. Yung, K.L. Hsu, T.S. Chin, The properties and structure of Sn-Ca-P-O-F glasses. *Materials Chemistry and Physics*, 82, (2003), 61-67.

[93] I. Konidakis, C.-P. E. Varsamis, E. I. Kamitsos, D. Möncke, D. Ehrt, Structure and properties of mixed strontium-manganese metaphosphate glasses. *Journal of Physical Chemistry C*, 114, (2010), 9125-9138.

[94] D. Möncke, D. Ehrt, Structure and properties of mixed phosphate and fluoride glasses. *Physics and Chemistry of Glasses*, 46, (2005), 67-71.

[95] G. N. Greaves, S. Senz, Inorganic glasses, glass-forming liquids and amorphizing solids. *Advances in Physics*, 56, (2007), 1-166.

[96] G. J. Owens, R. K. Singh, F. Foroutan, M. Alqaysi, C.-M. Han, C. Mahapatra, H.-W. Kim, J. C. Knowles, Sol–gel-based materials for biomedical applications. *Progress in Materials Science*, 77, (2016), 1-79.

[97] M.-S. Yim, K. L. Murty, Materials issues in nuclear-waste management. *Journal of the Minerals Metals & Materials Society*, 52, (2000), 26-29.

[98] R.K. Brow, Review: the structure of simple phosphate glasses. *Journal of Non-Crystalline Solids*, 263, (2000), 1-28.

[99] WH. Zachariasen, The atomic arrangement in glass. *Journal of the American Chemical Society*, 54, (1932), 3841-3851.

[100] J.U. Otaigbe, G.H. Beall, Inorganic phosphate glasses as polymers. *Trends in Polymer Science*, 5, (1997), 369-379.

[101] J R. Van Wazer, Structure and properties of the condensed phosphates. II. A theory of the molecular structure of sodium phosphate glasses. *Journal of American Chemical Society*, 72, (1950), 644-646.

[102] P.A. Tick, Water durable glasses with ultra-low melting temperature. *Physics and Chemistry of Glasses***,** 25, (1984), 149-154.

[103] P.A. Tick, Tin-phosphorus oxyfluoride glass containing aromatic organic compound, US Pat. US4379070, Assgn: Corning Glass Works N.Y., 05.04.1983.

[104] J. Schwarz, H. Tichá, L. Tichý, R. Mertens, Physical properties of PbO-ZnO-P2O5 glasses I. Infrared and Raman. *Journal of Optoelectronics and Advanced Materials,* 6, (2004), 737-746.

[105] J.E. Shelby, Introduction to Glass Science and Technology, Second edition, The Royal Society of Chemistry, Cambridge, UK, 2005, pp. 7-25.

[106] J.P. Fletcher, S.H. Risbud, R.J. Kirkpatrick, MAS-NMR structural analysis of barium aluminofluorophosphate glasses with and without nitridation. *Journal of Materials Research*, 5, (1990), 835-840.

[107] D. Moncke, D. Ehrt, Structure and properties of mixed phosphate and fluoride glasses. *Physics and Chemistry of glasses*, 46, (2005), 67-71.

[108] M. Moan, J. Huitric, M. Mederic, J. Jarrin, Rheological properties and reactive compatibilization of immiscible polymer blends. *Journal of Rheology*, 44, (2000), 1227-1245.

[109] D.R. Paul, C.B. Bucknall, Polymer blends - formulation, Polymer Blends, Wiley, New York, 2000, pp. 35-62.

[110] W. Donald, P.M. Mallinson, B.L. Metcalfe, A. Gerrard, J.A. Fernie, Recent developments in the preparation, characterization and applications of glass- and glass-ceramic-to-metal seals and coatings. *Journal of Materials Science*, 46, (2011), 1975-2000.

[111] C.M. Shaw, J.E. Shelby, Preparation and properties of stannous fluorophosphates glasses. *Physics and Chemistry of Glasses,* 29, (1988), 87-94.

[112] L. Serio, D.T. Gawne, Y. Bao, Effect of tin fluoride content on the structure and properties of phosphate glass-polyamide 11 hybrids. *European Polymer Journal,* 99, (2018), 134-141.

[113] S.B. Adalia, J.U. Otaigbe, Melt rheology of tin phosphate glasses, *Journal of Applied Physics*, 11, (2001), 10-18.

[114] K. Urman, J.U. Otaigbe, Rheology of tin fluorophosphate glass/polyamide 12 in the low concentration regime. *Rheology*, 51, (2007), 1171-1187.

[115] Y.M. Moustafa, K. El-Egili, Infrared spectra of sodium phosphate glasses. *Journal of Non-Crystalline Solids*, 240, (1998), 144-153.

[116] X.J. Xu, D.E. Day, Properties and structure of Sn-P-O-F glasses. *Physics and Chemistry of Glasses*, 31, (1990), 183-188.

[117] S. C Lao, J. H. Koo, T.J. Moon, W. Yong, C. Lam, J. Zhou, B. Hadisujoto, G. Wissler, L. Pilato, Z.P. Luo, Flame retardant intumescent polyamide 11 nanocomposites - Further study, 19th Annual International Solid Freeform Fabrication Symposium, Austin, TX, 2008, pp. 55-66.

[118] E. Giannelis, Polymer layered silicate nanocomposites. *Advanced Materials*, 8, (1996), 29-35.

[119] J.W. Gilman, T. Kashiwagi, J.D. Lichtenhan, Nanocomposites: A revolutionary new flame-retardant approach. *Sampe Journal*, 33, (1997), 40-46.

[120] J. Zhu, A.B. Morgan, J. Lamelas, C.A. Wilke, Fire properties of polystyrene−clay nanocomposites. *Chemistry of Materials*, 13, (2001), 3774-3780.

[121] J. W. Gilman, R. Davis, M. Nyden, T. Kashiwagi , J. Shields, W. Demory, Development of high-throughput methods for polymer nanocomposite research, Springer, Boston, 2003, pp. 415-427.

[122] T. Kashiwagi, E. Grulke, J. Hilding, R. Harris, W. Awad, J. Douglas, Thermal degradation and flammability properties of poly(propylene)/carbon nanotube composites. *Macromolecular Rapid Communications*, 23, (2002), 761-765.

[123] J. H. Koo1, S. Lao1, W. Ho1, K. Ngyuen, J. Cheng, L. Pilato, G. Wissler, M. Ervin, Polyamide nanocomposites for selective laser sintering, Sampe symposium, Covina, CA, 2005, pp. 392-409.

[124] F. Yang, R.A. Yngard, G.L. Nelson, Nanocomposites, San Diego, CA, 2002, pp. 23-25.

[125] A.B. Morgan, C.A. Wilke, Flame Retardant Polymer Nanocomposites, Wiley, New York, NY, 2007, pp 401-421.

[126] S. Hörold, B. Naß, O. Schacker W. Wanzke, A new generation of flame retarded polyamides based on phosphinates, Clariant GmbH, Division of Pigments & Additives, BU Plastic Industries, Ludwig-Hermann-Strasse 100, 86368 Gersthofen, Germany.

[127] UL 94, the Standard for Safety of Flammability of Plastic Materials for Parts in Devices and Appliances testing. Underwriters Laboratories of the United States (UL), Retrieved 17 October 2013.

[128] B. Arkles, Commercial applications of sol-gel-derived hybrid materials. *Materials Research Bulletin*, 26, (2001), 402-408.

[129] D.A. Loy, Hybrid organic-inorganic materials. *Materials Research Bulletin*, 26, (2001), 364-365.

[130] J.D. Mackenzie, Sol-gel research- achievements since 1981 and prospects for the future. *Journal of Sol-Gel Science and Technology*, 26, (2003), 23-27.

[131] A. W. Adamson, The surface tension of solutions. Physical chemistry of surfaces, John Wiley & Sons, New York, 1990, pp 51-105.

[132] W. Souheng, Calculation of interfacial tension in polymer systems. *Journal of Polymer Science Part C: Polymer Symposia*, 34, (1971), 19-30.

[133] L.A. Girifalco, R.J. Good, A theory for the estimation of surface and interfacial energies. I. Derivation and application to interfacial tension. *Journal of Physical Chemistry*, 61, (1957), 904-909.

[134] S.Y. Hobbs, M.E.J. Dekkers, V.H. Watkins, Effect of interfacial forces on polymer blend morphologies. *Polymer,* 29, (1988), 1598-1602.

[135] P.V. Puyvelde, P. Moldenaers, Rheology and morphology development in immiscible polymer blends. *Rheology Reviews*, (2005), 101-145.

[136] A. Rawal, K. Urman, J. U. Otaigbe, K. Schmidt-Rohr, Detection of nanometer-scale mixing in phosphate-glass/ polyamide-6 hybrids by 1H-31P NMR. *Chemistry of Materials*, 18, (2006), 6333-6338.

[137] E. Teunou, D. Poncelet, Batch and continuous fluid bed coating – review and state of the art. *Journal of Food Engineering*, 53, (2002), 325-340.

[138] D. Kunii, O. Levenspiel, Fluidization Engineering, 2nd edition, Butterworth-Heineman, Stonehan, 1991, pp. 337-395.

[139] L.O. Kornum, Rheological characterization of coatings with regard to application and film formation. *Rheologica Acta,* 18, (1979), 178–192.

[140] D. William, Jr. Callister, Jr. David G. Rethwisch, Materials Science and Engineering: An Introduction, 9th edition, Wiley, USA, 2014, pp.634-680.

[141] M.S. Sreekanth, S. Joseph, S.T. Mhaske, P.A. Mahanwar, Effects of mica and fly ash concentration on the properties of polyester thermoplastic elastomer composites. *Journal of Thermoplastic Composite Materials*, 24, (2011), 317-330.

[142]. H. Brody, Orientation suppression in fibers spun from polymer melt blends. *Journal of Applied Polymer Science*, 31, (1986), 2753-2786.

[143] W. Shen, L. Feng, X. Liu, H. Luo, Z. Liu, P. Tong, and W. Zhang, Multiwall carbon nanotubes-reinforced epoxy hybrid coatings with high electrical conductivity and corrosion resistance prepared via electrostatic spraying. *Progress in Organic Coatings*, 90, (2016), 139-146.

[144] R. Houwink, G. Salomon, Adhesion in paint technology-Adhesion and Adhesives, Second edition, Elsevier Publishing, Amsterdam, 1965, pp. 441-471.

[145] I.J. Zvonkina, Adhesion of polymer coatings: Principles and evaluation, Springer International Publishing, Switzerland, 2016, pp. 605-617.

[146] T.G Mezger, The rheology handbook : for users of rotational and oscillatory rheometers, 2nd Edition, Vincentz Network, Hannover, 2006, pp. 245-251.

[147] D. Salomon, H. Zhai, Ranking asphalt binders by activation energy for flow. *Journal of Applied Asphalt Binder Technology*, 2, (2002), 52-60.

[148] S.W. Haider, M. W. Mirza, A. K. Thottempudi, J. Bari, G. Y. Baladi, Characterizing temperature susceptibility of asphalt binders using activation energy for Flow. In Transportation and Development Institute Congress 2011: Integrated Transportation and Development for a Better Tomorrow, 2011, pp. 493-503.

[149] M. Garcı´a-Morales, P. Partal, F. J. Navarro, F. Martı´nezBoza, C. Gallegos, N. Gonza´lez, O. Gonza´lez, M. E. Mun˜oz, Viscous properties and microstructure of recycled eva modified bitumen. *Fuel*, 83, (2004), 31-38.

[150] R.A. Ellis, Review of applications of G.P.C.: Part 1. *Pigment & Resin Technology*, 2, (1973), 5-10.

[151] A.H. Kuptsov, G.N. Zhizhin, Handbook of Fourier Transform Raman and Infrared Spectra of Polymers, 1st Edition, Elsevier Science, Amsterdam, 1998, pp. 8-32.

[152] R.F. Egerton, Physical principles of electron microscopy, an introduction to TEM, SEM, and AEM, Springer International Publishing, Switzerland, 2016, pp. 121-147.

[153] R.F. Egerton, Physical principles of electron microscopy, an introduction to TEM, SEM, and AEM, Springer International Publishing, Switzerland, 2016, pp. 55-88.

[154] F. Mammeri, E. Le Bourhis, L. Rozes, C. Sanchez, Mechanical properties of hybrid organic-inorganic materials. *Journal of Material Chemistry*, 15 (2005), 35-36.

[155] J. Amirthalingam, J. Murugan, B. Neelakantaprasad, G. Rajarajan, FTIR, XRD, SEM, TGA investigations of ammonium dihydrogen phosphate (ADP) single crystal. *International Journal of Computer Applications*, 53, (2012), 15-18.

[156] W. P. Cox, E. H. Merz, Correlation of dynamic and steady flow viscosities. *Journal of Polymer Science*, 28, (1958), 619-622.

[157] B. Nandan, L. D. Kandpal, G. N. Mathur, Poly (ether ether ketone)/Poly(aryl ether sulfone) blends: Melt rheological behavior. *Journal of Polymer Science, Part B: Polymer Physics*, 42, (2004), 1548-1563.

[158] J.U Otaigbe, C. J. Quinn, G. H. Beall, Processability and properties of novel glass-polymer melt blends. *Polymer Composites*, 191, (1998), 18-22.

[159] C.J. Quinn, P. Frayer, G. Beall, Glass-polymer melt blends, Polymeric Materials Encyclopedia, J. C. Salamone CRC Press, New York, 1996, pp. 2766-2777.

[160] R.T. Young, M. A. McLeod, D. G. Baird, Extensional processing behavior of thermoplastics reinforced with a melt processable glass. *Polymer Composites*, 21, (2000), 900-917.

[161] B. Graebling, R. Muller, Linear viscoelastic behaviour of some incompatible polymer blends in the melt. Interpretation of data with a model of emulsion of viscoelastic liquids. *Macromolecules*, 26, (1993), 320-329.

[162] G.Y. Choi, H.G. Kim, Y.H. Kim, C.W. Seo, J.H. Choi, D.H. Han, D.H. Oh, K.E. Min, The rheological behaviour of immiscible polymer-blends. *Applied Polymer Science*, 86, (2002), 917-924.

[163] Y. Fang, P.J. Carreu, P.G. Lafleur, Thermal and rheological properties of mLLDPE/LDPE blends. *Polymer Engineering and Science*, 45, (2005), 1254-1264.

[164] G. Giridhar, R.K.N.R. Manepalli, G. Apparao, Thermal and rheological measurement techniques for nanomaterials characterization, Chapter 3 - Size-exclusion chromatography, Elsevier, Switzerland, 2017, pp. 51-65.

[165]https://www.agilent.com/cs/library/technicaloverviews/Public/59907890EN.pdf

[166] Y. Bazilevs, I. Akkerman, Large eddy simulation of turbulent Taylor–Couette flow using isogeometric analysis and the residual-based variational multiscale method. *Journal of Computational Physics*, 229, (2010), 3402-3414.

[167] S.H. Jafari, A. Yavari, A. Asadinezhad, H.A. Khonakdar, F. Bohne, Correlation of morphology and rheological response of interfacially modified PTT/ m- LLDPE blends with varying extent of modification. *Polymer*, 46, (2005), 5082-5093.

[168] F. Fenouillot, P. Cassagnau, J.C. Majeste, Uneven distribution of nanoparticles in immiscible fluids: Morphology development in polymer blends. *Polymer*, 50, (2009), 1333-1350.

[169] H. Merkus, Particle Size Measurements, Springer, Netherlands, 2009, pp. 259-285.

[170] S. Semion, E. Rabinovich, H. Kalman, Typical fluidization characteristics for Geldart's classification groups. *Particulate Science and Technology*, 32, (2014), 197-205.

[171] R.F. Cocco, F. Shaffer, R. Hays, S. B. R. Karri, T. Knowlton, Particle cluster in and above fluidized beds. *Powder Technology*, 203, (2010), 3-11.

[172] N. Epstein, J.R. Grace, Spouting of particulate solids in handbook of powder science and technology, Springer, New York, 1997, pp.532-567.

[173] https://www.rilsanfinepowders.com/en/processing/

[174] R. P. Wool, X. S. Sun, Bio-Based Polymers and Composites, Academic Press, NY, 2005, pp. 56-113.

[175] P. Atkins, J. De Paula, Atkins' Physical Chemistry (8th ed.). W. H. Freeman, Oxford, 2006, pp. 200-202.

[176] A. Rodriguez-Galan, L. Franco, J. Puiggali, Degradable Poly (ester amide)s for Biomedical Applications. *Polymers*, 3, (2011), 65-99.

[177] T-S. Fu, Y-H. Wei, P-Y. Cheng, I-M. Chu, W-C. Chen, A novel biodegradable and thermosensitive Poly(Ester-Amide) hydrogel for cartilage tissue engineering. *BioMed Research International*, 2018, (2018), 1-12.

[178] Rilsan PA 11. [ONLINE] Available at: http://www.arkema.com/en [Accessed 28 March 2015].

[179]https://www.rilsanfinepowders.com/en/

[180] https://www.rilsanfinepowders.com/en/processing/fluidized-bed-dipping/

# Appendix A: Polyamide

The information that is in Appendix A is taken from Arkema database [178]. Polyamides represent one of the most commonly synthetic polymers family used throughout the world. These materials are linear polymer and thus members of the so-called engineering thermoplastics.

Polyamides, developed by Wallace Carothers at the Dupont chemical company in the 1930s, have the common feature that the amide (–CONH–) linkage in their backbone (see Figure A.1)

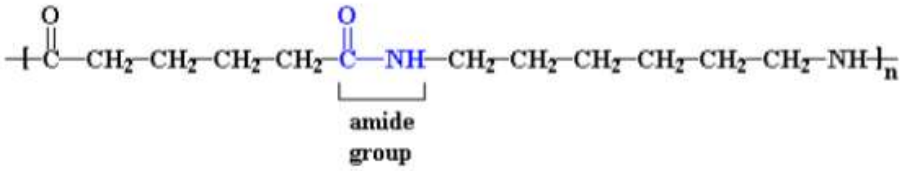


Figure A .1: Amide group of polyamides.

Polyamides are identified by a numerical suffix that specifies the numbers of carbon atoms in the monomer chains. Amino acid polymers are designed by a single number, as Polyamide 6 (see Table A.1). Polyamides from diamines and dibasic acids are designed by two number, the first representing the carbon atoms in the diamine, the second representing the carbon atoms in the acid. An example is polyamide 66 (see Table A.1).

The polar amine groups lead to the very regular and symmetrical polyamide backbone, characterized by a high degree of crystallinity. As a matter of fact, the polar amide groups, spaced out at regular intervals, lead to a high intermolecular attraction among the polyamide chains. These groups are responsible for the high resistance to swelling and dissolution in hydrocarbons, high stiffness and heat deformation resistance, increasing in water absorption, reducing electrical insulation resistance, particularly at high frequencies.

The hydrogen bonding between chains improves the inter-chain interaction, greatly influences the overall crystallinity. Crystallinity can also be controlled by processing condition. Slow cooling will lead to greater crystallinity, around 50-60%, versus 10%

crystallinity after rapid cooling. Cooling speed also affects the size of crystallites, which will be larger for slowly cooled polyamides.

Additionally, the polymer chains have aliphatic segments, which confer flexibility to the amorphous region, giving polyamides low melt viscosity for easy processing. The combination of high inter-chain attraction in the crystalline zone and flexibility in the amorphous zone, leads to polyamides polymers, which are tough above their apparent glass transition temperatures. Thus, an important variable that affects polyamides properties is the concentration of the amide groups (CONH–) in the polymer chain. As a rule, the higher the concentration of the amide groups (lower the $CH_2$/CONH ratio), the higher intermolecular attraction, the shorter the distance the amide groups, the higher the:

- Density
- Forced required to mechanically separate the polymer molecules and hence the higher.
- Tensile strength
- Rigidity
- Hardness
- Resistance to creep
- Melting Temperature
- Heat deflection Temperature
- Water absorption

The ratio between the $CH_2$ and CONH groups, which controls the amount of crystallinity, has a large effect on most properties of polyamides and is the most important differentiator between polyamide polymers. Polyamides like polyamide 66, which are made of diamines and dibasic acids, tend to crystallize more thanks to their lower $CH_2$/CONH ratio (higher CONH groups concentration). On the other hand, polyamide 11, polyamide 12 and other polyamides prepared of aminoacids or lactams tend to have lower crystallization (higher $CH_2$/CONH ratio). The $CH_2$/CONH ratios of the considered polyamides are summarized in the following table:

Table A .1 $CH_2$/CONH ratios of polyamides.

| Polyamide | Formula | $CH_2$/CONH Ratio |
|---|---|---|
| 66 | 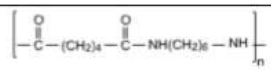 | 5 |
| 6 | 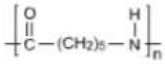 | 5 |
| 11 | 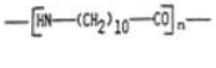 | 10 |
| 12 | 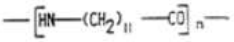 | 11 |

Polyamides have a good combination of the following properties over a relative wide temperature and humidity range: good tensile strength, good flexible properties, light weight, toughness, wear and abrasion resistance, low coefficient of friction, high chemical resistance (to oils, greases, aliphatic and aromatic hydrocarbons), good electrical insulation properties.

Polyamides are very sensitive to heat and should be washed and dried on cool settings. Polyamide can also be hung dry.

Rilsan PA 11 is a reference in the world of performance polyamides. Continuously developed by Arkema for more than fifty years, this polymer is produced from a renewable source (castor oil), and is used in a large number of applications thanks to its outstanding properties: excellent resistance to chemicals (particularly hydro-carbons), ease of processing, a wide range of working temperatures (-40 °C/+130 °C), high dimensional stability and low density to name a few. Rilsan PA 11 is easy to process, using most processing technologies (extrusion, extrusion-blow moulding, injection moulding and roto-moulding). For this reason, many industries around the world (automotive, transport, textile, oil and gas, wire & cables, electronics) have used Rilsan PA 11 for decades.

## A.1 Physical properties

Compared to other high-performance polymers, the Rilsan family and more specifically Rilsan PA 11 offers very low density some 3 to 6 times lighter than metal (see Figure A.2). This is a significant economic advantage when studying the cost versus performance aspect of using Rilsan PA 11.

Among all performance polyamides, the Rilsan family and more specifically Rilsan PA 11 has very low moisture pick-up. Other polyamides feature a more hydrophilic behaviour resulting from the polarity of the amide functions (Figure A.3). Thanks to its low concentration of amide groups, Rilsan PA 11 can be used in a wide range of humidity environments. This low moisture pick-up results in outstanding dimensional stability of final parts made out of Rilsan PA 11. The absorption characteristics of Rilsan PA 11 are similar when it is exposed to other polar liquids such as alcohols, acids and esters.

A low concentration of methylene ($CH_2$) groups lead does shorter distance between CONH groups causing an increase of the overall density. Thus PA 11, together with PA 12, has the lowest specific gravity.

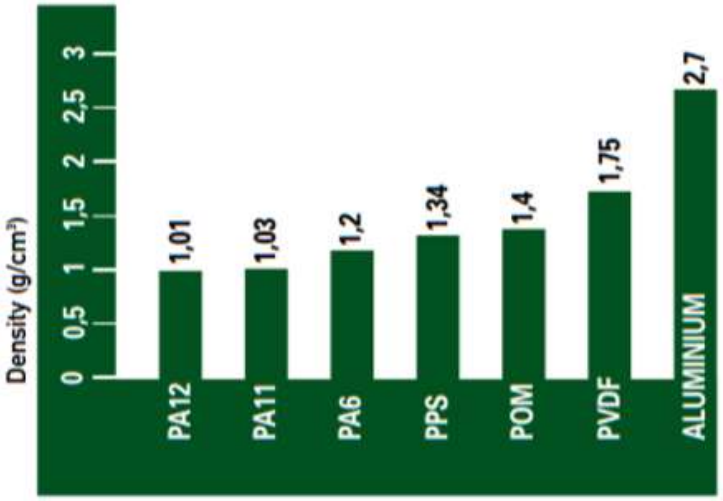


Figure A .2 : Comparative density of Rilsan® PA 11 and PA 12 vs various engineering polymers and aluminium, per ISO 1183 standard.

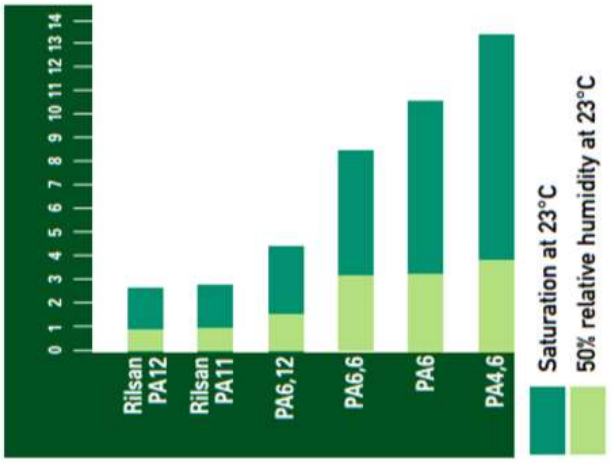


Figure A .3 : Water absorption based on relative moisture rate of Rilsan® PA 11 and PA 12 vs various polyamides (ISO 62 standard).

## A.2 Thermo-mechanical properties

Rilsan PA 11 is a semi-crystalline thermoplastic polymer featuring 2 phase transitions:

- Melting range between 180 °C and 189 °C (depending on the grade), which corresponds to fusion of the crystalline phase (see for comparison with other polyamides).
- A glass transition temperature (Tg) of around 45° C (measured via DSC), corresponding to transition of the amorphous phase.

Rilsan PA 11 offers good thermal stability and can be used continuously at 125 °C under certain conditions. Additionally, it can withstand intermittent peaks of up to 150 °C. It can also withstand cold temperatures, and maintains its impact resistance at -40 °C. For extreme climatic conditions, a special grade is available which can withstand temperatures down to 60 °C. Rilsan PA 11 is the only polyamide in the world capable of performing in such harsh environments.

The melting point of polyamide influences properties such as heat distortion temperature and softening point. The lower the melting point, the lower is the deflection temperature. A low melting point favours the processing conditions because the resulting melt is less sensitive to oxidation and degradation. Above the melting point, the melt viscosity is low because of increasing of atomic oscillation at such high temperatures, which are usually more than 200 ℃ above the Tg.

The glass transition temperature of aliphatic polyamides is of secondary importance to melting point. Dried polyamides have Tg values around 50 °C; when moisture has been absorbed Tg can go as low as 0 °C. Tg can have an effect on the crystallization of polyamides; for example, polyamide 66 at room temperature may be above its Tg; as crystallization will occur slowly it may lead to post mould shrinkage. This is less significant for polyamide 6.

The effect of relative humidity on dimensional thermal stability is shown in Figure A.4. The dimensional change is low in PA 11, like in and PA 12, and increase in PA 6 and PA 66.

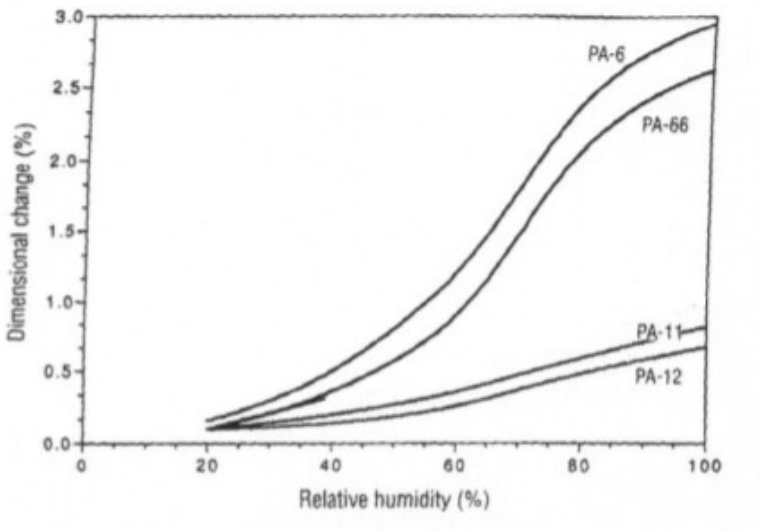


Figure A .4 : Dimensional stability versus relative humidity at 20 ˚C.

## A.3 Mechanical properties

Rilsan PA 11 exhibits excellent mechanical properties over a wide temperature range. It has high elongation at break and high tensile strength at break and at yield. It is one of the toughest high-performance polymers and is therefore used extensively in engineering applications. At ambient temperature, the tensile strength of rigid (unmodified) Rilsan PA 12 leads to noticeable necking at around 20% elongation. In the same conditions, rigid Rilsan PA 11 first produces diffuse necking, up to 40% elongation, beyond which necking occurs (see Figure A.5). Thus, Rilsan PA 11 provides a significant safety factor in mechanical stress over PA 12.

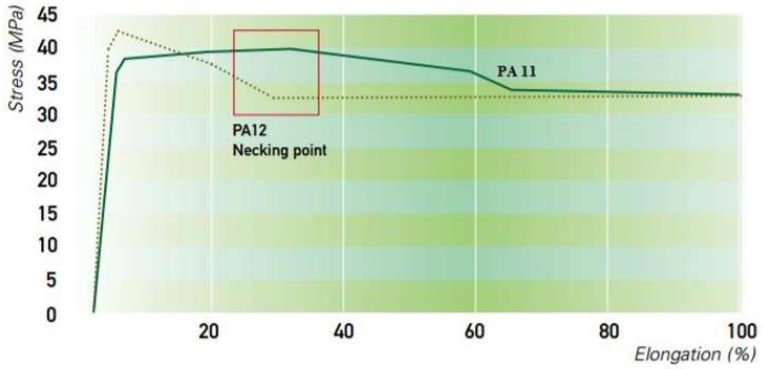


Figure A .5 : Comparative tensile strength curves for Rilsan® PA 11 and PA 12 at 23 °C (ISO 527 standard).

This very different performance can be attributed to the greater strength of the Rilsan PA 11 crystallites (triclinic/hexagonal) compared to the Rilsan PA 12 crystallites (monoclinic).This better stability of Rilsan PA 11 compared to Rilsan PA 12, observed above with rigid grades also applies to plasticised grades across the entire temperature range from 23 °C to the melting point. The difference increases with temperature. A very significant consequence of this difference in behaviour in actual use is that, at equivalent modulus, a Rilsan PA 11 plasticised tube exhibits a higher burst pressure than its Rilsan PA 12 counterpart.

Rilsan PA 11 is available in a wide range of flexibility. The modulus varies from 1200 MPa for non-plasticised grades to around 150 MPa for plasticised grades. Adding specific fillers (glass fibre, carbon fibre, etc.) enable an increase in modulus up to 8000 MPa. In dry conditions, PA 6 and PA 66 have significantly higher rigidity than Rilsan PA 11. After moisture pick-up however, the flexural properties of Rilsan PA 11 remain relatively stable (see Figure A.6).

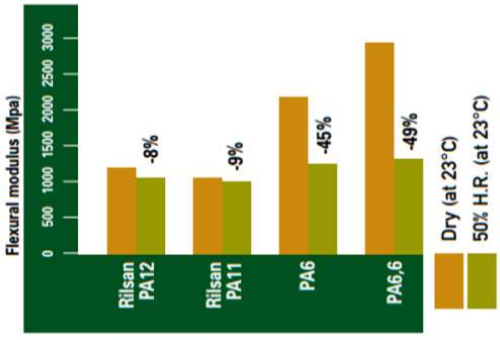


Figure A .6 : Effect of ambient conditions on the flexural modulus of Rilsan ® PA 11 and PA 12 vs PA 6 and PA 6.6. Tests conducted per ISO 178 standard.

Rilsan PA 11 demonstrates very good impact resistance at room temperature as well as at very low temperatures. It offers a significantly higher safety factor than Rilsan PA 12. In Charpy notched impact test at -30 °C, Rilsan PA 11 is twice as resilient as Rilsan PA 12. Its fragile/ductile transition is around 35 °C versus around 50 °C for Rilsan PA 12. This benefit of Rilsan PA 11 is equally seen in plasticised products. Glass transition temperatures are similar for Rilsan PA 11 and PA 12 (a slight advantage of some 5 °C for Rilsan PA 11) and do not explain differences in performance between the products. This is due to the finer crystalline grid and spherulitic structure in Rilsan PA 11. Its impact resistance is also influenced by molecular weight and polydispersity. The impact resistance of Rilsan PA 11 at low temperature is twice that of Rilsan PA 12 (Figure A.7).

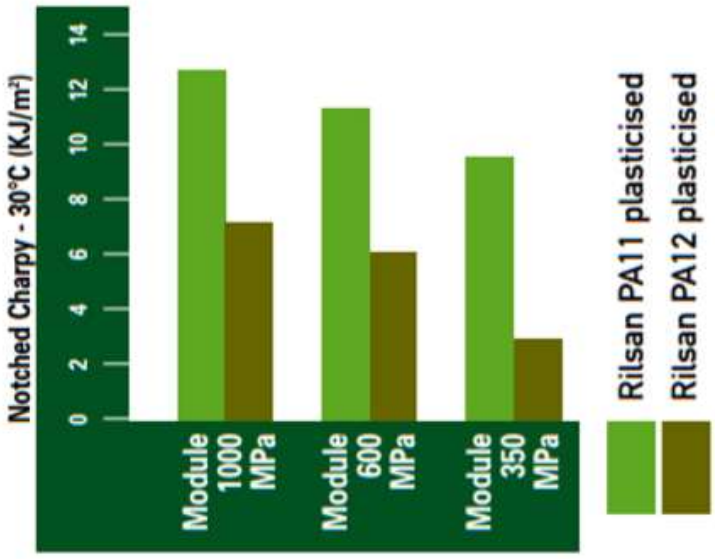


Figure A .7: Comparative impact resistance of Charpy notched plasticised Rilsan® PA 11 and PA 12 (-30°C), per ISO 179/1eA standard.

Compared to other engineering polymers, Rilsan PA 11 features good abrasion resistance and crack propagation resistance. This is largely due to its perfectly smooth surface finish, which induces an extremely low friction coefficient. Rilsan PA 11 features greater abrasion resistance than Rilsan PA 12.

## A.4 Long-term performance

The notion of a material's lifetime is an important factor when designing components requiring long-term performance in specific operating conditions. As a rule, Rilsan PA 11 features viscoelastic behaviour at ambient temperature. However, under permanent stress, above a certain limit, Rilsan PA 11 undergoes plastic deformation. Parts made from Rilsan PA 11 perform very well in a wide variety of climates around the world. Rilsan PA 11 is particularly resistant to degradation from the combined effect of the sun's rays and rainwater (see Figure A.8). The use of stabiliser packages also helps to further increase the weathering resistance of natural and coloured grades.

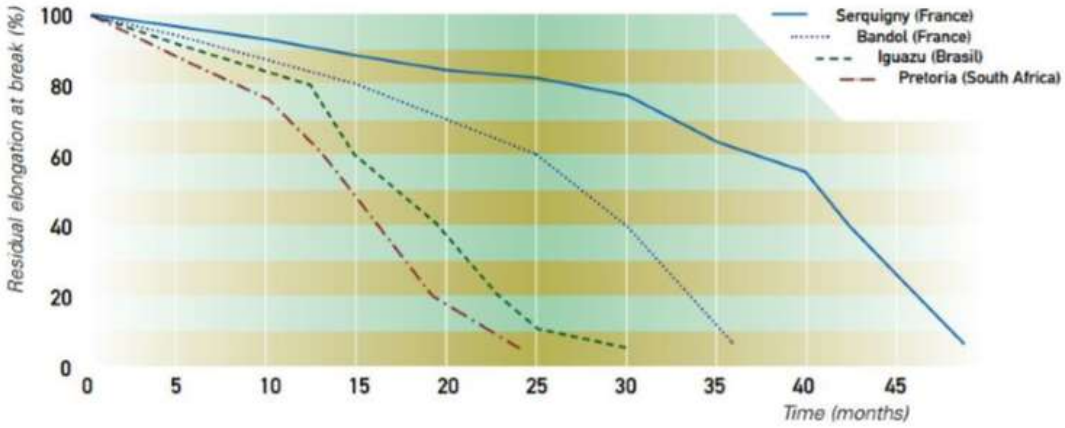


Figure A .8 : Weathering of Rilsan ® PA 11 based on exposure site.

## A.5 Chemical resistance

Rilsan PA 11 offers an ideal balance between the resistance of polyamides to grease and hydrocarbons and the resistance to acids, bases and salts of polyolefins. The excellent chemical resistance of Rilsan PA 11 is reflected both in high dimensional stability under harsh conditions and in the non-degradation of the polymer matrix. Additionally, Rilsan PA 11 features greater resistance to hydrocarbons than Rilsan PA 12, making it the ideal material for highly demanding applications in the oil and gas industry, such as offshore flowlines.

Rilsan PA 11 features outstanding resistance to oils, hydraulic fluids, and fuels. As a general rule, Rilsan PA 11 offers better barrier properties to gases and liquids than other flexible thermoplastics or rubbers. In particular, it is twice as impermeable to fuels and hydrocarbons versus PA 12. Because of the high cohesive energy density and their crystalline state, the polymers are soluble only in few liquids of similar high

solubility parameter at which are capable of specific interaction with the polymers. Polyamides are only weakly affected by non-polar solvents. However, because of the presence of the polar groups, Polyamides are sensitive to polar solvents, particularly water. Polyamides have very high resistance to aliphatic and aromatic solvents, engine fuels, lubricants, animal and vegetable oils, and aqueous solutions of many inorganic chemicals. Polyamides are not very resistance to acids, phenols, certain oxidizing agents, and chlorinated hydrocarbon (see Figure A.9).

G = Good

L = Limited (swelling of Rilsan® PA11 – suitability depends on specific use and duration)

P = Poor

* slight browning; ** swelling action

| CHEMICAL AGENT | CONCENTRATION (100%) | PERFORMANCE 20°C | 40°C | 60°C | 90°C |
|---|---|---|---|---|---|
| **Mineral acids** | | | | | |
| Hydrochloric acid | 1% | G | L | P | P |
| | 10% | G | L | P | P |
| Sulphuric acid | 1% | G | L | L | P |
| | 10% | G | L | P | P |
| Phosphoric acid | 50% | G | L | P | P |
| Nitric acid | any concentration | P | P | P | P |
| Chromic acid | 10% | P | P | P | P |
| Sulphur dioxide | | L | P | P | P |
| **Mineral salts** | | | | | |
| Calcium arsenate | concentrated or boiled solutions | G | G | G | |
| Soda carbonate | " | G | G | L | P |
| Baryum chloride | " | G | G | G | G |
| Potassium nitrate | " | G* | L* | P | P |
| Di-ammonium phosphate | " | | G | G | L |
| Trisodic phosphate | " | G | G | G | G |
| Alumina sulphate | " | G | G | G | G |
| Ammonium sulphate | " | G | G | L | |
| Copper sulphate | " | G | G | G | G |
| Potassium sulphate | " | G | G | G | G |
| Sodium sulphide | " | G | L | L | |
| Calcium chloride | " | G | G | G | G |
| Magnesium chloride | 50 % | G | G | G | G |
| Sodium chloride | satured | G | G | G | G |
| Zinc chloride | satured | G | G | L | P |

Figure A .9: Chemical resistance of Rilsan ® polyamide 11.

**Processing of Rilsan ® polyamide 11**

With a relatively low melting temperature, good melt fluidity and a high speed of recrystallization, Rilsan PA 11 is well-suited to a wide range of processing technologies: extrusion, extrusion-blow moulding, injection moulding, injection-blow moulding and rotomoulding.

Rilsan PA 11 grades are supplied in the form of granules in moisture proof sealed bags or octavins. Rilsan PA 11 granules do not require pre-drying before use. However, if the packaging has been left open and exposed to air for more than two hours, the product will need to be re-dried under specific conditions.

Due to its chemical structure, Rilsan PA 11 has lower moisture pick-up than other polyamides (PA 6, PA 66, etc.). This low water absorption provides excellent dimensional stability and causes only minimum variations in its mechanical and electrical properties. Rilsan PA 11 is produced by the poly-condensation of amino acid.

As a result, it undergoes an equilibrium reaction with water as shown by the following simplified formula:

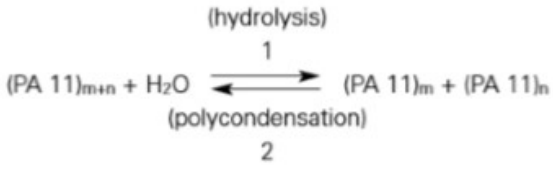


Figure A .10: Rilsan PA 11 produced by the poly-condensation of amino acid.

The presence of excess water promotes hydrolysis by reducing the length of the molecular chains. This change will result in a significant drop in mechanical properties but may not always be evident in the form of surface blemishes such as frosting or bubbles. Since excess moisture can pose problems during the processing of Rilsan PA11, it is always important for the granules to be kept dry. Necessary precautions should be taken to prevent any moisture pick-up during processing.

To prevent moisture pick-up, Rilsan PA11 should first be brought up to the temperature of the plant to prevent any condensation of the ambient moisture as the bags are opened. Additionally, it is essential for the product to be processed within two hours of opening the bag. If either of these conditions is not fulfilled, Rilsan PA 11 granules should be vacuum dried for at least 4 hours at a temperature between 80 °C and 90 °C. The migration speed of the moisture to the surface of the granules determines drying time. Raising the temperature does not significantly reduce drying time and presents a risk of oxidation.

# Appendix B: Rilsan PA11 for coatings

The information below is taken from Arkema company brochures [179].

Rilsan® polyamide resin is produced from castor oil obtained from the widely cultivated Ricinus communis. Castor oil is 100% vegetable, biodegradable, natural, non-toxic and renewable. Rilsan® Fine Powder is thus a thermoplastic not directly impacted by variations in crude oil prices. Moreover, Rilsan® Fine Powder is environmentally sound. Rilsan® Fine Powder is the right product for customers in search of eco-design. Rilsan® polyamide resins require less non-renewable energy than most performance polymers and offer a responsible choice for the environmentally aware.

Main benefits of Rilsan® fine powders include:

- Outstanding flexibility.
- Excellent impact resistance.
- Resistance to a wide variety of chemicals.
- Wide service temperature range.
- Low density.
- Low moisture picks up (high dimensional stability).
- Unrivalled wear resistance.
- Proprietary micronisation process producing a wide diversity of particle size distribution and formulations.

Rilsan® Fine Powders are constantly evolving and developing to meet your needs. Our proprietary micronisation process can produce a wide range of uniform particle sizes, offering a powder matched to your processing and performance requirements.

Metal coating

There is a Rilsan® Fine Powder for every standard powder coating method in use today. A variety of colours is available, produced by either the dry blend or the mass coloration process. The mass colour process provides a uniform finish colour and superior UV stability. Whatever the coating method used, careful surface preparation and proper primer application are necessary to achieve optimum performance.

T and FB grades have an average particle size around 100 microns. They are designed for the fluidized bed dip coating process. A desirable coating thickness between 250 and 500µm can be achieved.

These polyamide powders have an average particle size around 30 microns and are designed for the electrostatic spraying process. A desirable coating thickness between 80 and 150 µm can be achieved.

Successful results in a wide variety of applications.

Combining beauty and function, Rilsan® coatings offer a solution for the most demanding applications. The Rilsan® brand has become the reference for industries around the world looking for the ultimate solution in metal protection.

a) Automotive and transportation: spline shafts, sliding door and seat rails, springs, brackets, clips and safety belt fasteners

- Exceptional abrasion resistance.
- Noise and vibration dampening.
- Stone chipping resistance at low temperatures.

b) Fluid transfer: pipes and fittings, valves, flanges, couplings, flow meters, injection and production tubing

- Anti-corrosion properties.
- Compliance with the most demanding specifications for drinking water contact.
- High resistance to hydrocarbons and water treatment chemical.

c) Building and electrical: outdoor furniture, lamp posts, electrical cabinets and clips, bolts and screws, etc.

- Long term resistance to extreme maritime environments.
- Excellent outdoor ageing properties.
- Graffiti resistance and fire resistance.
- Electrical insulation.

d) Textile / printing / food / healthcare: undergarment wires and adjustors, printing and textile rollers, pharmaceutical and food processing equipment, hospital beds, wheelchairs, and ambulance stretchers, etc.

- Unique warm-to-the-touch, smooth surface finish with low friction.
- Easy to clean, high resistance to chemicals, inks, detergents and heat.
- Suitable for dyeing.
- Machinable.
- Limits bacterial growth.

e) Wire articles: dishwasher baskets, shopping carts, shelving, various cleaning trolleys

- Very easy processing.
- Excellent resistance to alkaline and chlorinated hot water.
- Bendable.
- Combines the best of thermoplastic impact resistance and thermoset hardness.

Specific properties of Rilsan® Coating

| | | |
|---|---|---|
| **Hardness measured with a Persoz pendulum** at 20°C | ISO 1522 | 200-280 |
| **Surface hardness** at 20°C, 10s under load | DIN 53-456 | 80N/mm² |
| **Scratch resistance**<br>Clemen apparatus; load necessary to induce a scratch which reaches the underlying metal for a coating of 0.4 mm thickness | ISO 1518 | 59 N |
| **Pencil hardness** | ECCA T4 | Note: B |
| **Shear strength** | ASTM D 732 | 35-42N/mm² |
| **Impact resistance**<br>Dip coating powder (thickness 350 µm)<br>ES powders (thickness 100 µm) | ASTM G14<br>ISO 3678<br>ISO 6272 | > 2 J<br>> 2.5 J<br>> 19 J |
| **Abrasion resistance**<br>Taber abrasimeter (wheel type CS 17, load 1 kg)<br>Loss of weight after 1,000 cycles | ISO 9352 | 15mg |
| **Coefficient of friction**<br>Black powders | NFT 54-112 (8)<br>Static K<br>Dynamic K | <br>0.15-0.3<br>0.05-0.2 |
| **Flexibility**<br>Conical mandrel folding | ISO 6860 | > 35% |
| **Specific heat** | | 2.09kJ/kg.K |
| **Thermal conductivity** | | 0.29 W/mK between 50° and 170°C |
| **Latent heat of fusion** | | 83.7kJ/kg |
| **Inflammability**<br>measured at a thickness greater than 3 mm to eliminate the influence of the substrate | ASTM D 635 | self-extinguishing |
| **Resistance to boiling water**<br>after 2,000 hours; neither bubbing nor modification | ISO 1521 | Excellent adhesion |
| **Resistance to outdoor exposure** | ASTM D 1235 | 3 years Florida exposure: Excellent adhesion |
| **Resistance to salt water** | | No corrosion after 10 years exposure |
| **Salt spray resistance** | ISO 9227on scribed primed plates (testing according to WIS 4-52-01) | < 1mm corrosion after 2000 hours |

Chemical resistance

- Rilsan® coating resistance as a function of temperature

In general, Rilsan® coatings have good resistance to inorganic salts, alkalis, most solvents, and organic acids. Greater caution must be observed in applications involving inorganic acids, phenols and certain chlorinated solvents. In such cases, it is advisable to consult the Arkema's Technical Service Department, specifying the practical problem involved: e.g nature of metal to be protected and the temperature and chemical composition of the liquid.

| Resistance (°C) | 20 | 40 | 60 | 90 |
|---|---|---|---|---|
| **Inorganic bases** | | | | |
| ammonium hydroxide (concentrated) | G | G | G | G |
| ammonia (liquid or gas) | G | G | | |
| lime-wash | G | G | G | |
| potassium hydroxide (50%) | G | L | P | P |
| sodium hydroxide (5%) | G | G | L | |
| sodium hydroxide (10%) | G | L | L | |
| sodium hydroxide (50%) | G | L | P | P |
| **Inorganic acids** | | | | |
| chromic acid (10%) | P | P | P | P |
| hydrochloric acid (1%) | G | L | P | P |
| hydrochloric acid (10%) | G | L | P | P |
| nitric acid (all concentrations) | P | P | P | P |
| phosphoric acid (50%) | G | L | P | P |
| sulphuric acid (1%) | G | L | L | P |
| sulphuric acid (10%) | G | L | P | P |
| sulphuric trioxide | L | P | P | P |
| **Inorganic salts** | | | | |
| alum | G | G | G | |
| aluminium suplhate | G | G | G | G |
| ammonium nitrate | G | G | G | |
| ammonium sulphate | G | G | L | |
| chlorides (barium/ calcium /saturated sodium) | G | G | G | G |
| calcium arsenate | G | G | G | |
| calcium sulphate | G | G | L | |
| copper sulphate | G | G | G | G |
| diammonium phosphate | G | G | L | |
| magnesium chloride (50%) | G | G | G | G |
| potassium ferrocyanide | G | G | G | |
| potassium nitrate | G[1] | G[1] | P | P |
| potassium sulphate | G | G | G | G |
| sodium carbonate | G | G | L | P |
| sodium silicate | G | G | G | |
| sodium sulphide | G | L | L | |
| trisodium phosphate | G | G | G | G |

| Resistance (°C) | 20 | 40 | 60 | 90 |
|---|---|---|---|---|
| **Other inorganic products** | | | | |
| agricultural sprays | G | G | | |
| bleach solution | L | P | P | P |
| bromine / chlorine / fluorine | P | P | P | P |
| hydrogen | G | G | G | G |
| hydrogen peroxide (20 volumes) | G | L | | |
| mercury | G | G | G | G |
| oxygen | G | G | L | P |
| ozone | L | P | P | P |
| potassium permanganate (5%) | P | P | | |
| sea water | G | G | G | |
| soda water | G | G | G | G |
| sulphur | G | G | | |
| **Hydrocarbons** | | | | |
| acetylene | G | G | G | G |
| alcanes (methane, propane, butane, hexane) | G | G | G | |
| benzene | G | G[2] | L | |
| cyclohexane | G | G | L | |
| decalin G | G | G | L | |
| HFA | G | | | |
| naphthalene | G | G | G | L |
| styrene / toluene / xylene | G | G[2] | L | L |
| **Various products** | | | | |
| beer, cider, fruit juices, milk, mustard, vinegar, wine | G | | | |
| crude petroleum, high-octane petrol, kerosene (paraffin), normal petrol, solvent naphta, town gas | G | G | G[1] | |
| greases | G | G | G | G |
| oils | G | G | G | G |
| solutions or emulsions D.D.T. or lindane | G | G | | |
| hydroxy-quionoline (agricultural sprays) | G | | | |
| soap solution | G | | | |
| stearin | G | G | G | |
| turpentine | G | G | G[2] | |

Condition after 18 months contact:
G: Good - L: Limited - P: Poor
1: Slight yellowing - 2: Yellowing - 3: Swelling action

| Resistance (°C) | 20 | 40 | 60 | 90 |
|---|---|---|---|---|
| **Organic acids and anhydrides** | | | | |
| acetic acid | L | P | P | P |
| acetic anhydride | L | P | P | P |
| citric acid | G | G | L | P |
| formic acid | P | P | P | P |
| lactic acid | G | G | G | L |
| oleic / stearic acid | G | G | G | L |
| oxalic acid | G | G | L | P |
| picric acid | L | P | P | P |
| tartaric acid (saturated solution) | G | G | G | L |
| uric acid | G | G | G | L |
| **Various organic compounds** | | | | |
| anethole | G | | | |
| carbon disulphide | G[3] | | | |
| diacetone alcohol | G | G[1] | L | |
| dimethyl formamide | G | G | L | |
| ethylene chlorhydrin | P | P | | |
| ethylene oxide | G | G | L | P |
| furfurol | G | G[1] | L | P |
| glucose | G | G | G | G |
| tetraethyl lead | G | | | |
| tetrahydrofurane | G | G | L | |
| phenols | P | P | P | P |
| **Organic bases** | | | | |
| aniline (pure) | L | P | P | P |
| diethanolamine (20%) | G | G[1] | G[2] | L |
| pyridine (pure) | L | P | P | P |
| urea | G | G | L | L |

| Resistance (°C) | 20 | 40 | 60 | 90 |
|---|---|---|---|---|
| **Salts, esters, ethers** | | | | |
| acetate esters (amyl, butyl, methyl) | G | G | G | L |
| phosphate esters (dioctyl, tributyl, tricesyl) | G | G | G | L |
| diethyl ether | G | | | |
| dioctylphtalate | G | G | G | L |
| fatty acid esters | G | G | G | G |
| methyl sulfate | G | L | | |
| **Alcohols** | | | | |
| benzyl alcohol | L | P | P | P |
| butanol | G[2] | L | P | P |
| ethanol (pure) | G[2] | G[2] | L | |
| glycerin (pure) | G | G | L | P |
| glycol | G | G | G | P |
| methanol (pure) | G[2] | L | P | |
| **Chlorinated solvents** | | | | |
| carbon tetrachloride | P | P | | |
| methyl bromide | G | P | | |
| methyl chloride | G | P | | |
| perchloroethylene | G | G | L | |
| trichloroethane | L | P | | |
| trichloroethylene | G | L | | |
| **Adehydes and ketones** | | | | |
| aldehydes (acetaldehyde / benzaldehyde / formaldehyde) | G | L | P | |
| acetone (pure) | G | G | L | P |
| cyclohexanone | G | L | P | |
| methylethylketone (MEK) methylisobutylketone (MIBK) | G | G | L | P |

Condition after 18 months contact:
G: Good - L: Limited - P: Poor
1: Slight yellowing - 2: Yellowing - 3: Swelling action

# Appendix C: The Geldart classification of the particles chart of fluidisation modes

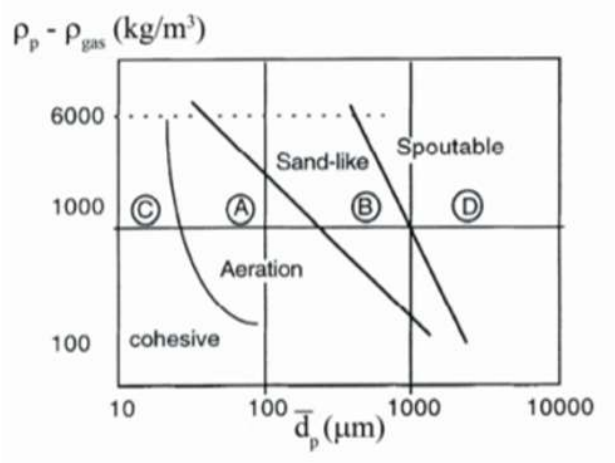


Figure C. 1 : The Geldart classification of particles chart. Four types of Geldart powders being A, B, C and D [137].

From the smallest to the largest particles, the four groups in Figure C.1 are: C, A, B, and D. The group C particles are cohesive or very fine powders, which are often very difficult to fluidise. Starch and flour are e.g. group C particles. Materials having a small mean particle size and/or density less than 1.4 g/cm$^3$ are grouped into group A. Particles from this group fluidise well and as group A particles have the aeration properties required for coating purposes, particles suited for coating often come from this group. The group B particles are sand like particles with mean particle diameters roughly between 40 microns and 500 microns and density between 1.4 g/cm$^3$ and 4 g/cm$^3$. The fluidisation mode of this type of particles is highly affected by the formation of gas bubbles in the bed and group B particles often fluidise well. As the air flow rate required to fluidise group D particles in necessarily high, group D particles are not normally processes in conventional fluid beds [137,138].

# Appendix D: Twin Screw 15 cm3 Xplore ® Micro- DSM

## D.1 Technical specifications

- Abrasion resistant barrel (hardness 60 HRc), coating hardness 2000 Vickers.
- Barrel and screws chemically resistant between pH 0 – 14.
- Batch volume: 15 ml (Vari-BatchTM: 3, 7 and 15 ml).
- Vertical barrel, fluid-tight - Heated by 8 thermo cartridges and controlled by 7 thermo couples (temperature gradient possible).
- Temperature control: in the melt and 2x3 barrel heating zones.
- Detachable conical screws, fully intermeshing (hardness 54 HRc), coating hardness 1000 Vickers.
- Maximum operating temperature 400 °C (optionally 450 °C).
- Easy to clean with dedicated cleaning cycle.
- Heating time (from 80 to 240 °C) in less than 10 min.
- Cooling time (from 240 to 80 °C) with cooling water in less than 10 min, with air in less than 35 min.
- Maximum vertical force: 8 kN (optionally 9 kN).
- Screw speed: continuously variable 1 - 250 RPM.
- Hopper volume : 15 ml;
- Supply voltage: 208 - 240 V AC, others on request.
- Main drive: DC controlled, 900 Watt.
- Computer control via : USB port;
- Maximum torque: 10 Nm per screw.
- Overall dimensions (h x b x d): 103 x 73 x 42 cm3 - Weight 150 kg.


Figure D. 1: Overall dimensions of the twin screw 15 cm3 Xplore ® Micro-DSM compounder [166].

## D.2 Screw design

The two screws are specially designed according the Taylor Couette geometry to simulate the dynamic of the melt inside the industrial scale extruder and to generate reproducible and stable data.

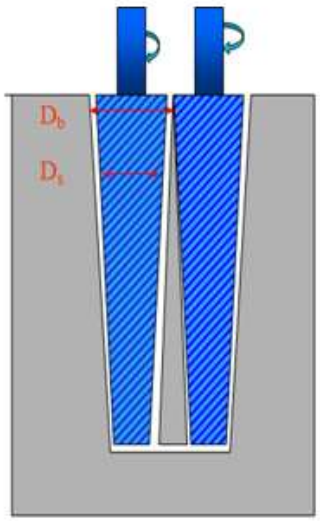


Figure D. 2 : Screws of the MC 15 Xplore Micro DSM compounder designed according the Taylor-Couette geometry.

According to the Tailor-Couette geometry [166]:

$$Db - Ds = 0.1mm$$

where $Db$ is the diameter of the barrel; $Ds$ is the diameter of the screw.

# Appendix E: Fluidized bed dipping process [180]

## E.1 Principle of the process

Fluidized bed dip-coating consists of immersing a heating part into powder suspended by rising air flow. As soon as the Rilsan® powder comes into contact with the preheated article, it melts and forms a film on the surface of the component. This process produces a consistent thickness, even on parts with complex profiles (internal and external coatings in one operation). The dip-coating process is efficient (100% transfer) and straightforward. All Rilsan® T/FB grades have been developed specifically for this technology along with a tailored primer range (For more information, please refer to the leaflet on Surface pre-treatments and primers).

## E.2 Criteria for choosing this process

Dip-coating application simplifies the coating process by combining excellent productivity with outstanding thickness reproducibility. It can be easily automated and is generally selected depending on the following criteria:

a. Thickness of the part: The process is particularly suitable for parts with a metal thickness of at least 3 mm. For small diameter wire articles, a post fusion operation may be required following the dip-coating operation.
b. Thickness of coating: The process allows the application of Rilsan® coatings with a thickness from 250 to 500 µm. For very massive parts, it is possible to apply thicker coatings by increasing dipping time, or by successive dipping operations.
c. Size of the part: The dimension of the part determines the size of the tank. Very heavy or very long components (tubes) can be coated by this method but will require specific handling equipment.
d. Nature of the substrate: Any type of material that can withstand the necessary oven preheat temperatures.

## E.3 Equipment for dip coating

Fluidizing Tank

The fluidizing tank should consist of 2 stainless steel sections separated by a porous tile. The air used for fluidization should be at ambient temperature, clean and dry. In the case of large tanks, air from a blower can be used. The temperature of the Rilsan® powder during fluidization should not exceed 60°C. Special fluid beds can be made with jacketed walls that circulate water to cool the powder.

Air Exhaust

An air exhaust should be installed near the top of the tank to capture dust particles that could contaminate the immediate environment.

Preheating Oven

Forced air circulation oven is recommended (air flow: minimum 6 m/s). Capability of the oven will depend on the coated parts: it should be designed to permit a maximum temperature of 330°C for massive parts and 420°C for thin parts or wire articles. Not all ovens have the same behaviour and different results can be obtained from one oven to another.

Operating Conditions

When handling Rilsan® Fine Powders, users are advised to refer to the product's safety datasheet and current regulations on the use of powder coatings.

Surface Treatment – Primer

A surface preparation is necessary, requiring cleaning, surface treatment and primer application. For further information, please refer to the leaflet Surface pre-treatments and primers.

Preheating Conditions

For any given part there is a minimum temperature below which it is not possible to obtain a coating with a smooth surface. There is also a maximum temperature above which coating and/or primer degradation may occur. Because parts usually have varying thicknesses, it is essential to adjust the pre-heating time as well as the temperature. The preheating temperature and time are determined respectively by the

minimum and maximum thickness of the part to be coated. It should always allow suitable curing conditions for the primer. Please refer to Surface pre-treatments and Primers. Large variation in metal thicknesses may render the part difficult to coat by dipping method. This should be taken into consideration when designing the part. To obtain a high quality Rilsan® coating over the entire surface, the temperature of the part should be as even as possible, around 280 °C -300 °C at the time of dipping for massive parts.

Masking

It is possible to locally mask areas that do not require coating by using caps, tapes, pastes or mineral fibres.

Handling and Touch-Up Of The Parts

The jig or hanger should be fastened to the part to allow good movements (shaking) of the part. Where possible, it is preferable to attach the hanger to an area of the part that does not require coating. Hanger marks can be touched up with a suitable epoxy or polyester resin.

# Appendix F: Arkema method adhesion test

Operations required to perform the test to measure the adhesion of a substrate coating is explained below. The method is for thermoplastic and thermosetting coatings.

The principle of this test is to evaluate the strength of a coating applied to metal support by adhesion measurement. The tests consist of peeling a sectioned strip from the coating and evaluating the tear resistance. It is a destructive test.

To perform the test the necessary equipment is metal plates/ cold rolled steel/aluminium, tubes, cutting tool with a cutting width of 10 mm, a ruler and a cutter.

Adherence assessment is performed according to:
- Adhesion control by detachment ARKEMA method
- According to WIS 4-52-01 specifications (V-cut)
- Standard EN 10310: 2003 (cross).

Description of the different approaches:

**1) Adhesion control by detachment ARKEMA method. Method inspired by NFT 58-112 which was cancelled in November 2011. No replacement standard.**

- Using a cutter apply 2 parallel notches spaced 10 mm on a length, sufficient to delimit a strip of at least 30 mm of length (Figure F.1).

Figure F. 1: Strip delimitation onto the coated plate for adhesion test.

- Make a third notch perpendicular to the two parallels. Insert the tool into the latter (Figure F.2), grasp the raised end, and try to take it off, pulling regularly from the metal support (Figure F.3).

Figure F. 2: Position of the testing tool.

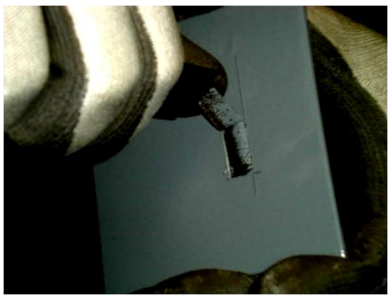

Figure F. 3: grasped raised end due to constant pulling force.

**2) According to WIS 4-52-01 specifications (V-CUT)**

- Using the cutting tool, make two incisions of 20 mm through the film to the surface of the metal, forming a "V" with an angle between 30 and 35 °.
- Detachment is evaluated from the tip of the "V".
- The cutter must be inserted horizontally under the coating from the tip of the "V", so that the tip of the blade is in contact with the metal surface. Make a lever action upwards, in a single vertical movement to peel off the coating.
- The adhesion loss of the coating in mm is measured between the tip of the “V” and the nearest point where the coating still adheres to the steel.

3) EN 10310: 2003 (on the cross)

- Using the cutting tool, straight incisions of 60 mm long must be done in the coating to the surface of the metal to form an X with an approximately an angle of 30 ° at the point of intersection.
- The tip of the cutting tool must be inserted horizontally under the coating at the point of intersection of the X incisions at 30 °, so that the tip of the blade is in contact with the surface of the metal. Lever action against the steel rod to move the plate away from the blade, from the metal surface, upwards, in a single vertical movement have to be applied to rip off the coating.

- The adhesion loss of the coating in mm is measured between the point of intersection of the X-incisions and the nearest point where the coating still adheres to the steel.

For the determination of peel adhesion by detachment using ARKEMA method, the result is expressed by a score from 0 to 4.

Grade 0: No adhesion. The separation of the coating is done as soon as the tool passes. Figure F. 4 shows the results onto the coated plate.

Figure F. 4: Score 0 results sample.

Grade 1: The coating separates easily, but with little resistance to tearing force, Figure F.5.

Figure F. 5: Score 1 results sample.

Grade 2: As score 1, but there are a few evenly distributed strong hooking points, Figure F.6.

Figure F. 6: Score 2 results sample.

Grade 3: The coating separates irregularly: there is a perfect connection on about 50% of the surface, Figure F.7.

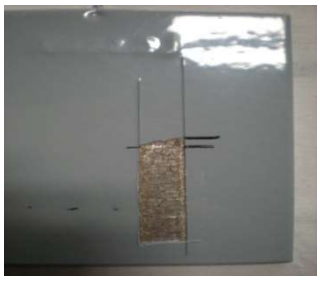

Figure F. 7: Score 3 results sample.

Grade 4: Good grip; no detachment, Figure F.8.

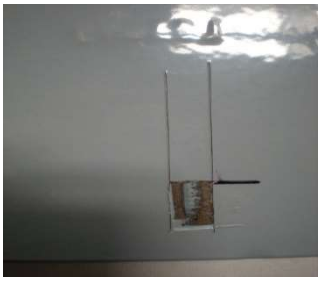

Figure F. 8: Score 4 results sample.

4) WIS 4-52-01 specifications

The result of adhesion by detachment is expressed in millimetres ignoring the first millimetre.

5) Standard NF EN 10310

The result of adhesion by detachment is expressed by a quotation.

-Quotation 1: No lifting of the coating, only that caused by the insertion of the tool blade at the intersection point (nominally less than 1mm).

-Quotation 2: No more than 2mm of adhesion breakage between the coating and the steel substrate.

-Quotation 3: No more than 3mm of adhesion breakage between the coating and the steel substrate.

-Quotation 4: No more than 4mm of adhesion breakage between the coating and the steel substrate.

-Quotation 5: No more than 5mm of adhesion breakage between the coating and the steel substrate.